Modelling of Gasification of Biomass in Dual Fluidized Beds

Seerup, Rasmus

Publication date:
2018

Document Version
Publisher's PDF, also known as Version of record

Modelling of dual fluidised bed gasification

Rasmus Seerup

PhD Thesis

2018

DTU Chemical Engineering
Department of Chemical and Biochemical Engineering

Technical University of Denmark

Modelling of dual fluidised bed gasification

Rasmus Seerup

Ph.D. Thesis

Principal Supervisor:	Kim Dam-Johansen	DTU
Co-Supervisor:	Weigang Lin	DTU

2018

DTU Department of Chemical and Biochemical Engineering

Combustion and Harmful Emission Control Research Centre

Table of content

List of figures

List of tables

Preface

The Ph.D. project is carried out as part of the Sino-Danish Center (SDC) program between the Chemical and Biochemical Department at the Technical University of Denmark and the Institute of Process Engineering at the Chinese Academy of Sciences. The project is co-funded by the Innovation Fund Denmark with the collaborator project of Development and Application of Circulating Fluidised Bed Gasification of Biomass (DANCNGAS)

The Ph.D. study was carried out from November 2013 to July 2017. The project was supervised by Professor Kim Dam-Johansen and Associate Professor Weigang Lin. The employment is under the DTU.

As the project description indicates, the focus is on fluidised bed gasification of biomass. There are several challenges regarding biomass gasification, but the focus has been narrowed down to tar formation in dual fluidised beds. The thesis shows the most critical underlying mechanisms for tar formation in dual fluidised bed gasification of biomass. This knowledge is used with mathematical models to investigate the tar formation and make recommendations for process optimisation and design changes.

The project has been partially conducted in China at the Chinese Academy of Sciences, Institute of Process Engineering, and in Denmark at the Technical University of Denmark, Department of Chemical and Biochemical Engineering. The torrefaction experiments have been conducted in China with a big help from Ze Wang to make the equipment work. The modelling part has been done in Denmark.

I would like to give my thanks to Ze Wang for helping with the experimental setup in China. I would also like to thank Michael Locht Michelsen for his input to the model solution method.

Abstract

The thesis investigated tar formation in fluidised bed gasification systems by starting with an introduction to gasification technology and the composition of biomass. Biomass consists of cellulose, hemicellulose, and lignin, which are referred to as pseudo-compounds. All the pseudo-compounds form tar, but lignin is the primary source for phenolic tar. The tar formation and evolution in gasification is similar to that of pyrolysis. The phenolic tar is degraded to phenol, which undergoes unimolecular removal of CO to form cyclopentadienyl. Cyclopentadienyl is the basis for repolymerisation to form polyaromatic hydrocarbons.

A pre-torrefaction experiment has been conducted. It showed a considerable tar release during torrefaction. In combination with dual fluidised bed systems, the tar formation in the gasifier will be reduced by separation of the torrefaction gas. To minimise the loss of energy of the separated tar filled gas, the gas may be used as fuel for the combustor or the co-production of valuable chemicals.

With the understanding of the tar release from biomass and tar evolution, the reactor system is simulated to understand the effect of process parameters on the tar yield. This is done by the use of three mathematical models. One for the devolatilisation of biomass particles under gasification conditions, one for the evolution of tar under gasification conditions, and one for the fluid dynamic and coking rate. The models are used to argue for a novel idea for tar removal by coke formation. Instead of converting the tar to useful product gasses, tar is catalytically reformed to coke and transported to the combustor and used as a fuel for heating the bed material.

The gas phase model shows that tar composition is primarily affected by the severity of the temperature. To a small degree some of the formation of larger tar species like naphthalene may be reduced by introducing radical forming gases that react with cyclopentadienyl to form benzene or light C2 and C4 gases. It is, however, unlikely that this will be economically feasible. Simulation of recirculation of the gasification product gas shows an increase of naphthalene if the catalyst for reforming is not utilised.

Dansk resume

Tesen undersøger tjære formation i forbindelse med fluidiseret leje gasifiseringssystemer, ved at starte med en introduktion til gasifiseringsteknologi og sammensætning af biomasse. Biomasse består af cellulose, hemicellulose og lignin, som også benævnes som pseudokomponenter. All pseudokomponenterne skaber tjære, men lignin er den primær kilde til phenolisk tjære. Tjære dannelse og udvikling under gasifisering er lignende det under pyrolyse. Phenoliske tjære bliver nedbrudt til phenol som gennemgår unimolekylær eliminering af CO som skaber cyclopentadienyl. Cyclopentadienyl er basis for repolymerisering til skabelse af polyaromatiske kulbrinter.

Et torrefaktion eksperiment er blevet udført. Det viser en betydelig frigivelse af tjære under torrefacktionen. I kombination med dobbelt fluidiseret leje systemer, vil tjære formationen i gasifieren blive reduceret ved separering af torrefaktionsgassen. For at minimere energi tabet af den separerede tjærefyldte gas, kan gassen bruges som brændsel til kombustoren eller til biproduktion af værdifulde kemikalier.

Med forståelse for frigivelse af tjære fra biomasse og tjære evolution, er reaktor systemet simuleret for at forstå effekten af procesparametrene på tjære udbyttet. Dette er gjort ved brug af tre matematiske modeller. En for afgasning af biomasse under gasifiserings betingelser, en for evolutionen af tjære under gasifiserings betingelser, og en for hydrodynamikken og koks dannelse. Modellerne er brugt til at argumenter for en ny ide til at fjerne tjære ved koks dannelse. I stedet for at omdanne tjæren til brugbar produktgas er tjæren omdannet to koks og transporteret til kombustoren og brugt som brændsel for opvarmning af lejematerialet.

Gas fase modellen viser at tjære sammensætningen primært er påvirket af intensiteten af temperaturen. I en mindre grad er dannelsen af større tjære arter som naphthalene reduceret ved introduktionen af radikale skabende gasser, som reagere med cyclopentadienyl for at skabe benzene og lette C2-C4 gasser. Det er dog usandsynligt at dette vil være økonomisk rantabel. Simulering af recirkulation af gasifiseringsproductgaseen viser en stigning af naphthalene hvis katalytisk omdannelse ikke bliver brugt.

1 INTRODUCTION

Today there is a large focus on renewable sources to create a sustainable society. This focus has been high on the energy sector, where oil and coal is a large resource for energy generation. These resources are not regenerated with the same rate as they are consumed, and thus there is a focus on finding other resources. One alternative may be biomass. Biomass can be utilised in a similar way as coal; it can be burned for heat generation or it may be gasified. The gasification product may be used with gas turbines for energy production, or it may be used in Fischer–Tropsch processes to form chemicals or liquid fuel. Depending on the use of the product gas there are varying requirements for the product gas. For Fischer–Tropsch processes the hydrogen content has to be high relative to CO, and the tar concentration low to avoid deactivation of the catalyst.

For this thesis, the focus will be on steam gasification of biomass in dual fluidised beds. The dual fluidised bed utilises pure steam gasification relying on heat from an external source. This process benefits from the conversion of not just the biomass but also the water to a gaseous product. The product gas has a high concentration of hydrogen and avoids a dilution of the product gas by nitrogen. This gives a relatively high energy density.

The problem with gasification of biomass in dual fluidised bed lies in the tar formed during gasification. Because the process is conducted at relatively low temperatures and purely with steam, tar reforming is a problem. Cleaning the gas before further use is a possibility but requires large investments in equipment and gives waste problems.

Optimally, the tar formed during the gasification should be reformed to product gas. This may be done by catalyst. These are often used downstream of the gasification process because they suffer from deactivation by coke formation when used inside the gasification chamber.

The thesis will thus investigate possibilities to reduce the tar in the product gas from dual fluidised beds.

The thesis structure is built up with a literature review to give the elementary understanding of the gasification process and the pheromone related to the tar formation. This also includes some of the models that are being used to model biomass devolatilisation and gas formation in bubbling beds. With a knowledge of tar formation, the thesis introduces pre-torrefaction experiment for the investigation of low-temperature pre-treatment for reducing the tar formation.

The thesis moves on to investigate the operating parameter effect on the tar formation and evolution. This part of the thesis is divided into three to simplify the models. The particle model is used to understand the devolatilisation rate of the biomass and whether simplification of the system is valid. The gas phase model focuses on the effect of the gas composition and homogeneous reactions to investigate possible manipulation of the tar evaluation. The reactor model focuses on fluid dynamic condition and the possibility of using a catalyst for novel tar removal approach.

2 LITERATURE REVIEW

2.1 GASIFICATION

Gasification is a general term for processes that convert solid fuels to gaseous fuels. Solid fuel is gasified by endothermic reactions with CO_2 (Eq 2-2) or H_2O (Eq 2-1).

$$\boldsymbol{C(s) + H_2O(g) \rightarrow CO(g) + H_2(g)} \quad +131 \text{ MJ/kmol} \quad \text{(R 2-1)}$$
$$\boldsymbol{C(s) + CO_2(g) \leftrightarrows 2CO(g)} \quad +172 \text{ MJ/kmol} \quad \text{(R 2-2)}$$

Gasification requires energy for the endothermic reactions. The gasification processes can be either allothermal or autothermal depending on how the energy is obtained. For an allothermal process the energy, required by the devolatilisation and gasification, is provided from external sources like hot bed material that is circulated in the system.

For the autothermal process, the energy is provided by exothermal reactions inside the gasifier like partial oxidation (Eq 2-3). This is done by introducing oxygen in a lower amount than the stoichiometric coefficient for full combustion.

$$C(s) + ½O_2(g) \rightarrow CO(g) \quad -111\text{MJ/kmol} \quad \text{(R 2-3)}$$

In this way CO is formed. Depending on the stoichiometric ratio of oxygen, CO_2 will also be formed to a larger or lesser extent. Often there will be a combustion zone in the case of partial oxidation, the energy from the combustion will then subsequently be consumed by the endothermic Boudouard reaction where CO_2 reacts with solid carbon to form CO as shown in reaction (R 2-2).

Gasification results in the gaseous products containing mainly CO and H_2 as shown in reaction (R 2-1) to (R 2-2). For high-pressure systems, there is a small contribution from methanation reaction [1], [2]. Depending on the product gas end use, methane may or may not be a desirable product.

$$C(s) + 2H_2(g) \leftrightarrows CH_4(g) \quad -75 \text{ MJ/kmol} \quad \text{(R 2-4)}$$

The composition of the product gas may be shifted by homogeneous gas phase reactions.

Steam reforming Reaction [3]

$$CH_4 + H_2O \leftrightarrows CO + 3H_2 \quad +206 \text{ MJ/kmol} \quad \text{(R 2-5)}$$

Oxidation [3]

$$CH_4 + ½O_2 \leftrightarrows CO + 2H_2 \quad -36 \text{ MJ/kmol} \quad \text{(R 2-6)}$$
$$CO + ½O_2 \leftrightarrows CO_2 \quad -284 \text{ MJ/kmol} \quad \text{(R 2-7)}$$
$$H_2 + ½O_2 \leftrightarrows CO + H_2O \quad -242 \text{ MJ/kmol} \quad \text{(R 2-8)}$$

Water shift reaction [3]

$$CO + H_2O \leftrightarrows CO_2 + H_2 \quad -41.2\text{MJ/kmol} \quad \text{(R 2-9)}$$

The gas composition is affected by the pressure, temperature, and the steam to biomass ratio for steam gasification.

By increasing the pressure of the reactor the equilibrium of the steam reforming reaction will shift slightly towards methane which is also observed in experiments [4], [5].

High temperature will increase the concentration of hydrogen and CO, but decrease those of CO_2 and methane [4]. This is a consequence of the change of thermodynamic equilibrium. Also, an increase in temperature will increase the conversion.

Steam to biomass ratio (S/B ratio) is defined as (the amount of steam fed to the system divided by the amount of fed biomass on a dry and ash-free basis)[6].

$$\varphi_{SB,wt} = \frac{\dot{m}_{steam} + x_{H_2O} \cdot \dot{m}_{bio}}{\left(1 - x_{H_2O} - x_{ash}\right) \cdot \dot{m}_{bio}} \quad \text{(Eq 2-1)}$$

Where $\dot{m}_j$ is the mass feeding rate of component j, and x_j is the fraction of component j.

A high value of steam to biomass ratio will increase steam reforming rate of tar species[4], [7] and shift the equilibrium towards CO_2 and hydrogen [4].

2.1.1 Types of gasifiers

Gasification has been used since the foundation of the London Gas Light and Coke Company in 1812 [2]. The gasification process has been developed since then. Three types of gasifiers are commonly used in industry: the moving bed, entrained flow, and fluidised beds reactors. The selection of gasifier type has a great impact on the composition and the heating value of the product gas and has different challenges. The main challenges for fluidised bed gasifiers are the high yield of tar in the product gas, bed agglomeration, and scale-up of the reactor. For moving bed gasifiers, the challenges are handling of small particles that clog the bed and temperature control across the radial length of the bed because of poor mixing [8]. The different types of gasifiers are discussed in more details below.

2.1.1.1 Moving bed gasifiers

For the moving bed, the feedstock (biomass or coal) is fed from the top to the reactor column where the particles are slowly discharged from the bottom. The gasification agent (oxygen or air mixed with steam, or CO_2) can be introduced either in the middle of the reactor and moves down (downdraft) or at the bottom and moves up (updraft). Choice of updraft or downdraft affects the placement of the gasification stages and the quality of the product gas.

For the updraft gasifier, the gasification agent, typically steam and air, is sent through the bottom and up through the reactor, where the gasification agent reacts with the feed and generates heat, H_2O, and CO_2. The moving bed is an autothermal gasifier and the heat from combustion is used for the endothermic reaction between the feed, the CO_2, and water to produce hot syngas (CO, H_2). The hot syngas is then drying and pyrolysing the feed as it flows up through the feed [3]. This leads to 4 zones as shown in Figure 2-1. Because the gas leaves the pyrolysis and drying zone as the last part, tar content in the gas is high.

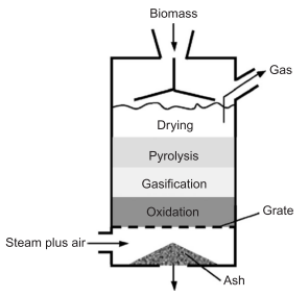

Figure 2-1: Updraft gasifier [3]

For the downdraft gasifier, the air is introduced in the middle of the reactor and follows the feed from the top in a co-current stream, down to the bottom. This forms a combustion zone in the middle and a gasification zone at the bottom. Because the gas passes the high-temperature gasification zone as shown in Figure 2 2, the product gas has a low content of tar in this type of gasifier [3].

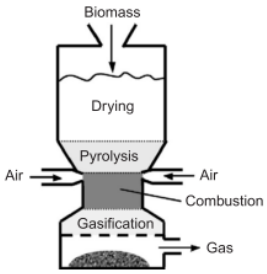

Figure 2-2: Downdraft gasifier [3]

The moving bed process is not suitable to process small particle sizes less than 6mm [2], as these particles clog the bed. The process has a very uneven temperature profile through the reactor.

Moving bed reactors are used in small capacity application<10MW_{th} [3] and was developed to operate with high pressure with the Sasol-Lurgi dry bottom process. With the British Gas/Lurgi (BGL) slagging gasifier, it is also possible to handle some fine particles by injecting them at the bottom of the reactor through tuyères [2]. The molten ash is drained at the bottom, which means that it is possible to operate with feeds with a low ash-melting point.

2.1.1.2 Entrained flow gasifiers

For entrained flow gasifiers, the gas velocity and temperature are high. The particle size is small to ensure that all particles are entrained with the gas, and complete conversion can be achieved. The entrained gasifier reactor is usually used for materials that are easy to grind, e.g. coal. [9], [10].

The feedstock flows co-currently with the gasification agent (oxygen). The reactor operates at the slagging condition. That means that the temperature is above the melting temperature of the ash. The high temperature (typically 1400°C) makes sure that there is no tar in the product gas [2]. The entrained flow gasifier comes in two types of designs, the top fed and side fed. For the top fed gasifier, the feed and the gasification agent are let in at the top of the reactor. Near the inlet, rapid heating and combustion of volatiles from the feed happen, followed by gasification of the remaining char down through the reactor [3].

For the side-fed reactor, the feedstock is introduced together with oxygen through opposite placed jet streams at the lower end of the reactor. The injected fuel is mixed with the gasification agent, which gives a fast reaction and increases temperature well above the ash-melting temperature. The slagging ash is thus separated from the feed and drained from the bottom while gas flows upwards [3].

Entrained flow gasifiers are used in large capacity applications >50 MW [3] like integrated gasification combined cycle plants (IGCC) for gasification of coal, petcoke, and refinery residue [3].

The necessity of small particles for this type of gasifier makes biomass an unfavourable fuel as biomass often requires a relatively large amount of energy for grinding [9], [10]. Furthermore, feeds with a high moisture content like biomass and lignite are not economically favourable to use in entrained flow reactor [3] and molten biomass is very reactive and will tear on the gasifier's refractory lining at the high temperatures [3].

2.1.1.3 Fluidised bed gasifier

In fluidised beds, solid particles behave as a fluid by introducing a high velocity gas flow through the particles. The drag from the gas on the particles generates a force on the particles. The force on the particles makes the bed expand, which allows particles to move around like a fluid.

Two types of fluidised beds are commonly applied for gasification; stationary fluidised beds, and circulating fluidised beds, which are used in medium capacity applications 5-100 MW_{th} [3]. Both

processes utilise an inert bed material for heat transfer inside the fluidised bed. This will contribute to the heat transport in the reactor as the feed collides with the heat carrier [3].

For the **stationary fluidised bed**, the upward gas flow from the bottom is sufficiently high to fluidise the particles, but there is a clear distinction between the dense bed and the freeboard. The stationary fluidised beds operate under the fluidisation bubbling fluidisation.

The fluidised bed has a limited conversion. As fuel particles are reacting the size is decreasing, and eventually reach a size where the gas exceeds the terminal velocity. At this point particles are elutriated from the bed, which may limit the degree of conversion [2]

For the **circulating fluidised bed**, the flow of the gas is higher than that of the stationary bed, and the drag of the gas will carry smaller particles, for which the terminal velocity is exceeded, out of the bed. The particles that are carried with the gas are separated from the gas in a cyclone and recycled back to the bed. The increased agitation of the bed and circulation of feed increases the mixing of gas and solid as well as the carbon conversion. At the same time, the particles that are too big to be carried out with the gas will continue to circulate inside the bed. The particles are thus present in the entire reactor and not limited to the dense phase of the reactor [3][2]. The circulation will increase the mixing inside the reactor and the contact time with the gas, which increases the conversion of carbon. Typical fluidisation regimes for the circulating fluidised bed are fast or turbulent fluidisation.

Stationary and circulating fluidised beds are favourable for biomass gasification because they are able to handle different kinds of feedstock even with high moisture content because of the vigorous mixing [3]. The circulating fluidised bed is less sensitive to particle size, as small diluted particles are recirculated and large particles will be circulated in the fluidised bed [2].

A drawback of fluidised bed processes is agglomeration inside the fluidised bed. In severe cases, the bed may suffer defluidisation and disrupt the gasification process [2].

For utilisation of the fluidised bed for biomass gasification, it is operated at temperatures around 850°C to avoid agglomeration. At this temperature, a part of the tar formed during the devolatilisation of biomass is not degraded. For pure steam gasification, the reforming of tar is not effective at these temperatures. Oxygen can be used to partially combust tar in the product gas at the cost of heating value. For these reasons tar is often a relatively large problem for fluidised bed gasifiers compared to the moving bed and the entrained flow reactor.

2.1.1.3.1 Dual fluidised bed

The dual fluidised bed consists of two interconnected reactors: an endothermal gasifier and an exothermal combustor. The separation of the combustor and the gasifier avoids the dilution of the product gas with nitrogen when air is used for combustion. In the gasification area the particles are fluidised by steam, which is used for gasification to generate the product gas[3] according to reaction (R 2-1).

Unconverted biomass and char from the gasifier are circulated to the combustion area together with inert bed material through a loop seal in the bottom. In the combustion chamber air is used for fluidisation and the material is lifted to the top of the reactor while all fuel is combusted and inert bed material is heated. At the top of the combustion chamber, the hot bed material is separated from the flue gas by a cyclone and returned to the gasification chamber [3], [11].

2.1.1.3.1.1 Temperature profile

When working with the dual fluidised bed it is not possible to keep the temperature constant over the entire bed.

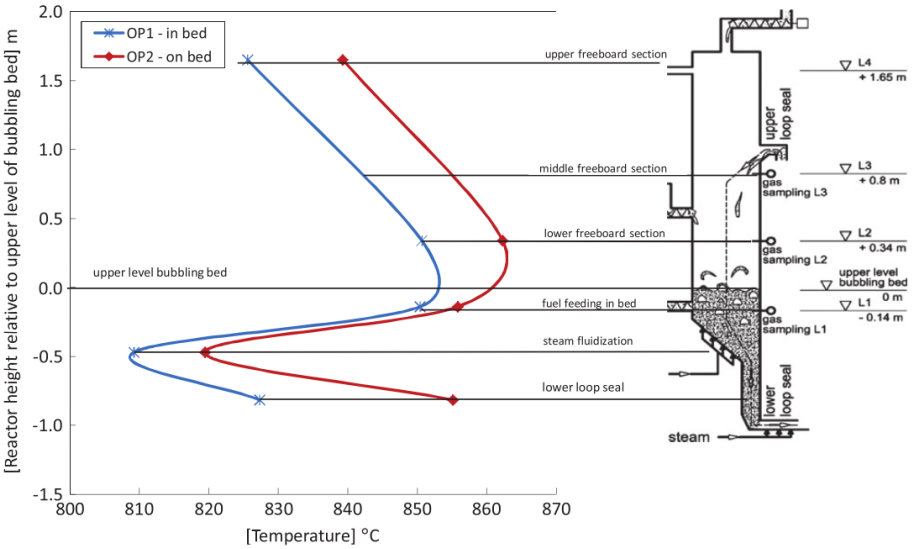

Figure 2-3: Temperature profile for a DFB. OP1 is feeding in-bed. OP2 is feeding from the middle of the freeboard[6]

In Figure 2-3, the characteristics of the temperature profile are shown in a gasification process in the gasification chamber. Two temperature curves which are shown in Figure 2-3 represent operations with two different feeding positions. OP1 is for feeding of fuel into the bed, while OP2 is for feeding of fuel onto the top of the bed. For the two operation conditions, the temperature varies with approximately 45°C. The minimum temperature of the curves is caused by the injection of steam for fluidisation, which is lower than the gasification temperature.

The higher temperature in the solid free area above the dense phase of particles (the freeboard), is due to the heated bed material from the combustor that is fed to the gasifier at the middle of the freeboard. The general cooling in the freeboard is caused by endothermic steam reforming, cracking, and heat loss to the surroundings [6], [12], [13]

2.2 GAS SOLID FLUIDISATION

Understanding the hydrodynamic behaviour of the fluidised bed is important for modelling of the system. The hydrodynamic behaviour of the solid and the gas affects the mixing and contact between gas and solid as well as the residence time of gas and solid.

2.2.1 Fluidisation regimes

For the fluidised bed the behaviour of the gas solid interaction can vary significantly. The behaviour of the fluidised bed is divided into regimes, for which some characteristics can be identified. There are seven regimes that are of interest for fluidised beds; minimum fluidisation, smooth fluidisation, bubbling fluidisation, slugging, turbulent fluidisation, pneumatic transportation, and spouting bed [14]. The difference of the fluidisation regimes is related to the way the gas and solid are in contact with each other, and are transported around the bed.

The fixed bed regime is characterised by low-gas velocity, below the minimum fluidisation, which percolates through the void between the solid particles, while the solid particles are at rest. This is illustrated in Figure 2-4. There is no actual fluidisation of the particles at the fixed bed regime, and no bubbles are formed.

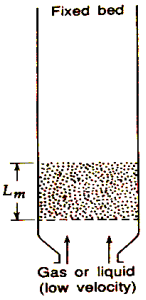

Figure 2-4: Fixed bed regime [14]

For fixed beds of randomly placed spheres, the void (ε) is generally in the range from 0.38 to 0.47. The lower value is obtained by the addition of particles one at a time, such that the sphere rests before another is dropped, while the higher value is obtained for the addition of several particles at the same time [15].

For minimum fluidisation the pressure difference over the bed counters the gravity of the particles [14], [16]. At the point of minimum fluidisation the particles are able to move around and mix, the bed will begin to expand, and the void in the bed will increase [15]. When the bed begins to expand, the particles may rearrange themselves in the loosest possible configuration denoted as ϵ_{mf}. A more lose packing of the bed results in a lower pressure drop over the bed [15]. A typical illustration of the pressure drop over a bubbling fluidised bed is shown in Figure 2-5.

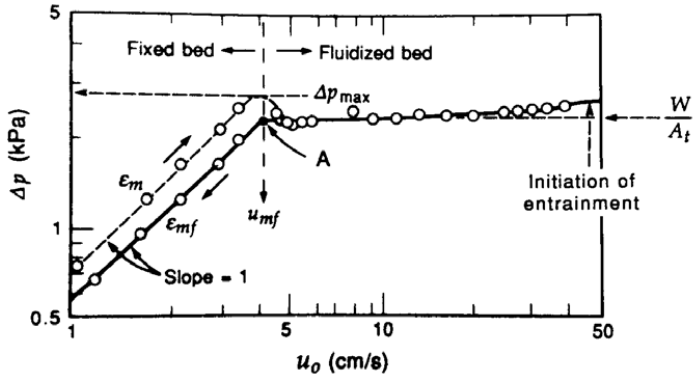

Figure 2-5: Pressure difference over static bed [14]

Above the minimum fluidisation the bed may show two different behaviours when gas velocity is increased. 1) The bed may keep expanding in a **smooth fluidisation** and increase the void. This is often the case for a fluidised bed with small particles (Geldart A particles). 2) A **bubbling regime** may form, where some of the gas bypasses the solid in the bed as shown in Figure 2-6. This is called aggregative fluidisation [15]. This is often the case for fluidised beds with Geldart B particles, where bubbling is initialised at small increases in gas velocity above the minimum fluidisation velocity [14]. Bubbling regime may also be seen for smaller Geldart A particles at gas velocities significantly larger than the minimum fluidisation velocity.

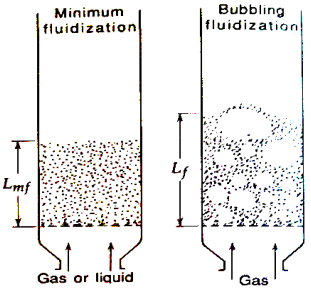

Figure 2-6: Illustration of Minimum fluidisation and bubbling fluidisation regime [14]

The slugging regime is seen in two ways, axial slugs and flat slugs as shown in Figure 2-7 left and right, respectively. The axial slugs are characterised by large bubbles that span across most of the reactor with particles moving around the bubble on the wall of the reactor. For flat slugs the bubbles fill the entire reactor diameter, and the particles are raised in the bed by the bubble and drop down through the slug [14].

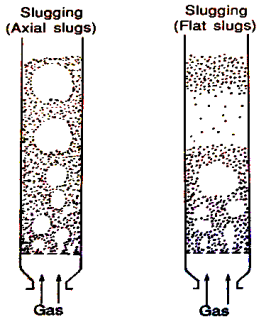

Figure 2-7: Illustration of slugging regime [14]

Slugging is often seen in shallow fluidised beds where the bubble diameters quickly reach the reactor diameter or where the cohesive forces may hold small particles together across the bed.

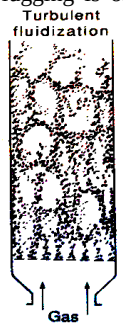

Figure 2-8: Illustration of turbulent regime [14]

At the turbulent regime, the gas bobbles have many sizes and shapes [14] and it may be very difficult to distinguish between bubble and emulsion phase as illustrated in Figure 2-8. At the transition to the turbulent regime the pressure fluctuation increases at first to a maximum for then to decrease again and slightly level off with the gas velocity [14].

The spouting regime creates a channel of gas going up through the bed where the particles are carried to the top of the bed as shown in Figure 2-9. Around the channel, particles may slowly flow down to the bottom, as solids are removed from the bottom by entering the channel while the gas percolates upwards through the void. Along the entire spout channel, the particles enter the channel and are carried up through the bed [14], [15]. The channelling may also leave a large part of the solid stationary if the bed is not designed for leading the particles towards the channel which is problematic.

Figure 2-9: Illustration of spouting regime [14]

For pneumatic transport, gas velocity significantly excides the terminal velocity of the particles, which is the free fall velocity of the particles. This results in entrainment of the particles which follows the gas in a co-current flow. The solid density will often below and there will not be any visible bubbles as illustrated in Figure 2-10.

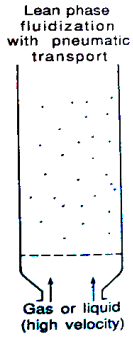

Figure 2-10: Illustration of pneumatic fluidisation regime [14]

2.2.2 Conditions for fluidisation regimes

The fluidisation regime is dependent on the gas velocity, density, viscosity, and the particle size and density. In Figure 2-11 a generalised fluidisation regime map is shown. This shows the relation between the dimensionless particle size and the dimensionless gas velocity together with the respective regions for the fluidisation regimes [6].

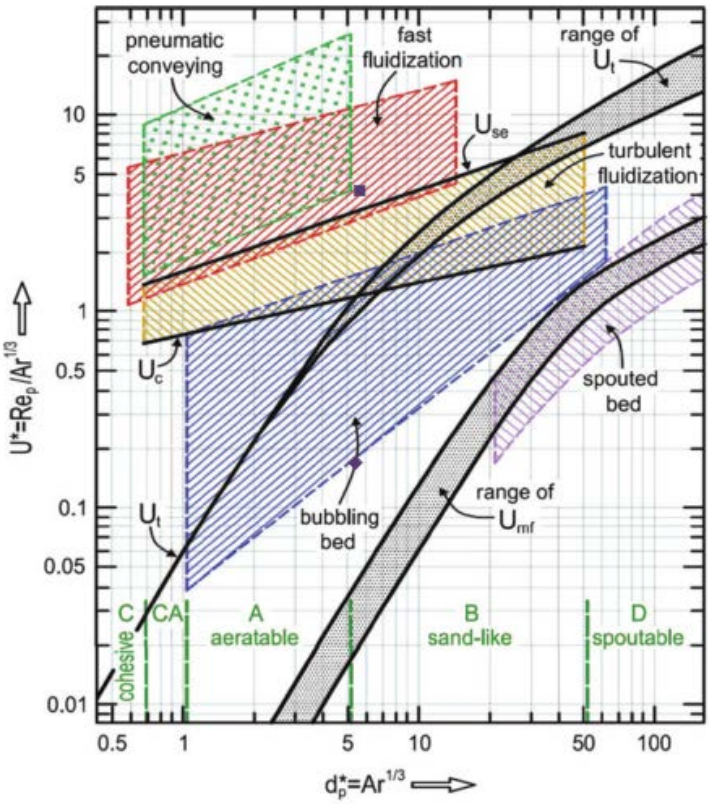

Figure 2-11: Generalised mapping for fluidisation regimes [6]

In Figure 2-11 the Y-axis represents the dimensionless velocity and the x-axis represents the dimensionless particle size by the following relations:

$$d_p^* = Ar^{\frac{1}{3}} \quad \text{(Eq 2-2)}$$

$$Ar = \frac{\rho_g d_{sv}^3 (\rho_p - \rho_g) g}{\mu^2} \quad \text{(Eq 2-3)}$$

Where d_{sv} is the mean sauter diameter that represents a sphere that has the same volume to surface ratio as the average particle, ρ_g and $\rho_p$are the density of the gas and particle, respectively, g is the gravitational acceleration, and μ^2 is the dynamic viscosity.

$$U^* = \frac{Re_p}{Ar^{\frac{1}{3}}} \quad \text{(Eq 2-4)}$$

$$Re_p = \frac{\rho_g U_s d_{sv}}{\mu} \quad \text{(Eq 2-5)}$$

where U_s is the superficial gas velocity.

U_{mf} is the minimum superficial gas velocity that is required for fluidisation, and below this line the bed will be a fixed bed. U_t is the terminal velocity at which particles begin entrainment. At U_{se} there is a significant entrainment of particles. U_c is the transition to turbulent fluidisation. The particle size is divided into C, CA, A, B, and D areas which refers to Geldart particle classification which will be explained later.

For gasification in dual fluidised beds, the gasification chamber is often operated as a bubbling fluidised bed, and thus the particle sizes often belong to the Geldart A or B group. As shown in Figure 2-11 this requires a gas velocity that is above the minimal velocity and below the terminal velocity for Geldart B particles. For Geldart A particles the bubbling regime may be preserved even above terminal velocity without too much elutriation.

2.2.3 Particle classification

The Geldart classification of particles is used when identifying the fluidisation properties of particles. Particle size together with gas properties is used to group particles according to the Geldart classification in four groups of particles C, A, B, and D as shown in Figure 2-12. [14]

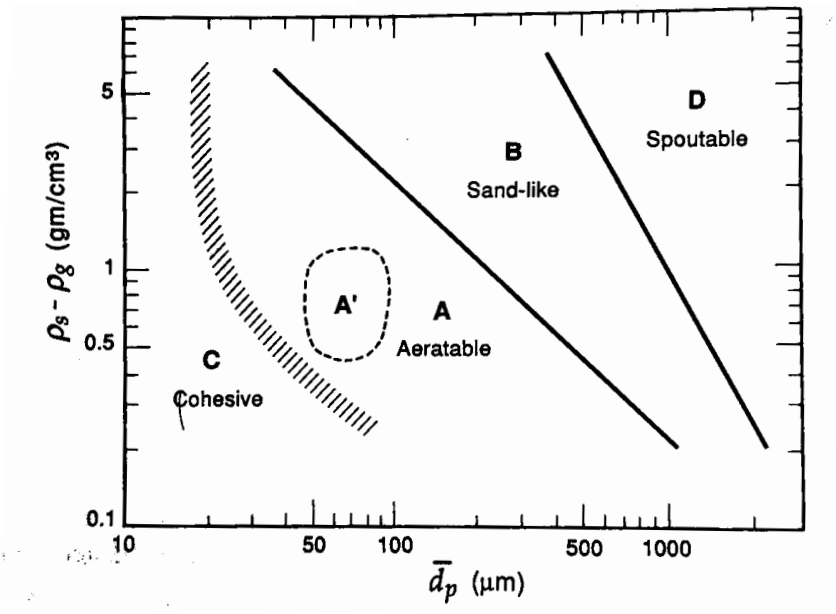

Figure 2-12: Geldart classification [14]

- Group C particles are very fine particles where cohesive forces are dominant, which makes them hard to fluidise. In narrow fluidised beds they give slugging fluidisation and in wide fluidised beds they give channelling. The difficulties of fluidisation of Group C is also indicated in the fluidisation regime diagram Figure 2-11 by limiting the regimes to the crossing of Groups C and A particles.
- Group A particles are aeratable. They have a small diameter or low density. These particles show smooth fluidisation and have small bubbles at bubbling fluidisation. In

Figure 2-11 the onset of bubbling regimes is seen for the velocity of several magnitudes of the minimum fluidisation. Thus, there is a considerable bed expansion before bubbling begins. Often the bubbles are below 10cm in diameter because the bubbles coalesce and split frequently as they rise through the reactor.

- Group B particles are sand-like. These particles are well suited for bubbling fluidisation as bubbling begins almost after the minimum fluidisation velocity have been reached. The bubbles grow large and roughly linear with the bed height. There is a large recirculation of solids caused by the vigorous bubbling.
- Group D particles are spoutable. The particles are large or have a high density and are hard to fluidise. They give server channelling and spouting if the gas distribution is uneven. Bubbles coalesce fast and give large bubbles. Bubbles rise more slowly than the gas percolating through the emulsion.

2.2.4 Fluidisation velocities

There are two fluidisation velocities that are of particular interest with regards to the fluidisation regimes, which are the minimum fluidisation and the terminal velocity.

The minimum fluidisation velocity of particles is the point at which the drag force of upward flowing gas equals the weight of the particles. This may be formulated as [14]:

$$\Delta P_b A_t = A L_{mf}(1-\epsilon_{mf})\left[(\rho_s-\rho_g)g\right] \qquad \text{(Eq 2-6)}$$

where ΔP_b is the pressure difference over the bed, A is the cross-sectional area of the bed, L_{mf} is the height of the bed at minimum fluidisation, ϵ_{mf} is the void fraction at minimum fluidisation, ρ is the density, and g is the gravitational force.

For small particles the minimum velocity can be estimated by combining (Eq 2-6) with the equation for frictional pressure drop through a fixed bed [14]

$$\frac{\Delta p_{fr}}{L_m} g = 150\frac{(1-\epsilon_{mf})^2}{\epsilon_{mf}^3}\frac{\mu u_0}{(\phi_s d_p)^2} + 1.75\frac{1-\epsilon_{mf}}{\epsilon_{mf}^3}\frac{\rho_g u_0^2}{\phi_s d_p} \qquad \text{(Eq 2-7)}$$

which results in [14]

$$u_{mf} = \frac{d_p^2(\rho_s-\rho_g)g\epsilon_{mf}^3\phi_s^2}{150\,\mu(1-\epsilon_{mf})} \qquad Re_{p,mf} < 20 \qquad \text{(Eq 2-8)}$$

where ϕ is the sphericity

The minimum fluidisation velocity decreases with a rise in pressure for large particles $d_p \cong 0.36mm$ for which it can affect the minimum fluidisation velocity with up to 40%. The increase in pressure increases the ratio between the minimum bubbling velocity and minimum fluidisation velocity $\frac{u_{mb}}{u_{mf}}$ [14]. Thus, increasing pressure will give a smoother fluidisation of the bed.

The terminal velocity is the free falling velocity of a particle in the gas. This velocity can be estimated from fluid mechanics by the expression [14]:

$$u_t = \left(\frac{4d_p(\rho_s - \rho_g)g}{3\rho_g C_D}\right)^{1/2} \quad \text{(Eq 2-9)}$$

where u_t is the terminal velocity and C_D is the drag coefficient. For spherical particles $\phi = 1$, the drag coefficient can be estimated from [14]:

$$C_D = \frac{24}{Re_p} + 3.3643Re_P^{0.3471} + \frac{0.4607Re_P}{Re_p + 2682.5} \quad \text{(Eq 2-10)}$$

2.2.5 Bubbles

Gas bubbles in a fluidised bed apply only to the bubbling bed regime as this is the only one with distinct bubbles. The behaviour of the bubbles is similar to bubbles in a liquid. For the two systems, the shapes are alike; small bubbles rise more slowly than larger ones, bubbles may coalesce to give larger bubbles, wall effect on rise velocity is in the same direction, and the rise velocity is dependent on the same factors [14]. Gas-solid system differs from gas-liquid system by an interchange of gas in the bubble, and the gas between particles in the emulsion [14]. Excess of gas, beyond that for fluidisation, passes through the fluidised bed as bubbles [14].

For a single bubble rising up through a fluidised bed with no wall effect, the rising velocity can be expressed as[14]:

$$u_{br} = 0.711(gd_b)^{1/2}, \qquad \frac{d_b}{d_t} < 0.125 \quad \text{(Eq 2-11)}$$

where d_b is the diameter of a sphere of the same volume as the bubble and d_t is the diameter of the tube. When $0.125 < \frac{d_b}{d_t} < 0.6$, the wall will affect the bubble velocity. For $\frac{d_b}{d_t} > 0.6$ the bed should be considered to be slugging [14].

The Davidson model predicts the solid and gas movement around a bubble and the pressure. In the Davidson model, pressure inside the bubble is considered constant, while in the emulsion there is a pressure gradient as illustrated in Figure 2-13

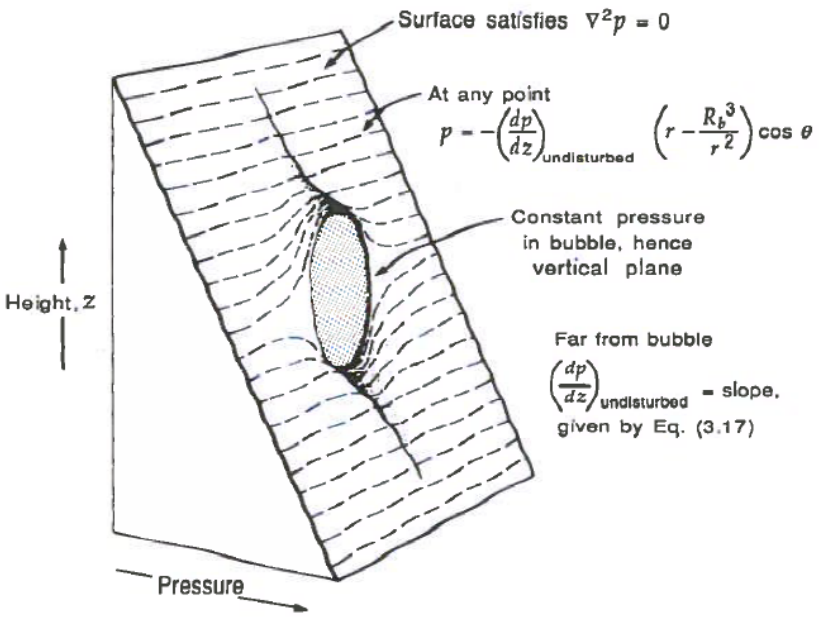

Figure 2-13: Pressure distribution in the vicinity of a bubble as predicted by the Davidson model [14].

At the bottom of the bubble, the pressure is thus higher in the emulsion phase than inside the bubble, and at the top of the bubble, the pressure is higher inside the bubble than in the emulsion. The pressure difference leads to gas flowing into the bubble at the bottom and out at the top [14].

Figure 2-14 shows the streamlines of gas around a single bubble. From Figure 2-14.a through c, the gas percolates through the emulsion phase faster than the bubble rises. For these cases, the gas will bypass through the bubble. From Figure 2-14.d through f, the bubble rises faster than the gas through the emulsion. This happens as the bubbles become bigger and increase in speed, which results in a recirculation of gas from the top of the bubble to the bottom of the bubble. The recirculating gas around the bubble is called the cloud. As the bubble velocity increases, the cloud becomes thinner [14].

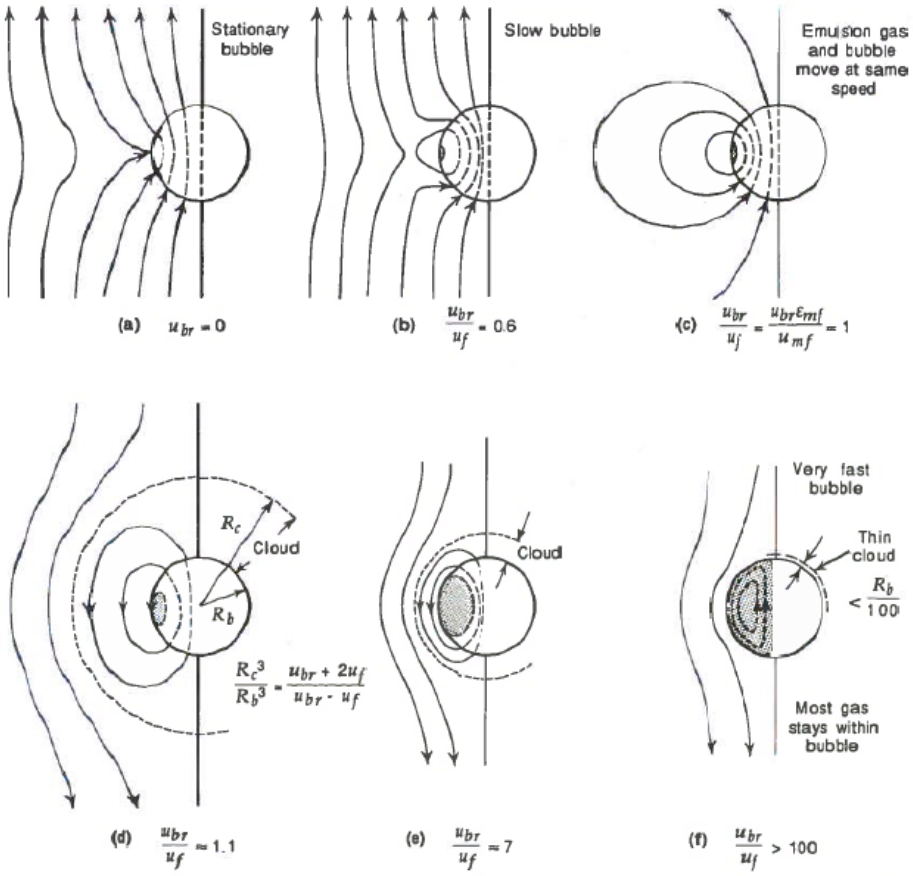

Figure 2-14: Gas streamlines near a single bubble [14].

The cloud formation at higher velocities and the by-pass through the bubble at low velocities have been observed by experiments [14]. There is, however, some interchange between the gas bubble and the emulsion gas at the bottom of the bubble [14].

The flow rate of gas into and out of a bubble is described by the Davidson model [14]:

$$v = 3u_{mf}\pi R_b^2 \qquad \text{(Eq 2-12)}$$

The upwards velocity inside the bubble is three times the minimum fluidisation velocity, and it is this upward flow in the bubbles that prevent the bubble from collapsing [14]. The bubbles formed in the fluidised bed are not spherical but have a more concave base. The region just below the bubble is called the wake. The wake is most likely formed by the pressure gradient between the emulsion and the bubble, which creates some turbulence and drags the solid up. This explains some of the gas being transported to the emulsion gas as observed in experiments. The turbulence may also contribute to a small fraction of 0.2–1% solids by volume inside the bubble, as the particles are observed to enter from the bottom of the bubble [14].

Bubble size is not constant but increases up through the reactor because of bubbles splitting and coalescing. Bubbles in the fluidised bed will move from the sides towards the centre of the bed and coalesce with other bubbles to form larger bubbles. Forces between the bubbles will be visible when the trailing bubble is closer than 3 times the radius of the circumscribed circle around the leading bubble. At this point the leading bubble will begin to flatten and the trailing bubble will be elongated. Large bubbles absorb smaller ones, as they pass by, through the base of the larger bubble. [14].

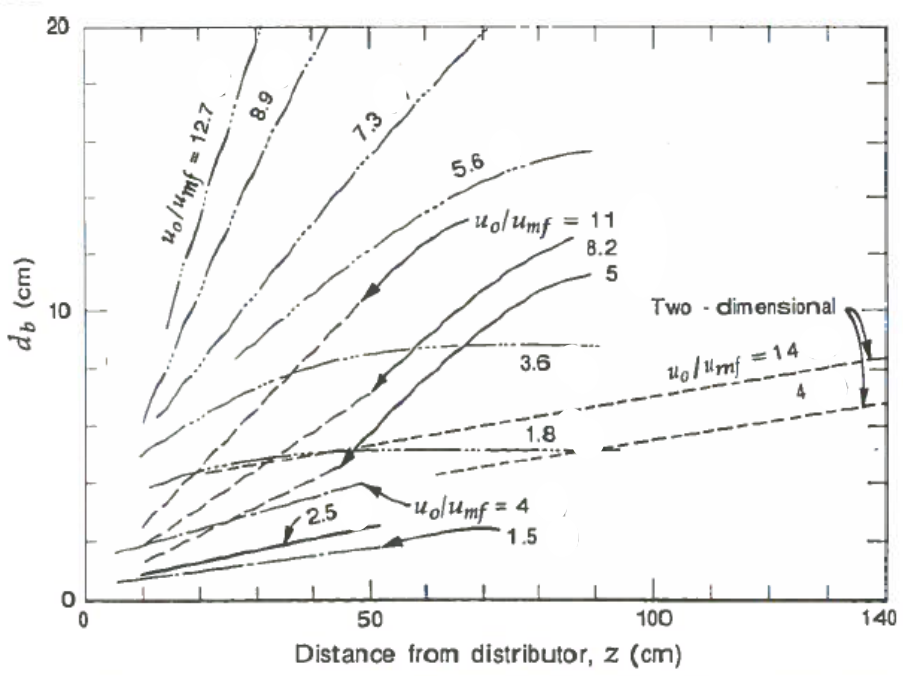

Figure 2-15. Bubble size of Geldart A and B particles. [14]

Bubble size increases with an increase in gas velocity and increases up through the bed. It is, however, not only the ratio $\frac{u_0}{u_{mf}}$ that is important for bubble size but also the excess flowrate $u_0 - u_{mf}$. [14] Bubble size limits is seen for fluidised bed with small particles because of frequent split of the bubbles where particles from the roof of the bubble will move down and split the bubble. The splitting frequency is inversely proportional to u_{mf} and almost independent of bubble size. The maximum bubble size is thus lower for Geldart A solids compared to larger particles.

Figure 2-15 shows the variation of bubble formation. Particularly, it shows that even with the same ratio of $\frac{u_0}{u_{mf}}$ the bubble size can be widely different.

The wake is the bottom part of the bubble where solids are dragged along with the bubble because of the upward flow of gas near the bubble bottom. As the bubble rises up through the fluidised bed, solid is entering and exiting the bubble wake.

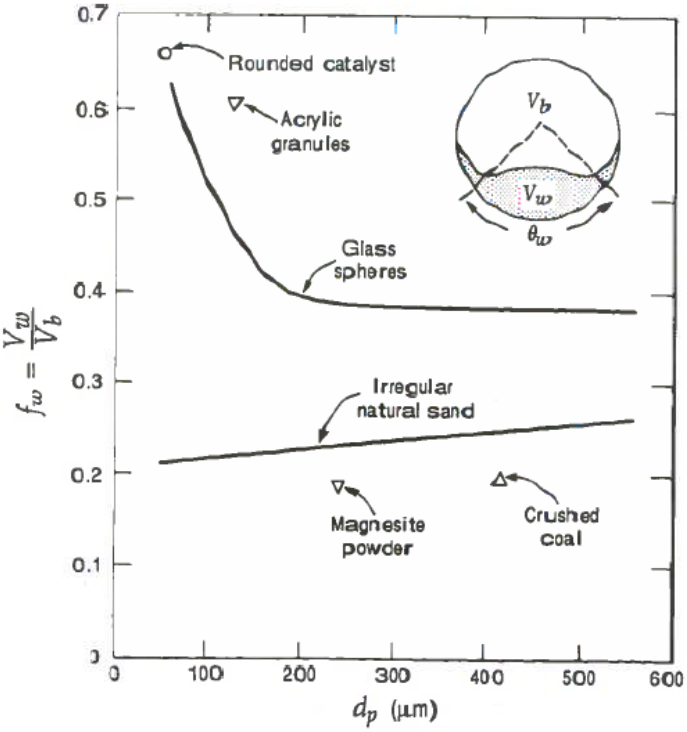

Figure 2-16 Bubble wake fraction as a function of particle diameter. [14]

The size of the wake is dependent on the size and shape of the particles. For spherical particles, the wake fraction increases as particle size decreases while it decreases for irregular shapes, as shown in Figure 2-16 [14]. For Geldart C particles the wake fraction is small, as almost spherical bubbles are formed [14].

2.2.6 Emulsion

The emulsion is the dense phase of the bubbling fluidised bed. In the emulsion section, gas percolating the solid is assumed to flow at minimum fluidisation velocity relative to the particle velocity. For condition with large excess of fluidisation gas where many bubbles are formed, the solid transport in the wake may give a recirculation of solid sufficient to reverse the flow of gas in the emulsion. This happens when the emulsion solid downward velocity exceeds the minimum fluidisation velocity.

The circulation pattern of the solids in bubbling fluidised beds may take different forms depending on the height to diameter ratio and gas velocity. For bubbling beds with low velocities and a height-to-diameter ratio close to, but less than 1, the emulsion-solid flow is upwards at the wall and downwards in the middle (Figure 2-17 a). At higher gas velocities, the solid may be reversed due to heavy bubbling in the middle that drags particles up (Figure 2-17 b) [14].

For beds with a higher height-to-diameter ratio, the solid moves upwards from the side at the bottom and towards the middle of the top. The solid downwards flow is at the side in the top of

the reactor and in the middle at the bottom of the reactor (Figure 2-17 c) [14]. This expands to include a second vortex as the bed height is increased as shown in Figure 2-17 d.

Figure 2-17e is formed for shallow bed vortexes with a height to diameter ratio of 1 unless tuyeres are introduced, for which they will determine the circulation pattern as shown in Figure 2-17 f [14].

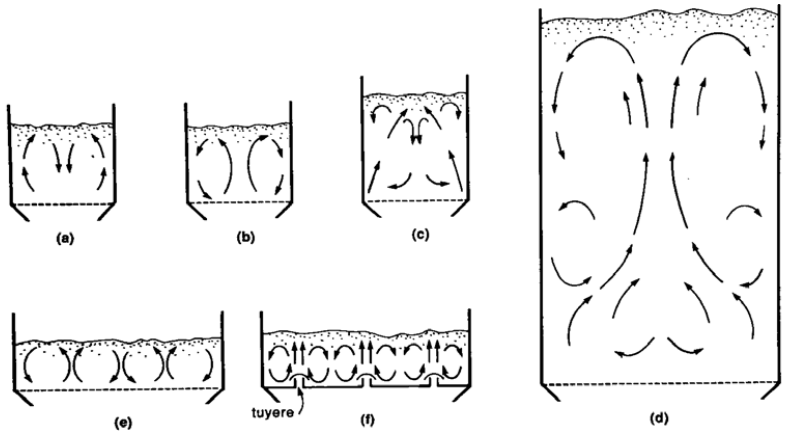

Figure 2-17: Movement in bubbling fluidised beds. a) z/d≅1, low u_0; b) z/d≅1, high u_0; c) z/d≅2, high u_0; d) general pattern in deep beds; e) shallow bed uniform distributor; f) shallow bed with tuyeres [14].

2.3 BIOMASS

Renewable energy is a broad range of sources that include biomass. Biomass is considered a renewable energy resource due to its short life circle. When utilising biomass for energy, the main purpose is to have a renewable source of energy which is often wood, straw or other agricultural products. The definition of biomass by the United Nations Framework Convention on Climate Change is [17]:

> *Biomass means non-fossilized and biodegradable organic material originating from plants, animals and micro-organisms. This shall also include products, by-products, residues and waste from agriculture, forestry and related industries as well as the non-fossilized and biodegradable organic fractions of industrial and municipal wastes. Biomass also includes gases and liquids recovered from the decomposition of non-fossilized and biodegradable organic material.*

This definition of biomass covers fuels that are significantly different in chemical composition, heating value, and moisture content. In this work, biomass refers to non-fossilized and biodegradable organic material originating from plants or trees.

Agricultural products, like corn and soybeans, are being used for biomass fuel production, but the supply is seasonal which means that there is a large cost associated with storage [18], [19] to provide a steady supply of biomass throughout the year. Additionally, the annual yield may be affected by weather condition, insect population, plant diseases, and farmers' planting decisions for the season[18]. For trees, the production can be spread out over the entire year, and thus the need for storage is less. Transportation cost of biomass is also dependent on the bulk density; for loose straw the bulk density is between 0.02 and $0.04\ t/m^3$, while for wood it is about $0.23\ t/m^3$ [20]. Straw will thus have to be compressed to bales to have a similar density. This process adds extra cost to the production. For these reasons wood may be an attractive biomass material. Thus, biomass will be treated in a general manner, but wood will be treated with more depth than other biomaterials because of the advantages mentioned above.

2.3.1 Biomass composition

Biomass comprises of a wide variety of sources, thus it will vary in composition between sources. The composition of the biomass is in turn important to understand its degradation behaviour. Thus a more generalised characterisation of biomass will make biomass more comparable.

Figure 2-18 shows the chemical composition of different types of biomass material [21]. To get such a detailed information of the biomass requires extensive analyses. The composition is thus often reduced to a few dominant species.

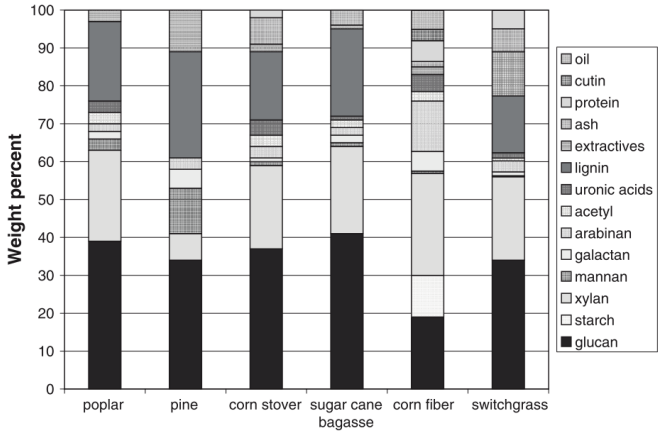

Figure 2-18: Chemical composition of biomass feedstock [21]

The compounds listed in Figure 2-18 are often summarised in 4 categories, cellulose (glucan), hemicellulose (xylan, mannan, galactan, arabinan, and uronic acids), lignin (lignin and extractives), and ash. Cellulose and hemicellulose are sometimes grouped together as hollocellulose as shown in Figure 2-19 [1], which shows the composition of lignin and hollocellulose for a larger range of biomass. Commonly for the wood sources are that lignin is a minor fraction of the biomass of about 30% [22]–[25]. The nuts are, however, rich in lignin with a fraction of about 40 to 50% of the biomass.

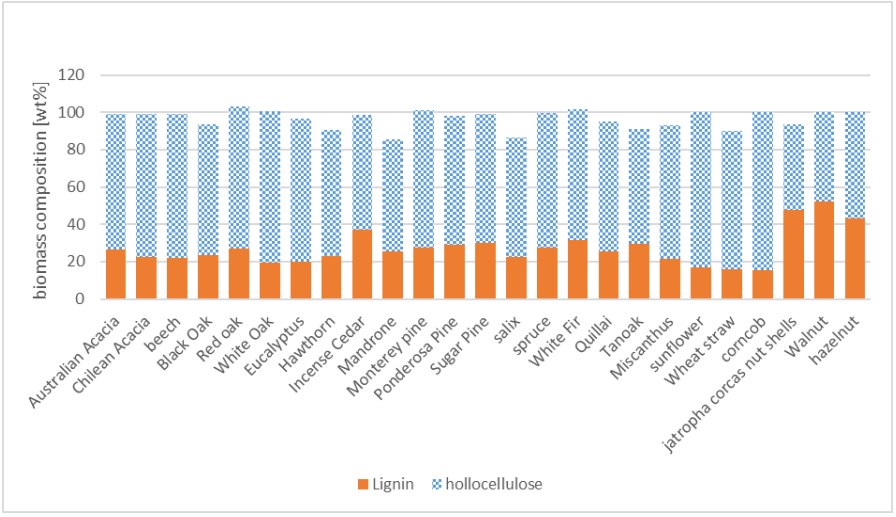

Figure 2-19: Biomass composition for different types of biomass. (Hollocellulose is the sum of cellulose and hemicellulose) [22]–[25]

The ash distribution between biomass types varies both in fraction and composition, which is shown in Figure 2-20 [22], [25]. Wood varies between 0.25 and 1.5% ash, while herbaceous biomass has about 3% ash content. Additionally, the micro-level distribution of ash across a few

[1] The deviation from 100% is attributed to a non-closed mass balance

wood rings is seen in Figure 2-21. The figure shows a piece of wood stretching over a 3 by 3 mm area. The centre of the trunk is in the lower left corner from which the rings can be seen spreading out toward the upper right corner. The concentration of Ca, Fe, Zn and Si are seen to fluctuate between the wood rings. There are high concentrations in the latewood and thus the high cell density area. Even though there are patterns that follow the rings, spots of higher concentration of Si and Cl are observed. Other metals like K, Cl, Mn, and Cu have a more uniform distribution in the wood.

The distribution of ash in bark is shown in Figure 2-22, where the upper part is the surface of the bark and the lower part is the interface with bark and some of the wood. For bark, S, Cl, K, and Fe are primarily found at the surface while Ca, Mn, Cu, and Zn are more randomly distributed across the bark.

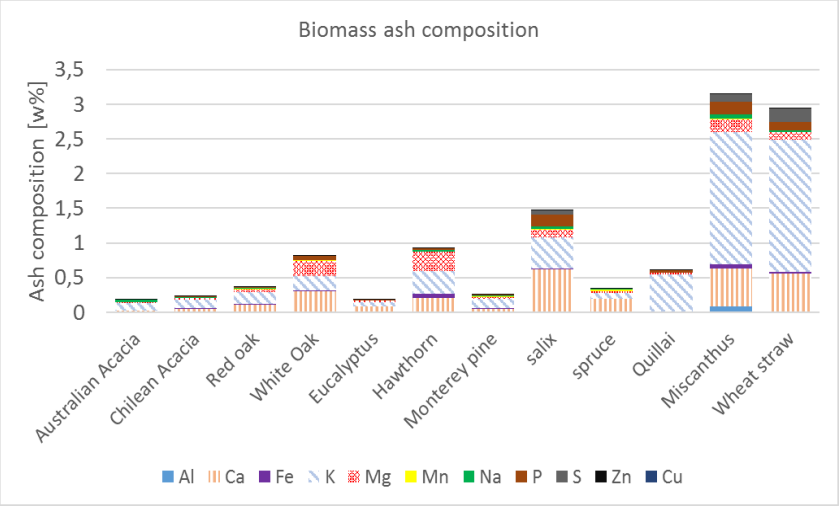

Figure 2-20: Biomass ash composition from different wood materials [22], [25]

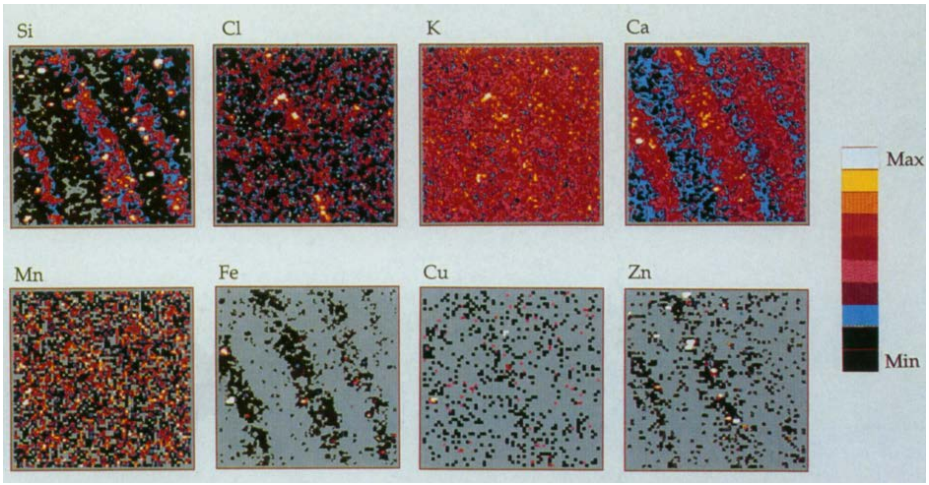

Figure 2-21: Shows the distribution of inorganics across several wood rings on 3 by 3 mm wood section [26]

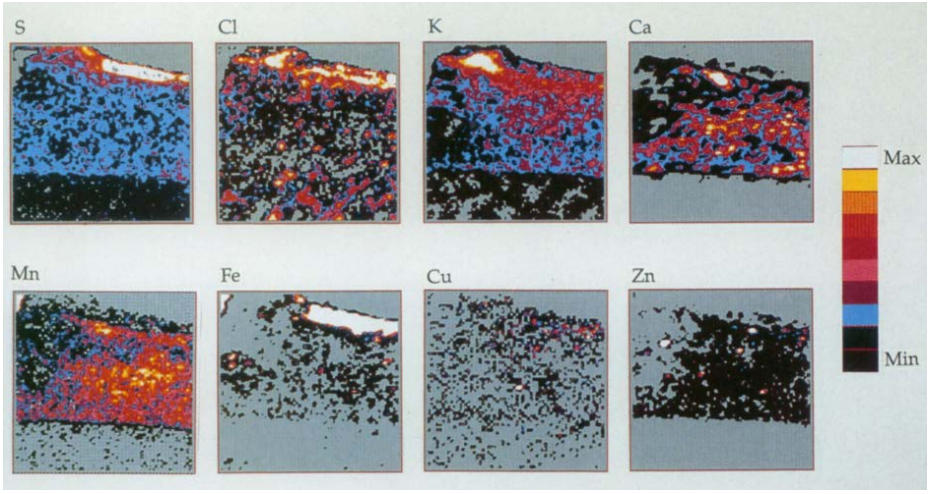

Figure 2-22: Shows the distribution of inorganics in bark. The bark layer covers approximately the top ¾ of the pictures and the bottom part is the tree trunk [26].

2.3.2 Wood structure

Wood not only differs in composition between species and wood rings but varies throughout the tree trunk and at cellular levels. In Figure 2-23 is shown a cross-section of a tree trunk, showing the three major parts of the tree trunk, heartwood, sapwood, and bark, from the centre and outwards. Depending on the part of the tree, the cells perform different functions and have different compositions of cellulose, hemicellulose, and lignin.

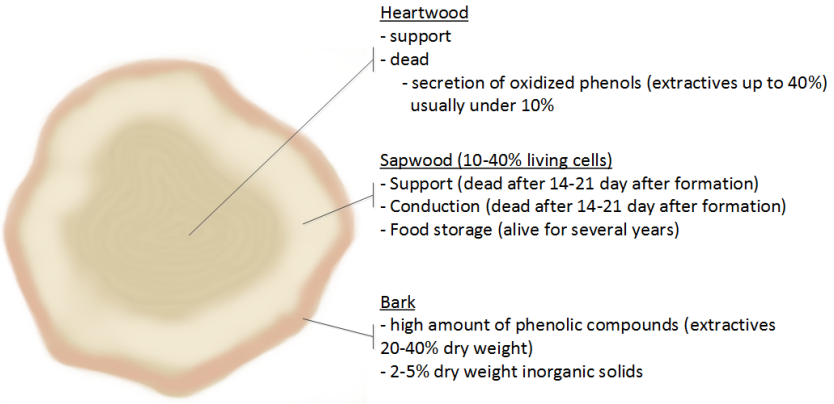

Figure 2-23: Sketch of a tree trunk

Heartwood is dead wood cells whose primary function is support. When the wood cells die, they produce extractives in the form of monomeric oxidized phenols, which is stored in the centre of the cells called the lumen. For heartwood, the extractives are usually oxidized phenols but other extractives, such as resin acid, are located in the resin canals and fat and waxes are in the parenchyma cells [27]. **Sapwood** is the living part of the tree even though it only contains 10-40% living cells. Their function is to provide support, water conduction, and food storage [28]. **Bark** grants a protective layer for the tree and contains more extractives and inorganic material than heart- and sapwood. Furthermore, it contains suberins [2% (pine) - 40% (birch or cork oak)] and phenolic acid that may be confused with lignin because they are insoluble in 72% sulphuric acid like lignin is [28].

The stem is built of cells. The size of the cells changes with the time of year at which they are formed. This affects the density of the wood along the radius for both heart- and sapwood. For the earlywood (formed during springtime), cells have a large cross-section (300 μm), a small cell wall, and a large lumen, which is good for water transport. For the latewood (formed during summer) the cells have a smaller cross-section and thicker cell walls (up to 10 μm) and narrow lumen, which is good for support [28].

For the cell composition, there are three primary parts, the middle lamella, primary cell wall, and the secondary cell wall. The middle lamella contains primarily lignin (20% of total lignin). The primary cell wall consists of cellulose, hemicellulose, pectin, and protein and is embedded in lignin. The secondary cell wall contains the main part of cellulose, which is divided into three parts, separated by layers of hemicellulose and lignin[27]

The wood cell is orientated primarily in the longitudinal direction (longitudinal tracheid makes up 90–94% of softwood) which gives conduction and support. These cells are connected by pits, which are areas of the wall that are perforated so that liquid may flow from cell to cell. Transverse cells are also present, which are placed in the radial direction. Resin canals exist in longitudinal and transverse direction and are typically larger than tracheid cells [28]. The long porous structure influences the transport of heat and mass to have anisotropic properties. This, in turn, influences the pyrolysis behaviour [3].

Hardwood is different from softwood in that it contains a higher number of different cells. The vessel cells, especially, have a considerable volume and can be distributed equally over the wood or in rings. This gives hardwood considerably more varying microstructure than softwood. [28]

2.3.3 Pseudo components of biomass

The pseudo-components, cellulose, hemicellulose, and lignin are common for all biomass but differ slightly in chemical composition and properties. The monomeric structure, composition, and the bonding will affect the degradation of the pseudo-component and the composition of gas, char, and tar formation during the thermal treatment.

2.3.3.1 Cellulose

Cellulose is one of the major components in biomass and can form a large amount of liquid under the right conditions. Cellulose consists of β-D-glucose, $(C_6H_{10}O_5)_n$, connected by β-1-4 covalent bonds and has a high degree of polymerisation; 6000–10000 monomers are connected [29] without branching as illustrated in Figure 2-24 [3], [29], [30].

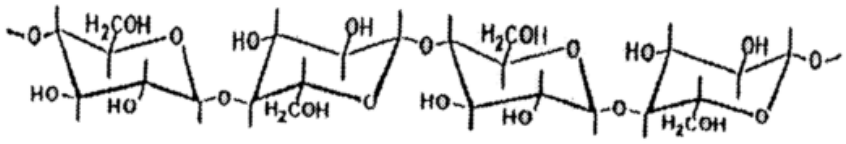

Figure 2-24: Cellulose structure [30]

The cellulose chains are placed in parallel and the many hydroxyl substituents of the glucose form hydrogen bonds between the cellulose chains [29]. This creates a partially crystalline structure, which together with a high molecular weight makes cellulose insoluble in water and resistant to hydrolysis by mild acids [3], [29]. The solubility of cellulose can be increased by substituting some of the hydroxyl groups with methyl. This lowers the binding force between the chains and, consequently, the cellulose becomes more soluble [29].

2.3.3.2 Hemicellulose

Hemicellulose was first used to distinguish between the extractable polysaccharides by alkaline solutions and cellulose [31] and does not include pectic polysaccharides, which are extractable by hot water or weak acids [31]. Hemicellulose is thus a grouping of polysaccharides with similar properties, but the most common for woody biomass is Xylan [31], which is also used for many investigations of hemicellulose.

The Xylan backbone is β-D-Xylopyranose linked by β-1-3 or mixed β-1-3 and β-1-4 covalent bonds. Contrary to cellulose, Xylan branches out with a variety of different carbohydrate chains [31] as sketched in Figure 2-25. The degree of polymerisation of xylan is low compared with cellulose and is usually less than 200 monomers [32].

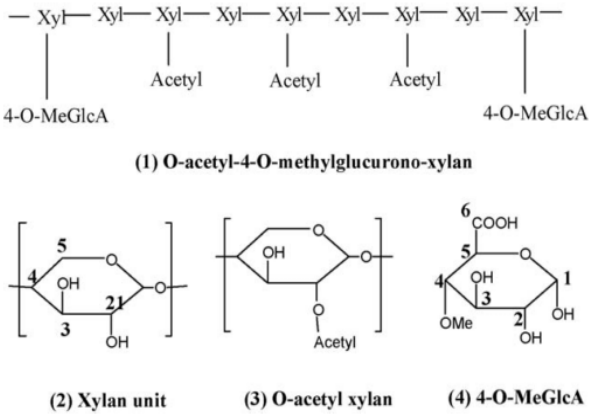

Figure 2-25: Example of hemicellulose structure [32]

2.3.3.3 Lignin

Lignin is considerably different from the other polysaccharides, both in chemical composition and structure. The lignin structure is amorphous and consists of three-man units, p-coumaryl alcohol, coniferyl alcohol, and sinapyl alcohol [33] shown in Figure 2-26, which are also referred to as monolignols [34], [35]. The carbons placed on the aliphatic chain is named α, β, and γ.

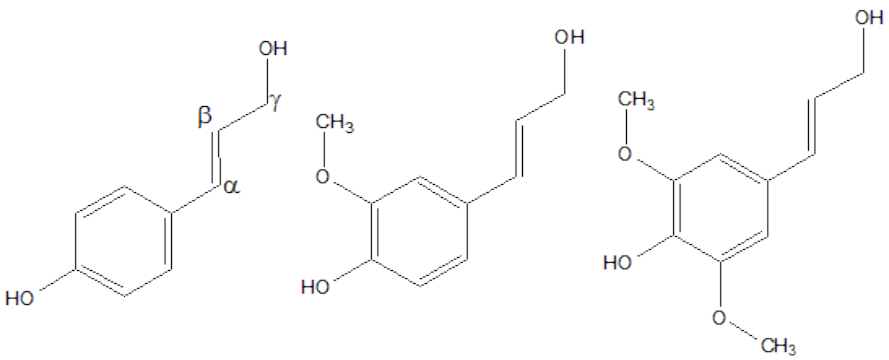

Figure 2-26: Three important structures of lignin. 4-hydroxyphenyl (1), guaiacyl (2), and syringyl (3) [33].

The overall structure of lignin is not completely defined but creates many ether and C-C bonds between the monolignols to form the three-dimensional structure, thus creating an irregular macro-structure [33], [36], [37].

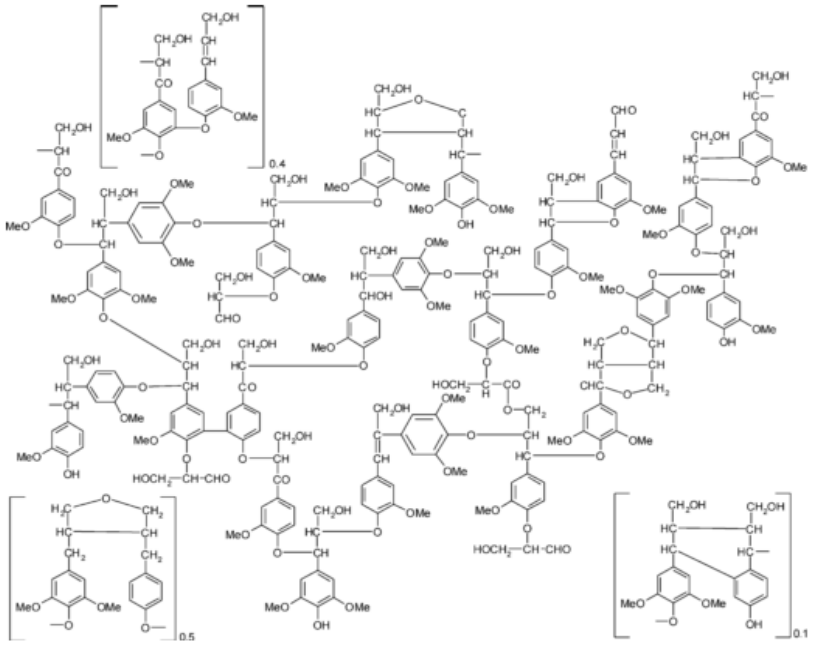

Figure 2-27: Lignin structure example[37]

The three-dimensional structure of lignin in softwood primarily consists of guaiacyl (2), whereas hardwood primarily consist of guaiacyl (2) and syringyl (3) [38]. Thus, lignin may be characterised by its monolignol units. The formed phenolics from thermal treatments often varies from the monolignols in Figure 2-26. This is because of bonds in the lignin and removal of α, β, and γ carbon. The phenolic compounds are thus grouped according to derivatives of phenol, guaiacol, and syringol, which shows relation to p-coumaryl alcohol, coniferyl alcohol, and sinapyl alcohol, respectively [39].

Figure 2-27 shows an example of a lignin structure and Table 2-1 shows the composition of the different linkages in the lignin structure for the softwood spruce and hardwood birch. This shows that the primary linkage in lignin is β-O-4 Aryl ether, but other bonds also take up a significant amount.

Table 2-1: Proportion of major linkages in lignin [40]

Linkage type	Softwood (Spruce) [%]	Hardwood (Birch) [%]
β-O-4 Aryl ether (1-3 Figure 2-28)	46	60
α-O-4 Aryl ether	6-8	6-8
4-O-5 Diaryl ether(11 Figure 2-28)	3.5-4	6.5
β-5 Phenylcoumaran (25 and 26 Figure 2-28)	9-12	6

5-5 Biphenyl (12 Figure 2-28)	9.5-11	4.5
β-1 (1,2-Diarylpropane)(9 Figure 2-28)	7	7
β-β (Resinol) (6 Figure 2-28)	2	3
Others	13	5

Figure 2-28 shows how the three main monolignols may form linkages in the lignin macro-structure. The identified linkages in Figure 2-28 make up 80–85% of lignin, where the linkages 21–28 in Figure 2-28 is produced during Kraft pulping along with the original linkages. Linkages A–C show connections between lignin and other hydrocarbons like cellulose or hemicellulose [36].

2.3.3.3.1 Method for separation of lignin

Many investigations of biomass are based on separated pseudo-components. The separation method used affects the bonds and structure of the product, which may lead to different primary tar and devolatilisation behaviour. For lignin, the most common separation methods are milling, Kraft processing, steam explosion, organosolv, and Klason process, which will be discussed further below. The use of Klason, steam-explosion, Kraft, or organic solvent extraction will affect the product distribution and the activation energy for devolatilisation, where the activation energies are in the order of Klason lignin>MWL>organosolv lignin>Kraft lignin [41], [42]

The Bjorkman's method, which produces milled wood lignin, uses neutral solvents like toluene at room temperature and a ball mill to extract lignin[42]. This process produces lignin with bonds and structures that are close to that found in untreated wood [43]. Lignin unchanged in structure and bonds may also be extracted by ball mill without the use of a solvent, where enzymes are used to remove attached carbohydrates. The milling increases free phenolic hydroxyls and α-carbonyls [38].

Kraft lignin, also known as alkali lignin or pulp lignin, is produced by alkali hydrolysis, where the alkyl-aryl ether is hydrolysed at elevated temperatures, but the weak ether bonds are still relatively well preserved compared to Klason lignin [42]. This leaves a lignin with a low molecular weight that contains phenolic hydroxyl group in almost every phenylpropane unit [38]. The hydrolysis of alkyl-aryl ether means that fewer bonds need to be cleaved and thus less free hydrogen needed to form methoxyphenols [44]. Kraft lignin can be found as a by-product of the paper industry.

Steam explosion (the mason process) also creates a low-molecular-weight product with free phenolic content[38]. The material is separated by steam at 200°C and high pressure, which forms acid from the hydrolysis of acetyl groups of the hemicellulose. The acid formed hydrolyses the weak lignin bonds and leaves alkali soluble lignin with a low molecular weight [44].

Organosolv lignin is extracted by organic solvents, often a mixture of ethanol and water [42], [45] at elevated temperatures and pressures [44]. This produces a product similar to lignin from the steam explosion but with a greater extent of intact β-O-4–ether bonds if done under mild conditions [44]. Oxygen is considerably reduced due to hydrolysis of esters [42].

Klason lignin is isolated by removing other carbohydrates using acid [42] and differs the most from milled wood lignin compared to kraft lignin and organosolv lignin. A considerable amount of functional groups are removed from Klason lignin[42] and a condensation of the lignin structure happens during the Klason process [42].

A decrease in gas and an increase in tar or condensable can be seen when wood is acid-washed [46]–[48]. The increase of volatiles is believed to be because of a change in structure by cleavage of ether linkages when washed in acid [33], [49] and may also be caused by a decrease in ash content.

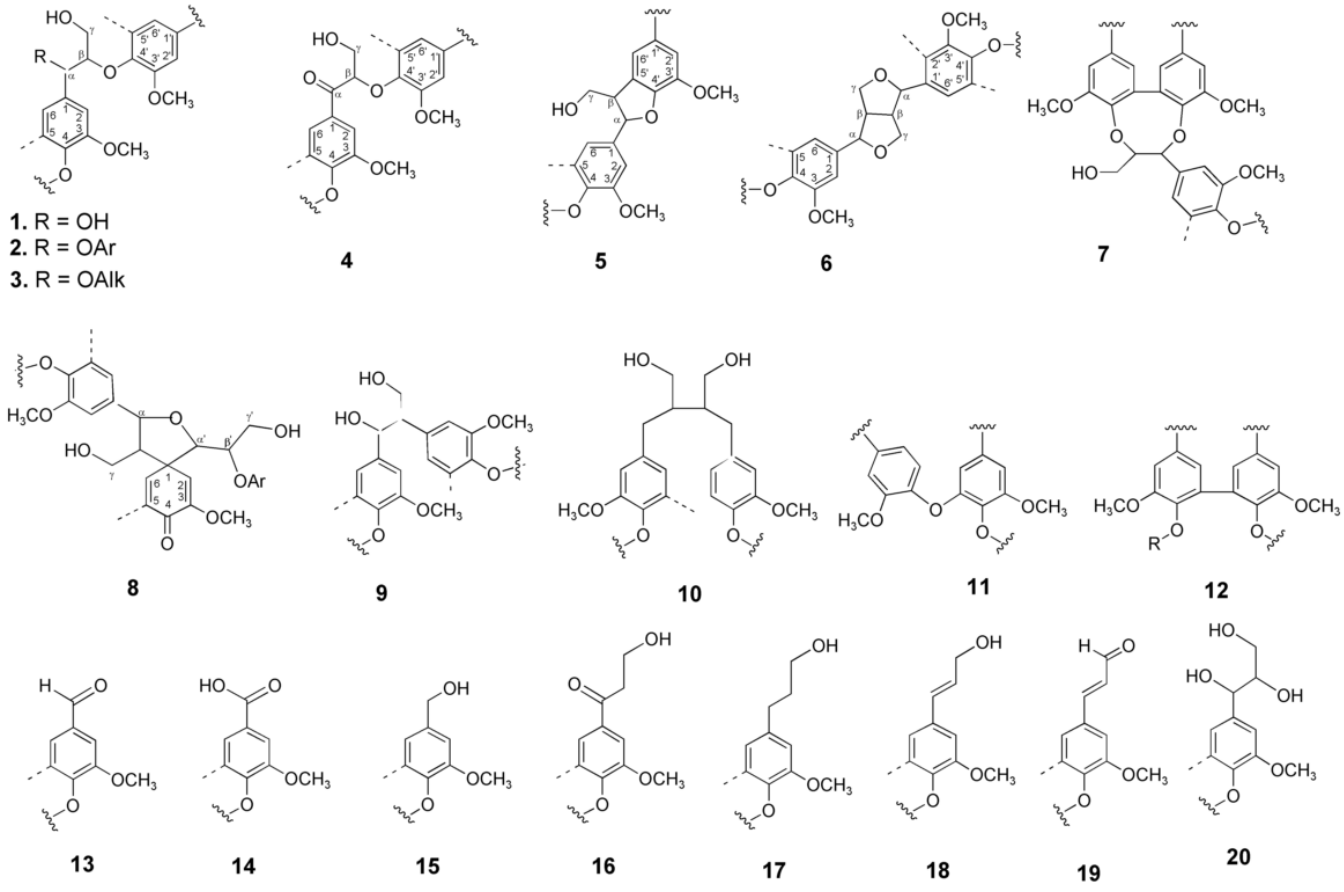

Figure 2-28: Structural moieties of MWL (1-20), kraft lignin (21-30), hydroxyphenyl (H), guaiacyl (G), and syringyl (S) units and major LC bounds (A-C) as detected by high resolution NMR techniques [36]

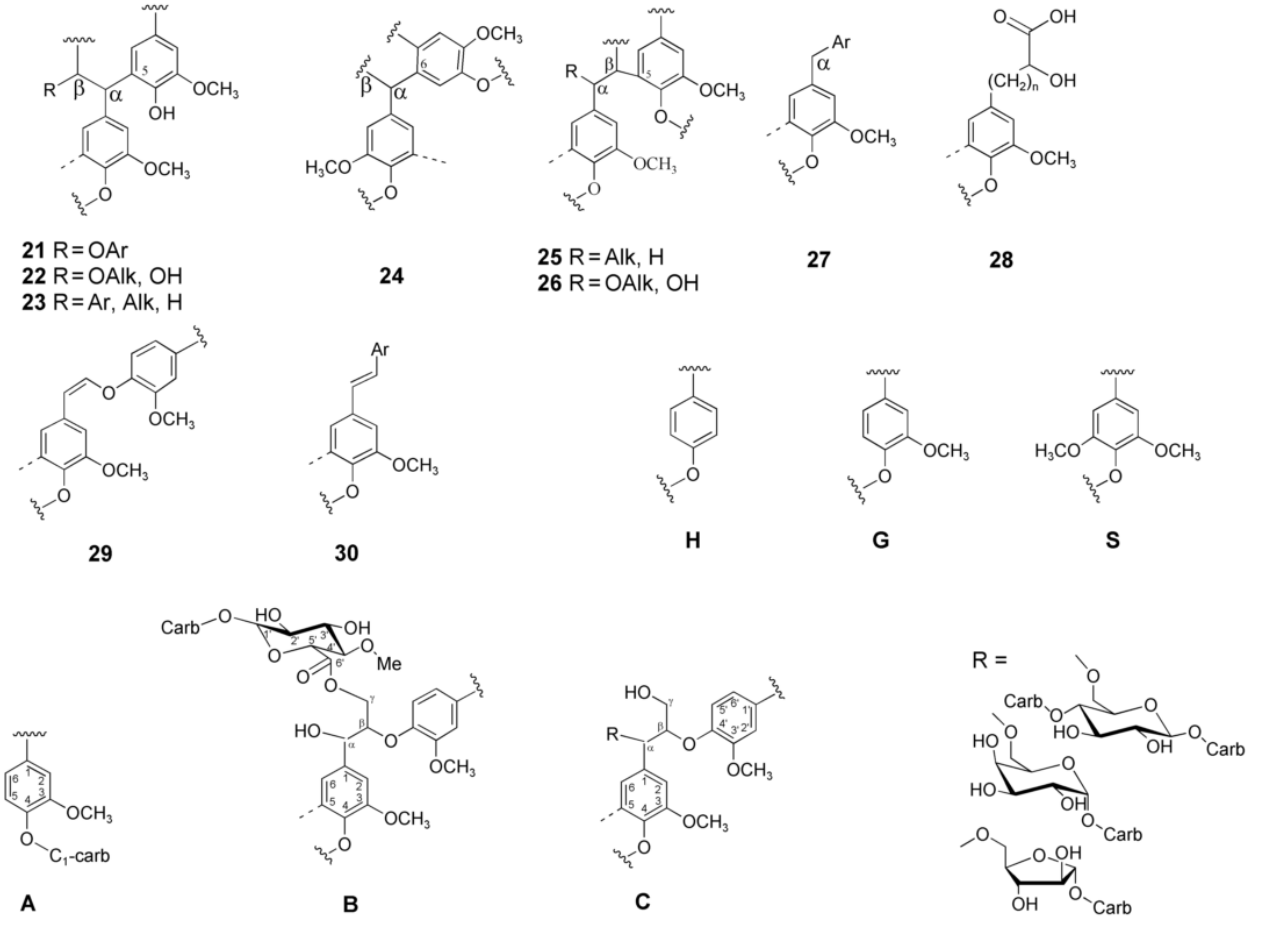

Figure 2-28 Continued

2.3.3.3.2 Bonding energies of lignin

Figure 2-29 and Table 2-2 shows calculated bond dissociation energies (BDE) for different bond types in the lignin structure. The substituents on the aliphatic chain affect the bonding energy of the bond type. Thus, the bonding energies represent an average of the calculated bonding energies.

The variance in bonding energy by side chains is illustrated in Figure 2-29 by a maximum and minimum. As can be seen from Figure 2-29, the bonding energies for carbon-carbon connections are not heavily affected by the side chains. The high difference seen for the β-C in the β-5 connection is due to a high difference between the two datasets used to depict the variance in bonding energy in Figure 2-29. However, for the separate dataset, the standard deviation is low, which indicates that the variance may be related to the calculation method. The high bonding energy for α-β bond in β-1 connection is due to a double bond. The ether bonds (C-O) show a higher dependency on the side chain compared to the carbon-carbon bonds [50], [51].

There is about a factor of 1.5 in the difference between the bond strength of the most occurring ether bond, β-O-4, and the most occurring carbon-carbon bonds, β-5 and 5-5. It is thus reasonable that ether bonds are easier to cleave.

Table 2-2: Average calculated BDEs for different chemical bonds [50], [51]

Linkage type	BDEs (kcal/mol)							
	β-C	C-α	β-O	α-C	α-β	α-O	O-C	C-O
β-O-4	None	NA	63,93	None	76,85	None	NA	β-O
α-O-4	None	NA	None	None	NA	57,67	56,25	α-O
4-O-5	None	NA	None	None	NA	None	80,14	82,28
β-5	110,56	102,60	None	None	NA	None	None	None
5-5	116,11	NA	None	None	NA	None	None	None
β-1	67,68	NA	None	None	163,95 (double bond)	None	None	None
β-β	NA	NA	None	None	NA	None	None	None
α-1	None	NA	None	91,10	NA	None	None	None

NOTE: “None”, means that this kind of binding does not exist for the specific linkage type
NOTE: “NA”, means that the information is Not Available but the binding does exist

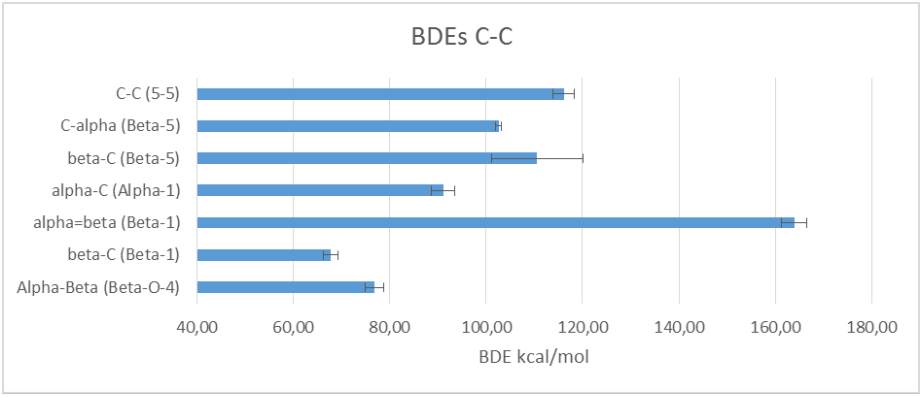

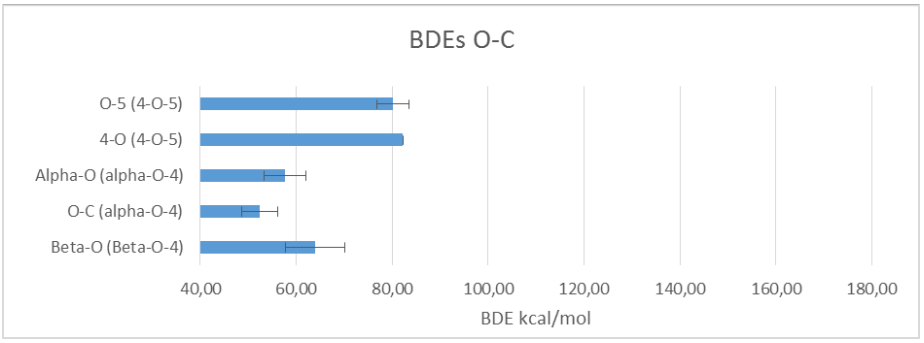

Figure 2-29: Comparison of bond dissociation energies for carbon-carbon linkage and carbon-oxygen linkage between monolignols [50], [51]

2.4 TAR FORMATION

Tar formation is one of the large problems in biomass gasification. It forms as the biomass is broken down during thermal treatments and the yield and composition are highly dependent on the biomass composition. Lignin is the origin of some of the most thermally resistant tar species because of its phenolic composition. The tar yield and composition is furthermore affected by processing conditions like heating rate, pressure, and temperature.

The initial tar formation from biomass starts as low as 200°C where it is released from the solid. In the gas phase it is degraded and reformed as the temperature rises. Reactions related to the release of tar is referred to as primary reaction while the reforming and degradation of tar after release is referred to as secondary reactions. Both primary and secondary reactions will be discussed further below.

For the gasification environment where the temperature is about 800°C tar is quickly released and is degraded and reformed fast in the gas phase. But because of the thermal stability of some of the degraded products, a part of the tar species is still present in the product gas.

Because the tar is formed from the solid biomass inside the reactor and evolves throughout the reactor, the resulting tar yield and composition may be assumed to be affected at any point of the formation and evolution of the tar. This means that, to control the tar formation, it is necessary to know the parameters affecting the release of tar from the biomass and the reforming at the end of the process.

2.4.1 Devolatilisation of biomass

A biomass particle in a steam gasification environment is subjected to a fast heat transfer from the surrounding bed and will devolatilise quickly. The tar species are released during this fast devolatilisation and any diffusion of gasification agents to the biomass will not be significant for the initial release of tar. The initial stage of the gasification of biomass can thus be assumed to be under pyrolytic conditions which is the thermal decomposition of large hydrocarbons to smaller molecules in the absence of oxygen[3].

Biomass shows a decomposition behaviour that can be interpreted as a combination of the three pseudo-components. Cellulose decomposes in the temperature range 300–400°C, hemicellulose between 220 and 400°C and lignin between 250 and 700°C [30], [52]–[55]. Some extractives are also present in the cavity in the middle of the wood cell, consisting of mostly oxidized phenols [27] that are released between 100 and 250°C.

The main steps in the pyrolysis are thus:

- <100°C mainly moisture evaporates
- 100–250°C extractives start decomposing
- 250–350°C mainly hemicellulose is decomposing, and lignin begin its decomposition
- 350–500°C mainly cellulose and lignin is decomposing
- >500°C mainly lignin is decomposing

Thermogravimetric analysis (TGA) shows the biomass devolatilisation and is often used to understand the decomposition of biomass or pseudo-components. As a compliment to the devolatilisation analysis, the differential of the thermogravimetric curve (DTG) may be depicted instead. The DTG shows more clearly if there are more than one devolatilisation maximum. These analyses can, however, vary for the same substance because of heat transport limitations to the solid and inside the solid for large samples.

The measured DTG in Figure 2-30 is an example of this. The temperature is thus not that of the sample but that of the air surrounding the sample. This will give a thermal lack of the actual sample temperature. As the heating rate is increased, the thermal conduction inside the sample will become a limiting factor for devolatilisation. Thus, different apparent devolatilisation temperatures are observed. For this reason, TGAs are mainly done for low heating rates to avoid a temperature lack from heat transport limitations.

2.4.1.1 Devolatilisation behaviour of cellulose

The apparent cellulose devolatilise is between 300˚C and 400˚C as shown in Figure 2-30 [30], [56] depending on the heating rate. The single speak from cellulose would indicate that the degradation is dominated by one reaction.

The char formation during cellulose pyrolysis also varies depending on the heating rate. For low heating rates cellulose produces up to 20 w% char [30], [57], [58], while for high heating rates char formation is between 2 w% and 10 w% [58]–[60]. The char formation may be increased if the mass transport can be limited because of increased radical repolymerisation reactions between monomers and solid residue, which are referred to as condensation reactions [58], [60], [61].

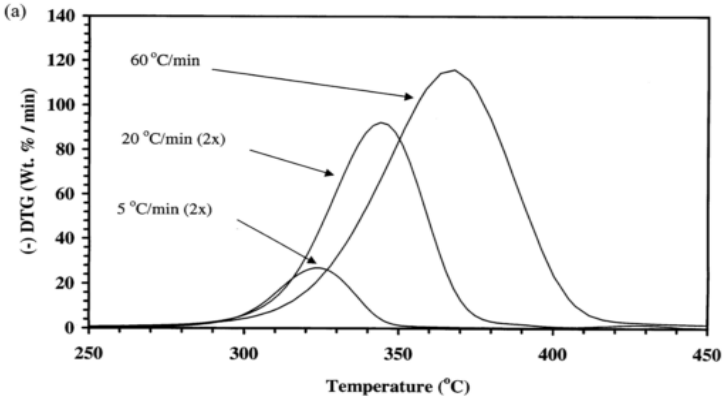

Figure 2-30: DTG for cellulose at varing heating rates [30]

In general, the presence of alkaline earth metals and alkali metals increases the char yield and decreases the tar yield [62].

The residual from thermal treatment of cellulose at 350°C still contains β-D-glucose units while at 400°C they have been completely removed, and the remaining char mainly consists of aromatic groups with intermittent paraffinic groups [63].

2.4.1.2 Devolatilisation behaviour of hemicellulose

Under section 2.3.3.2, Hemicellulose, the composition is shown to be a variety of different compounds, with Xylan being the most dominant. Each compound will exhibit a different devolatilisation behaviour. Figure 2-31 shows the devolatilisation of several different kinds of hemicellulose [60]. Most of them degrade between 200°C and 350°C. Here Xylan shows two peaks in the range 200°C to 350°C which indicates two different mechanisms. The first and second peaks are attributed to the cleavages of side chains and depolymerisation, respectively [32], [54].

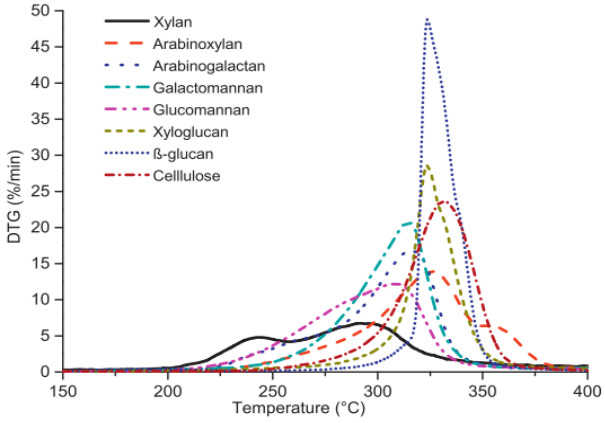

Figure 2-31: DTG curves of different hemicellulose species and cellulose [60]

Hemicellulose decomposition occurs mainly between 220°C and 400°C as shown in Figure 2-31. Above 400°C there is a small mass loss rate[54], [57], [64]. This indicates that another reaction is occurring with considerably different activation energies. It is believed that the small weight loss above 400°C is related to condensation reaction of the residual char because a minimum of furans is detected and mainly light gases are released above 400°C [54].

Considerably more char is formed from the xylan compared to cellulose, about 13–30% char depending on the heating rate [32], [54], [57], [60]. Hemicellulose, other than xylan, forms char in the order of 1 w% to 8w% [60].

2.4.1.3 Devolatilisation behaviour of lignin

As already stated in section 2.3.3.3.1, Method for separation of lignin, the lignin structure can be affected by the separation method, which can result in distribution of bonds that are more or less like lignin found in native biomass. But lignin often experiences a moderate decomposition that starts at less than 200°C before cellulose and hemicellulose and continues to high degrees about 700°C [55], [57]. Depending on the source and the separation method, lignin can exhibit different devolatilisation curves.

For Kraft lignin, two peaks are observed at 250°C and 390°C as shown in Figure 2-32 [55].

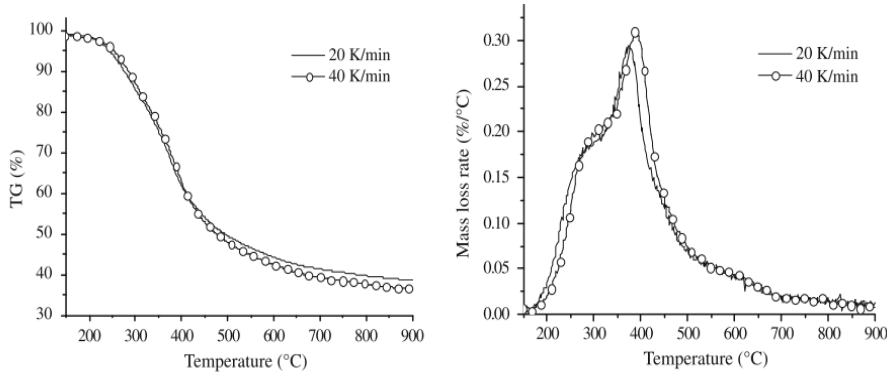

Figure 2-32: TGA (left) and DTGA (right) for kraft (pulp) lignin [55] *(less than 5g under inert atmosphere)*

For milled wood lignin the extent of the shoulder on the DTGA is not as significant as seen in Figure 2-33 [65]. For heating rates lower than 10°C/min, a considerable separation of the peaks is seen which would suggest two separate reactions. Like for the hemicellulose, the peaks begin overlapping at higher heating rates.

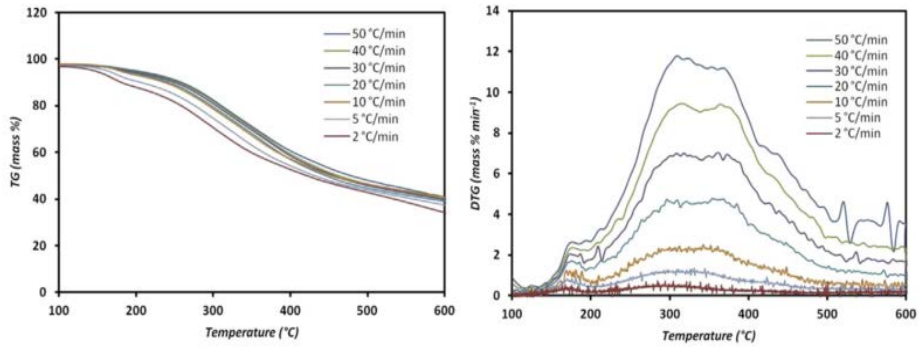

Figure 2-33: TGA and DTGA for ball milled wood lignin [65] *(6-8g under nitrogen atmosphere)*

Lignin has the highest char yield of the pseudo-components often above 40% [57]. At 20°C/min and an end temperature of 800°C, milled wood lignin has 42%, organosolve has 45%, alkali has 49% and Klason lignin has 50% of solid residue (char and ash) [42]. There seems to be a correlation between the lignin with the lowest amount of methoxyl groups and high char formation [42], [66].

2.4.2 Tar classification

Tar is a composition of chemical species that may be condensed at room temperature and is of the same weight or heavier than benzene. Some of the important properties that may differ in tar species are the drew point, water solubility, thermal and chemical stability, and oxygen content. Tar is classified for easier understanding of its properties.

Two different ways of classifying tar are commonly used in the literature. Milne [67] set up a classification of tar that is based on its refractory composition after thermal treatment. Tar is thus grouped into primary, secondary, and tertiary tar. Primary tar is released directly from the biomass, secondary tar has changes in the substituents to the aromatic ring and the aliphatic side chain, while tertiary tar has an increased size because of polymerisation of the tar species. This tar classification is useful for identifying tar bypass in processes where primary tar is not expected in the product gas.

Another classification is based on solubility and condensability properties of the tar and is shown in Table 2-3. Categorising tar in this manner gives a better idea of necessary process condition to avoid condensation and adsorption in the downstream processing. There are 5 classes. Class 1 is the heavy tar that is not possible to detect in GC because of its large structures, which prevent them from being vaporised without degradation. Class 2 is heterocyclic and oxygenated compounds that are highly water-soluble. Class 3 is light aromatics that are easy to condense but less soluble in water than class 2 because of the lack of polarisation from side groups. Benzene is sometimes not considered a tar because the saturation point is often higher than what is found in the gas and it is at the border of the tar definition [68]. For this thesis benzene is included for class 3. Class 4 is compounds consisting of 2-3 carbon rings, which condense at low temperature. Naphthalene that belongs to this group is one of the most important tar species because it seems to be one of the most difficult kinds of tar to degrade[69]. Class 5 is heavy tar of the size 4–7 rings, giving condensation at even higher temperatures.

Table 2-3: Examples of tar compounds that are considered for different tar classes[70]

Tar class	Class name	Property	Representative compounds	Chemical structure of typical compounds[71]
1	GC-undetectable	Heavy tar that cannot be detected by GC	NA	NA
2	Heterocyclic and oxygenated	Highly water soluble	Pyridine, phenol, cresols, quinolone, isoquinoline, dibenzophenol	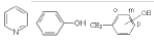
3	Light aromatic (1 ring)	Easy to condense and dissolve.	Toluene, ethylbenzene, xylenes, styrene, benzene	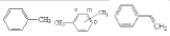
4	Light PAH compounds (2-3 rings)	Condense at low temperatures even at low concentration	Indene, naphthalene, methylnaphthalene, biphenyl	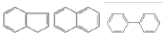
5	Heavy PAH compounds (4-7 rings)	Condense at high temperatures	Fluoranthene, pyrene, chrysene, perylene, coronene	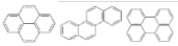

NA = Not available

The term condensable includes all tar species and organic compounds lighter than benzene that may be condensed at 0°C.

2.4.2.1 Primary tar constituents

The pyrolysis product of biomass consists of a large amount of different compounds. Hosoya et al. [72] summarised the major primary products from the pyrolysis of cellulose, hemicellulose and lignin, produced from softwood as shown in Figure 2-35 and Figure 2-36. The primary tar compounds are related to the monomer structure of cellulose, hemicellulose and lignin.

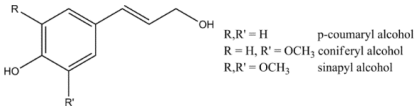

Figure 2-34: Monolignol structure [35]

Because of the aromatic nature of the lignin, the primary tar consists of aromatic mono- and oligomers with substituents as shown in Figure 2-35.

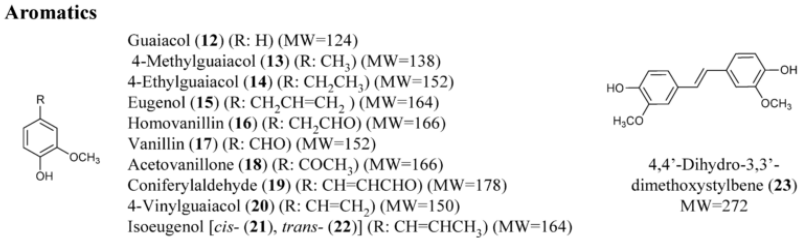

Figure 2-35 Major primary product from the pyrolysis of lignin [72]

Cellulose is a structured compound, consisting of glucose units and thus produce C6 compounds (carbonyls and anhydrosugars) as primary tar (levoglucosan being the dominant tar), whereas hemicellulose is a combination of different monomers and thus creates C5 and C6 compounds (carbonyls, anhydrosugars, and furans) as primary tar. Tar from cellulose and hemicellulose are easily broken down into gases at gasification temperatures within a few seconds, [73], [74] and only a small amount of the tar will result in phenol derivatives [75].

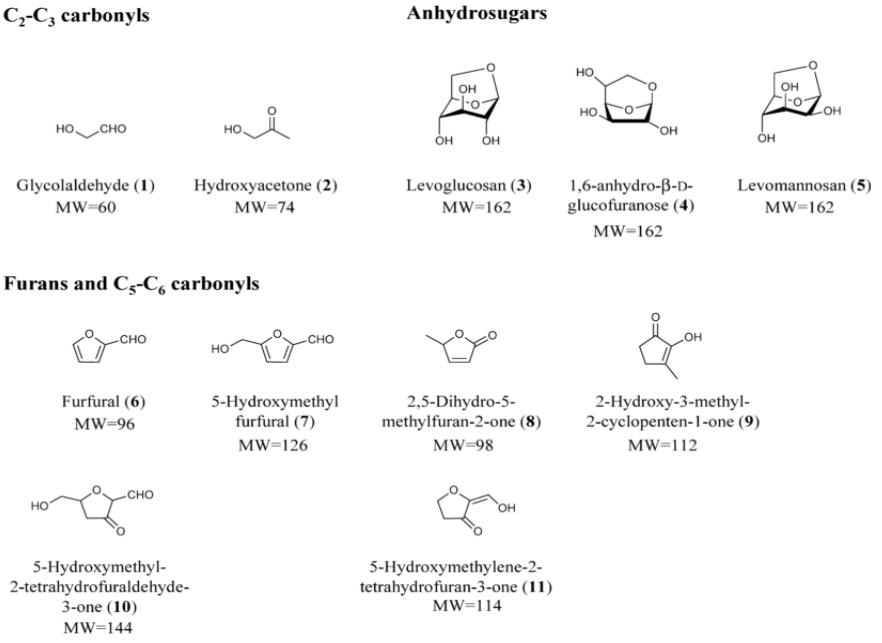

Figure 2-36 Major primary product from the pyrolysis of cellulose, and hemicellulose [72]

The aromatic nature and resilience of lignin tar mean that lignin tar is a problem even at elevated temperatures, where it will repolymerise to polyaromatic hydrocarbon and form char in the downstream process. Dealing with the lignin tar problem requires an understanding of how the competition between char, gas, and tar works as well as the consecutive repolymerisation and reforming.

2.4.3 Primary reactions

The release of tar from lignin is a complicated process because of the many linkages and structures that are possible in lignin. The bonding energy shows that β-O-4 bonds are more unstable than the carbon-carbon bonds and become important for the low-temperature release of the primary tar. This has made β-O-4 linkage one of the more investigated linkages of lignin.

Both radical and concerted[2] reaction mechanisms have been suggested to affect the primary pyrolysis of lignin. For tar to be released, all the bonds connecting the monolignol to the lignin

[2] Concerted reaction is a chemical reaction in which radical intermediate is not present.

structure have to be broken, and the radical formation has to be stabilised to prevent condensation reactions [44].

The primary release of tar from lignin is illustrated in Figure 2-37. At low temperatures between 120 and 300°C, light gases (CHOOH, CH_2O, CO_2, CO, H_2O) are released, which is attributed to the breakages of functional groups in the aliphatic side chains, α-O-4, and β-O-4 linkage. Furthermore, some monolignols that are bound by weak ether bonds may also be released[40], [76]–[79].

Increasing the temperature further to 380°C, the methoxy groups may be removed by homolytic cleavage but require a hydrogen donor [37], [77], [80]. For a unimolecular cleavage of the methoxy group, bond energy calculation shows that the O-CH_3 bond is more unstable than the C-OCH_3 bond [81].

Vanillin and 2-methoxy-4-methyl phenol are the major products from β-O-4 cleavage and H-abstraction. H-abstraction, double bond formation, rearrangement, isomerization and concerted reaction contribute to a more diversified product distribution of the primary tar species [82].

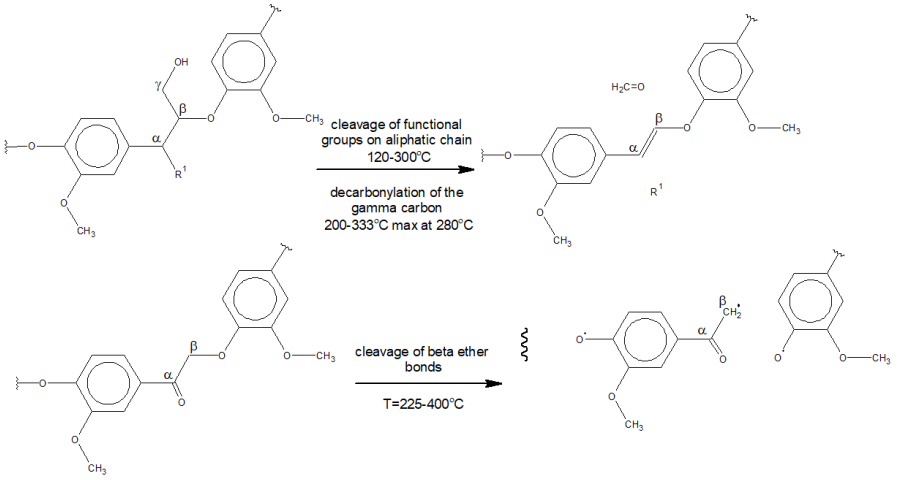

Figure 2-37: Proposed release of aromatics from lignin structure

A condensed char formation is believed to be formed by polymerisation of radical species as aromatics, alkanes, and alkenes that propagate further polymerisation [82]. The radicals are believed to be initially formed from homolytic cleavage[3] of β-O-4 linkages [82]. The hydroxyl group on the γ-carbon has been speculated to be a source of transferable hydrogen [44] that may terminate radicals and diminish condensation reactions. An experiment with ferulic acid, however, shows that this hydroxyl group is removed and forms CO_2 at a low temperature between 200°C and 330°C by a radical mechanism [83].

For temperatures higher than 450°C, the main substituents of the aromatic rings are CH_3 and OH. It is speculated that CH_4 is produced by the mechanism shown in Figure 2-38, which will generate

[3] Homolytic cleavage: Each product retains an electron from the bond and generates two radicals.

more carbon bonds between the monolignols or char, thus forming a more rigid char. Similar reactions may occur with OCH_3, OH, and H substituents to form CH_3OH, H_2O and H_2 [77].

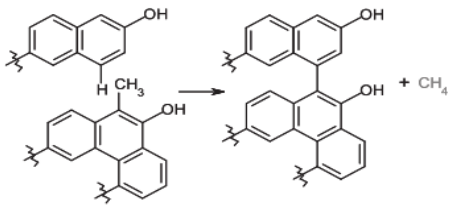

Figure 2-38: Conversion of substituent [77].

2.4.4 Secondary reactions of tar

When the tar is released from the biomass it may further degrade, reform, or repolymerise by secondary reactions that result in:

1. Formation of higher tar classes by homogeneous reaction between individual tar species
2. Formation of char by heterogeneous reaction
3. Formation of light gasses by thermal cracking, heterogeneous and homogeneous reforming

Furthermore, tar is also known to be affected by partial oxidation, steam and CO_2 reforming, catalytic cracking, and char.

2.4.4.1 Repolymerisation and cracking mechanism of tar

The repolymerisation of tar is a process involving unimolecular breakdown as well as hydrogen abstraction and donation. The gas phase repolymerisation of tar in steam gasification is similar to that found in pyrolysis as steam shows little effect on the tar reforming. A lot of research in polyaromatic hydrocarbon (PAH) formation mechanism is also done under pyrolysis and combustion conditions [81], [84]–[91].

The formation of PAH and char from tar is highly related to the radical formation in tar, and subsequent to the temperature [92]. As the temperature increases, the radical concentration increases in the tar [92]. The fraction of radicles between coke and tar is also shifted towards the coke fraction with the temperature increase [92]. Coke formation in condensed tar is seen already at 300°C, but homogeneous secondary gas phase reactions become important at 650°C [93].

The main tar repolymerisation and cracking are illustrated in Figure 2-39 [81], [84]–[91], [94]–[106]. This shows a range of different reactions involving unimolecular breakdown, hydrogen abstraction and donation, and repolymerisation to form both light gases and heavy tar [37], [107], [108].

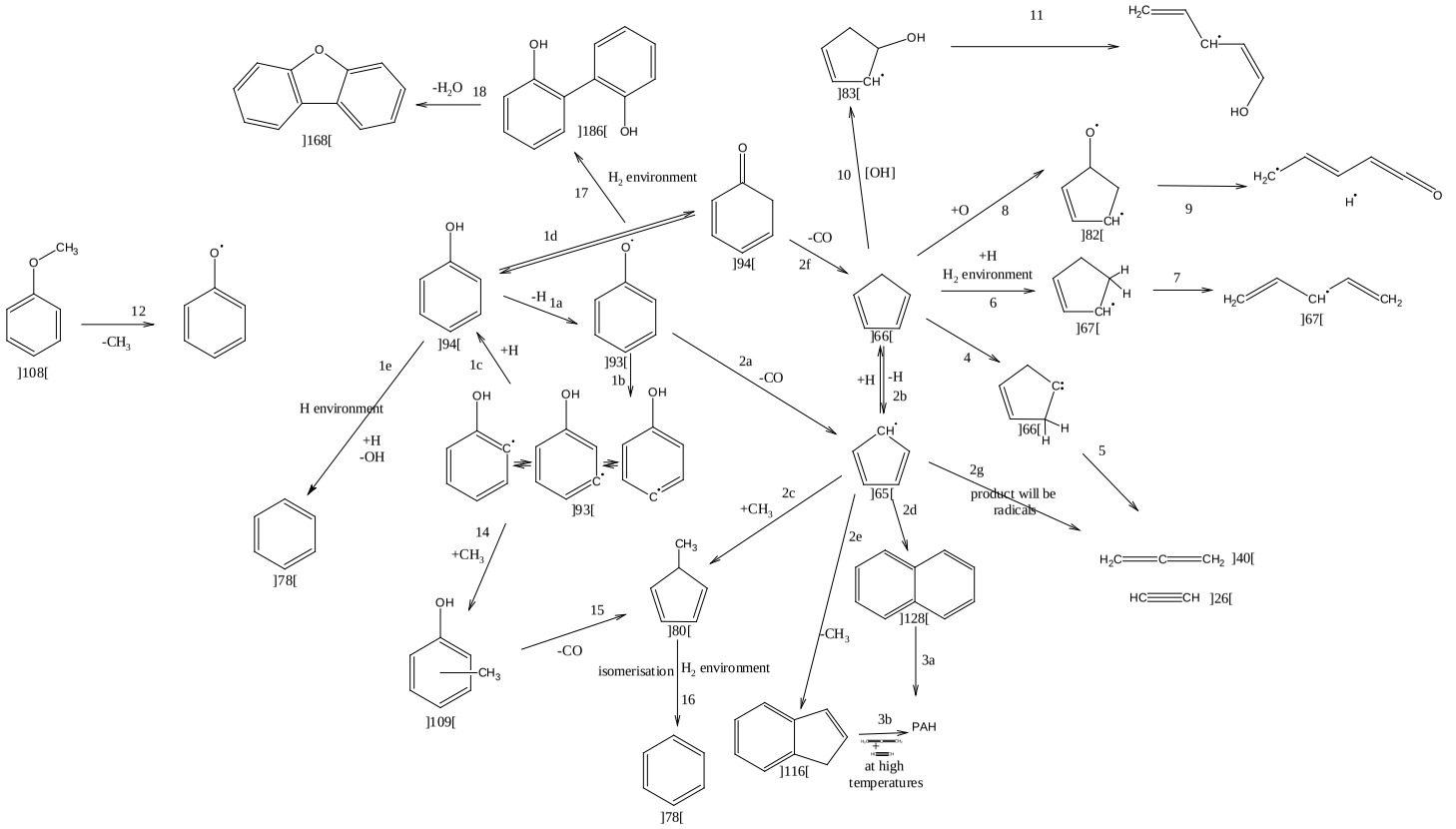

Figure 2-39: Proposed tar evolution mechanism. Numbers indicate the reaction number, numbers indicated by]x[shows the molecular weight. [81], [84]–[91], [94]–[106]

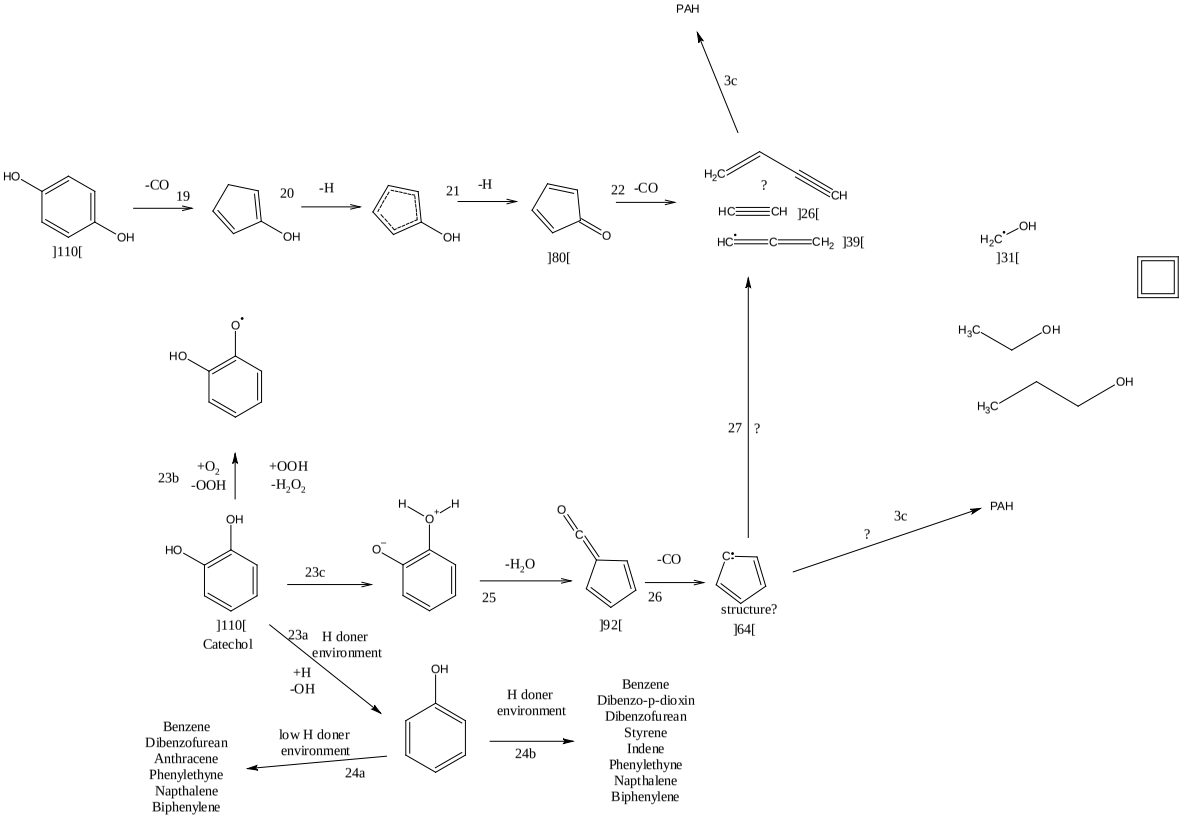

Figure 2-40: Continued

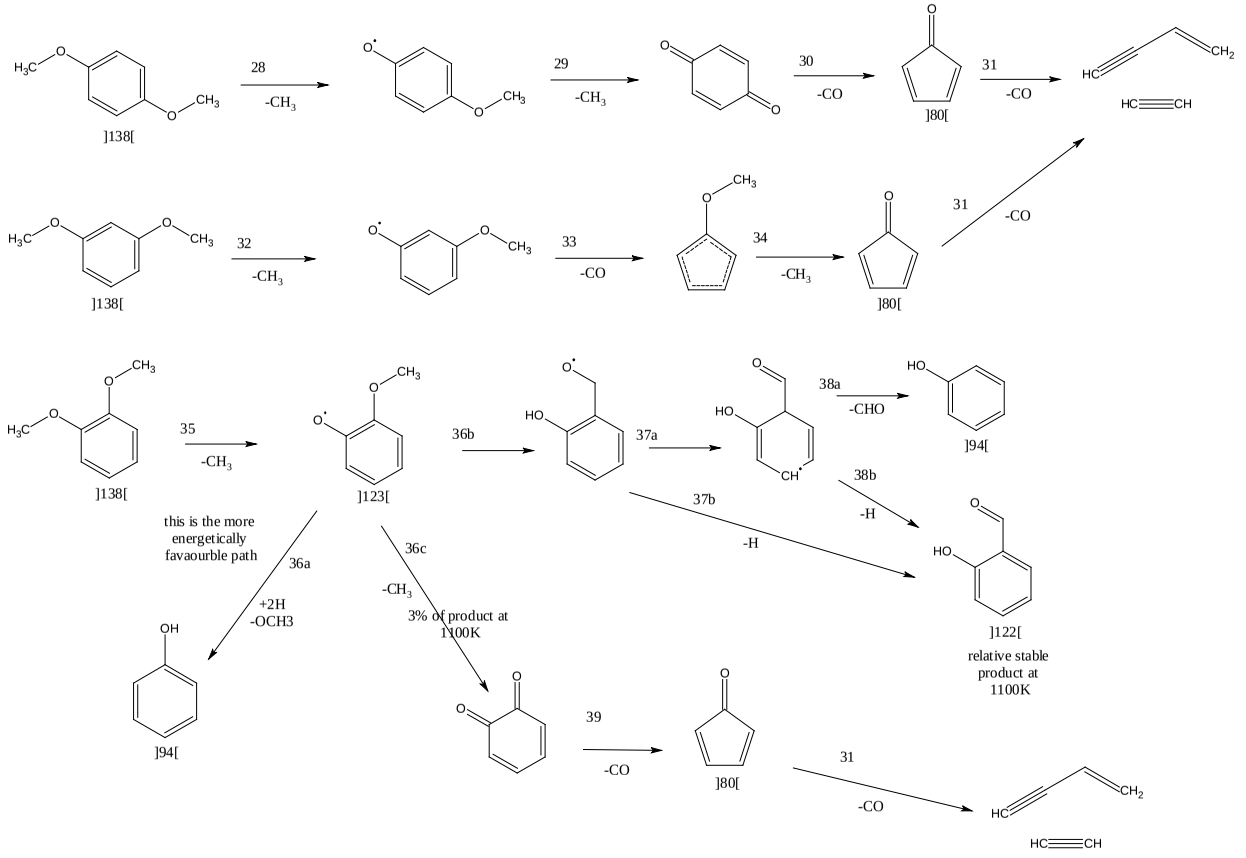

Figure 2-41: Continued

2.4.4.1.1 Unimolecular breakdown

Unimolecular breakdown is when molecules are broken down without the interaction of other molecules. This is an important part of understanding the repolymerisation of tar. Reactions 12, 19, 23, 28, 32, and 35 in Figure 2-39 show the initial unimolecular breakdown step of some of the model lignin tar compounds that have been used in the literature (Anisole, Dimethoxybenzene, and Catechol). All except reactions 19 and 23, which do not have methoxy groups, are initialised by methyl elimination and form radical intermediates. This fits well with O-CH3 bound being the weakest bound [81] [94].

The thermal decomposition of o- m- and p-dimethoxybenzene is interesting because the initial demethylation produces tar that is close to the primary tar from lignin. For the m- and p-dimethoxybenzene, experiments and calculations show that elimination of CH_3 and CO will lead to cyclopentadienone, which will quickly decompose to acetylene and vinyl acetylene [86], [88]. The o-dimethoxybenzene does not show the same CO elimination because of the close methoxy group that performs an aryl-shift instead. This, in turn, leads to the formation of phenol instead of cyclopentadienone [86]. The monolignols in biomass consist of o-methoxyphenol derivatives, and it would thus be expected that initial aryl-shift will be part of the initial reaction.

For gasification and pyrolysis condition, the unimolecular degradation may, however, not be the most favourable. H-abstraction and donation may shift the degradation mechanism.

2.4.4.1.2 H-abstraction and H-donation

In mixtures of hydrocarbons, hydrogen may be transferred by being abstracted from one molecule and donated to another. For conditions with significant hydrogen abstraction and donation, a widely different pyrolysis product composition is seen compared to what is expected from the unimolecular decomposition. Pyrolysis of catechol, with isopropyl alcohol as an added hydrogen donor, shows an increase in the formation of phenol and benzene of about 10 times. Many other aromatics increase as well, compared to pyrolysis without isopropyl [87]. Tar-like anthracene (class 4) is removed by the introduction of isopropyl, but more tar species with two aromatic rings are detected [87]. Additionally, the destruction of catechol starts at a lower temperature by the introduction of isopropyl alcohol, indicating that hydrogen availability provides an initial route different from the initial unimolecular breakdown (Figure 2-39, reaction 23a).

Activation energy calculations for methoxyphenol decomposition also shows that the addition of hydrogen and subsequent elimination of OCH_3 is more favourable than methoxy elimination or aryl shift. This supports the alternative decomposition of methoxyphenol to phenol in hydrogen donor-rich environments (Figure 2-39, reaction 36a). [89], [90].

H_2 is also found to have similar effects as it inhibits the conversion of benzene and naphthalene to form heavier tar species. H_2 also increases the cracking of tar species to gases and increases the conversion of toluene and phenol to benzene [109], [110].

Under gasification environment, pyrolytic volatiles are released into the emulsion phase, giving a high concentration of hydrocarbons that may perform hydrogen abstraction and donation. The bubble phase will consist primarily of a gasification agent at the bottom of the reactor, while at the top of the bed and the freeboard, considerable gasification has been performed to give a significant concentration of hydrogen. Therefore, hydrogen addition and abstraction reactions must be considered to understand the formation and evolution of tar.

2.4.4.1.3 The role of phenol and cyclopentadiene

Phenol and cyclopentadiene are important compounds for understanding the tar evolution. Phenol is the primary product of hydrogen abstraction and donation reaction with primary tar [87], [89], [90] and is a relatively stable compound because of the resonance stability (Figure 2-39, reaction 1b) [84].

Hydrogen abstraction from phenol (Figure 2-39, reaction 1a) leads to the formation of phenoxy radical, which decomposes by unimolecular elimination of CO to form cyclopentadienyl (Figure 2-39 reaction 2a) [84], [94], [99], starting already below 500°C [84]. This reaction is widely accepted as one of the main reactions for PAH formation [35], [84], [94], [106].

Alternatively, phenol will form benzene by hydrogen addition and hydroxyl elimination (Figure 2-39, 1e). A small fraction of other compounds from two phenol radicals like dibenzofuran has been reported as well [84], [85], [87], [96] (Figure 2-39, reaction 17 and 18).

The main product from phenol degradation, cyclopentadienyl, reacts with other cyclopentadienyl to form naphthalene [81], [84], [102], [103] (Figure 2-39, reaction 2d). Formation of naphthalene has also been suggested to be formed by 2 cyclopentadienes or cyclopentadiene and cyclopentadienyl.

Naphthalene is one of the major products of the pyrolysis of cyclopentadiene where only a small part forms aliphatics (Figure 2-39, reaction 2g). The pyrolytic formation of naphthalene from cyclopentadiene is about 74% while only about 10% forms naphthalene in H_2-rich environment at about 727°C [81], [99]. The presence of other radicals (CH_3, OH, H, or O) reacts with cyclopentadiene, forming e.g. methylcyclopentadiene or cyclopentadienone in competition with the formation of naphthalene [81], [98], [103], [104] (Figure 2-39, reaction 10, 8, and 6).

2.4.4.2 CO_2 and steam tar reforming

For gasification, CO_2 and H_2O are a significant part of the gas phase and contribute to the reforming of tar, which is the conversion of tar to lighter gas compounds. CO_2 and steam reforming happens in the gas phase when the tar is exposed to steam or CO_2 in condition with no or little oxygen and forms H_2 and CO. The reactions can be generalized by reaction (R 2-10) to (R 2-14) [3]

$$C(s) + H_2O(g) \rightarrow CO(g) + H_2(g) \qquad +131 \text{ MJ/kmol} \qquad \text{(R 2-10)}$$

$$C_nH_x + nH_2O \rightarrow \left(n + \frac{x}{2}\right)H_2 + nCO \qquad \text{(R 2-11)}$$

$$C_nH_x + 2nH_2O \rightarrow \left(2n + \tfrac{x}{2}\right)H_2 + nCO_2 \qquad [111] \qquad \text{(R 2-12)}$$

$$C_nH_x + nCO_2 \rightarrow \left(\frac{x}{2}\right)H_2 + 2nCO \qquad \text{(R 2-13)}$$

$$C_nH_x + \left(n + \tfrac{x}{2}\right)CO_2 \rightarrow \left(\tfrac{x}{2}\right)H_2O + \left(2n + \tfrac{x}{2}\right)CO \qquad [111] \qquad \text{(R 2-14)}$$

Steam reforming forms hydrogen, CO, and CO_2 while CO_2 reforming forms CO, water, and hydrogen. The advantage of steam reforming is the highly endothermal nature that adds to a

higher heating value of the product gas and gives a high H_2/CO ratio, which is important for synthesis gas.

It is known that the total tar yield decreases as the steam to biomass (S/B) ratio increases [4], [112], [113]. This is in good correlation with the steam tar reforming equation, for which an increase in steam would favour the formation of hydrogen and carbon monoxide.

The reforming process is, however, not fully elucidated. As previously mentioned water does not have an effect on the thermal decomposition of phenol and seems to have little effect on class 2 tar, toluene, benzene, and naphthalene [109], [112], [114].

To explain this, it has been suggested that steam reforming of tar only affects higher level tar species with more than 2 aromatic rings [115]. This may also partially explain why naphthalene is one of the most prevailing species of tar in gasification, as the heavier tar species are gasified.

2.4.4.3 Catalytic reforming

Because of the difficulty of reforming the primary tar by homogeneous reactions, a catalyst is often utilised [111], [116]–[124]. The effect of the catalyst is related to how well the contact is between the gas and the catalyst, the contact time, operating temperature, the possibility of fouling, and attrition [120]. Catalysts are thus often used in separate reactors placed downstream of the gasification reactor; where the catalyst is the only bed material, the temperature can be higher than in the fluidised bed, and fouling is minimised. The major problems with catalyst used inside the fluidised bed are fouling and attrition.

In fluidised bed it is often not possible to reactivate the catalyst and it thus deactivates fast by coke formation on the surface [120]–[122]. If the catalyst is impacted by attrition, it will continue to decrease in size until it is elutriated from the reactor. In such a case, the catalyst will end with the rest of the elutriated particles (e.g. carbon and ash particles) and will be hard to recycle. In such a case the catalyst has to be cheap to be attractive as an in-bed catalyst.

An optimal catalyst for reforming will have to fulfil the following criteria [122]

- Effective at tar removal
- Capable of reforming CH_4, if used for synthesis gas production
- Provide suitable H_2 to CO ratio for the intended process
- Resistant to deactivation caused be carbon deposits and sintering
- Easy regeneration
- Resistant to attrition
- Inexpensive

Some of the commonly used catalysts used for reforming of tar are Dolomite ($MgCO_3$ or $CaCO_3$), olivine (Mg_2SiO_4 or Fe_2SiO_4), alkali salts mixed with the biomass (K_2CO_3, Na_2CO_3, $Na_3H(CO_3)_2 \cdot H_2O$, or $Na_2B_4O_7 \cdot 10H_2O$), Ni catalyst on different kinds of support structures, char, and alumina (Al_2O_3).

The result of reforming with different catalysts is shown in Table 2-4. There is a wide variety of results for in-bed use and for secondary reactor use, which is caused by a large variation in operating conditions like residence time, temperature, pressure, and degree of catalyst filling. This makes it very difficult to compare the results in a meaningful way.

Table 2-4: Catalyst performance. The tar reduction is given as a percentage for use inside the gasification chamber and in parentheses for use in a separate downstream reactor.

Catalyst	Recorded reduction in tar	Cost (Euro/metric ton)	Deactivation time	Optimum operating temperature	Reference
Ni-based catalyst	-	-	Fast (deactivation starts after about 40 hours) Carbon in the primary reactor deactivates the catalyst fast [117]	800-900°C [119]	-
Limestone	≈90%$^{\alpha}$[118] (≈88$^{\beta\gamma}$%[120])	Low [118]	Medium [118] (≈20% reduction after 9h[120])	-	-
Alumina extrudes	(70% [121]); (87%$^{\beta\gamma}$ [120])	-	(≈15% reduction after 9h [120])	400°C[121]	-
Olivine	>90% [117]; ≈29%$^{\alpha}$[118]; ≈47% $^{\alpha}$[116]; (89%[121])	120 [125]	High [118]	-	-
Fe-olivine	50%$^{\delta}$[123]	High [118]	-	-	-
Ni-olivine	80%$^{\alpha}$[118]	High [118]	-	-	-
NiMo	(≈100%$^{\beta\gamma}$ [120])	-	(More than 168h at 550°C [120])	-	-
Char	-	-	-	950°C[117]	-
Alkali	(<80% [122])	-	-	-	-
Dolomite	(89-92% [121])	-	-	800°C[121]	-
Silica	(≈82%$^{\beta\gamma}$ [120])	-	(≈17% reduction after 9h [120])	-	-
Y-zeolite	(≈100$^{\beta\gamma}$% [120])	-	(More than 168h at 550°C [120])	-	-

α: With silica sand as a reference
β: no gasification agent (thermal cracking)
γ: model tar (1-methylnaphthalene (1-MN))
δ: with olivine as a reference
Note: The data is on a mass basis

Ni-catalyst has proven to be effective for steam reforming but deactivates fast by carbon deposition and H_2S [117], [119], [124]. Other drawbacks of Ni-catalyst is the cost and toxicity [118]

Dolomite is a naturally occurring and relatively inexpensive catalyst. Because it is a natural product, it is found in different chemical compositions, pore sizes, and pore distributions depending on the source [118]. This means that the activity of the catalyst will have to be analysed, as the reactivity can be directly related to the pore size and distribution [111], [122]. The catalyst works well at 800°C but considerably reduces in efficiency when the temperature goes down [121]. Attrition is a problem for dolomite when used as a primary measure for tar reduction as it may break and create large amounts of fines [117]. Olivine is another naturally occurring mineral and is advantageous over dolomite in being more resistant against attrition [117]

For a temperature of 400°C, it is considerably better to use alumina extrudes, which have an efficiency of about 70%, than dolomite or olivine with about 47% and 40%, respectively [121]

Limestone shows a high reduction of tar, as much as the Ni-based catalyst (<2g/Nm^3 dry basis[118]), but has a low attrition resistance, which means that it will have to be carefully handled or replaced more than the Ni-based catalysts.

Char has a catalytic effect on the cracking of tar and has been used in downstream secondary reactors for tar removal. Because char is gasified, it may be necessary to add char to the process to keep the same level of conversion [117].

The ash from the biomass contains alkali metals and may be used as a catalyst. With the addition of alkali metals by wet impregnation, the yield of tar, methane, and other hydrocarbons are reduced. The addition of alkali metals also increases the reaction rate of the biomass gasification [118]. The disadvantages of using alkali-metal as a catalyst are the extra step of impregnating the biomass, the possibility of agglomeration [122], and ash deposits downstream of the process.

2.4.4.3.1 Coke formation

One of the big reasons for not using catalysts in the gasification chamber is because of fast deactivation by coke formation. Coke formation on catalyst happens as hydrocarbon is adsorbed to the catalyst surface in the reforming process, and insufficient reactants are present to reform the hydrocarbons to light gases. Consequently, a layer of carbon is deposited on the catalyst.

At temperatures lower than 200°C, the deactivation of the catalyst is related to the tar species strong adsorption and low volatility rather than formation of coke. The composition of the carbon layer is dependent on the tar species. No polyaromatic hydrocarbons are thus formed at these temperatures. At temperatures higher than 350°C, the coke formation begins and forms a polyaromatic hydrocarbon surface[126].

The process of carbon deposit on Ni-catalyst starts with an initial layer of metal carbides, monoatomic carbons or carbonaceous species on the surface, from which a porous carbon layer is built on top. Porous carbon seems to be formed by participation of Ni as these are found on top of the layer [127]. The coke formed at the surface has a higher reactivity than the porous carbon formation on the top of the initial carbon layer [127].

The coke formation affects the activity of the catalyst. The activity is reduced by blocking active sites and blocking pores.

Different catalysts have different amounts of active acidic sites, which governs the initial coke formation [128]. Thus, if coke formation is wanted, a number of acidic sites should be high. For Ni catalyst larger size of Ni particles in the catalyst also show an increased coking rate [129]. The decoking of the catalyst is, however, independent of a number of active sites [128].

Some initial coking rates for zeolites are listed in Table 2-5

Table 2-5: Coking rates for some zeolites with methanol at 650K, 1Nl/h, methanol:N2 =1:25, Weight hourly space velocity = 10 h^{-1} and 0.1g catalyst [128]

Catalyst	Si/Al ratio	Pore volume (cm^3/cm^3 cat)	Maximum amount of coke (w%)	Initial coking rate (g/Al site/min) [g/H site/min] ($x10^{-23}$)
H-ZSM-5	34.6	0.29	2.2	0.164 [0.166]
H-mordenite	8.1	0.28	8.7	0.137 [0.154]
H-offretite	4.0	0.4	16.8	0.118 [0.142]

A 15% nickel catalyst on an alumina support showed that different tar components have different abilities to form coke on the surface of the catalysts. In Table 2-6 the minimum steam to carbon (S/C) ratio necessary to keep the catalyst working at a steady state is noted for different model tar components.

Table 2-6: Limit of the S/C ratio for carbon formation[69]

Compound	Catalyst temperature	Limit (S/C) ratio
Toluene	725	2.5
Naphthalene	795	3.7
Anthracene	790	6.6
Pyrene	790	8.4

There is thus a continuous build-up of coke at a ratio below that, which has been provided in Table 2-6, because the coke formation is faster than the reforming. The minimum S/C ratio can thus be seen as the tendency of the tar species to form char at the catalyst surface. This clearly shows that larger aromatics more easily forms char. The most favourable conditions for carbon deposit is at low temperatures [69]. It is seen that the ability of tar species to react with the surface is in the order phenanthrene>naphthalene>benzene [130], [131].

2.4.4.4 Partial oxidation

The formation of tar can be reduced by the addition of oxygen to the product gas. However, for low concentration of oxygen up to about 35% of the stoichiometric air requirement, there is an increase in the yield of naphthalene which is attributed to an increase of radical formation. For a higher concentration of oxygen, the tar yield is reduced [132] [133] by a partial combustion. In gasification, oxygen will also react with some of the product gas, reducing the heating value.

2.4.4.5 Char interactions

Tar species may also participate in condensation reactions or reforming reactions with the char in the bed [134]. The effectiveness of char as a tar cracking catalyst is believed to be related to the oxygen content of the char [135]. The effectiveness has shown to be increased by the presence of steam beyond the individual contribution from steam reforming and the char bed. Hydrogen and methane have been reported to interact with the char and inhibit the gasification of the char [136][137][138]. Furthermore, it is indicated that steam transforms the char from small aromatic

structures (3-5 rings) to large aromatic structures (>5 rings) and introduces oxygen groups to the char [136].

As the tar makes condensation reaction with the char, the surface of the char is decreased but does not show signs of decreasing efficiency [139][4].

In coal pyrolysis experiments, methane is used to increase the tar formation, and it is believed that the radicals formed from methane stabilise the phenolic and char radicals[5] [140]–[142]. Carbonisation of the char with methane gives a more amorphous surface but also closes pores, which results in a reduced overall surface [143], [144].

There are no studies showing the detailed composition of the tar after char bed treatment to the author's knowledge.

The char from the biomass is changed during gasification. At high temperatures, the char becomes more aromatic and losses oxygen-containing species and substitutional groups. At 700°C the char is very amorphous because of the tarry depositions that make the alkali and alkaline earth metals be distributed more homogenously than for very structured char. A higher degree of homogeneity of the char leads to a more heterogeneous distribution of the alkali and alkaline earth metals, which affects the reactivity of the char [145].

2.4.5 Process conditions

The process conditions of the gasification affect the extent of primary and secondary reactions. The primary reaction is to a large extent affected by heating rate, size of particle, moisture content, pressure, and the transport through the biomass particle while the secondary reactions are mostly affected by temperature.

2.4.5.1 Heating rate

The heating rate is probably one of the most investigated influences. Optimal temperatures and times for high yields of char, gas, and tar are well-known.

- For a maximized char production, a slow heating rate and low final temperature and long gas residence time should be used
- For a maximized tar formation, a high heating rate to a temperature between 400–600°C and short gas residence time (<1s) should be used [146], [147]. This is known from the production of bio-oils, which is, to a large extent, composed of the primary volatiles from lignin and hollocellulose.
- For a maximized gas production, a moderate-to-slow heating rate to a final temperature between 700 and 900°C and a long residence time should be used.

The heating rate thus affects the competition between the primary reactions proceeding in the biomass.

The heating rate of a particle is dependent on the surrounding temperature and the size of the particle. This may give a particle that is more or less uniformly heated. Furthermore, moisture in the biomass may delay the heating because energy is consumed by evaporation. For large particles or high-heat transfer, there may be areas with both drying and pyrolysis. The Biot number (Bi) represents the relation between the heat transferred to the surface and the heat conducted through

[4] For 500°C
[5] Use nitrogen and methane atmosphere

the particle and can be used as an indication of what thermal regime the particle is in. Thermally thin (Bi<0.2), thermally thick (0.2<Bi<10) or thermally wave (Bi>10)

$$Bi = \frac{hL_c}{\lambda} \quad \text{(Eq 2-13)}$$

with h being heat transfer coefficient, L_c the characteristic length $\frac{Volume}{surface\ area}$, and lambda the thermal conductivity of the particle. For Bi number above 10, both drying and pyrolysis may be present in the same particle. For the thermally thin, shrinkage can be neglected. For the thermally thick, pyrolysis time is affected by both char shrinkage and moisture. For thermal wave the pyrolysis time and products are affected by the shrinkage and moisture [148].

2.4.5.2 Size

The size of the particle affects intraparticle residence time and the heating rate. This, in turn, affects the degree of secondary reactions. The feeding size used in an industrial application for biomass gasification is dependent on the gasifier design. 1-10mm in diameter has been used for the pilot scale fluidised bed [118], [149], and it is thus larger than what is seen for most pyrolysis experiments, where the particles are kept small to avoid secondary reactions.

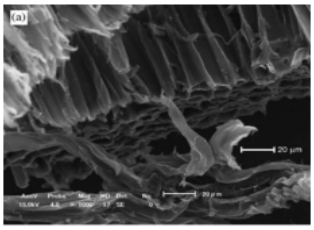

Figure 2-42: Hinoki sawdust after pyrolysis [151]

For large particles the mechanism for which the tar is transported out of the biomass to the gas phase may become important for the degree of condensation reactions of the primary tar.

When lignin is heated it becomes soft and may form a more or less liquid intermediate, where it has not completely depolymerised but does not preserve its structure [65].

The transport of the lignin-derived tar or liquid intermediate in woody biomass is through the pores of the biomass and is anisotropic because of the pore structure of the biomass [28]. The process may be affected by the heating rate as the pores in the biomass decreases in size as the heating rate increases [150]. This will restrict the mass transport because of increased resistance.

For low-heating rates the pore structure of the wood remains the same after thermal treatment, as shown in Figure 2-41, even for high-end temperatures such as 1200°C [150]–[152].

At very high heating rates (10^4-10^5 °K/s), the structure of the biomass can change and entrap gases, which is seen in the form of large internal cavities when the residual char is analysed [153] and may leave cracks in the char[150].

The initial integrity of the biomass structure comes from the cellulose and hemicellulose, which have a melting point of ca 260°C [154]. Lignin in itself will begin to soften between 154°C and 218°C. Furthermore, lignin will begin to swell due to the formation of foams that indicate pyrolysis is happening, which intensify with increased temperature [65].

Transport models often assume no liquid phase but strictly diffusion of tar gases through the pores. In the time it takes for tar to diffuse out of the biomass, heterogeneous condensation reactions may occur.

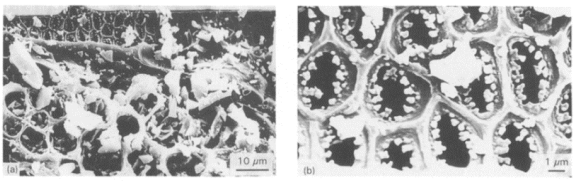

Figure 2-43: SEM of acacia wood after slow pyrolysis [150]

The real process may be more complicated than that. If isolated lignin is heated fast, tar is released as oligomer by the bursting of bubbles that send the liquid out, "thermal ejection", and form primary oligomeric lignin. The monomeric lignin is then formed from oligomeric lignin by secondary reactions [65].

It may be imagined that liquid lignin intermediate in biomass may be thermally ejected by a build-up of pressure inside the pores by rapid heating. This would fit well with the observation of embedded particles in the pores of slowly pyrolysed wood as seen in Figure 2-41, where lignin is assumed to form small intermediate liquid sites which the gas circumvents. The absence of the particles for fast pyrolysis as seen in Figure 2-42 is then explained by a high-pressure difference that ejects the liquid lignin intermediate [150]. The particles in the pores are speculated to be pyrolytic carbon that is formed from the melted/liquid lignin. A softening of the lignin, as a first step to char formation by radical reaction and the thermal ejection, may partly explain the observation of higher char yield at low heating rates by leaving a relatively high amount of tar for homogeneous condensation reaction.

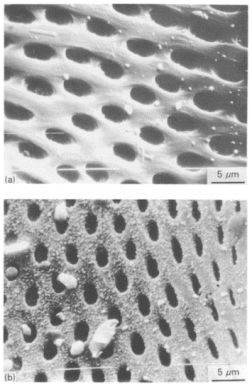

Figure 2-44: SEM of acacia wood after rapid pyrolysis [150]

2.4.5.3 Pressure

A reactor pressure increase may decrease the tar output. As pressure is increased the driving pressure gradient for transport of tar species out of biomass pores is decreased. This gives a longer residence time, which promotes condensation reaction within the biomass [155], [156]. It is also speculated that a pressure increase may make the tar species condense inside the pores, which in turn closes of the pores and changes the permeability. Model prediction shows an inter-particle over-pressure of 1bar at 850K [157].

2.4.5.4 Temperature

Temperature has a great deal of influence on the decomposition and re-polymerisation of tar. In Figure 2-43 is shown how the different classes of tar develop with temperature. The primary tar, which includes cellulose, hemicellulose and lignin-derived products are completely reduced at 800°C because of cracking or the removal or reduction of functional groups, which leads to the formation of secondary tar. Tertiary tar like methyl naphthalene begins to form at about 650°C because of the repolymerisation. A combination of both primary and tertiary tar in the product gas would suggest that there is channelling or process upsets [132].

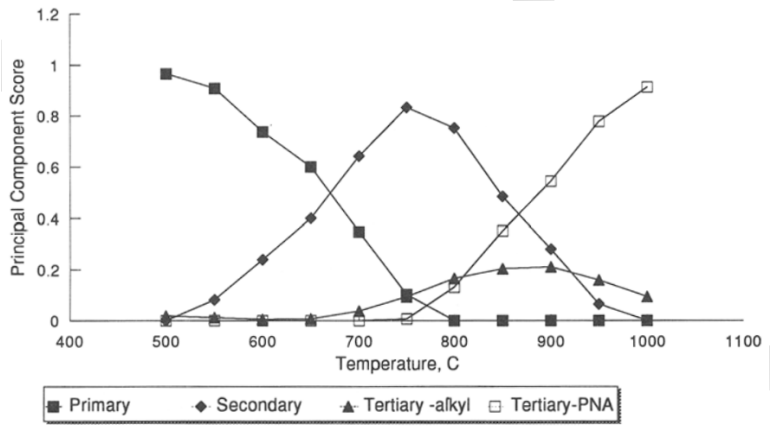

Figure 2-45: The distribution of tar over the temperature range from 500 to 1000°C[132]

As the temperature rises, the total amount of tar is reduced along with the change in composition. This has been seen in several studies with both steam and air for gasification [4], [7], [112], [158]–[160]. To get a complete cracking of the tar the temperature has to be higher than >1100°C [3], [161]. This is, however, difficult with fluidised bed because agglomeration may accrue.

For gasification with temperatures around 800°C, no primary tar are expected. The tar composition is expected to primarily consist of phenolic and aromatic compounds and a few PAHs.

2.5 REACTOR MODELLING

A few suggestions for modelling the bubbling bed system have been made. These models range from very simplified systems that may be expressed analytically to systems that include the consideration of bubble and solid movement.

2.5.1 Bubbling bed model

The bubbling bed model developed by Kunii and Levenspiel in the 60s is used to predict the flow of solid and gas in bubbling fluidised beds, based on the knowledge of the effective bubble size [162]. The model is developed to model gas-solid heat transfer, gas-solid mass transfer, and catalytic reforming [162].

The model assumes that the gas flow around a bubble follows the behaviour of the Davidson model for a single rising bubble [162]. A Constant bubble size is assumed, and thus an effective bubble size is used in the modelling. This assumption is not valid for shallow beds but is more plausible for deep bed where the maximum bubble size is reached [162]. The model disregards the small fraction of solid inside the bubble [162]. The emulsion void of the bed is assumed to be that of the minimum fluidisation [162]. This assumption is valid if the onset of bubbles starts at the minimum fluidisation velocity. If there is an expansion of the bed before bubbling begins, the void may be even higher, as is the case for Geldart A particles [14]. The bubbling bed model concentrates on the dense bubbling region of the fluidised bed [162].

The model does not say anything about how to handle the growth of bubbles by devolatilisation or gasification of solids or addition of extra gas.

The bubbling bed model is advantageous because it only requires a small amount of information about the system in the form of bubble size and minimum fluidisation.

2.5.1.1 Bubble velocity

A bubbling bed consists of particles that are fluidised by gas. When the bed is fluidised by a gas at a superficial velocity[6] u_0 that is above the minimum fluidisation velocity u_{mf}, gas bubbles are seen to rise through the emulsion[163]. The bubble rise velocity of a single bubble relative to the solid is derived by the Davidson model as [162], [164]:

$$u_{br} = 0.711(gd_b)^{1/2} \qquad \text{(Eq 2-14)}$$

For small bubbles, the rise velocity is lower than that of the gas percolating through the emulsion $u_{br} < u_f = \frac{u_{mf}}{\epsilon_{mf}}$. The gas in the emulsion will thus travel through the bubble. For larger bubbles,

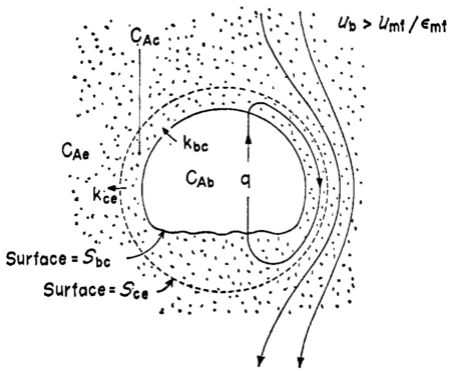

Figure 2-46: Individual contributions to flow of gas between bubble and emulsion [162]

[6] Velocity based on an empty reactor

where $u_{br} > u_f$, a cloud of gas surrounds the bubble and circulates into the bubble as shown in Figure 2-44.

The cloud size is related to the bubble size by the following relation [162]

$$\left(\frac{d_c}{d_b}\right)^3 = \frac{u_{br} + 2\,u_f}{u_{br} - u_f} \quad \text{(Eq 2-15)}$$

For velocities, $\frac{u_{br}}{u_f} > 5$, the cloud size is 10% of that of the bubble. This will be considered a negligible cloud size.

From [164] the bubble velocity from a crowd of bubbles can be related to the velocity of a single bubble by

$$u_b = u_{br} + u_0 - u_{mf} \quad \text{(Eq 2-16)}$$

For large bubbles, where the cloud can be neglected and the bubble carries its own gas with it, the total flow through the two phases is related by [162]

$$u_0 = (1 - \delta)\,u_{mf} + \delta\,u_b \quad \text{(Eq 2-17)}$$

The fraction of bubbles in the bed is calculated from combining equation (Eq 2-16) and (Eq 2-17):

$$\delta = \frac{u_{mf} - u_0}{2 \cdot u_{mf} + \alpha u_{mf} - u_{br} - u_0} \quad \text{(Eq 2-18)}$$

2.5.1.2 Emulsion phase

For the emulsion phase, the upward flow of gas may not be the same as the flow for minimum fluidisation because of drag from downward flowing particles from the solid circulation. [162]

$$u_e \neq u_f = \frac{u_{mf}}{\epsilon_{mf}} \quad \text{(Eq 2-19)}$$

The bubbles drag a wake of solid behind them, increasing circulation of solids with a downward movement of the solid in the emulsion phase to counter the solid movement.

The relative velocity between gas and solids remains at u_f. The upward velocity of gas flowing through the emulsion is then [163]

$$u_e = \frac{u_{mf}}{\epsilon_{mf}} - u_s \quad \text{(Eq 2-20)}$$

The solids travelling downwards in the emulsion occupies everything except for the bubble and the wake. The solid transport in the emulsion should be equal to the solid travelling upward in the wake [162]

$$(1 - \delta - \alpha\delta)u_s = \alpha\delta u_b \quad \text{(Eq 2-21)}$$

The solid velocity downwards in the emulsion is thus

$$u_s = \frac{\alpha\delta u_b}{1-\delta-\alpha\delta} \quad \text{(Eq 2-22)}$$

where α is the wake size as a fraction of the bubble size.

$$\alpha = \frac{volume\ of\ wake\ following\ a\ rising\ bubble}{volume\ of\ a\ bubble}$$

For large fast bubbles with negligible clouds ($u_b > 5u_f$ or $u_0 > 2u_{mf}$), the relationship between total flow of gas and the flow in the emulsion phase and bubble phase is [162]

$$u_0 = (1-\delta-\alpha\delta)\epsilon_{mf}u_e + \left(\delta + \alpha\delta\epsilon_{mf}\right)u_b \quad \text{(Eq 2-23)}$$

Combining the equations (Eq 2-20), (Eq 2-22), and (Eq 2-23) gives the bubble velocity as a function independent of the solid or emulsion velocity

$$u_b = \frac{u_0 - (1-\delta-\alpha\delta)\,u_{mf}}{\delta} \quad \text{(Eq 2-24)}$$

Combining equations (Eq 2-20), (Eq 2-22), and (Eq 2-24) leads to an expression of the gas velocity in the emulsion phase [162]

$$u_e = \frac{u_{mf}}{\epsilon_{mf}} - \left(\frac{\alpha u_0}{1-\delta-\alpha\delta} - \alpha u_{mf}\right) \quad \text{(Eq 2-25)}$$

For vigorous bubbling, the circulation of the solid may become so large that gas is flowing downwards in the emulsion phase. This flow reversal should occur when [163]

$$\frac{u_0}{u_{mf}} > 6\sim11 \quad \text{(Eq 2-26)}$$

A modified version of the bubbling bed where the solid circulation to the combustor is also included is available in Appendix C – Modified bubbling bed model.

2.5.1.3 Gas interchange between phases

To describe the interchange of gas between the bubble and emulsion, the bubble model utilises three zones: the bubble phase, the cloud phase, and the emulsion phase.

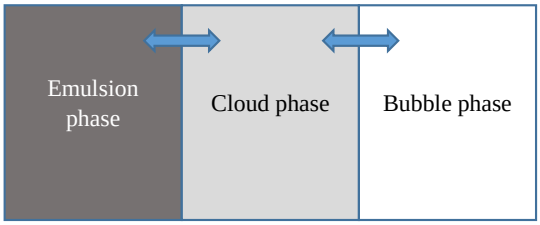

Figure 2-47: sketch of the gas interaction

The three phases are in contact as sketched above, where the bubble phase is only in contact with the cloud phase as this surrounds the bubble. The cloud phase is in contact with the emulsion phase and the bubble phase.

The interchange of mass between the bubble and the cloud is affected by the circulation of gas and diffusion between the bubble and the cloud as illustrated in Figure 2-44. [14, Ch. 10–11], [162]

The mole transfer is set up with respect to change in time. This may be related to the concentration change with length by the relation $-\frac{1}{V_b}\frac{dN_{Ab}}{dt} = -u_b\frac{dC_{Ab}}{dl}$ [162]. From a mole balance perspective, the change of mole in the bubble, with the initial N_{Ab_0} mol of A in the bubble, is increased by:

$$-\frac{\partial N_{Ab}}{\partial t} = (q + k_{bc}S_{bc})\,(C_{Ab} - C_{Ac}) \qquad \text{(Eq 2-27)}$$

where C_{Ac} is the concentration of A in the cloud, C_{Ab} is the concentration of A in the bubble, k_{bc} is the effective mass transfer coefficient, S_{bc} is the surface contact area between cloud and bubble, and q is the volumetric flow and is defined by [162]

$$q = \frac{3\pi}{4}u_{mf}d_b^2 \qquad \text{(Eq 2-28)}$$

From Davidson and Harrison, the following expression describes the mass transfer coefficient between bubble and cloud [162]

$$k_{bc} = 0.975\,D^{1/2}\left(\frac{g}{d_p}\right)^{1/4} \qquad \text{(Eq 2-29)}$$

where D is the diffusion coefficient.

This differential equation may further be described by position by the following relationship

$$-\frac{\partial N_{Ab}}{\partial t} = -V_b u_b\frac{\partial C_{Ab}}{\partial L} \qquad \text{(Eq 2-30)}$$

A similar expression as the differential of the bubble can be set up for the cloud and emulsion. The cloud is in contact with the bubble and the emulsion. Thus, there is a convective and diffusive mass transfer with the bubble. This results in the following differential equation for the cloud[162]

$$-\frac{\partial N_{Ac}}{\partial t} = (q + k_{bc}S_{bc})\,(C_{Ac} - C_{Ab}) + S_{ce}k_{ce}(C_{Ac} - C_{Ae}) \qquad \text{(Eq 2-31)}$$

Again, the following relation with the position of the reactor can be set up

$$-\frac{\partial N_{Ac}}{\partial t} = V_c u_c\frac{\partial C_{Ab}}{\partial L} \qquad \text{(Eq 2-32)}$$

The cloud follows the bubble, thus $u_c = u_b$.

The mass transfer coefficient between the emulsion and the cloud is described according to the Higbie penetration model [162]

$$k_{ce} =\cong 1.13\sqrt{\frac{4D_e\epsilon_{mf}\left(u_{br}-u_{fr}\right)}{d_b}}\left(\frac{1-\frac{u_f}{u_b}}{1+\frac{2u_f}{u_b}}\right)_r^{\frac{1}{6}} \quad \text{(Eq 2-33)}$$

The emulsion is not in contact with the bubble, and thus only the contribution from the diffusion between the cloud and the emulsion is included.[162]

$$-\frac{\partial N_{Ae}}{\partial t} = S_{ce}k_{ce}(C_{Ae}-C_{Ac}) \quad \text{(Eq 2-34)}$$

2.5.1.4 Solid transfer

The solid transfer is set up in a similar way to the gas transfer. For the solid transfer there is only a transfer between the cloud, which includes the wake and the emulsion.

The solid transfer between the cloud and the emulsion will thus have the form

$$-\frac{\partial N_{ic}}{\partial t} = S_{ce}k_w(C_{ic}-C_{ie}) \quad \text{(Eq 2-35)}$$

The solid transfer coefficient for particles between the cloud and the emulsion is given by [165].

$$k_w = \frac{V_w}{S_w}K_w = \frac{V_w}{S_w}\frac{4u_{mf}}{\pi d_b\epsilon_{mf}} \quad \text{(Eq 2-36)}$$

$$K_w = \frac{4u_{mf}}{\pi d_b\epsilon_{mf}} \quad \text{(Eq 2-37)}$$

2.5.1.5 Comparison with data

The bubbling bed model is able to explain the lower values for Sherwood numbers that are observed for the bubbling bed because of the bypassing of gas in the bubbles by choosing appropriate values for mass transfer and bubble size [166] as shown in Figure 2-46.

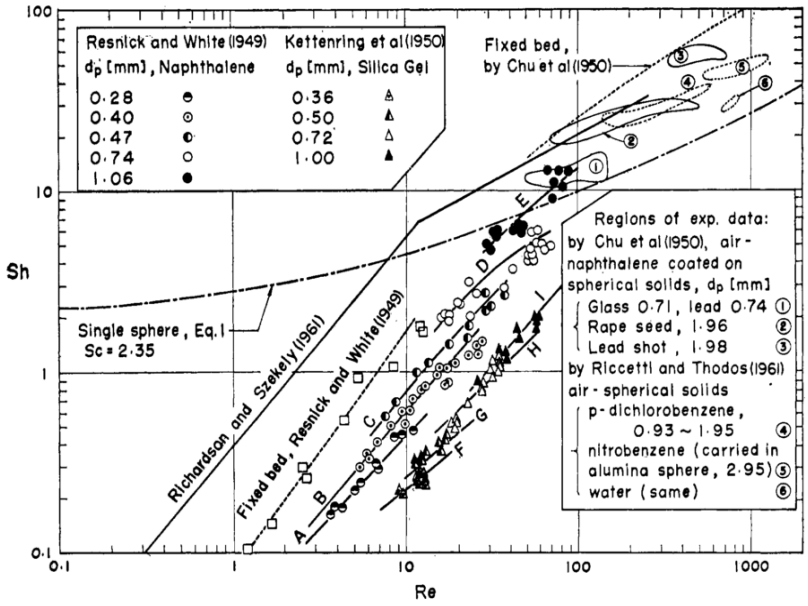

Figure 2-48: Comparison of gas-solid mass transfer in fluidised bed and the bubbling bed model [166]

The bubble size has been fitted to represent the data because no data of the bubble diameter is present.

The bubbling bed model also shows good estimations of catalytic conversion. Figure 2-47 presents the data for ozone decomposition under conditions where downwards flow of gas in the emulsion is possible. For the comparisons, the rate term related to the transport between cloud and bubble and the catalytic conversion are the dominant factors [166].

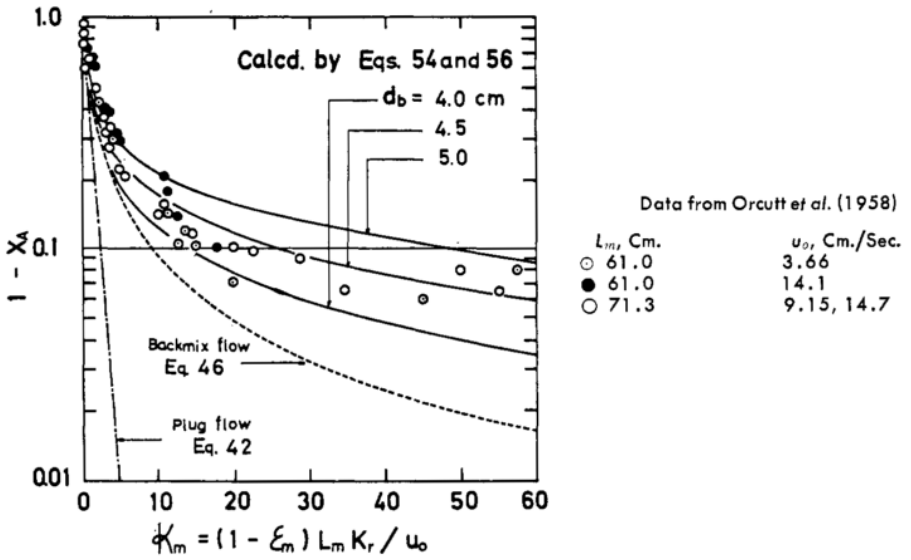

Figure 2-49: Conversion vs. dimensionless reaction rate for catalytic decomposition of ozone [166]

2.5.2 Bubble Assemblage Model

The Bubble Assemblage model uses a variable bubble size. The model compartmentalises the reactor with each compartment having a height equal to the size of the bubble. Here it is assumed that the percolation of gas through the emulsion can be neglected, the bubble phase includes clouds and voids, the reactants is perfectly mixed inside each phase in each compartment, and there is no back-mixing of bubble gas between compartments. The bubbles are considered to grow continuously while passing through the bed until they reach the maximum stable size or the diameter of the bed. The model assumes isothermal conditions.

The concentration profile under catalytic cracking is described by the following equation [167]

$$C_{Ab_n} = \frac{C_{Ab_{n-1}} u_0 A}{k_{w_n} V_{b_n} - \frac{\left(k_{w_n} V_{b_n}\right)^2}{kV_{e_n} + k_{w_n} V_{b_n}} + kV_{c_n} + Au_0} \quad \text{(Eq 2-38)}$$

and

$$C_{Ae_n} = \frac{C_{Ab_n} k_{w_n} V_{b_n}}{kV_{e_n} + k_{w_n} V_{b_n}} \quad \text{(Eq 2-39)}$$

The model gives a good prediction of the bubble phase concentration but over predicts the emulsion phase [167].

2.5.3 Dense Phase Perfectly mixed (DPPM) and Dense Phase in Plug Flow (DPPF)

Other simple models have been proposed for describing the gas concentration in a bubbling bed like the dense phase perfectly mixed (DPPM) model and the dense phase in plug flow (DPPF).

The DPPM model assumes that gas in the entire dense phase is perfectly mixed. The perfect mixing of gas in the dense phase facilitates a back-mixing.

For both models the gas phases are assumed to be upwards-flowing [16]. The model is aimed at the catalytic reforming of gas, and thus solid conversion and movement are not incorporated.

For the DPPM the mass balance for the dens and bubble phase for a boundary condition $\frac{C_{Ab}}{C_{Ai}} = 1$ at $y = 0$ yields the concentration profiles [16]:

$$C'_{Ae} = \frac{C_{Ae}}{C_i} = \frac{1 - \beta e^{-x}}{k' + 1 - \beta e^{-x}} \quad \text{(Eq 2-40)}$$

$$C'_{Ab} = \frac{C_{Ab}}{C_{Ai}} = C'_{Ae} + (1 - C'_{Ae}) e^{-Qy/u_b V_b} \quad \text{(Eq 2-41)}$$

The outlet concentration is given by

$$C'_{A0} = \frac{C_{A0}}{C_{Ai}} = \beta C'_{Ab}|_{y=L_f} + (1 - \beta) C'_{Ae}|_{y=L_f} \quad \text{(Eq 2-42)}$$

where $\beta = \left(1 - \frac{u_{mf}}{u_0}\right)$ is the fraction of the flow associated with the bubble phase, $Q = q + k_{ec} S_{be}$ is the overall volumetric rate of exchange between bubble and the emulsion, $X = \frac{QL_f}{u_b V_b}$ is the number of transfer units, L_f is the mean expanded bed height, $k' = \frac{kL_{mf}}{u_0}$ is the dimensionless reaction rate constant, k is the reaction rate constant based on unit volume of dense phase at ϵ_{mf}, and y is the distance above the distributer plate. [167]

The DPPF model is similar to the DPPM but the emulsion phase is modelled as a plug flow. For the purely catalytic conversion with boundary conditions $C'_{Ab} = C'_{Ae} = 1$ at $y = 0$, the concentration profiles are described as:

$$C'_{Ab} = C_1 e^{-m_1 y} + C_2 e^{-m_2 y} \quad \text{(Eq 2-43)}$$

$$C'_{Ae} = C'_{Ab} - \frac{L_f}{X}(C_1 m_1 e^{-m_1 y} + C_2 m_2 e^{-m_2 y}) \quad \text{(Eq 2-44)}$$

$$C'_{A0} = \frac{u_0 - u_{mf}}{u_0} C'_{Ab}|_{y=L_f} + \frac{u_{mf}}{u_0} C'_{Ae}|_{y=L_f} \quad \text{(Eq 2-45)}$$

where C_1, C_2, m_1, and m_2 are constants [16], [167].

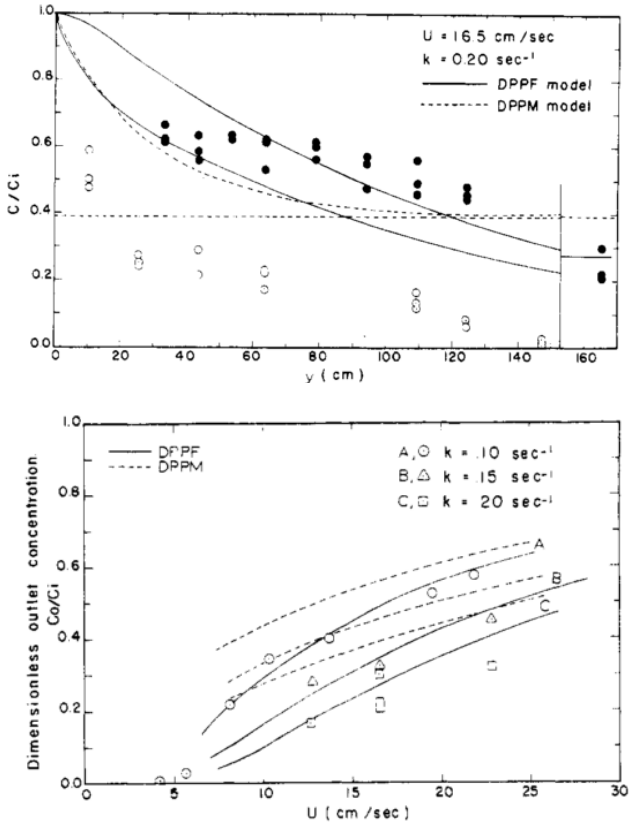

Figure 2-50: Comparison of experimental result from catalytic decomposition of ozone and model prediction from Orcutt Dense Phase Perfectly mixed (DPPM), and Dense Phase in Plug Flow (DPPF) models. To the left is seen the concentration profile. To the right is seen the overall concentration at the outlet. [167]

DPPM results in an overestimation of the concentration in the emulsion and does not give good predictions, as can be seen in Figure 2-48 [167]. The DPFF model gives a better prediction for the overall results and gives similar trends as the experiment for the concentration profile. The value of the concentration profile in the emulsion is, however, still overestimated. This is speculated to be from an over-prediction of mass transfer[167]. The model does not include a cloud phase, and thus the circulation of gas inside the bubble will be treated as being transported to the emulsion phase.

2.5.4 Resume of models

Chavarie et al. [167], [168] investigated the fluidised bed models. They suggest that the primary discrepancy with the models is the ability to predict the start and end development of the concentration profile. They propose that the reactor modelling may be divided into three sections because these discrepancies are related to different hydrodynamic behaviours of the bed. Near the distributor plate, a rapid concentration drop is seen, which may be related to back-mixing; the middle section has a relatively flat profile, and for the top is seen a drop in the bubble phase concentration, which is thought to be because of a relatively fast expansion of the bubbles at the surface of the bed.

Several of the models are valid for the approximation of the reactor behaviour. Chavarie et al. [167], [168] conclude that the bubble model success is in the magnitude of interphase mass transfer coefficient and the negligible percolation of gas in the emulsion phase. Furthermore, the variation in bubble size does not seem to be of over-riding importance for reactor performance.

Table 2-7: Resume of fluidised bed models

Model name	Advantages	Disadvantages
Bubbling bed model	It is a one-dimensional model that includes transfer to and from bubbles. The bubble model explains back-mixing in the reactor by an emulsion phase that drags gas down in the bed with adsorption to the particles. It utilises the bubble size to describe the hydrodynamics of the bed. It gives a good prediction for the bubble and emulsion phase except in the bottom of the bed.	The model is not particularly usable for upscaling as it does not include wall influence. It assumes a fixed bubble size that may be changed by discretising the model in the axial direction. The model will be moderately hard to discretise.
DENSE PHASE PERFECTLY MIXED model	The model is very simple.	The model over-predicts the concentration and does not show the correct trend for the concentration profile in the dense phase. It will need modification to include reaction in the bubble phase.
Dense Phase in Plug Flow	The model is simple. The model is able to predict the outlet concentration reasonably well.	It is suggested that the mass transfer is too high [167]. The concentration profile for the emulsion phase is overestimated and only the trend is predicted.
Bubble Assemblage Model	The model allows for variation in bubble size. The model includes clouds like the Bubbling bed model. Complete mixing in each phase in each compartment is assumed.	The model neglects the backflow of gas in the emulsion and bubble phase.

2.6 SINGLE PARTICLE MODELLING

The devolatilisation of a biomass particle experiences several physical and chemical processes. Which steps are dominating the devolatilisation process will depend on the conditions for the particle environment, e.g. temperature, pressure, gas velocity, bed material contact. For very high heating rates the pore structure of woody biomass may change and be closed off, but for most conditions the overall porous structure is maintained during the pyrolysis step and volatiles may be transported through the pores of the biomass.

The devolatilisation is initiated by a heating of the particle. This heat is supplied by radiation and thermal conduction to the surface of the particle. This is often reported by an effective heat transfer coefficient h, which is dependent on direct contact with other bed materials, gas velocity radiation and thermal conductivity. As heat is transported to the surface of the particle, it increases in temperature and creates a temperature gradient inside the particle. The degree of the temperature gradient is dependent on the relation between the heat transfer to the surface, the conduction inside the particle, and the size of the particle. The Biot number $Bi = \frac{hL_c}{\lambda}$ is used to characterise the thermal behaviour of particles as described in section 2.4.5.1. Thus, for small particles or low heating rates the particle may be assumed to be isothermal, whereas for large particle or high heating rates a significant temperature gradient is expected. Furthermore, the parallel pore structure [28] gives anisotropic properties for both permeability and heat conduction.

Humid biomass will experience a drying before the pyrolysis at around 100°C. For a particle with a low Biot number, the water will evaporate all through the particle at the same time. The particle will thus keep the same temperature throughout the evaporation process. For a particle with a high Biot number, the large temperature gradient leads to water evaporating at the edge of the particle followed by pyrolysis before the particle is fully dried.

As the biomass heats up, the dry biomass lignin will begin to soften, followed by beginning degradation of lignin, hemicellulose and cellulose. Lignin forms a liquid intermediate that may diffuse into the lumen, as evident by small residual particles after pyrolysis [150]. Cellulose and hemicellulose begin to depolymerise, and gases and primary tar are formed. The gas and liquid formation in the particle form overpressure inside the particle, which will contribute to the mass and heat transport besides the diffusion and conduction.

During devolatilisation, the particle only shrinks slightly and thus the density of the overall particle will decrease. The inner part of the cell wall (the secondary wall) is primarily cellulose [27], and as it degrades, the pore radius is expected to increase because of the low char formation from cellulose [30], [57], [58]

To estimate the dominating phenomena, Dufour et al. [157] looked into the time-scale between different phenomena related to the pyrolysis of biomass. The time-scale used is defined as given in Table 2-8.

k is the reaction rate, L the particle diameter, D_L the diffusion coefficient for gas in hydrocarbon liquid, D_G the diffusion coefficient for gas in porous char, μ_L the dynamic viscosity of intermediate liquid, μ_G the dynamic viscosity of gas, ΔP the pressure difference between the inside of the particle and the outside of the particle, K_0 the permeability, ρ the density, C_p the specific heat capacity, and λ the thermal conductivity coefficient.

Table 2-8: Characteristic time-scale of the major intra-particle processes during wood pyrolysis [157]

Phenomenon	Equation
Chemical reaction: The time scale of biomass conversion	$t_{ch} = \frac{1}{k}$
Liquid diffusion:	$t_{DL} = \frac{L^2}{D_L}$
Gas diffusion in porous char:	$t_{DG} = \frac{L^2}{D_G}$
Liquid convection in porous solid	$t_{CL} = \frac{\mu_L L^2}{\Delta P \, K_0}$
Gas convection in porous solid	$t_{CG} = \frac{\mu_G L^2}{\Delta P \, K_0}$
Internal heat transfer	$t_h = \frac{L^2 \rho C_p}{\lambda}$

Dufour et al. analyses a 1 cm particle at temperatures near that used for gasification (1000K). This shows that chemical reaction is faster than the heat transfer to and through the particle as well as the convective transport from the pressure gradient. The time-scale of chemical reaction was also the only parameter that significantly changed with temperature [157]. Thus, for low temperatures, chemical reaction may be a limiting factor. The internal heat transfer time-scale is lower than convective transfer time-scale and thus the limiting factor for the conversion.

Dufour et al. [157] also compare the time-scale with an experiment of a 1.5mm particle that takes 30 s to devolatilise. Here the time-scale for internal heat transfer is in the order of 1s, reaction 0.1s, and convective transport 10^{-5} s, and is thus not able to account for the slower devolatilisation. Diffusion through the particle is, however, much higher in the order of 10^4s, and thus Dufour et al. [157] suggest a combination of effects. The limiting factor lies in the diffusion of gas formed inside the cell wall to the surface of the cell wall from which gas is transported by convection through the pores to the surface of the particle.

2.6.1 Modelling approaches

Particle models for biomass are often modelled as a transport model with a temperature gradient [169]–[171] or as an isothermal particle [172] [78]. As has just been discussed, heat transfer is the limiting step for larger particles with high heating rates, where a temperature gradient will be present in the particle. For small particles with a low heating rate, the temperature gradient will be close to 0 and reaction rate or convection will be the limiting step. For gasification of biomass in fluidised beds, the wood particles can be relatively large, up to 6mm times 15mm for some pilot scale plants [173], because it is expensive and difficult to grind biomass to fine particles. At the same time, the particles will be exposed to a hot bed material, which will give high heating rates. Because of the relatively large particles and the high heating rate, the best prediction in a fluidised bed will be from modelling the particle with heat transport.

Simply modelling the particle in its transport models may be a reasonable task, but incorporating the model into a larger and more complicated system may be too complicated. Thus, often the isothermal particle model is utilised when combined with reactor simulations [106], [174] or when complicated reaction schemes are used.

The incorporation of a particle model is done by considering the amount of particles in a control volume. The differential equation for the mass change of the particles is then introduced to the

mass change of the control volume. If the particle is considered uniform, only one value of each particle is necessary, while if a transport model is used, several values of each particle is necessary, which means that computational requirements increase with increased particle complexity.

Reaction schemes, as well as a variety of particle models incorporating different aspects of the particle phenomenon, have been developed and some of them are shown in Table 2-9.

Table 2-9: Overview of particle models

Model	Differential equations	Advantages and disadvantages	Reference
Isothermal model with instant devolatilisation The model assumes instant devolatilisation and that the particle is isothermal. The reference assumes that biomass consists of cellulose, hemicellulose and lignin for which their devolatilisation may be described by the scheme: 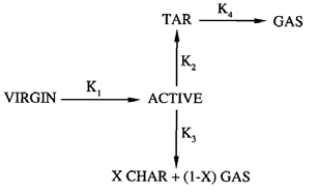 	$\frac{dm_{virgin}}{dt} = -k_1 m_{virgen}$ $\frac{dm_{aktive}}{dt} = k_1 m_{virgen} - (k_2 + k_3) m_{aktive}$ $\frac{dm_{tar}}{dt} = k_2 m_{aktive} - k_4 m_{tar}$ $\frac{dm_{char}}{dt} = X k_3 m_{aktive}$ $\frac{dm_{gas}}{dt} = (1 - X) k_3 m_{aktive} + k_4 m_{tar}$ $k_j = A_j \cdot \exp\left(-\frac{E_j}{RT}\right)$	The model is limited to small particles at low heating rates where temperature can be assumed to be uniform. This is often the case for kinetic investigation. It will not be possible to accurately simulate systems with large particles and high heating rates.	[172] Similar for [78] but with a different reaction scheme
Mass transport model The model incorporates mass transport through the pores by Darcy's law. It may also include diffusion as in [175]. Diffusion is, however, a minor contribution in most cases. The temperature is assumed to be uniform. The reference assumes biomass to be a single component that forms intermediate components that are in competition between forming char and tar.	Reactions of solid $\frac{dy_B}{dt} = -k_1 y_B$ $\frac{dy_I}{dt} = k_1 y_B - (k_2 + k_3) y_I$ Chemical reaction of solids and liquids $\frac{dy_{S_1}}{dt} = (1 - \gamma) k_2 y_I$ $\frac{dy_{S_2}}{dt} = (1 - \delta) k_4 y_{T_L}$	The mass transport model includes convective transport. For the convective transport to be of importance, the time-scale has been lower than the reaction rate. This may happen when the gas formation is low by low heating rates. A low heating rate also justifies the assumption of an isothermal particle. The model is advantages when secondary char	[157]

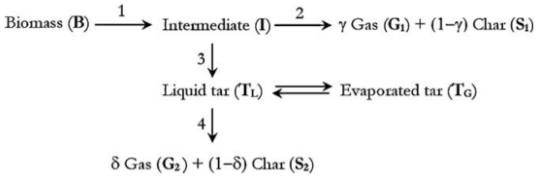 Tar evaporation is included by an equilibrium constant.	$\frac{d(y_{T_L}+y_{T_G})}{dt} = k_3 y_I - k_4 y_{T_L} - \frac{KRT\rho_{b0}}{\mu L^2}\left(\frac{y_{T_G}}{M_T} + \frac{y_{G_1}}{M_{G_1}} + \frac{y_{G_2}}{M_{G2}}\right) y_{T_g}$ The conservation equations has been expressed in terms of fraction relative to the initial mass $y_j = \frac{\rho_j}{\rho_{b0}}$ Equilibrium to describe the evaporated tar $y_{T_G} = \frac{M_T \exp(A) \exp\left(-\frac{B}{T}\right)}{RT\rho_{b0}}$ Conversion and convective transport of gases $\Delta P = RT\rho_{b0}\left(\frac{y_{T_G}}{M_T} + \frac{y_{G_1}}{M_{G_1}} + \frac{y_{G_2}}{M_{G2}}\right)$ $\frac{dy_{G_1}}{dt} = \gamma k_2 y_I - \frac{K\Delta P}{\mu L^2}$ $\frac{dy_{G_2}}{dt} = \delta k_4 y_{T_L} - \frac{K\Delta P}{\mu L^2}$	formation inside the particle is important. Thus the model may be primarily advantages at low heating rates and low temperatures. For high heating rates simpler models may be more computationally favourable while keeping the same accuracy.	
Heat transport model The model treats the temperature as a gradient throughout the particle. Heat is provided by exchange with surroundings as specified by a boundary condition. The heat of reaction contributes to the temperature profile. The transport of formed gases is assumed to instantly leave the particle.	Chemical reactions $\frac{d\rho_B}{dt} = -(k_1 + k_2)\rho_B$ $\frac{d\rho_{G_1}}{dt} = k_1\rho_B - k_3\rho_{G_1}\rho_{C_1}$ $\frac{d\rho_{C_1}}{dt} = k_2\rho_B - k_3\rho_{G_1}\rho_{C_1}$	This model is primarily advantageous for large particles or high heating rates where thermal conduction is the limiting step. The addition of heat of reaction makes it possible to simulate a	[169]–[171]

The reference assumes biomass to be one component with a competing reaction to form char and tar. 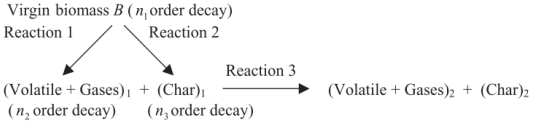 .	$$\frac{d\rho_{G_2}}{dt} = k_3\rho_{G_1}\rho_{C_1}$$ $$\frac{d\rho_{C_2}}{dt} k_3\rho_{G_1}\rho_{C_1}$$ Heat equation $$\frac{\partial\left(T \cdot C_p(T) \cdot \rho_{total}\right)}{\partial t} = \lambda(T) \cdot \left(\frac{\partial^2 T}{\partial r^2} + \frac{b}{r}\frac{\partial T}{\partial r}\right) + (-\Delta H) \cdot \left(-\frac{\partial \rho_{bio}}{\partial t}\right)$$	more accurate temperature profile and cases where the internal temperature exceeds the external temperature. The disadvantages of this is a more complex numerical scheme. The model cannot be used for secondary reaction inside the particle because all volatiles are assumed to leave instantly. The weakness of the transport models lies in the physical properties and kinetics that are hard to determine. Especially the density and thermal conductivity are sensitive for the model prediction [176].	
Heat and mass transport model This is a combination of the mass and heat transport models. The energy balance is thus extended to include the energy loss by mass transport. For the example heat of reaction is not included but this may also be added when significant. The reference assumes biomass to be a simple one-component biomass with competing reactions between gas, tar, and char.	Chemical reactions of solid $$\frac{d\rho_B}{dt} = -(k_1 + k_2 + k_3)\rho_B$$ $$\frac{d\rho_C}{dt} = k_3\rho_B$$ Chemical reaction and mass transport of tar and gas. $$\frac{d\epsilon\rho_T}{dt} + \frac{1}{r^2}\frac{d}{dr}(r^2\rho_T u) = k_2\rho_B - k_4\epsilon\rho_T$$	The advantage of this model is that it may be accurate over a large span of conditions because of the complexity. This may, however, also limit its use to the cases where there is a lager change in condition, which is rarely seen. The complexity makes it more computational and	[177] A similar setup for [178]. This reference includes diffusion that is in the same order of magnitude as heat transport but neglects to identify convective transport as a significant mass transport that will

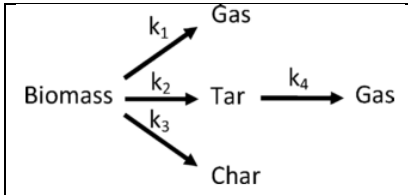	$\frac{d\epsilon\rho_g}{dt}+\frac{1}{r^2}\frac{d}{dr}\left(r^2\rho_g u\right)$ $=(k_1+k_2)\,\rho_B$ Energy conservation $\frac{d}{dt}\sum_i(\rho\hat{h}_i)+\frac{1}{r^2}\frac{d}{dr}\left(r^2\rho_g u\hat{h}_g\right)$ $=\frac{1}{r^2}\frac{d}{dr}\left(r^2\lambda\frac{dT}{dr}\right)$	more difficult to implement into a system. A simpler model will be advantageous when less change is seen in the condition.	make the diffusion insignificant A similar setup for [179] but they include heat of reaction in energy conservation
Anisotropic mass and energy transport model This model extends the mass and energy transport by introducing transport in two dimensions with different properties of permeability and thermal conduction. The reference assumes that biomass is composed of lignin, cellulose and hemicellulose with multiple competing reactions and multistep reactions.	Conversion of solid $\frac{d\rho_{s,i}}{dt}=\omega_{s,i}$ Gas conversion and mass transport $\frac{d\rho_g}{dt}=\omega_g-\frac{1}{r}\frac{d}{dr}\left(\hat{\rho}_g u_r r\right)-\frac{d}{dz}\left(\hat{\rho}_g u_z\right)$ Individual gas components $\frac{dy_i\rho_g}{dt}=\omega_{g,i}-\frac{1}{r}\frac{d}{dr}\left(\hat{\rho}_g y_i u_r r-\rho_g r D\frac{dy_i}{dr}\right)-\frac{d}{dz}\left(\hat{\rho}_g y_i u_z-\rho_g D\frac{dy_i}{dz}\right)$ Energy conservation $\frac{d\left(\rho C_p\right)_{tot}T}{dt}=q-\frac{1}{r}\frac{d}{dr}\left(\hat{\rho}_g u_r r C_{p,g}T-r\lambda_r\frac{dT}{dr}\right)-\frac{d}{dz}\left(\hat{\rho}_g u_z C_{p,g}T-\lambda_z\frac{dy_i}{dz}\right)$	This model will be good for cases where the heat or mass transport is of equal importance in radial and axial directions of the particle. The model also includes diffusion of gas species which may be unnecessary as convection in most cases will be largely dominating.	[175] Similar model by [180]

No matter what kind of biomass model is chosen, a number of kinetic schemes may be combined with the mass and energy transport of the particle. The kinetic schemes can vary from a single biomass material that devolatilises [176] to more complicated models based on pseudo-elements of the biomass that forms a range of gases, tar species, liquid intermediates, and solids [181] [106].

The single biomass component scheme assumes that biomass is a uniform mass for which the devolatilisation may be described by competing reactions as illustrated in Figure 2-49.

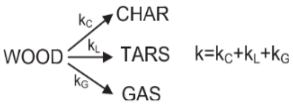

Figure 2-51: One-component mechanisms [176].

Many of the schemes lump the products into gas, tar, and char [176], which means that they can only be used for determination of the weight of each fraction unless some information of the composition of the fraction is given or assumed. To use this kind of schemes, it is necessary to have kinetic information about each material used because of the different composition of biomass.

Multicomponent schemes assume that biomass is composed of more than one pseudo-component. Each pseudo-component undergoes devolatilisation individually without interaction between the pseudo-components. The devolatilisation of the pseudo-component is happening by competing reactions that form tar, char, and gas. Multicomponent schemes may also include intermediate compounds to get a better fit with thermogravimetric measurements as shown in Figure 2-50 and Figure 2-51.

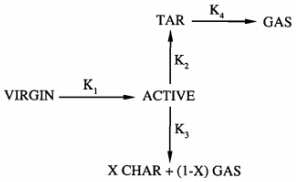

Figure 2-52: Multicomponent mechanisms proposed by [203]

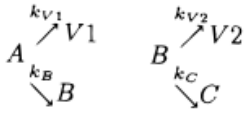

Figure 2-53: Multicomponent mechanisms used by [204]

The intermediate components may be a partial degradation of one of the pseudo-components, like a depolymerisation of cellulose, hemicellulose, or lignin.

Multicomponent schemes utilise general kinetics for pseudo-components in any biomass. Thus, the schemes only require information about the composition of pseudo-components. The majority of the multicomponent schemes consist of devolatilisation mechanisms [176], which are only used to determine the rate of weight loss.

They may, however, also include detailed information on the biomass composition and utilise specific reactions to form a more comprehensive understanding of the product formation as shown in Figure 2-52, Figure 2-53, and Figure 2-54. There are models for lignin where 100 molecules and 500 reactions are used to predict the primary tar release [34] that includes the radical formation and termination which are related to lignin degradation. These schemes may be used

to identify the best condition for a specific product that may be valuable or problematic like tar species.

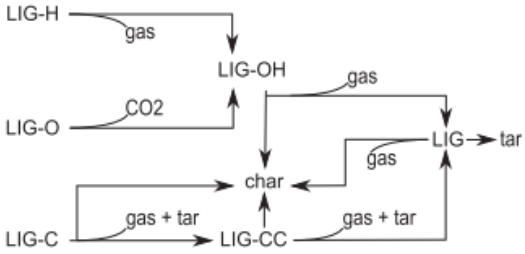

Figure 2-54: Lumped reaction path for lignin [175] *adopted from*[181]

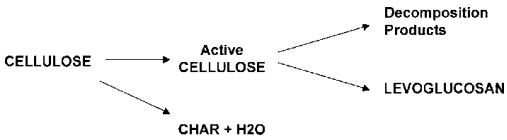

Figure 2-55: Reaction path for cellulose [181]

Figure 2-56: Reaction path for hemicellulose [175] *adopted from*[181]

The activation energy (E) for single component schemes ranges from 69-91 kJ/mol for high-temperature data (up to 1400K) to 56-174 kJ/mol for low-temperature data (below 800K).

For the multi-component the activation energies vary slightly as well [176]

- Hemicellulose 80-116kJ/mol
- Cellulose 195-286 kJ/mol
- Lignin 18-65kJ/mol

The variation in activation energy may be related to different heating conditions and mathematical treatments of the experimental results. If heat and mass transfer has been neglectable where it is significant for the pyrolysis, the apparent kinetics will be lower than the true value [176].

3 EXPERIMENT

The literature study on tar release from biomass (2.4.1 Devolatilisation of biomass) shows that the heating process of biomass has a significant effect on the char formation. In general, char formation is maximised by low-temperature heat treatments over many hours without oxygen. This process is known as pyrolysis. Cellulose and hemicellulose, especially, have been shown to form considerably more char by low-temperature treatment. The tar from cellulose and hemicellulose, however, is relatively easy to decompose at gasification temperatures. The tar formation from lignin is the most problematic tar and forms precursors for PAH. Heat treatment is also indicated to affect lignin char formation. It is thought to be a result of the condensation reaction of the monolignols at temperatures around 300°C forming fixed char. It has, however, not been possible to find literature that shows how the tar formation from lignin is reduced because of low-temperature treatment.

If the monolignols can be manipulated to participate in condensation reactions, it is expected that the tar formation will be reduced and the char formation will be increased. If such a process should be integrated with the gasification process, it will have to be pre-heat-treatment, as the temperature in the gasifier is constant. The implementation of such a pre-treatment would be limited in time to avoid the cost of large pre-processing equipment. At the same time it is known that a large part of the biomass is lost during pyrolysis as gas and tar; this is, however, valuable energy that would have to be used. Most optimally this would be reformed in the gasifier to product gas. Thus, for the pre-treatment to be effective the cumulative tar formation from both torrefaction and gasification would have to be lowered. The analysis of tar thus focuses on a cumulative formation of tar from both torrefaction and gasification.

3.1 EQUIPMENT AND MATERIALS

The experimental setup consists of a pyrolysis unit (pyroprope 5200 from CDS Analytical Inc.) connected to GC/MS analysis equipment (TR-WaxMS 30m by 0.25mm by 0.25micrometer column combined with ISQ MS by TermoFisher Scientific, America) by a heated transfer line. Pyrolysis and torrefaction have been performed using the same pyroprope 5200 that is designed for fast pyrolysis analysis of samples (dealkalised lignin from TCI Shanghai). A PI-diagram of the setup is shown in Figure 3-1 where the position of the pyroprope and the cooling trap can be switched to use a different analysis method. Both the method is utilised to analyse the pyrolytic product, a trap mode analysis and a direct injection method as they have different advantages. Direct injection mode ensures that no reaction is happening in a condensed phase on the cooling trap. The trap mode conserves more of the tar and excludes light gases that are not condensed, making it easier to separate the components.

3.2 SETUPS AND METHODS

Two kinds of setup have been used for the experiment the trap mode and the direct injection mode as shown in Figure 3-1 at the top and bottom, respectively.

3.2.1 Trap mode analysis

A sample of approximately 1-2 mg is placed in a quartz tube between quartz wool that is placed in a heating coil and the pyroprope. The pyroprope is placed in the pyrolysis chamber that has a standby temperature of 100°C. As the sample is loaded in the pyroprope, the gas is diverted to the purge through L7 and potential water in the sample may thus be removed before sampling. The carrier gas, helium (He), is introduced through the low-pressure inlet during the pyrolysis (L1a).

The carrier gas transports the pyrolytic products from the pyroprope to the trap (L3 and L4) during the sampling. The tar is condensed in the trap, which is held at 40°C during sampling to purge light gases through L8. After pyrolysis sampling, carrier gas is introduced from a second source of He from L1b through the trap and to the GC/MS (L5 and L6). The tar is released from the trap by heating it to 300°C. The valve and pipes (L5) in the valve oven and the transfer line (L6) to the GC/MS are kept at 300°C to avoid condensation in the pipes.

During the sampling, the temperature is initially held constant at 300°K for a varying time period between 0 min, 10 min, and 30 min, from which the temperature is rapidly heated (20°K/ms) to 600°C for pyrolysis of the biomass. This is done to simulate a heating pre-treatment before fast pyrolysis conditions as those in fluidised bed and to minimise any reactions that may occur because of gradual heating except for during the torrefaction. The fast cooling in the trap and the low end-temperature ensure a minimum of secondary reaction and leave primary tar for analysis. The samples are performed in triplicates.

The GC absorption is an integral over the peak and has been divided by its sample mass to get comparable results.

The GC results presented in the article are only qualitative. The amount of absorption per molecule may differ from compound to compound, and it will not be possible to conclude to which degree one compound is forming another compound.

3.2.2 Direct injection mode analysis

A direct injection method is utilised to investigate possible condensation in the trap mode. For the direct analysis the pyrolysis is done the same way with the same conditions, except the pyrolysis product gas is injected directly to the GC/MS as shown in the bottom of Figure 3-1, including light gases, without being condensed in the trap. There is thus no purging through L8 during the sampling as for the trap mode. Water may still be purged through L8 during the sampling preparation in a similar manner as for the trap mode where it was through L7. The analysis has been done in triplicates.

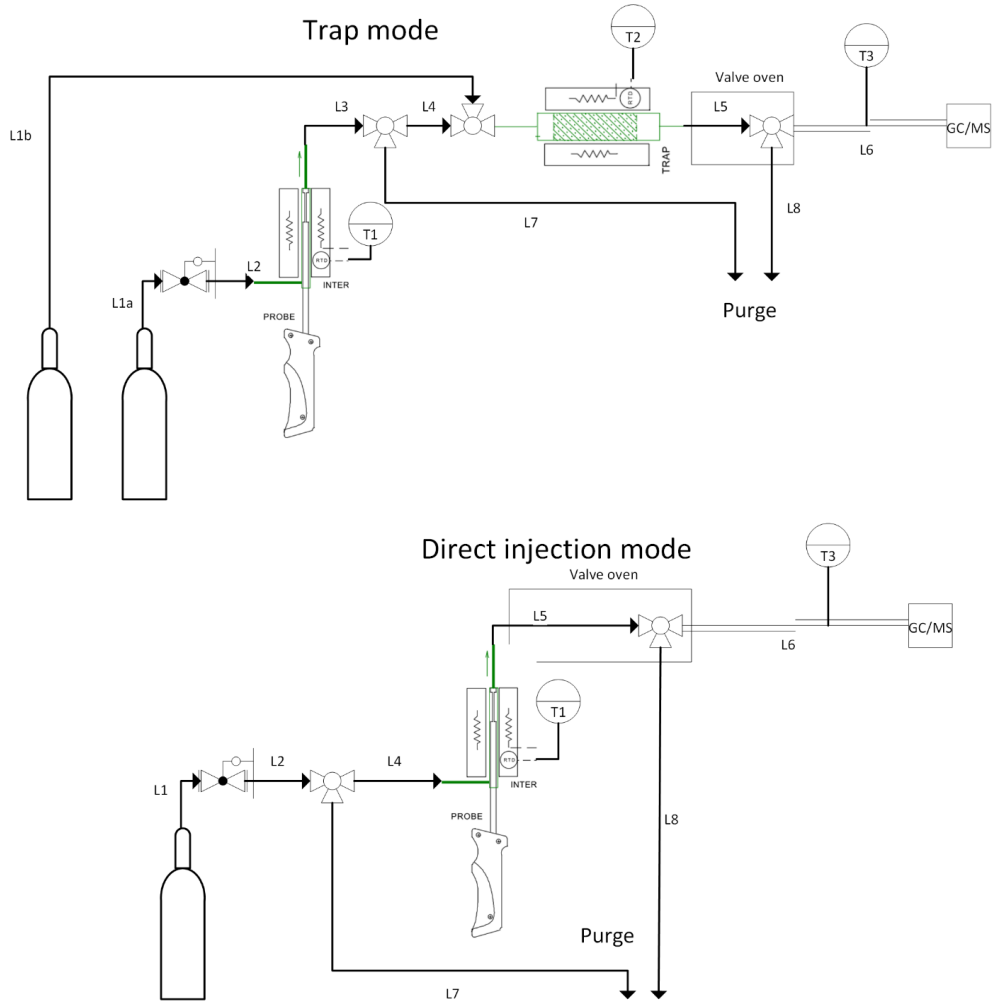

Figure 3-1: Simplified schematic setup for the pyrolysis of biomass

3.2.3 Incremental pyrolysis experiment

Incremental analysis of a biomass sample has been performed using the direct injection mode. This is done to get information about the temperatures at which the tar species are released. A sample of approximately 2g is placed in a quartz tube that is placed in the heating coil. The sample is not pre-treated but rapidly heated (2000K/s) to the temperature of interest for 30 s at which the temperature is lowered to the standby temperature of 100°C. The gas composition is then analysed by the GC/MS. The same sample is rapidly heated to the next temperature and analysed in the same manner. This is repeated for the temperatures 200, 225, 250, 275, 300, 325, 350, 400, 450, 500, 550, 600, and 650°C.

For the incremental pyrolysis analysis, the temperature ramp for the GC column is increased as this experiment is used to identify at which temperature specific compounds are released rather than the quantity. This resulted in some overlap of the peaks and, consequently, the absorption has been estimated by peak height rather than integral area for some compounds and is prone to error if used as a quantitative measure.

3.2.4 TGA

The TGA is performed by placing 9.586g of pulp lignin in a ceramic cuvette and increasing the heat by 10K/min under nitrogen atmosphere.

3.2.5 Pulp lignin

Ash measurement has been done on a 0.3884g sample by being slowly heated to 550°C over 4 hours and kept for a minimum of 1 hour. The ultimate analysis of the sample is shown in Table 3-1.

Table 3-1: Ultimate analysis

Compound	C	H	N	S	Oα	O/C	H/C
Pulp lignin (w%)	49.6 ± 2.8	4.4 ± 0.2	nd	16.0 ± 9.6	29.9 ± 11.1	0.60	0,09
Pulp lignin (mol%)	37.9 ± 2.1	40.4 ± 2.1	nd	4.6 ± 2.8	17.1 ± 6.4	0.45	1.06

nd = not detected
α = identified by difference

3.3 RESULTS AND DISCUSSION

Both the direct and the tap-mode analysis have been used to analyse the effect of pre-torrefaction. The two methods have shown different behaviours for the formation of vanillin, which is attributed to the differences in residence time and temperature that the tar products experience in the two analysis methods. The results of this will be discussed in the next section.

3.3.1 Product distribution with torrefaction time

For gasification processes the tar content has to be kept at a minimum and formation of PAHs should be avoided. For that, the tar yield and the tar species distribution formed by the torrefaction and pyrolysis are of particular interest, as not all tar species are equally thermally stable. Phenol derivatives are the precursor for PAHs and should be minimised [108]. The torrefaction experiment aims to investigate the effect of torrefaction as a pre-treatment to gasification on the tar yield and distribution.

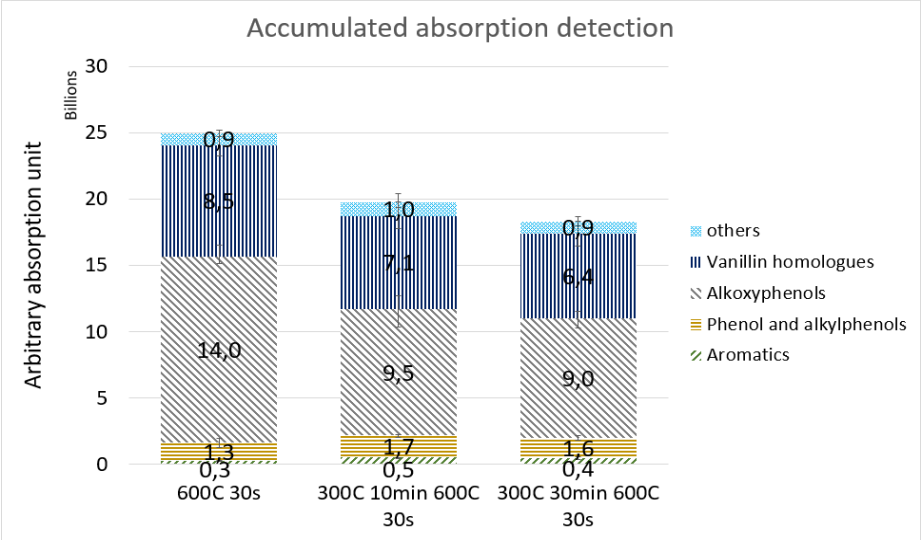

Figure 3-2: Accumulated tar detection, grouped according to functional groups (phenol is grouped with aliphatic phenol) using trap mode

Figure 3-2 shows the accumulated absorption of the detected tar species from the GC/MS analysis. The absorption of the individual species is summed in groups according to substituents. Alkylphenols include phenol with the functional groups of ethyl, methyl, ethanyl and propenyl. Alkoxyphenols include phenol with the functional group methoxy. Aromatics include toluene and benzene. Vanillin homologues are Vanillin and Apocynin.

Figure 3-2 shows a considerable reduction of tar by the utilisation of pre-torrefaction; Alkoxyphenols, especially, seems to decrease with torrefaction. Aromatics, phenols and alkylphenols are kept steady. Vanillin homologues show a slight decrease as the torrefaction time increases.

If the tar species are analysed by direct injection to the CG/MS and summed, a much smaller effect from the torrefaction compared to the trap mode is seen as shown in Figure 3-3. For direct injection it would seem that there is a relation between the increase in Vanillin homologues and the decrease in alkoxyphenols. Also, Vanillin homologues are increasing for direct injection rather than decreasing as for the trap mode.

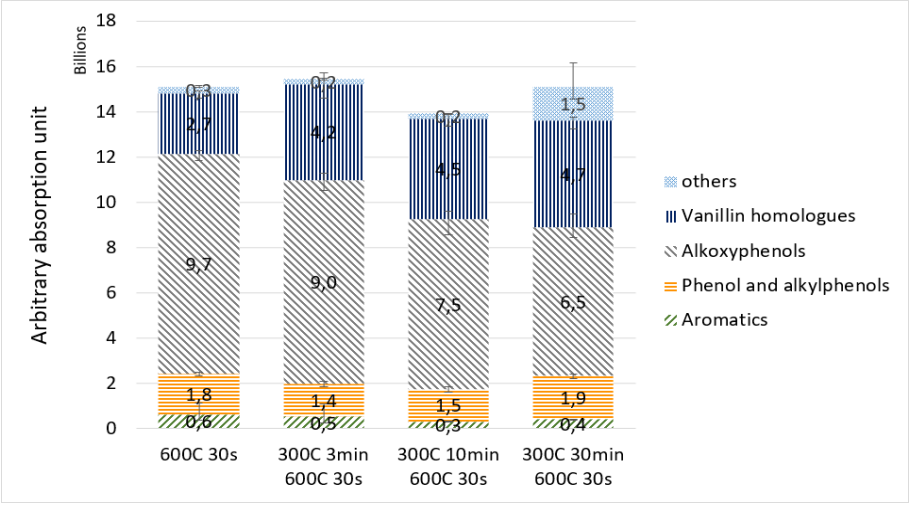

Figure 3-3: Summed tar release for direct injection method from pulp lignin

A comparison of the major tar species in Figure 3-4 and Figure 3-5 show that a considerably higher relative reduction is seen for phenol o-m-p-methoxy at direct injection compared to a tramp mode.

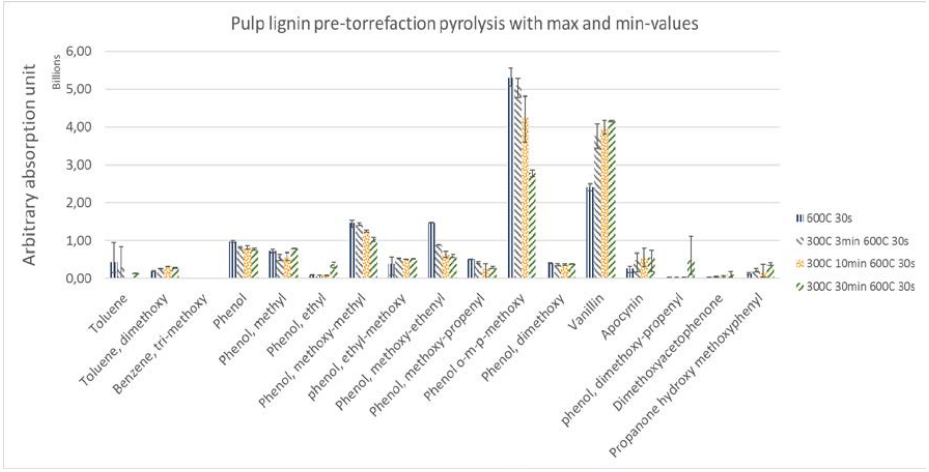

Figure 3-4: Detailed view of detected tar composition from a combined torrefaction and pyrolysis using a direct injection of pyrolysis to the GC/MS. (3 samples have been done for each condition)

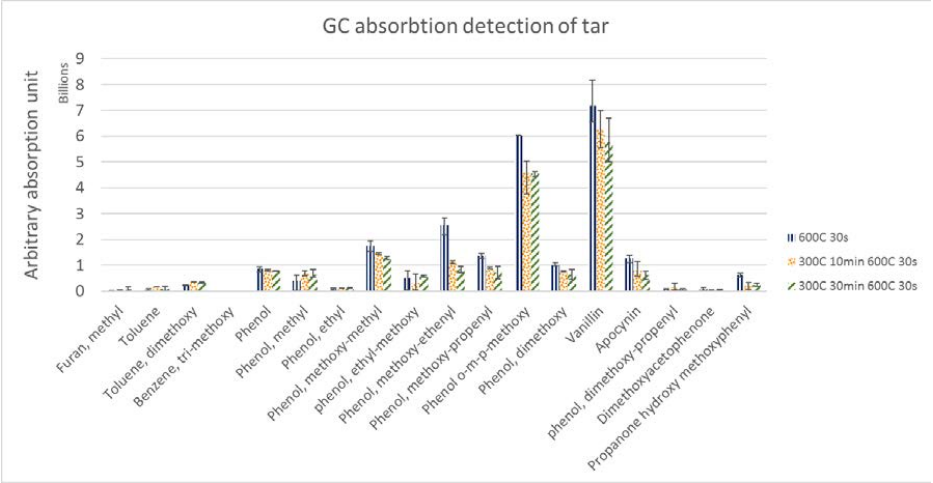

Figure 3-5: Detailed view of detected tar composition from a combined torrefaction and pyrolysis using a trap for condensing followed by a reheating and injection to the GC/MS. (3 samples have been done for each condition)

For both experiments a small reduction in the adsorption is noticeable for the majority of the tar species with the primary reduction related to methoxyphenol. Methoxyphenol is a minor product of unimolecular degradation of vanillin [182]. It may, however, be formed by hydrogen abstraction of the aldehyde and subsequent loss of CO [182]. This will, however, require hydrogen abstractions from a radical. Radical for hydrogen abstraction may be available in the char as tar species are released. Thus for no pre-torrefaction where Vanillin is released as the char is heated to 600°C the radicals for reforming may be available. When pre-torrefaction is introduced, Vanillin will be removed before radicals become a significant factor for reforming.

The different yields between the direct injection method and the trap mode method is thought to be related to the different temperature and residence time for the two analysis methods.

Figure 3-6 shows the distribution of the released tar at torrefaction (300°C) and the subsequent pyrolysis (600°C). Vanillin is here shown to be primarily released during the torrefaction. Thus, under direct injection, Vanillin will be transported to the GC column before the temperature is increased to 600°C. Vanillin degradation from subsequent pyrolysis gas is reduced as any gas during the pyrolysis will be cooled down in the tubes (line L5 and L6 on the PI-diagram) during the transport to the GC/MS. For the trap mode, Vanillin will be condensed in the trap and, subsequently, hot air will be transported through the trap that may degrade some of the vanillin. This may explain the difference in the vanillin behaviour and the large variations of vanillin measurements.

Additionally, when the tar fraction is condensed in the trap the hydrocarbons are concentrated, and possible condensation reaction or cracking may happen during the heating of the trap for trap mode. This may explain some of the reduction in Vanillin.

The significantly higher, relative reduction of phenol o-m-p-methoxy for the direct injection may be caused by the increased time at high temperature. For the direct injection, tar released during pyrolysis will experience a longer time of high temperature when travelling from the pyroprope to the GC column (line L5 and L6 on the PI-diagram) (between 300°C and 600°C) because of the

lack of cooling from the trap in between. Thus, the tar fraction is lower for direct injection, and it is not possible to compare the absolute values from the direct and the trap mode analysis directly.

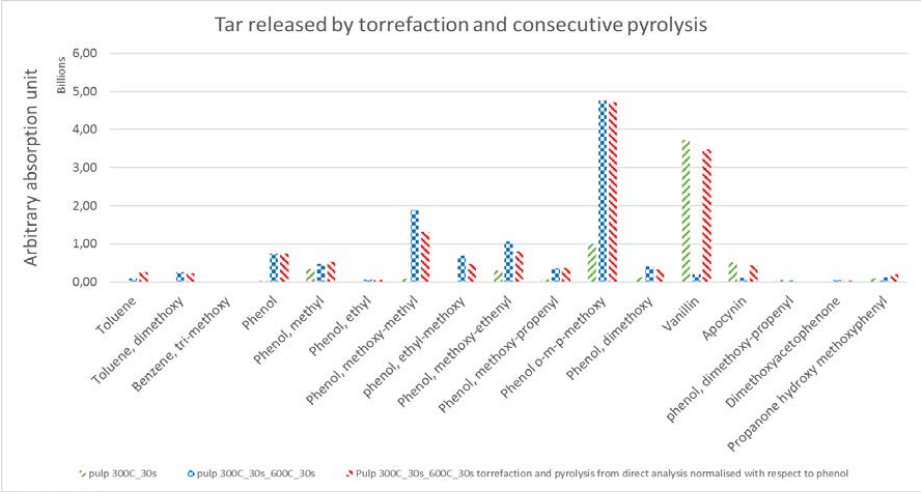

Figure 3-6: Tar fractions relation torrefaction and pyrolysis, using direct analysis method

3.3.2 Residual char measurements

If tar reduction from the trap mode is a consequence of condensation reaction of tar and the fixed carbon, a reduction in the mass loss should be noticed. Figure 3-7 shows the measured residual mass after the torrefaction and pyrolysis. The description of the columns in Figure 3-7 describes the torrefaction condition and pyrolysis conditions (torrefaction temp. torrefaction time pyrolysis temp. pyrolysis time). The char residual from each pyrolysis shows a significant drop from torrefaction at 300°C to pyrolysis at 600°C. This is expected because not all bonds are broken at 300°C.

A small increase is seen from torrefaction for 10 min to 30 min. For other torrefaction times, the deviation is too large to conclude a difference. The char residual deviation is attributed to small changes in the equipment when it has been taken apart and reassembled, together with a small deviation in the ash composition through the biomass sample, and the deviation from the weight. The lack of increased char suggests that the process during the torrefaction does not contribute to char formation.

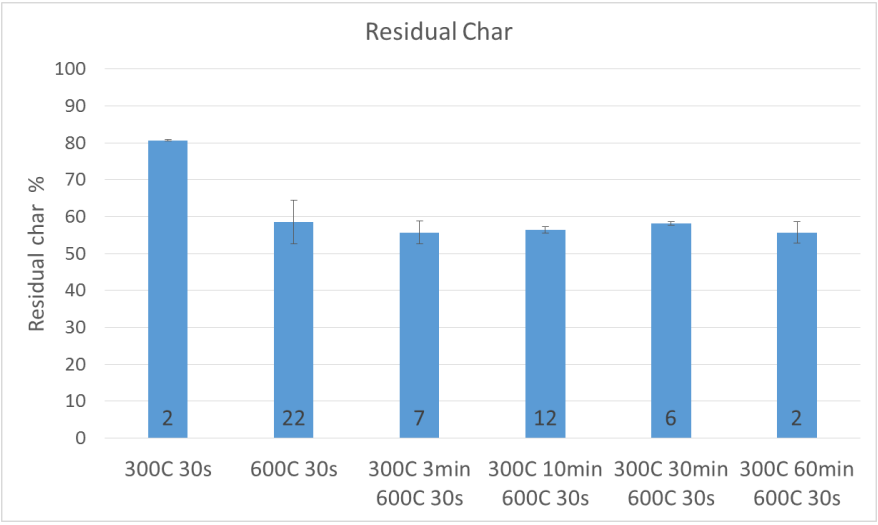

Figure 3-7: Mass lose in percentage with varied torrefaction times (the number in the bottom of the column show the number of samples used)

3.3.3 Temperature for release of tar species

Knowledge about the temperature at which specific tar components are released may lead to tar specific actions to reduce them.

Figure 3-6 shows which tar species are released during the torrefaction (300°C) and the pyrolysis (600°C). Vanillin is the primary tar specie released at low temperatures whereas alkoxyphenol is the primary tar released at higher temperatures [82].

Figure 3-8 shows the incremental pyrolysis experiment. Phenol and alkylphenols are primarily released around 350°C to 450°C. Aromatics are released around 350-450°C. Alkoxyphenols are formed from 200°C to 600°C. Vanillin is formed at 200-250°C. Water is only detected at temperatures over 400°C.

The tar species released from the pulp lignin is thus largely separated by a temperature interval between 225°C to 325°C. This is also seen in the TGA (Figure 3-9) where a shoulder is observed on the main weight loss peak. Vanillin is taking up a relatively large part of the lignin tar fraction during torrefaction as shown in Figure 3-6. If the gas from torrefaction is separated from the feed before gasification, it might be possible to reduce a large part of the problematic tar in the gasification process. For whole biomass a large part of the hemicellulose will, however, also be removed and form tar. The tar product from the torrefaction may be used for a co-production of chemicals directly from the pyrolysis, or it may be used as fuels for the combustor if integrated with a dual fluidised bed.

Figure 3-9 shows the DTG and DSC of pulp lignin under an N_2 atmosphere at a heating rate of 10°C/min. The result shows a small weight loss at the beginning that is an endothermic process up to about 100°C. This is usually attributed to the evaporation of water.

The DTG curve indicates three peaks in the range of 150°C–600°C. A small shoulder from 150–250°C is observed. This is consistent with other lignin TGAs [55], [65] and no furans were detected as would be the case if it was associated with cellulose or hemicellulose [72]. Thus it is

attributed to the release of Vanillin when compared with the GC/MS result in Figure 3-8 and Figure 3-6.

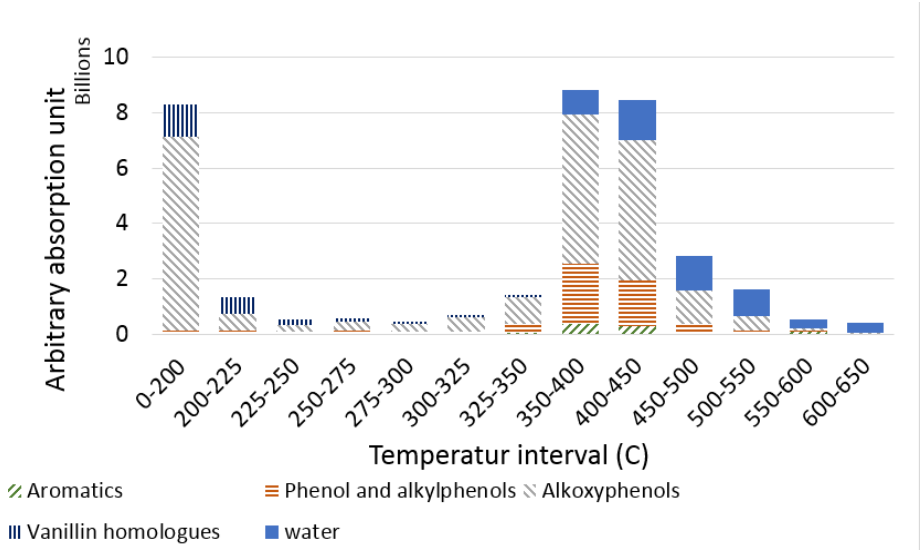

Figure 3-8: Tar release with temperature from pulp lignin

From 250°C to 420°C, a major peak is shown which is attributed to the release of alkoxyphenols, phenol, and alkylphenols. A low-amplitude peak, forming the tale on the TGA from around 400°C, seems to control the rest of the species. At about 750°C the third peak in mass loss (6.92% from 70min to 80min) is seen that is highly endothermal, which is attributed to the evaporation of some inorganics. A simple ash test by heating a small sample (0.3884g) to 550°C under atmospheric conditions showed a residual ash of 16.1w%.

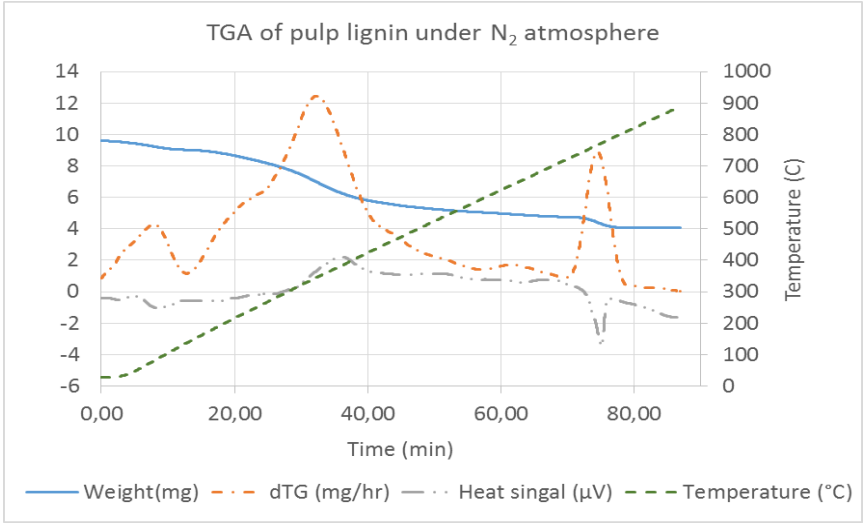

Figure 3-9: TGA and DSC of 9,586mg pulp lignin under N_2 atmosphere at 10C/min

The DSC (heat signal) in Figure 3-9 is negative and shows that the process is endothermal in the torrefaction region (T<300°C) and indicate pyrolysis [183]. Around this temperature the DSC changes to an exothermic process that indicates condensation reaction [183]. This supports that condensation reaction of monolignols in the lignin is not occurring at the torrefaction temperatures that are utilised. Additionally, the high heating rate of the pyrolysis experiment over the exothermic region of the lignin would lessen the time for condensation reactions of monolignols.

3.4 CONCLUSION

Torrefaction in small periods between 0 and 30 min at 300°C with subsequent pyrolysis at 600°C has been tested to see its impact on the tar distribution and amounts.

The yield of tar from pulp lignin showed different trends depending on the way the sample was collected. Only very little reduction of tar from pre-torrefaction at 300°C for up to 30 min was observed for direct injection while a larger reduction was observed for trap mode. It is believed that the difference is related to different thermal treatments of the sample. It was not possible to see the reduction of tar as a consequence of condensation reactions. The residual char remained the same, and the DSC analysis showed endothermic reactions at the torrefaction temperatures, which both support that condensation reaction is not present.

The distribution of tar species is, however, affected. It is seen that mostly alkoxyphenol yield decreases with torrefaction of the pulp lignin. Vanillin stood out in this case, in that it seems to increase as a consequence of the torrefaction conditions for the direct injection method used contrary to the trap mode. This is attributed to the early release of vanillin during the torrefaction and thus a mild temperature treatment. Non-phenolic compounds are not seen to increase by any significant level. Thus the precursor for PAHs is not affected significantly by pre-torrefaction.

4 MODELLING OF FLUIDISED BED GASIFICATION OF BIOMASS

As discussed, the tar formation from dual fluidised beds is very complicated, and tar is affected by the initial release from the biomass until it leaves the reactor system. Mathematical models are good tools to understand the process and how parameter changes may affect the outcome. These models are often limited in the assumption that has been made and are not perfect, but will still give insight with regards to the trends that are seen in a system.

The tar formation from gasification of biomass has been divided into three parts to simplify the mathematical modelling of the system and give a more precise view of the parameters' influence. The three parts consist of a single-particle model, a gas phase model, and a reactor model that utilises a simplified particle and gas model.

The single-particle model investigates some of the assumptions that are often made about the biomass particles in fluidised beds. The gas phase model focuses on how tar development may be affected by additives of other gas species to prevent PAH formation. The reactor model focuses on the possibility of using in-bed coking on the catalyst as a means of removing tar from the gasification area to the combustor instead of just catalytic conversion to light gases.

4.1 SINGLE PARTICLE MODEL

Particle models may provide valuable information on how different parameters affect the first step of gasification, the pyrolysis process, or the sensitivity of parameters for accurate prediction. A single-particle model may be of interest to understand the timescale for the conversion of biomass particles compared to other effects in the reactor for developing a reactor model. The model can be used to understand the limitation of the prediction and deviations from the experimental data caused by simplifications. For example, a commonly used simplification is instant devolatilisation of biomass particles for a small particle size and high heating rates [106]. However, this simplification may not be valid for large biomass particles.

The present particle model assumes that kinetics, external heat transfer, and heat conduction are the limiting steps for devolatilisation of biomass. This fits well with the time-scale analysis from Dufour et al. [157] that shows the time-scale of convective transport of volatiles is much lower than that of the chemical reaction and the heat transport. Thus, the model assumes that all volatiles formed during devolatilisation are transported out of the particle instantaneously.

The heat accumulation at any location in the particle can be written as [170], [171]:

$$\underbrace{\frac{\partial\left(T \cdot C_p(T) \cdot \rho_{total}\right)}{\partial t}}_{\substack{energy\ accumulated\ by\ heat \\ transport\ and\ generation}} = \underbrace{\lambda(T) \cdot \left(\frac{\partial^2 T}{\partial r^2} + \frac{b}{r}\frac{\partial T}{\partial r}\right)}_{\substack{conductive \\ energy\ transport}} + \underbrace{(-\Delta H) \cdot \left(-\frac{\partial \rho_{bio}}{\partial t}\right)}_{energy\ from\ reaction} + \underbrace{T\ C_p(T)\left(\frac{\partial \rho_{total}}{\partial t}\right)}_{energy\ by\ mass\ transport} \quad \text{(Eq 4-1)}$$

Where T is the temperature, $C_p(T)$ is the heat capacity, ρ_{total} is the total density of solids at any given time, t is time, ΔH is heat of reaction, r is the radial position, $\lambda(T)$ is the thermal conductivity, and ρ_{bio} is the density of biomass.

Both the temperature and the density are assumed to change with respect to time, while the heat capacity is a state equation dependent on temperature. If the temperature and density in the accumulation term are separated, the equation is

$$\underbrace{C_p(T)\cdot\rho_{total}\cdot\frac{\partial T}{\partial t}+T\,C_p(T)\left(\frac{\partial \rho_{total}}{\partial t}\right)}_{\substack{energy\ accumulated\ by\ heat\\ transport\ and\ generation}} = \underbrace{\lambda(T)\cdot\left(\frac{\partial^2 T}{\partial r^2}+\frac{b}{r}\frac{\partial T}{\partial r}\right)}_{\substack{conductive\\ energy\ transport}} + \underbrace{(-\Delta H)\cdot\left(-\frac{\partial \rho_{bio}}{\partial t}\right)}_{energy\ from\ reaction} + \underbrace{T\,C_p(T)\left(\frac{\partial \rho_{total}}{\partial t}\right)}_{energy\ by\ mass\ transport} \quad \text{(Eq 4-2)}$$

which may be simplified to

$$\underbrace{C_p(T)\cdot\rho_{total}\cdot\frac{\partial T}{\partial t}}_{\substack{energy\ accumulated\ by\ heat\\ transport\ and\ generation}} = \underbrace{\lambda(T)\cdot\left(\frac{\partial^2 T}{\partial r^2}+\frac{b}{r}\frac{\partial T}{\partial r}\right)}_{\substack{conductive\\ energy\ transport}} + \underbrace{(-\Delta H)\cdot\left(-\frac{\partial \rho_{bio}}{\partial t}\right)}_{energy\ from\ reaction} \quad \text{(Eq 4-3)}$$

It is assumed that the reaction scheme of biomass devolatilisation follows three parallel reactions to form tar, gas, and char as shown in Figure 4-1.

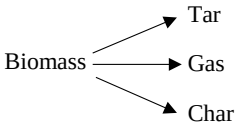

Figure 4-1: Simple kinetic scheme used for particle simulation

This scheme is represented by the following ordinary differential equations:

$$\frac{\partial \rho_{bio}}{\partial t} = -(k_c + k_L + k_G)\,\rho_{bio} \quad \text{(Eq 4-4)}$$

$$\frac{\partial \rho_{char}}{\partial t} = -k_C\,\rho_{bio} \quad \text{(Eq 4-5)}$$

$$\frac{\partial \rho_{tar}}{\partial t} = -k_L\,\rho_{bio} \quad \text{(Eq 4-6)}$$

$$\frac{\partial \rho_{gas}}{\partial t} = -k_G \, \rho_{bio} \quad \text{(Eq 4-7)}$$

$$\frac{\partial \rho_{total}}{\partial t} = \frac{\partial \rho_{bio}}{\partial t} + \frac{\partial \rho_{char}}{\partial t} \quad \text{(Eq 4-8)}$$

where k is the reaction rate coefficient.

The model is discretised in space using a central difference scheme as shown in Appendix A – Particle model. This generates a system of ordinary differential equations (ODE), which may be solved in time using one of the build-in ODE solvers in matlab.

4.1.1 Comparison with the experimental data

The result of the single-particle model is compared with the experimental results of Pyle et al [184]. Table 4-1 shows a parameter that has been successfully used for simulating particle devolatilisation in literature [170], [184].

Table 4-1: Parameters for the particle simulation

Parameter	Value or formula	Source
Heat transfer coefficient	$h = 8.4\ W/m^2K$	[184]
Wood specific heat	$C_{p,wood} = 1112.0 + 4.85 \cdot (T - 273)\ , \frac{J}{kg\ K}$	[170]
Char specific heat	$C_{p,char} = 1003.2 + 2.09 \cdot (T - 273)\ , \frac{J}{kg\ K}$	[170]
Wood thermal conductivity	$k_{wood} = 0.13 + 0.0003 \cdot (T - 273), \frac{W}{m\ K}$	[170]
Char thermal conductivity	$k_{char} = 0.08 - 0.0001 \cdot (T - 273), \frac{W}{m\ K}$	[170]
Heat of reaction	$\Delta H = -255\ kJ/kg$	[170]
Initial density	$\rho_0 = 650\ kg/m^3$	[170]
Initial thermal diffusivity of wood	$\alpha = 1.79 \cdot 10^{-7}\ m^2/s$	[170]

The simulation uses a kinetic scheme different from the reference articles, which is thought to be the reason for the why the parameter does not give a good result. To get better fitting of the simulation to the experimental data with the present reaction scheme, new values of heat transfer coefficient ($84\ W/m^2K$) and heat of reaction ($-65\ kJ/kg$) are used. The comparison of the experimental results and the simulated results is shown in Figure 4-2.

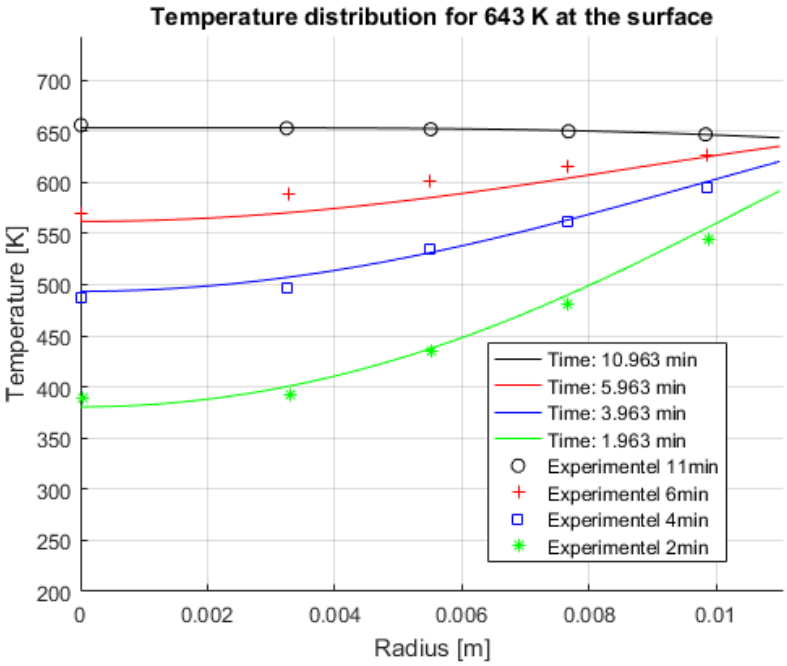

Figure 4-2: Comparison of temperature curves for 22mm cylindrical particle, with alternative heat transfer coefficient and heat of reaction. Data points from Pyle et al 1984 [184].

Both the initial temperature at 2 min and the temperature overshoot at the centre of the particle for 11 min pyrolysis are well predicted. Some of the discrepancies between the model and the reference may be because of the rather simple kinetics that is used. A different set of kinetics will affect the devolatilisation rate and consequently the temperature profile.

4.1.2 Simulation of devolatilisation under fluidised bed conditions

The Single particle is extrapolated to investigate the devolatilisation of biomass in the dual fluidised bed. The environmental condition like temperature, heat transfer coefficient, and size is changed to reflect the condition of the dual fluidised bed. The heating rate is higher because of the direct contact with hot bed material, and a typical heat transfer coefficient is between 250 and 700 W/m^2K [185], and the temperature surrounding the particle is higher, around 850°C, which creates a higher driving force for the heat flow. Furthermore, the wood particles used in the industrial application are smaller than those used in the compared pyrolysis experiments. To give an idea of the time for conversion in fluidised bed, the size of particles used in the model is 3mm in radius cylinders, which is similar to the 6mm in diameters cylinders used in pilot plant by van der Meijden et al. [173].

Figure 4-3 shows the particle temperature profiles for different simulation times (1s, 5s, 10s, and 30s) under fluidised bed conditions. The surface temperature of the particle increases rapidly, and in less than 5 seconds it has reached the same as for the surrounding temperature. A large part of the particle conversion is thus limited by heat conduction inside the particle.

The particle is assumed to be fully converted when there is no original biomass left at the centre of the particle. Thus, the time for which there is no biomass at the centre is found as the time for full conversion of the particle.

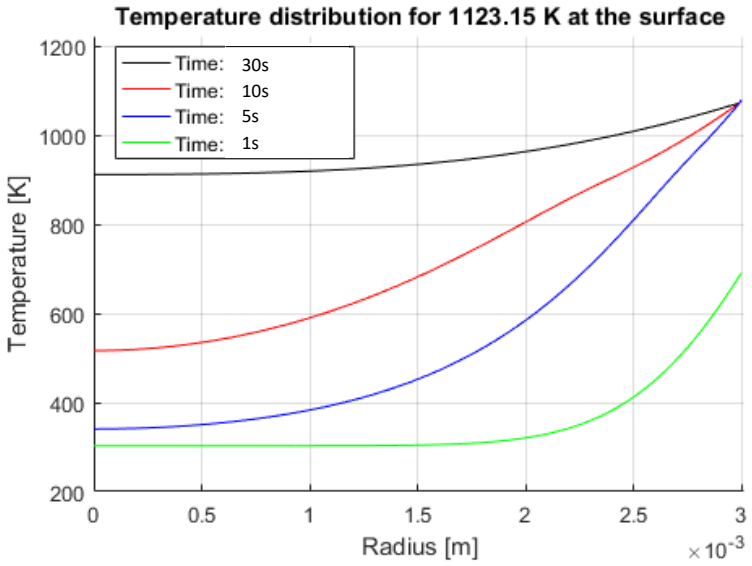

Figure 4-3: Simulation of a 3mm in radius cylindrical particle with surrounding temperature of 850C, using a heat transfer coefficient of 250 W/m^2K and a heat of reaction of -65 kJ/kg

Calculation shows that it takes 28.3 s for the particle to fully devolatilise. For comparison, the sizes that a particle would need for 60 s and 10 s conversions are 4.8mm and 1.5mm in radius, respectively. A devolatilisation time of 10 s would mean that the particle may be circulated a few times in the fluidised bed before full devolatilisation. The assumption of instant devolatilisation will thus be prone to errors for biomass of this size.

The model encounters numerical instability for very small particles. To understand at what size the heat transfer becomes the limiting step for the fluidised bed conditions, a time-scale analysis is done instead.

The characteristic times relating to heat transfer and heat conduction is set up. For a time-scale analysis, $t_{h_{ex}} = \frac{C_p \rho V}{hS}$ is defined as the time-scale of the heat transfer to the surface, where S is the surface area and V is the volume, h is the heat transfer coefficient, ρ is the density, and C_p is the heat capacity. $t_h = \frac{L^2 C_p \rho}{\lambda}$ is the time-scale of the internal heat transfer where L is the diameter of the particle. This analysis shows that the heat transfer to the surface begins to be the liming factor for particles of 0.13mm. Thus, for fluidised bed the heat transfer is much too high to assume an isothermal particle.

For the assumption of isothermal and instant devolatilisation to be true, the biomass particles have to be much smaller than 1mm. If instant devolatilisation is present, bubble gas concentration will change in a narrow range around the point of entry of the biomass. For non-instant release, the

biomass will be distributed throughout the reactor, and the bubble gas is expected to absorb gas as it rises through the reactor. This would give a gradual change of the bubble concentration.

4.2 GAS PHASE MODEL

The complexity of the tar evolution in the gas phase makes it difficult to implement in the reactor model. The large amount of reactions increases the likelihood of mistakes in the implementation that may be difficult to identify. Thus the tar evolution in the gas phase is modelled separately.

The literature review shows that the tar evolution is dominated by unimolecular degradation and hydrogen abstraction and donation. The main reaction path for the tar evolution is shown in Figure 4-4. The scheme shows possibilities for shifting the formation from naphthalene to benzene by the introduction of methyl. It also shows higher degradation of cyclopentadienyl to light gasses by increased radicals of OH, O, and H.

The aim of the model is to see the consequence of introducing these radicals. The radicals cannot be introduced directly but have to be formed from stable compounds. Thus the model simulated hydrogen and methane addition as a source for radical formation. These are also products of the gasification that may be added by a recirculation of the gas which is also simulated. The typical process parameters like temperature, pressure, and residence time are simulated as these often have a high effect on gas composition.

Figure 4-4 shows the kinetic scheme used for modelling the development of the gas phase. It is here emphasized that the reaction is not occurring in a closed system of only hydrocarbon under pyrolytic conditions. Instead, the tar components are diluted in steam.

The model does not include tar larger than naphthalene. Because steam gasification is only expected for tar larger than naphthalene, the model essentially neglects steam reforming of tar. Naphthalene is assumed to be the precursor for larger tar species even though other two ring tar may be formed without the use of cyclopentadienyl. The further growth of naphthalene is not considered because only at high temperatures (1200K) do larger PAHs become a dominant part of the tar fraction [132].

The kinetic scheme is a simplification of a more elaborated reaction schemes [186] and is focused on predicting the effect of hydrogen and methane on tar evolution. The reactions included in the model is available in Appendix K – Content of electronic appendix

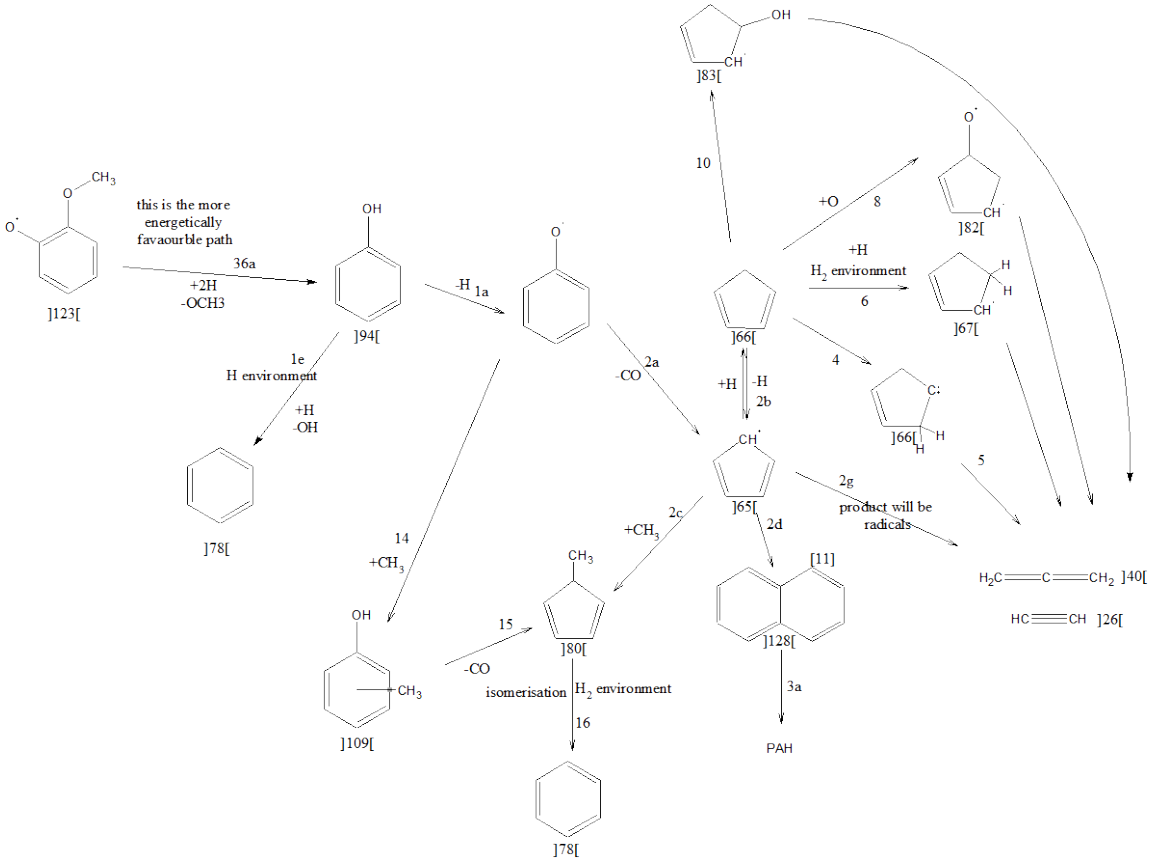

Figure 4-4 : Kinetic scheme for the gas phase model.

4.2.1 Comparison of model to pyrolytic decomposition of anisole

The gas model is compared to literature data for pyrolysis of the model compound, Anisole, by Nowakowska et al. [81] The reference data has been collected using a jet-stirred reactor with a volume of 88 cm^3 and a residence time of 2 seconds. The inlet mole fraction of the Anisole is 0.01, with helium as the carrier gas. The pressure in the reactor is kept at 106kPa.

The system is simulated as an ideal stirred reactor.

$$\frac{dC_i}{dt} = \frac{C_{i,in}U_{in}}{V_{reactor}} - \frac{C_i U_{out}}{V_{reactor}} - r_i$$

Where C_i is the concentration of species i, $C_{i,in}$ is the inlet concentration, U_{in} is the volumetric flow in, U_{out} is the volumetric flow out, $V_{reactor}$ is the reactor volume, and r_i is reaction rate of disappearance of species i.

The volumetric flow out of the reactor is corrected by the increased formation of molecules

$$U_{out} = U_{in}\frac{\sum C_j}{\sum C_{j,in}}$$

Below is seen some of the model output from the simulation for pyrolytic conditions. The blue curve shows the simulation result and the circles represent data from the reference data.

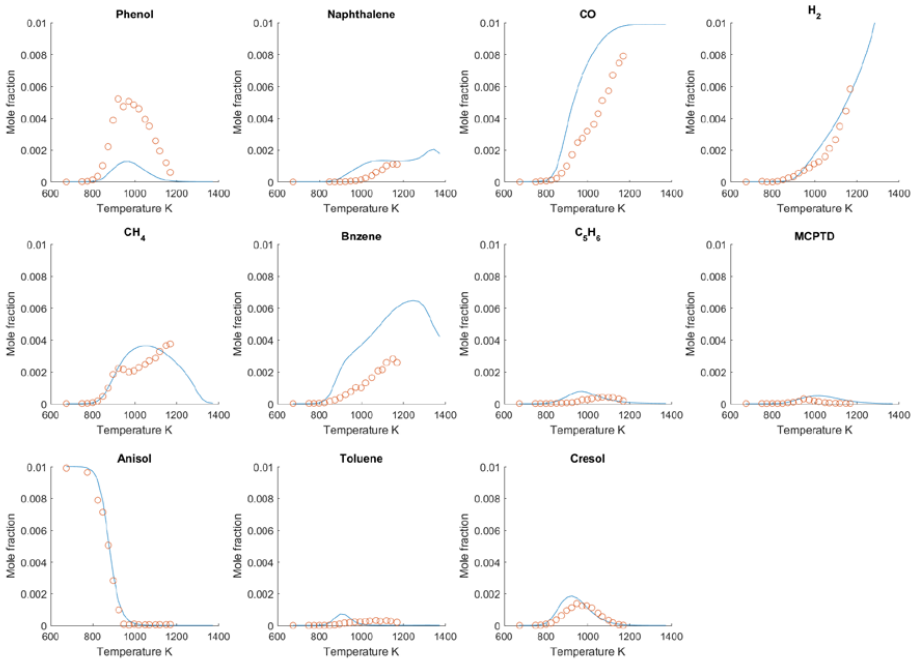

Figure 4-5: Comparison between reference and simulation for pyrolysis of anisole

The gas phase simulation has some discrepancies between the data and the simulation result. The formation of phenol is under-predicted. This is, however, consistent with the model used by Nowakowska et al. [81] The formation of benzene, toluene, C_5H_6, and MCPTD are over-predicted, and the peak is a bit off, which gives a lower temperature for the peak fraction compared to the peak of the reference data. Naphthalene formation is predicted to start at a lower temperature than the data and is expected to decrease at higher temperatures. The model, however, does not include further repolymerisation, which may explain the high prediction of naphthalene at even higher temperatures. The decrease of methane is only expected to be small at high temperatures and not of the magnitude that is seen in the simulation. The simulation is thus able to give a reasonable order of magnitude of relevant tar species until 1170K (897C).

4.2.2 Parameter simulation

The gas phase model is used to investigate how the homogeneous reactions are affected by different parameters. The parameters that are simulated are temperature, hydrogen addition recirculation, methane addition, pressure, and residence time.

The simulations are performed for the gas phase only and for a plug flow reactor, to simulate the gas behaviour of a gasifier. The residence time is set to 3 seconds which is in the range of the residence time of gas in a dual fluidised bed system. Unless anything else is mentioned the primary tar formed is assumed to be Anisole and will be the starting point. The initial tar fraction is set to 0.06.

4.2.2.1 Temperature increase

For simulation of the temperature change, the residence time and pressure are kept constant, resulting in a lower concentration of gas as the temperature is increased. The decrease in concentration with temperature is a minor effect which is evident from a mole fraction that follows the same trend as the concentration curve. The effect of lower concentration is primarily visible for Anisole before 550°C and water before 1000°C where a light slope is observed.

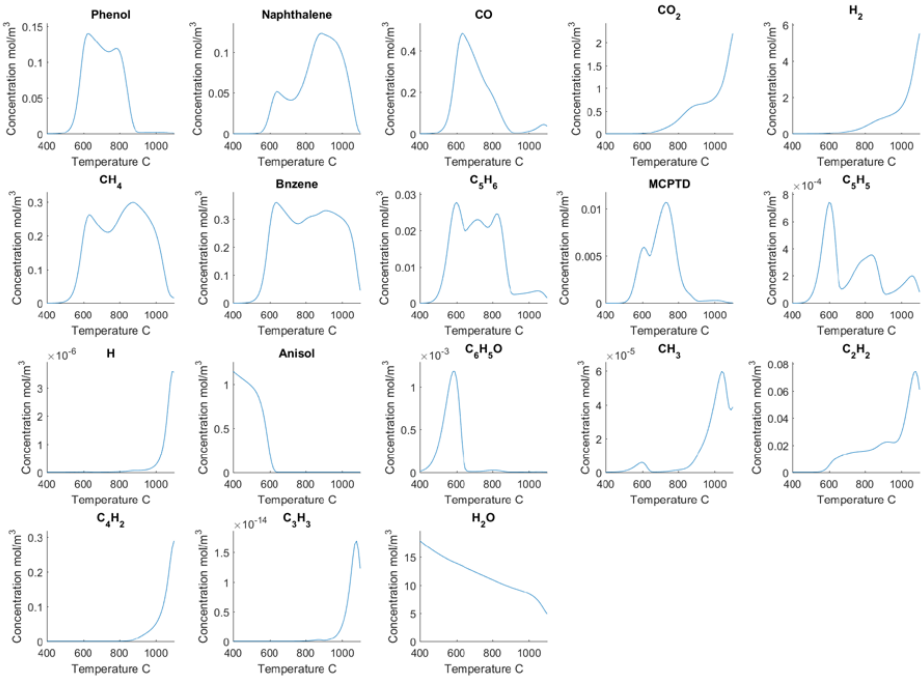

Figure 4-6: Concentration for simulated tar output with respect to temperature. The tar is assumed to be Anisole.

The above figure shows the gas composition as a function of the temperature. It is seen that Anisole as the starting tar species begins to degrade around 500°C and where the first observation of other species is done. Phenol is one of the primary products under pyrolytic conditions and is formed at temperatures between 500 and 900°C. Benzene seems to be of a stable formation throughout the 500 to 1000°C range. Naphthalene has its maximum around 900°C where phenol is also completely depleted. The depletion of naphthalene is especially seen at temperatures above 1000°C. This is also the temperature where the free hydrogen radicals begin to increase significantly.

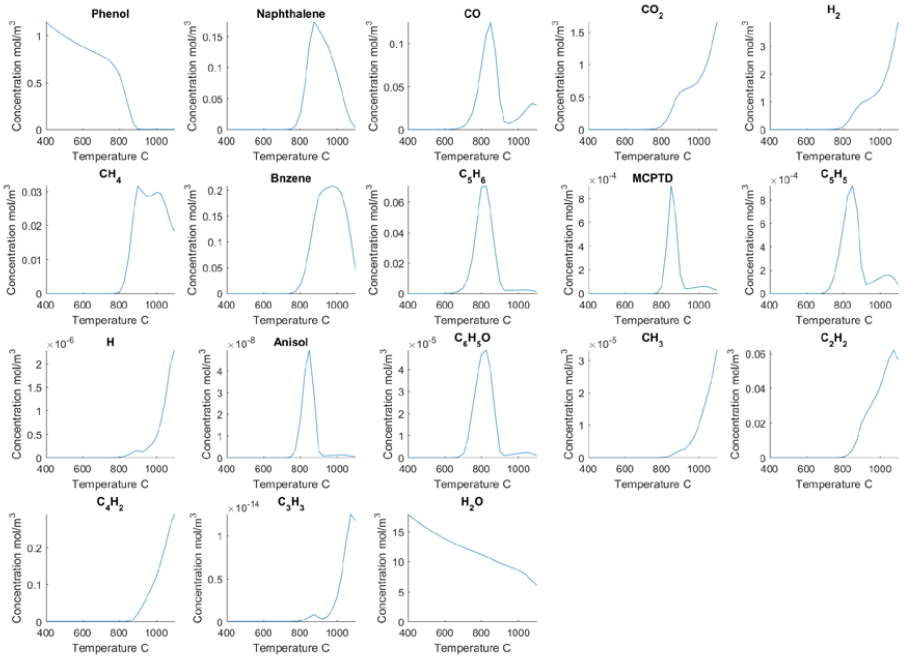

Figure 4-7: Concentration for simulated tar output with respect to temperature. The tar is assumed to be phenol.

The same trends are seen when phenol is used as the starting tar species, with the exception that formation of other tar species are shifted to a higher temperature because phenol begins degradation at a higher temperature.

4.2.2.2 Hydrogen addition

As hydrogen seems to be an integral part of the naphthalene degradation, the addition of hydrogen to the gas phase is expected to lower the amount of naphthalene. The simulation is done with shifting initial concentrations of hydrogen.

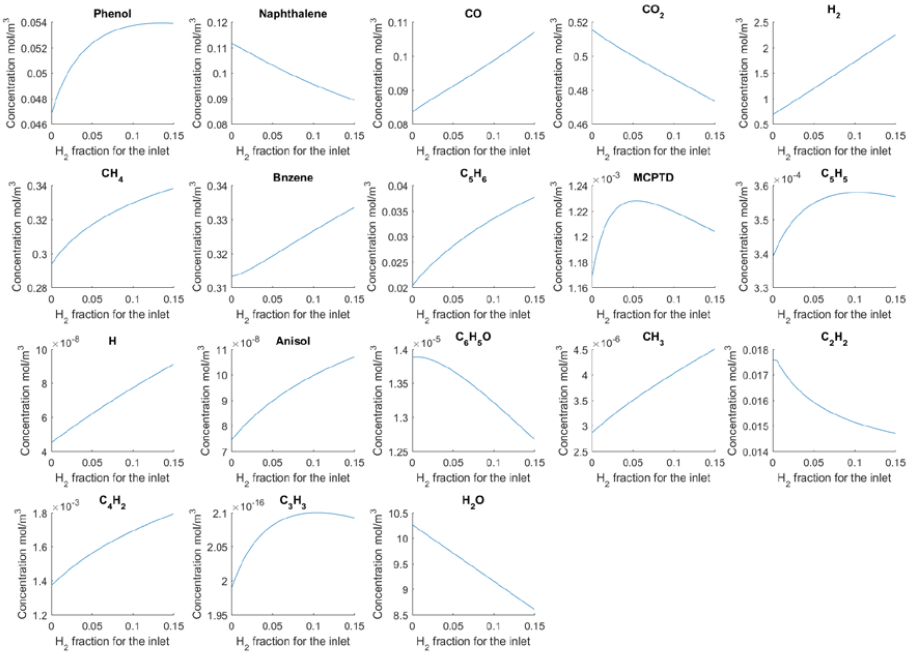

Figure 4-8: Concentration for simulated tar output with respect to hydrogen fraction.

The figure above shows the concentration of important gas species with respect to the initial hydrogen fraction. The increase in hydrogen also leads to an increase of free hydrogen radicals. As expected, the concentration of naphthalene decreases as the concentration of hydrogen increases. This leads to a small increase in benzene.

4.2.2.3 Methane

Looking at the primary reaction path for the naphthalene, it is expected that the addition of methane may prevent the formation of naphthalene in favour of benzene. This is expected by the formation of methyl radicals that react with cyclopentadienyl. This prevents cyclopentadienyl from forming naphthalene and instead degrades to benzene.

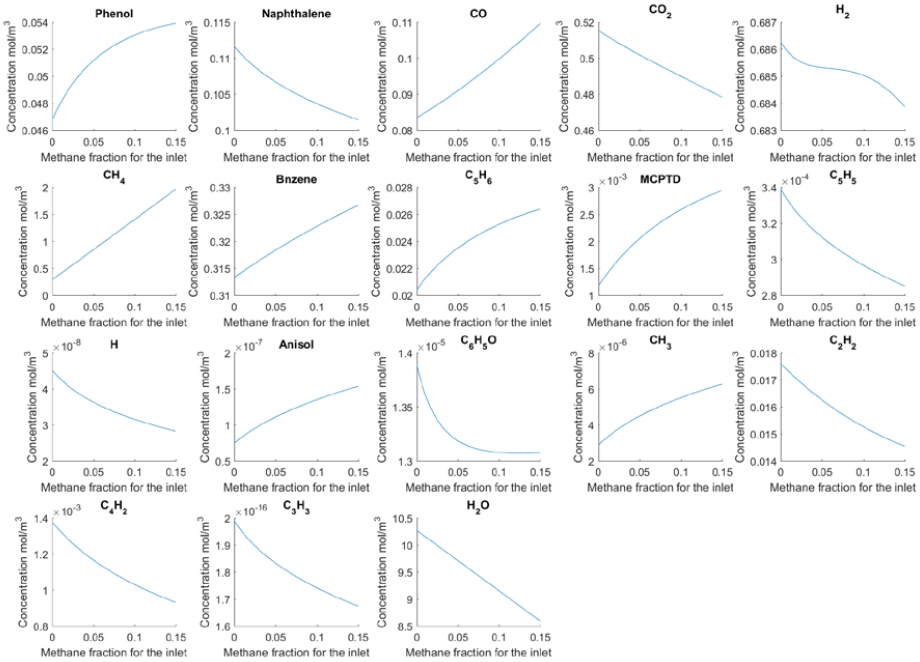

Figure 4-9: Concentration for simulated tar output with respect to methane fraction.

The figure above shows the concentration of important gas species with respect to initial Methane fraction. Both the methane and methyl concentration increase as expected. MCPTD, which is a product of cyclopentadienyl reacting with methyl, also increases and, consequently, naphthalene decreases. The effect of methane is, however, small.

4.2.2.4 Recirculation

It will not be economical to introduce pure hydrogen or methane into the gasifier to reform the heavy tar. But as hydrogen is a large part of the product gas, the hydrogen concentration may be increased by recirculating a part of the product gas to the inlet of the gasifier.

For the recirculation simulation, the gas flow through the reactor is kept constant by lowering the amount of water that enters as recirculation is increased. The tar inlet is not affected by the recirculation. This is to simulate the tar formation inside the gasification environment. The circulation of product gas is a fraction of the gas throughput. The fraction is simulated from 0 to 40% volume recirculation.

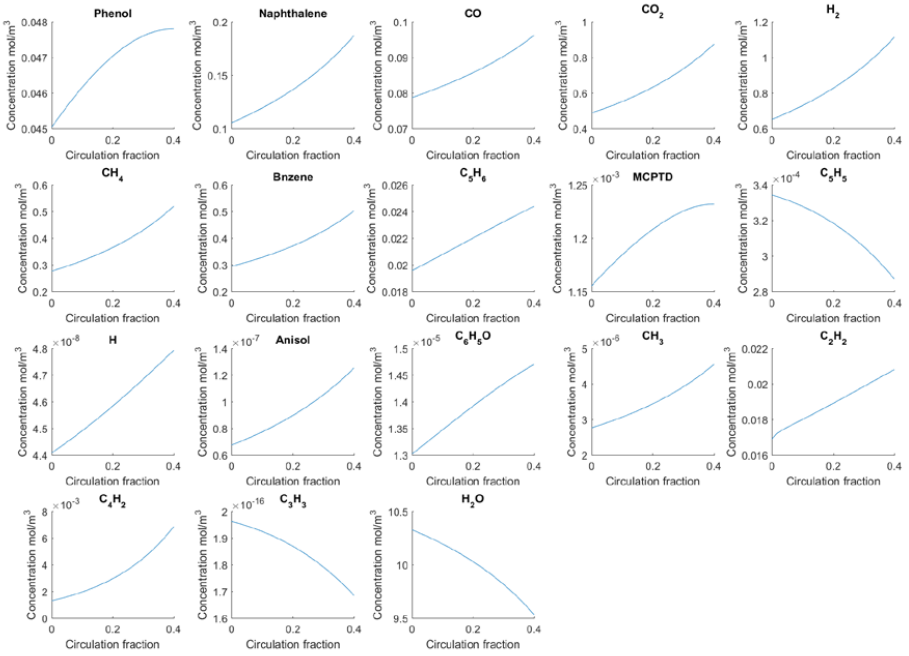

Figure 4-10: Concentration for simulated tar output with respect to the fraction of product gas circulation.

The figure above shows the concentration of important gas species with respect to circulation fraction. The recirculation of gas shows an increase of hydrogen as expected. The increase at 40% volume recirculation is equivalent to about 5% volume pure hydrogen gas addition when measured with respect to the hydrogen concentration. For the pure hydrogen addition, this gave almost a 50% increase of free hydrogen radicals. For the recirculation, the amount of free hydrogen radicals is increased by about 10%. The lack of radical increase may partially explain the lack of conversion of naphthalene. In general all the aromatic tar species increases with a recirculation of the product gas.

When the temperature is increased to 1050°C (not shown here), the concentration of naphthalene begins to decrease. At this temperature the concentration of free hydrogen radicals is also a factor 100 higher. Recirculation is thus only effective when the temperature is sufficient for degradation of naphthalene. For this temperature the benzene is, however, the dominant tar and still growing with recirculation. This is likely because the model predicts benzene to be more stable than naphthalene. Benzene is also slightly more stable than naphthalene when looking at the reference data, where benzene peaks at a higher temperature than naphthalene.

Within the temperatures of gasification, recirculation only gives a minor increase in tar formation, based on the homogeneous reactions.

4.2.2.5 Pressure

Pressure is often a factor that may change the equilibrium of the reaction and affect the product distribution. The pressure is thus simulated within 1 to 50 bar which is a pressure range that may be seen within practical applications. The initial concentration is kept constant by modifying the tar fraction and multiplying it with the reference pressure over the simulation pressure $x_{tar} = x_{tar_{ref}} \frac{P_{ref}}{P_{sim}}$.

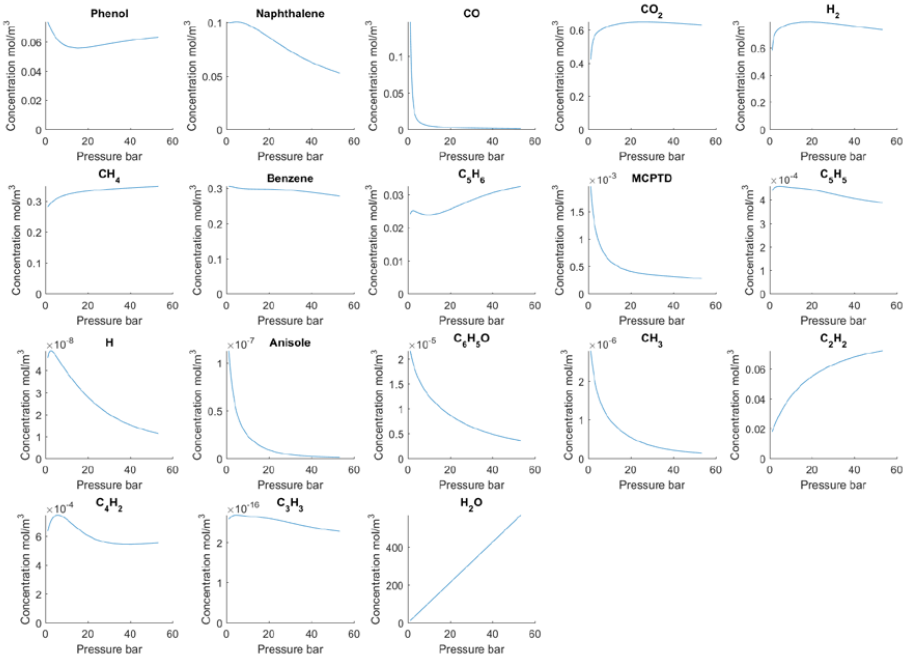

Figure 4-11: Concentration for simulated tar output with respect to pressure.

The figure above shows the concentration of important gas species with respect to pressure. At about 10 bar naphthalene concentration starts to decrease as the pressure increases. A relatively large reduction of naphthalene is shown at 50 bar. Other significant tar species have a relatively stable concentration.

4.2.2.6 Residence time

Increased residence time is expected to give a composition that is closer to equilibrium. This will only decrease the tar formation if the temperature is high enough to degrade the end tar species.

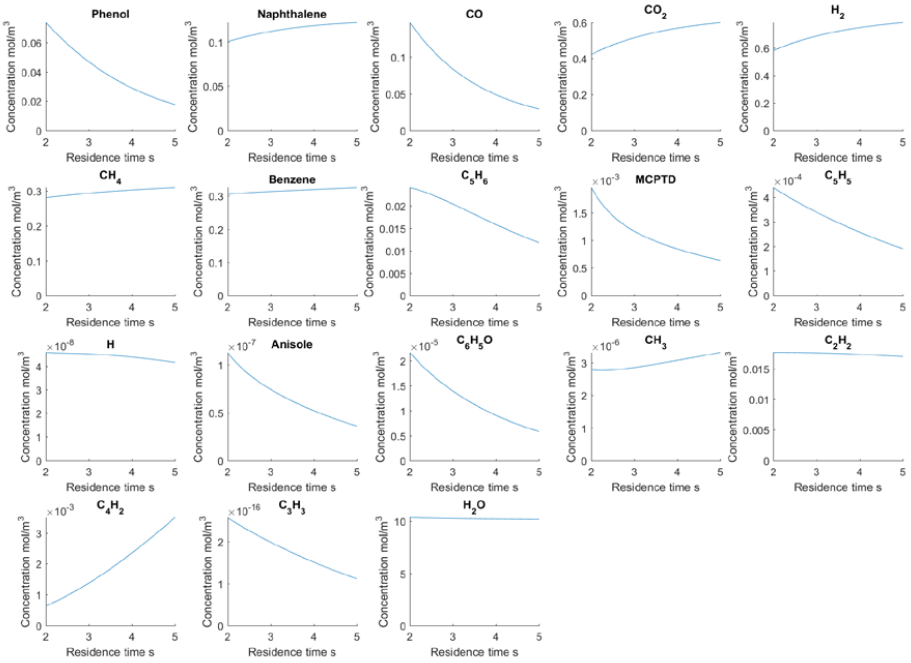

Figure 4-12: Concentration for simulated tar output with respect to residence time.

As expected, Phenol and Anisole decrease as the residence time increases. Naphthalene and Benzene increases as a temperature of 850°C is not sufficient to degrade benzene or naphthalene at a faster rate than they are created.

4.3 REACTOR MODEL

The reactor model is used to identify how gas and tar yield is affected by operating parameters, like temperature, pressure, minimum fluidisation velocity, bubble size, solid circulation, etc. The effect of the parameter is used to understand the best operating condition for the dual fluidised bed and suggest a new process design.

The design of the dual fluidised bed with a combustor also makes it possible to include catalyst into the reactor for the removal of tar from the product gas. Thus, the possibility of using a regenerative catalyst for removing tar is investigated as a novel approach for removing tar from the product gas. The concept is shown schematically in Figure 4-13, illustrating how biomass devolatilises and forms gases and tar. The hydrogenous sugars and aliphatics are converted to light gases relatively easily while the phenol and cyclopentadiene are converted to troublesome tar-like naphthalene. The idea is to remove tar from the product gas by forming a char on the catalyst and transporting it to the combustor with the bed material for the combustion. The char will be burned in the combustor and the catalyst will be sent back to the gasifier.

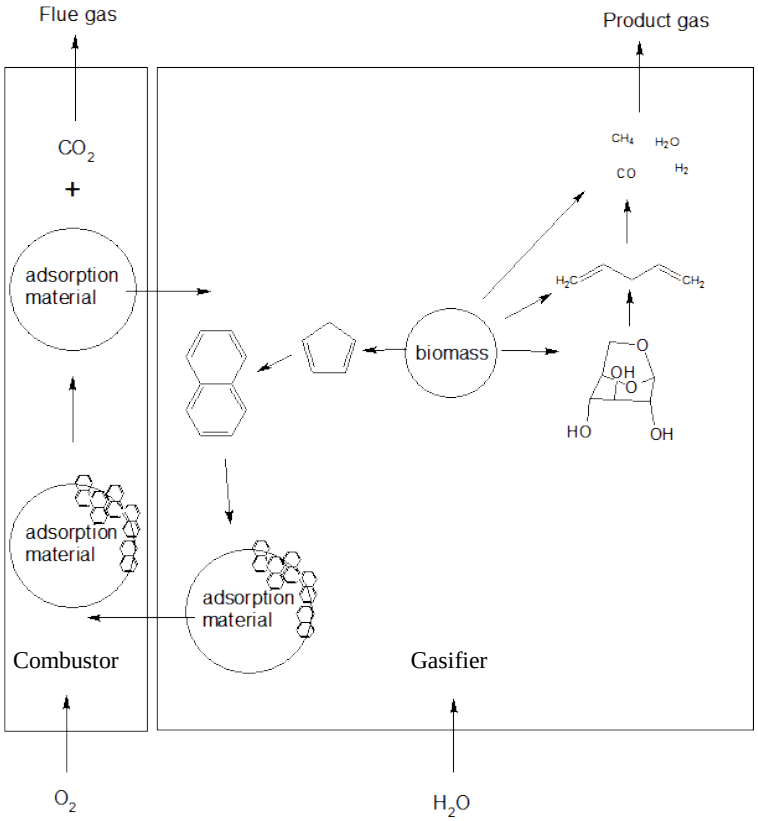

Figure 4-13: Schematic concept of catalytic coke formation for tar removal.

To investigate the possibility of using a catalyst for tar removal in this way, some crude estimation for the limiting factors for the tar removal is done.

4.3.1 Consideration for tar coking onto catalyst

Tar can be controlled by limiting the formation of tar from the biomass, cracking in the gas phase, or catalytic reforming. Catalyst is an effective measure to reduce tar in the product gas, and for the dual fluidised bed with a combustion chamber it will also be possible to reactivate the catalyst.

The problem with using catalysts for tar reforming in dual fluidised beds arises from a limited contact time between the tar-filled gas and the catalytic surface. In the emulsion the tar-filed gas is in contact with the catalyst for a relatively long time, like for a packed bed. The contact between tar and catalyst in the emulsion is dependent on the mass transfer rate to the surface of the catalyst.

For the bubble, which is mostly solid-free, the contact time between the gas and catalyst is much lower. The bubble gas will primarily circulate inside the bubble and the wake. The amount of gas-to-solid ratio is thus much higher for the bubble compared to the emulsion. This means that the conversion rate has to be that much high for the bubble region to have the same conversion as for the emulsion. Furthermore, conversion may simply be limited by the transport of gas to the catalyst, which is dependent on the gas circulation rate between the solid-free bubble and the wake.

For tar that is adsorbed on the catalyst surface, the conversion happens by deforming the structure of the tar species to minimise the activation energy needed for reform. The presence of a char layer is seen when insufficient reforming of the adsorbed tar is occurring [77] [133]. Thus, for catalysts the surface reaction may be the limiting step as char deactivation is one of the problems within bed tar conversion.

Thus, the limiting steps for removing tar from the bubble by coke formation on a catalyst can be at 4 points:

1. Mass transfer from bubbles to the wake
2. Mass transfer from bubble to the emulsion
3. Mass transfer from the emulsion/wake gas to the catalyst
4. Coking formation rate

From a downstream processing view, it does not matter whether the tar is converted or whether it is removed in some other way. Thus, if tar may be removed by the rate of adsorption instead of by the catalytic conversion, a more effective tar removal will take place.

From catalyst technology, it is already known how to create sites that to a larger extent prevent tar species from desorbing again [187]. This would shift the adsorption equilibrium and thus increase the overall rate of adsorption.

Using a catalyst is only possible when the char layer may be burned in a combustor as is the case for the dual fluidised bed.

The coking rate that is possible to obtain is unknown but it cannot exceed the mass transfer to the surface of the particle, and it is expected to be faster than the conversion rate of a catalyst.

4.3.1.1 Mass transfer from gas to catalyst in the bubble wake and emulsion.

To get an idea of the limiting step, some simple calculation of mass transfer at the different limiting steps will be performed.

The mass transfer from the bubble wake gas to the wake solid is investigated. The mass transfer is dependent on the diffusion coefficient and the gas velocity relative to the solid. For the bubble the gas exits the top of the bubble and moves downwards relative to the bubble together with the

surrounding solid. The gas enters the bubble at the bottom again counter-current to the solid. Thus the highest relative velocity between gas and solid would be expected in the wake of the bubble.

The flow condition in the wake is chosen as the reference condition for the calculation of mass transfer. A conservative estimation of the mass transfer will be made, and thus I will assume that the particles follow the bubble and the velocity of the gas is that of the maximum cross-section of the bubble (3 u_{mf} [162]).

The mass transfer is affected by several factors, the diameter of the particle, diffusivity, viscosity, density, gas velocity, and temperature. The mass transfer coefficient is determined by use of the Sherwood number in accordance with Appendix F – Mass transfer coefficient calculations.

The calculation of the transfer coefficient is based on a system of 800°C. Diffusion coefficient is calculated from the expression for $\mathfrak{D}_{AB}$ at low pressures (<10atm) [188] for phenol in steam, see Appendix G – Diffusion coefficient estimation. Viscosity have been calculated from Lennard-Jones parameters with the composited viscosity calculated as shown in the appendix of viscosity estimation based on a gas composition of $H_2O = 0.48$, $CO = 0.14$, $CO_2 = 0.13$, $H_2 = 0.2$, and $CH_4 = 0.05$, see Appendix H – Viscosity estimation. The size of the bed material is assumed to be 600µm.

Table 4-2: Comparison for calculation of mass transfer and catalyst reaction rate

Rate	Conditions			Transfer rate to a single particle/ reaction rate of a single particle (g/s)
	l_0 characteristic diameter mm	T temperature in K	u Gas velocity relative to particle m/s	
Transfer rate in bubble wake	0,6	1073	0.12	$5.4 \cdot 10^{-6}$
Transfer rate in emulsion	0,6	1073	0.04	$4.5 \cdot 10^{-6}$
Reaction rate for an equivalent catalyst size$^{\alpha}$	0,6	1073	Independent	$3.8 \cdot 10^{-9}$
Transfer rate	36	1073	0.12	$1.1 \cdot 10^{-3}$
Transfer rate	36	1073	0.04	$3.6 \cdot 10^{-4}$
Reaction rate for an equivalent catalyst size$^{\alpha}$	36	1073	Independent	$1.0 \cdot 10^{-3}$
Transfer rate	0,6	873	0.12	$5.5 \cdot 10^{-6}$
Transfer rate	0,6	873	0.04	$4.5 \cdot 10^{-6}$

α=Based on a rate of 1 $\frac{g_{org}}{g_{cat}\, min}$ [69]

Calculation results of the reaction rate of the catalyst compared to the mass transfer rate to the same size particle are shown in Table 4-2. The calculation can be found in the electronic appendix. The table shows little influence of the temperature on the transfer rate.

Large catalyst sizes of 0.6mm (The upper end of the Geldart b particle size) ensure a fast transport to the catalyst surface with a factor 1000 faster than the conversion. This is the case for both the bubble wake gas transfer to the wake catalyst and for the emulsion gas transfer to the emulsion catalyst. The catalyst size has to be increased to about 30mm to get a limiting effect on the transport of the material. This is with the assumption of $0.085\frac{mol}{m^3}$ (0.6 vol% phenol) tar in the gas phase and a zero concentration at the surface. An increase of the concentration of tar species will only further increase the transfer rate, and the potential for reducing tar is in the order of 1000 at which point the transfer rate will be limiting because of the driving concentration difference.

With the transport of tar to the surface of the catalyst being of the order of 1000 times higher than the reaction rate, the catalyst will most likely be saturated with tar if sufficient tar is available. It is known that, if insufficient steam is available for gasification of the tar, it will begin to polymerise on the surface of the catalyst[69], [126]. As the tar species increases in the number of aromatic rings, the ratio between steam and carbon have to be increased to prevent coke formation [69].

4.3.1.2 Mass transfer from bubble to wake

As there is a large part of the bubble where there are no particles or a very small fraction of particles, the adsorption may be limited by the transfer from the bubble to the wake. The transfer of gas from the solid-free bubble to the solid-dense wake is described by

$$v = 3u_{mf}\pi R_b^2 \qquad \text{(Eq 4-9)}$$

for a minimum fluidisation velocity of 0.04m/s and a bubble diameter of 0.05m [14]. The concentration of tar is considered to be 0.085mol/m^3 as for the transfer rate calculations and is considered to be of phenol. Giving a transfer to the cloud of

$$\dot{m} = 1.89 \cdot 10^{-3}\frac{g}{s} \qquad \text{(Eq 4-10)}$$

This, of course, has to be distributed across all the particles in the wake. The wake is assumed to be 20% of the solid-free bubble size, and the void is assumed to be a fraction of 0.4, and particle radius is 0.3mm. The number of particles in the wake is thus

$$N_{p,wake} = \frac{V_b \cdot x_{wake} \cdot \left(1 - \epsilon_{mf}\right)}{V_{cat}} = 69444 \qquad \text{(Eq 4-11)}$$

The transfer rate per particle in the wake is thus

$$r_{bubble\ transfer} = 2.71 \cdot 10^{-8}\frac{g}{s\ cat_{particle}} \qquad \text{(Eq 4-12)}$$

The transfer from the solid-free bubble to the cloud wake is thus not the limiting step as this is a factor 10 times larger than the comparable reaction rate. This is still in the case that the entire wake is considered to be a catalyst which most likely will not be the case for expensive catalysts. If only 20% of the volume is a catalyst, the transfer from the bubble to the wake will be of a factor 100 times faster than the reaction. As the particle diameter is in the upper limit of the Geldart b particles, it will be difficult to manipulate the minimum fluidisation velocity to increase the

transfer rate from the bubble. Instead, the maximum size of bubbles may have to be limited mechanically. Smaller bubbles will increase the residence time for which conversion can take place.

For tar species larger than phenol, the weight transfer rate may increase with a factor 2 if only the molecular weight changes. This change is not significant to change the order of magnitude of the transfer rate.

4.3.1.3 Measures for improving the adsorption equilibrium

With a mass transfer from the bubble gas to the catalyst that is 10 times faster than the conversion, the catalyst is the limiting step for the tar removal. The catalytic activity of the catalyst comes from the ability to perturb the electronic structure of the chemisorbed molecule[187]. The conversion rate of tar is highest at moderate bonding strength at the catalytic sites which is determined by the number of vacant d-orbitals. Co, Ni, Rh, Ru, Os, Pd, Ir and Pt have moderate bonding strengths and are good for hydrogenation and dehydrogenation reactions. V, Cr, Nb, Mo, Ta, and W (group 5 and 6) have a large number of vacant d-orbitals that lead to a much lower desorption rate [187]. The moderate bonding strength ensures that tar species are desorbing from the surface again, which limits the net coking.

To get a catalyst that has the best possibility of removing tar, the net coking rate should be increased. A high coking rate to form coke on the surface will lead to blockage of pores. Thus to be able to form as much coke as possible the pores should be kept large. This will also benefit the transportation of oxygen for combustion of the char. A high amount of active sites with large metal particles will increase the formation of char formation and help the net coking rate.

From the understanding of the coke formation, the ideal catalyst for tar removal by coke formation will have:

1. Large metal particles in the support material
2. V, Cr, Nb, Mo, Ta or W for the active sites
3. Maximum of active sites
4. Large pore to prevent blockage and maximise diffusion in the catalyst

4.3.1.4 Catalyst coverage time

For the catalyst to be effective, there will have to be active sites for the tar to be adsorbed. As the coking progresses, the number of active sites will decrease. The time it takes to saturate the catalyst surface is of interest as the catalyst should stay in the gasification area for less time than it takes for complete saturation of the surface.

To make a conservative guess, we assume that coke is formed as a monolayer on the outer surface of a smooth spherical catalyst. The surface of a catalyst, with a diameter of 0.6mm is

$$A_{cat} = 4\pi r^2 = 1.13 \cdot 10^{-6} m^2 \qquad \text{(Eq 4-13)}$$

The carbon in the monolayer has been estimated by using the radius of graphite 0.75Å [189]

$$N_C = \frac{A_{cat}}{A_{aromatic}} \cdot \frac{6 \frac{atoms}{molecule}}{N_A} = 1.59 \cdot 10^{-10} mol_c = 1.91 \cdot 10^{-9} g_c \qquad \text{(Eq 4-14)}$$

If the coking happens as fast as the conversion, the particle will be covered in coke in the order of 0.5s. If the coking rate happens in the order of the transfer rate, it will be in the order of $4 \cdot 10^{-4}$s. This gives an estimation of the minimum time that the catalyst can be in the bed. The possibility for full coverage depends on whether there is an excess of tar to form a full monolayer of the particles.

4.3.2 Model development

To successfully model a fluidised bed with a catalyst, the model needs to include the mixing of solid particles. This will make it possible to predict the release of tar through the reactor.

Additionally, the model needs to model the flow pattern of the gas and the transport of bed material to the combustor. The ability of the bubbling bed model to account for the solid circulation and gas circulation in the gasification chamber makes it suitable for this problem. The bubbling bed model will, however, be extended to account for circulation of solid to the combustor and will be limited to situations with a downwards flowing emulsion gas.

The reactor system of the fluidised bed is separated as shown in Figure 4-14. Yellow arrows are gas streams and green arrows are solid streams. The reactor is divided into 4 sections, the bottom, middle, top, and freeboard because of the introduction of gas or solid or by hydrodynamic changes. The bottom to the top section is the bubbling bed with a dens region of solid (emulsion) and a bubble region. The bubble region is moving upwards in the reactor and the emulsion region is moving downwards.

For the bottom section, gasification gas is introduced from below together with recycled gas from the freeboard and gas from the emulsion phase. Solid in the bottom section is transported to both the bubble wake and the combustor.

Before the middle section, solid fuel is fed into the system, changing the concentration of the emulsion solid. The solid addition is assumed to be relatively small compared to the solid flow, and thus solid volume expansion is neglected.

Before the top section, the gas from the devolatilisation of cellulose and hemicellulose is introduced, increasing the gas flow and consequently adding recirculation of solid and gas in the top section. All incombustible solids are also added to the top section at the top of the section.

The freeboard only consists of a gas phase, and because of the negative gas flow in the emulsion it will have same concentration as the gas from the bubble phase.

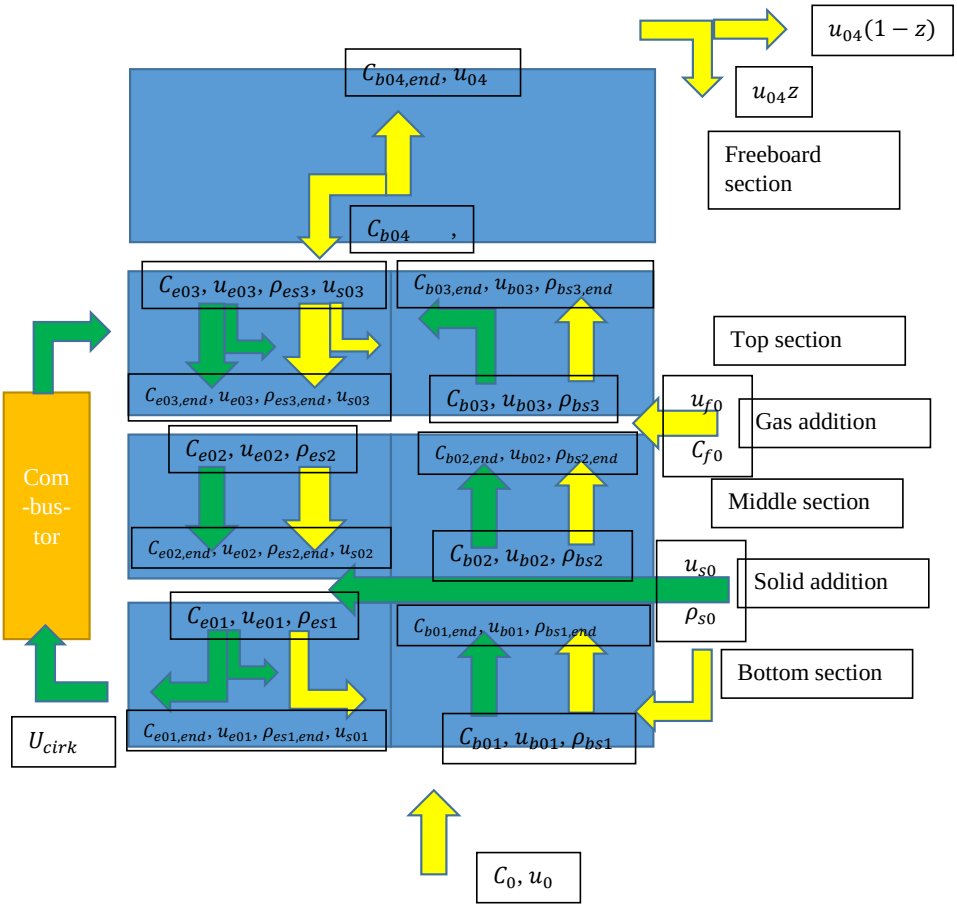

Figure 4-14: Schematic of the reactor model, with initial values and separation of sections.

The parameters indicated at the start and end of the reactor sections is the initial concentration for that part of the system.

Each reactor section is divided into solid and gas fraction in a downwards-going emulsion region and an upwards-going bubble region.

4.3.2.1 Assumptions for model setup

The bubbling bed model is subject to some simplification. Furthermore, some simplification is done to reduce the complexity of the model. The following simplifications are done for the model setup of the reactor model.

1. The system is at a steady state and isothermal. From literature it is seen that the temperature profile changes very little throughout the bed (<50°C) [6].
2. The fluidised bed is simplified to a one-dimensional model, varying concentration only by the height of the reactor.
3. The hydrodynamic behaviour is described by the bubbling bed model [162], allowing counter current bubble and emulsion flow.

4. All gases and solid in the separated bubble and emulsion regions are assumed to follow a plug flow.
5. The biomass particles are assumed isothermal.
6. Cellulose and hemicellulose will devolatilise immediately while lignin devolatilisation will be modelled.
7. Transfer between emulsion and bubbles is assumed to follow a diffusion mechanism. Mass transfer resistance from particle to gas is assumed to be neglectable.
8. Biomass particles are assumed spherical and of uniform size. The conversion of biomass material is assumed to be small compared to the solid transport giving little change to the hydrodynamic behaviour with the conversion.
9. Bubble size is assumed to be constant and represented by an effective bubble size.
10. The bubble cloud is assumed to be neglectable.
11. Addition of gas beyond that needed for minimum fluidisation is assumed to form bubbles or add to the bubble phase.

The reactor area is simplified to two regions consisting of the bubble region and the emulsion region, each with a solid and gas phase. The fractions of the different phases are sketched in Figure 4-15. The bubble region flows upward in the reactor and the emulsion region flows downward in the reactor. The bubble region is divided into gas and solid phase. The gas phase consists of the bubble area with no solid and the gas between the solids in the wake. The solid bubble phase is the solid wake. The emulsion region consists of a solid emulsion phase and an emulsion gas phase. The emulsion gas phase is in contact with a bubble area of S_{be}. The cloud of the bubble is assumed neglected.

Bubble with its wake take up in average over time an area fraction that equals its volume fraction in the reactor $\delta + \delta\alpha$, where δ is the bubble fraction of the bed, and α is the wake size as a fraction of the bubble size. The wake of the bubble, which consists of solid and gas, has a volume fraction of the bubble of α, thus the wake fraction in the reactor is $\delta\alpha$. The gas fraction in the emulsion region and the wake region equal that of a static bed at minimum fluidisation ϵ_{mf}, thus the fraction of the emulsion gas is $(1-\delta-\delta\alpha)\epsilon_{mf}$. The solid occupies the remaining of the emulsion, giving a total fraction of the area of $(1-\delta-\delta\alpha)(1-\epsilon_{mf})$.

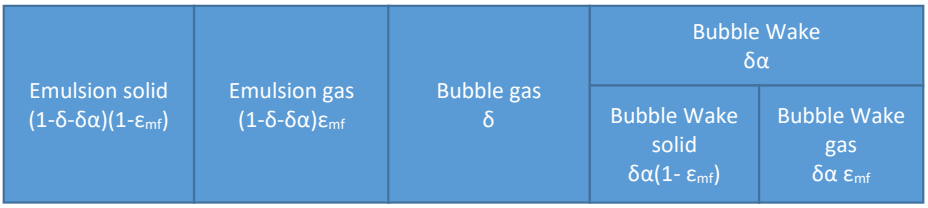

Figure 4-15: Distribution of gas and solid phases

4.3.2.2 Bubble phase

The equations for calculating the concentration change in the bubble phase is set up by considering the mass balance (Eq 4-15) for the differential area from L to $L + \Delta L$, which is illustrated in Figure 4-16, where L is a point in the reactor height.

$$in + prod = auc + out \quad \text{(Eq 4-15)}$$

The change in concentration with respect to the height of the reactor arises from the flow of bubbles from the bottom of the reactor to the top. The bubble travels up the reactor with the speed of u_b and an average cross-section of $\delta(1-\alpha)A$. The concentration at the inlet of the control area is C_{Ab_L}. Furthermore, there is a transport of mass from the emulsion across the surface of the bubble that are in the control area (S_{be}). The concentration contribution to the control area from mass transport into the system is thus described by Eq 4-16.

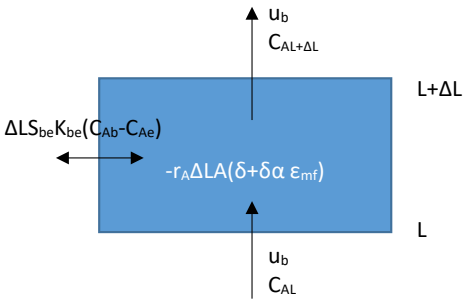

Figure 4-16: Differential space for mass balance

$$in = C_{Ab_L} - \frac{S_{be}K_{be}(C_{Ab} - C_{Ae})\Delta L}{\mathrm{u_b}(\delta + \delta\alpha\epsilon_{mf})A}[=]\left[\frac{mol}{m^3}\right] \quad \text{(Eq 4-16)}$$

where $S_{be}[=]\frac{m^2}{m}$ is the surface area between the bubble phase and emulsion phase per meter of reactor. $K_{be}[=]\frac{m}{s}$ is the mass transfer coeffecint between bubble and emulsion. $\Delta L[=]m$ is the length of the control area. $\mathrm{u_b}(\delta + \delta\alpha\epsilon_{mf})A[=]\frac{m^3}{s}$ is the volume flow passing through the control area per second.

The concentration out of the system $C_{Ab_{L+\Delta L}}$ is simply described by Eq 4-17.

$$out = C_{Ab_{L+\Delta L}}[=]\left[\frac{mol}{m^3}\right] \quad \text{(Eq 4-17)}$$

The production term is formed by 3 contributions: homogeneous gas phase reforming, gas release from the solid emulsion that contributes to the bubble [14], and gas release from the wake solid. It is assumed that an equal bubble area is available throughout the reactor and thus the bubble surface area for the control volume becomes ΔLS_{be}. The gas release from biomass particles is assumed to form bubbles and merge with the other bubbles and thus only contribute to the bubble phase. This counts for both the solid in the bubble wake and the solid in the emulsion.

$$produced = -reforming\ in\ the\ gas\ phase + gas\ from\ biomass\ in\ bubble\ wake + gas\ from\ biomass\ in\ the\ emulsion$$

The reaction takes place during the time it takes for the bubble to pass the control area $\left(\frac{\Delta L}{u_b}\right)$ and the contribution from reforming is thus $-\frac{r_{Ab}\Delta L}{u_b}$. The formation from solid devolatilisation from the wake is found by the concentration change $\rho_{s_{wake}}k_{s_b}[=]\frac{mol}{s}$ multiplied by the volume of the wake in the differential area $\Delta L\delta\alpha(1-\epsilon_{mf})A$. Where k_{s_b} is the reaction constant for gas species in $\left[\frac{m^3\ mol}{kg\ s}\right]$. The contribution from the devolatilisation is divided by the volume flow through the control area $u_b(\delta + \delta\alpha\epsilon_{mf})A$.

Something similar is done for the solid devolatilisation contribution from the emulsion, where the emulsion volume is $\Delta L(1-\delta-\delta\alpha)(1-\epsilon_{mf})A$.

$$produced = -\frac{r_{Ab}\Delta L}{u_b} + \frac{\Delta L \rho_{s_{wake}} \delta\alpha(1-\epsilon_{mf})Ak_{s_b}}{u_b(\delta+\delta\alpha\epsilon_{mf})A} + \frac{\Delta L \rho_{s_e}(1-\delta-\delta\alpha)(1-\epsilon_{mf})Ak_{s_e}}{u_b(\delta+\delta\alpha\epsilon_{mf})A} \quad \text{(Eq 4-18)}$$

The accumulation term for the change of concentration with time for a specific point in the reactor is 0 because the model is set up for a steady state system.

This leads to the following differential equation for the concentration change of compound *A* in the bubble phase with respect to the reactor height.

$$\frac{dC_{Ab}}{dL} = \lim_{\Delta L\to 0}\frac{C_{Ab_{L+\Delta L}} - C_{Ab_L}}{\Delta L} = -\frac{r_{Ab}}{u_b} + \frac{\rho_{s_w}\delta\alpha(1-\epsilon_{mf})Ak_{s_b}}{u_b(\delta+\delta\alpha\epsilon_{mf})A} + \frac{\rho_{s_e}(1-\delta-\delta\alpha)(1-\epsilon_{mf})Ak_{s_e}}{u_b(\delta+\delta\alpha\epsilon_{mf})A} - \frac{S_{be}K_{be}(C_{Ab}-C_{Ae})}{u_b(\delta+\delta\alpha\epsilon_{mf})A} = \quad \text{(Eq 4-19)}$$

Rearrange to get the following expression for the concentration change.

$$\frac{dC_A}{dL} = -\frac{r_{Ab}}{u_b} - \frac{S_{be}K_{be}(C_{Ab}-C_{Ae})}{u_b(\delta+\delta\alpha\epsilon_{mf})A} + \frac{\rho_{s_w}\alpha(1-\epsilon_{mf})k_{s_b}}{u_b(1+\alpha\epsilon_{mf})} + \frac{\rho_{s_e}(1-\delta-\delta\alpha)(1-\epsilon)k_{s_e}}{u_b(\delta+\delta\alpha\epsilon_{mf})} \quad \text{(Eq 4-20)}$$

4.3.2.2.1 Initial concentration for bubble interface

The split of the reactor system into several sections with changes of gas or solid makes it necessary to calculate a new initial concentration for each section.

At the top of the reactor, the gas bubble will burst and the gas will be released into the freeboard. It is, however, expected that the emulsion gas is downward-flowing and emulsion gas will thus not contribute to the composition of the freeboard, thus $C_{b03,end} = C_{b04}$. The downward gas will subtract from the total flow in the freeboard as particles drag down air.

At the bottom of the reactor, the hydrodynamic behaviour is more complicated. The bubbles are formed from the bottom inlet gas through holes in a distributor plate. The downwards-moving particles from the emulsion are either transported to the combustor or to bubble wakes. The emulsion gas that is being dragged down is prevented from entering the combustor because of the fluidisation gas in the connection between the gasifier and the combustor. To conserve the mass balance the emulsion gas has to be added to the bubble phase.

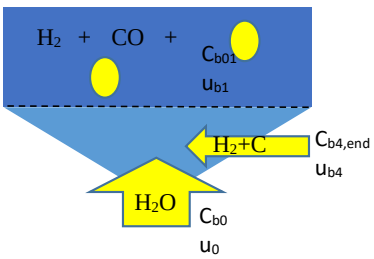

Figure 4-17: Illustration of premixing with product stream

The fluidisation gas added to the system consists of pure steam, but additional gas species can be present by pre-mixing with a recirculation stream from the product gas or other gas sources, changing the fixed concentration. A new concentration and velocity are then calculated by a simple dilution calculation.

$$C_{b01} = \frac{C_{b0}u_0A + C_{b4,end}u_{b4}Az + C_{e01,end}(-u_e)A(1-\delta-\delta\alpha)\epsilon_{mf}}{u_0A + u_{b4,end}A + (-u_e)A(1-\delta-\delta\alpha)\epsilon_{mf}} \quad \text{(Eq 4-21)}$$

$$u_1 = \frac{u_0A + u_{b4}Az}{A} \quad \text{(Eq 4-22)}$$

The possibility of recirculation of gases is not just limited to the bottom; it could potentially be introduced to any place in the bed. The model assumes a constant bubble size in the reactor, and thus a new bubble fraction is calculated. This is calculated from a new superficial velocity

$$u_{0_i} = \frac{u_{0_{i-1}}A + U_f}{A} \quad \text{(Eq 4-23)}$$

The concentration of the gas at the point "*i*" at which the addition of gas is introduced is calculated from the concentration from the previous compartment of the reactor and the additional inlet gas (C_{f0}). The increase in the bubble velocity also results in a new emulsion velocity. This further adds to the new bubble concentration because the additional gas is not transported further down the reactor and thus has to be added to the bubble to conserve the mass balance.

$$C_{ib} = \frac{C_{i-1}u_{b_{i-1}}(\delta+\delta\alpha\epsilon_{mf})A}{u_{b_i}(\delta+\delta\alpha\epsilon_{mf})A} + \frac{C_{ie}(u_{ei}-u_{ei-1})A(1-\delta-\delta\alpha)\epsilon_{mf} + C_{f0}u_{f0}A}{u_{b_i}(\delta+\delta\alpha\epsilon_{mf})A} \quad \text{(Eq 4-24)}$$

4.3.2.3 Emulsion phase

For the emulsion phase, the equations are similar to that of the bubble phase, except the area fraction. The area fraction of the emulsion gas flow is $(1-\delta-\delta\alpha)A\epsilon_{mf}$. The production term for the emulsion consists of homogeneous reforming, gasification of solid, and that which are transported to the bubble area by mass transport. The gas formation from the devolatilisation of biomass has been left out as it is added to the bubble phase.

$$produced = -\frac{r_{Ae}\Delta L}{-u_e} + \frac{\Delta L\rho_{s_e}(1-\delta-\delta\alpha)(1-\epsilon_{mf})Ak_{s_e}}{-u_e(1-\delta-\delta\alpha)A\epsilon_{mf}} \quad \text{(Eq 4-25)}$$

Leading to a similar differential equation

$$\frac{d}{dL}C_{Ae} = -\frac{1}{-u_e}r_{A_e} + \frac{\rho_{s_e}(1-\delta-\delta\alpha)(1-\epsilon)Ak_{s_e}}{-u_e(1-\delta-\delta\alpha)A\epsilon_{mf}} - \frac{S_{be}K_{be}(C_{Ae}-C_{Ab})}{-u_e(1-\delta-\delta\alpha)A\epsilon_{mf}} \quad \text{(Eq 4-26)}$$

4.3.2.4 The solid transport

The solid is circulating in the dual fluidised bed and are transported up the bed by the bubble in the wake of the bubble. As solid is removed from the bottom of the bed, the emulsion solid will move down by gravity. The circulation and velocity of solid are described by the bubbling bed.

The two solid phases (emulsion solid and bubble wake solid) exchange solid material. This transport is set up similarly to an effective mass transport. The solution for the gas phase can thus be used with small alterations.

During feeding of biomass and gasification of solid, the volume of solid will change; this would result in a change in solid velocity. However, the solid biomass fraction is assumed to be small compared to the bed material; thus the biomass decrease by gasification will not significantly affect the overall flow of particles. Similarly, the circulation flow rate is assumed to be much higher than the feeding rate, and thus the volume change by mass addition is also neglected.

Furthermore, the biomass is assumed to be uniformly heated and to form char, gas, and tar. Char particles are only assumed to produce gas by gasification.

4.3.2.4.1 Solid wake

The solid exchange coefficient between wake and emulsion can be expressed as [165]

$$K_{sbe} = \frac{3}{2}\frac{\alpha}{\delta + \delta\alpha}\frac{u_{mf}}{\epsilon_{mf} d_b}, \qquad [s^{-1}] \tag{Eq 4-27}$$

The differential for the concentration can be set up in an analogy manner as for the gas phase. For the solid wake, it is only the gasification of solids that is included in the production term. The solid in the wake still rises with the velocity of the bubble

$$\begin{aligned}\frac{dC_{s_{Ab}}}{dL} &= \frac{-K_{sbe}\left(C_{s_{Ab}} - C_{s_{Ae}}\right) - \rho_{s_w}\delta\alpha(1-\epsilon_{mf})Ak_{s_b}}{u_b\alpha\delta(1-\epsilon_{mf})A} \\ &= -\frac{K_{sbe}\left(C_{s_{Ab}} - C_{s_{Ae}}\right)}{u_b\alpha\delta\left(1-\epsilon_{mf}\right)A} - \frac{\rho_{s_w}k_{s_b}}{u_b}\end{aligned} \tag{Eq 4-28}$$

4.3.2.4.2 Solid emulsion

An analogue solution is available for the emulsion solid as well. The solid emulsion is transported to the solid wake and reacts to form gases.

$$\frac{d}{dL}\,C_{s_{Ae}} = -\frac{K_{sbe}\left(C_{s_{Ae}} - C_{s_{Ab}}\right)}{u_s(1-\delta-\delta\alpha)A\left(1-\epsilon_{mf}\right)} - \frac{\rho_{s_e}k_{s_e}}{u_s} \tag{Eq 4-29}$$

4.3.2.5 Reactions

The reactor system is complicated in itself, and thus it is decided to keep the complexity of the reaction scheme to a minimum to primarily investigate the presence of a catalyst in the reactor.

The simple reaction scheme used for investigation of the efficiency of a catalyst is shown in Table 4-3. For this scheme the char residue from the lignin pyrolysis is assumed to consist of only carbon. Cellulose and hemicellulose are assumed to instantly devolatilise and only form light gases as in Appendix E – Composition of instant devolatilisation gas from cellulose and hemicellulose.

Table 4-3: Reaction scheme implemented into the fluidised bed reactor

Counter	Reaction	A $\left[\frac{\text{mol}}{\text{sec}\, cm^3\, K^n}\right]$	n	E $\left[\frac{cal}{mole}\right]$	Ref.	comments
Gas-solid reactions						
1	$C + H_2O \rightarrow CO + H_2$	$\frac{d[C]}{dt} = -k[H_2O]$ mol/cm²/s $k = T_s\, A\, exp\left(-\frac{T_a}{T_s}\right)$ $A = 3.42$ cm/s/K $T_a = -15600\, K$	0	129705.57288 J/mol	[190]	
2	$C + 2H_2 \rightarrow CH_4$	$\frac{d[C]}{dt} = -k[H_2]$ $k = T_s\, A\, exp\left(-\frac{T_a}{T_s}\right)$ $A = 3.42 \cdot 10^{-3}$ cm/s/K $T_a = -15600\, K$	0	129705.57288 J/mol	[190]	
3	$C + CO_2 \rightarrow 2\, CO$	$\frac{d[C]}{dt} = -k[CO_2]$ $k = T_s\, A\, exp\left(-\frac{T_a}{T_s}\right)$ $A = 3.42$ cm/s $T_a = -15600\, K$	0	129705.57288 J/mol	[190]	
4	Lignin $C_{37.9}H_{40.4}O_{17.1} \rightarrow 26.53\ C + 3.79\ CH_4 + 7.58\ CO + 9.52\ H_2O + 3.1\ H_2$	0.107 [min^{-1}] Or 1.783·10^{-3} [s^{-1}]	0	8025.37 [J/mol]	[78]	
5	Lignin $C_{37.9}H_{40.4}O_{17.1} \rightarrow 3.79\ C_6H_5OH + 15.16\ CO + 1.5\ H_2O + 7.33\ H_2$	0.988 [min^{-1}] Or 1.647·10^{-2} [s^{-1}]	0	11318.48 [J/mol]	[78]	

Catalytic reactions						
8	$C_6H_5OH + A \rightarrow C_6H_5OH \cdot A$	$5.33 \cdot 10^{-4} \frac{\text{mol}}{\text{s m}^2_{Ni}}$	0	0	[69] [191]	This is based on the conversion rate from [69] at 800C based on the catalyst surface area information from [191], giving a constant reaction rate per surface are of metal. Metal surface area is $0.4 \frac{m^2}{g}$.
Gas phase reactions						
7	$CH_4 + H_2O \rightarrow CO + 3H_2$	$\frac{d[CH_4]}{dt} = -k\,[CH_4][H_2O]$ $k = Aexp\left(-\frac{E}{RT}\right)$ $A = 3015$ m^3/mol/s $E = 125.52\ kJ/mol$	0		[192]	
8	$CO + H_2O \rightarrow CO_2 + H_2$	$\frac{d[CO]}{dt} = -k\left[[CO][H_2O] - \frac{[CO_2][H_2]}{K_p(T)}\right]$ $k = Aexp\left(-\frac{T_a}{T}\right)$ cm^3/mol/s $A = 2.780$ $T_a = 1510\ K$ $K_p(T) = 0.0265 \exp\left(\frac{3958}{T}\right)$	0	12554.834298 J/mol	[190]	
17	$C_6H_5OH + 7H_2 \rightarrow 5CH_4 + CO$	$1 \cdot 10^{11}$	0	$324 \cdot 10^3$ [J/mol]	[109]	Based on the degradation of naphthalene $\frac{dC_{10}H_8}{dt} = k_c C_{C_{10}H_8} \cdot C_{H_2}^{0.4}$

4.3.2.6 Model solution

The reactor model is split into 4 sections. Each section consists of a system of ordinary differential equations that describe the concentration changes for both the emulsion and bubble region. The exact conditions at the bottom of the reactor are not known because the emulsion and bubble region is moving in counter-current flow. Instead, the relations between the regions at the top of the reactor and the bottom of the reactor is known. The boundary conditions for bubble region at the bottom of the reactor and the boundary condition for the emulsion region at the top of the reactor can thus be set based on an initial guess.

The reactor model is solved by iteration of the reactor model where the boundary conditions are updated between each iteration. If a similar simulation has been done previously, these can be used with advantage as an initial guess of the concentration profiles.

4.3.3 Comparison of tar development in gasifier

To validate the reactor model it is compared to literature data. The gas and tar concentration across the reactor height is compared to a fluidised bed. Furthermore, the reactor is compared to dual fluidised bed with the catalyst. Even though the catalyst is forming coke in the model, the result may be comparable to the catalyst data if saturation of the catalyst material is low. The data for comparison of fluidised beds are limited by a lack of operational data that will have to be estimated.

4.3.3.1 Comparison to fluidised bed

The reactor model is compared to a small fluidised bed with an internal diameter of 154 mm and a length of 1500mm. The fluidised bed is equipped with two 20mm times 660 mm heating pipes that are placed vertically through the bed. The heating pipes influence the fluidisation and create a slug flow. The slug flow is considerably different from the bubbling flow that is modelled and thus some discrepancies are expected. Feeding of biomass is done at the height of 200mm through a screw conveyor [193].

The information about the operating condition of the reference is shown in Table 4-4.

Table 4-4: Operating condition for the reference system

Feed rate (kg/h)	1.6
Steam feed rate (kg/h)	2
Temperature of bed (degrees C)	800
Bed material density (kg/m^3)	2650
Bed material size mm	0.25
Biomass particle size mm	8x20
Superficial gas velocity m/s	0.175
Bed height mm	800

For the simulation, an effective biomass radius has been chosen to be half of the smallest dimension of the biomass pellets. In the referenced article, there is a discrepancy between the gas flow rate they use and the steam-to-carbon feeding rate they state. The superficial gas velocity has been changed from 0.175m/s to 0.037m/S to match the mass feed rate of steam, and the minimum fluidisation velocity has been decreased from 0,03m/s to 0,00420m/s to get a small reversal of the gas velocity in the emulsion phase, which is required to make the model work.

The bubble size is assumed based on relations between bubble size and ratios of $\frac{u_0}{u_{mf}}$ [14]. The bubble size is set to be about 10cm based on the fact that the sand is a Geldart B particle, and the ratio $\frac{u_0}{u_{mf}} = 5.8$.

The comparison of the reference data [193] with the simulation result for the total tar sum is shown in Figure 4-18. The reference shows an exponential increase in tar up through the reactor which is expected as tar is developed all through the reactor.

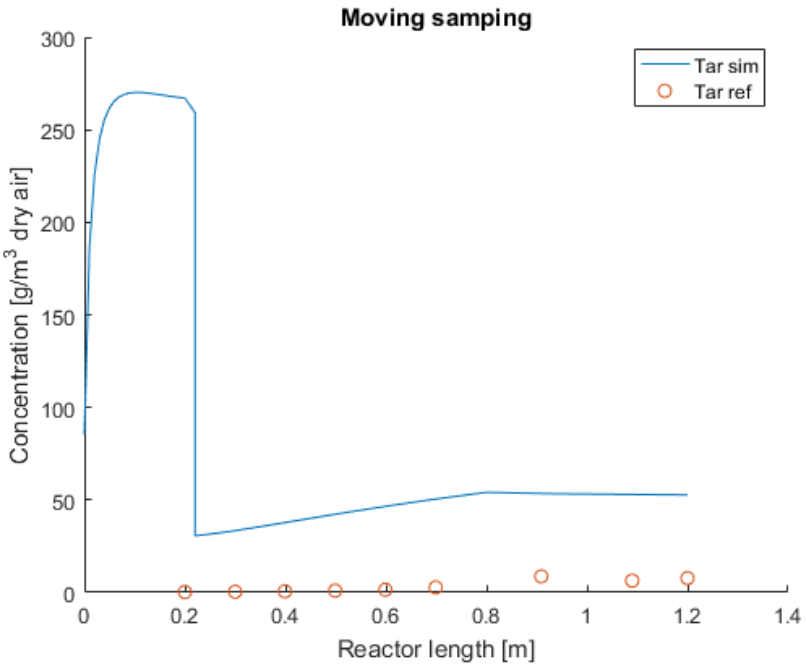

Figure 4-18: Comparison of tar formation from simulation and reference with respect to the height of the reactor.

Accumulation of tar up through the reactor is also seen for the simulation result. The initial high peak is related to the measurements method. At the lower end of the reactor, the tar is the only dry phase and thus the concentration will be high on a dry basis. As the gas released from the biomass is introduced, the dry basis tar concentration drops. The linear increase of tar is explained by an almost even distribution of lignin in the simulation (not shown here), which generates an equal amount of tar all through the reactor. Furthermore, the reference system is behaving more like a slugging flow than a bubbling bed, which may inhibit the back-mixing of solid to generate a more even distribution of lignin.

The total tar formation in the simulation exceeds that of the reference, which may be related to the kinetics that determines the competition between char and tar. The thermal cracking of the tar is also neglected, and phenol degradation is assumed to follow that of naphthalene. This indirectly assumes that all tar forms naphthalene. There might also be effects that have not been included in the reactor model, such as the catalytic effect from the char that affects the tar yield.

The concentration of some of the major gas species is shown in Figure 4-19. This shows a decreasing water concentration while CO_2, CH_4, and H_2 are increasing. CO is decreased by a steam shift reaction, which also contributes to the increase of hydrogen and CO_2. The order of magnitude seems to be in good agreement with the reference data.

For the reference, about 20% of the steam that enters the reactor is participating in reactions [193]; thus the majority of the water concentration change is due to dilution by gas from the biomass. For the simulation this dilution is primarily accounted for by an assumption of an instant devolatilisation of cellulose and hemicellulose. The decrease in water fraction is seen at the injection point of cellulose and hemicellulose. This accounts for about 45% of the water fraction drop.

Most of the gas concentration comes from the devolatilisation of cellulose and hemicellulose and only slight changes occur as a consequence of shift reaction ($CO + H_2O \leftrightarrows CO_2 + H_2$). The composition of the initial devolatilisation gas is based on the elementary composition of cellulose and hemicellulose which may differ from that given in the reference. This may explain the difference in CO at the feed injection point.

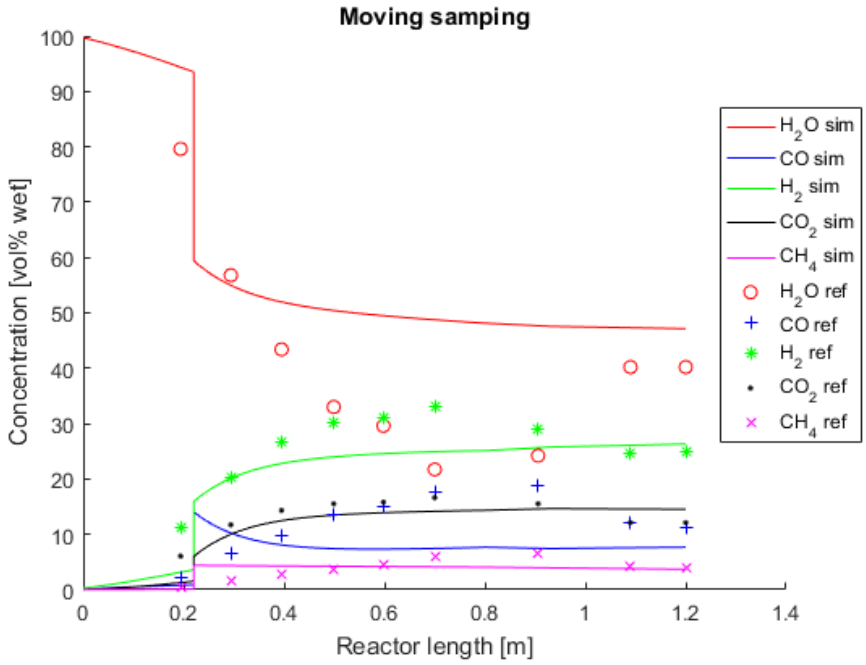

Figure 4-19: Comparison of simulation and reference for fluidised bed for light gas composition with respect to gasifier height

4.3.3.2 Comparison to dual fluidised bed

The reactor model is compared to the product gas composition found for a dual fluidised bed by Pfeifer et al. [119] The reference [119] [194] [195], does not include all information about the operating parameters. The solid circulation to the combustor, especially, and the bed and reactor height, which affects the result greatly, are not included.

The reactor is the dual fluidised bed at the Vienna University of Technology [194]. The gasification chamber is square but has a cross-section that is equivalent to a diameter of 304mm. The feeding rate $25\frac{kg}{h}_{wet}$ and the feed consist of 7.3wt% water. The water-free content is reported in Table 4-5.

Table 4-5: Fuel characteristic on dry basis [194]

Parameter	value	Unit
C	49	Mass % wf
H	6.52	Mass % wf
N	0.12	Mass % wf
S	<0.05	Mass % wf
O	44.31	Mass % wf
Ash	0.26	Mass % wf

The reactor operates with a bed material made up of olivine and Ni-catalyst with a grain size of 400-600 micrometres. The density of olivine and catalyst are $3250 - 3300\frac{\mathrm{kg}}{\mathrm{m}^3}$. The temperature, steam to fuel ratio, and catalyst weight fraction are given in Table 4-6.

Table 4-6: Experimental operating parameters [194]

Parameter	Value						
Temperature (C)	750	800	850	900			
Steam/fuel		0.3	0.6	0.9			
Catalyst			0	5	10	20	43

The bed height is not given directly but is read out from a diagram of the setup to be 0.5 [6]

The fluidisation velocity is calculated from the steam-to-biomass ratio and the cross-section of the reactor. The minimum fluidisation is set to 0.15 m/s [195].

The main superficial gas velocity of the combustor is between 8.8 and 10.1 m/s [195]. The solid circulation rate is based on the experiment of Karmakar et al. [196] that shows the relation between the mass flow in a riser and the gas velocity and particle size. Because the data does not include the range of velocities for the combustor, the highest circulation rate for the particle size is used. It is thus assumed that, at least, 14kg/m^2/s is transported up through the combustor. With an inner diameter of the combustor of 98mm [194], the mass flow will be 0.11kg/s or $3.2 \cdot 10^{-5}\ \mathrm{m}^3/\mathrm{s} = 117\mathrm{L/h}$.

The gas residence time is about 3-4s with a superficial gas velocity of 0.41-0.56m/s [195]. This gives a mean length of 1.66m for the freeboard.

Four cases have been simulated. 0, 5, 10, and 20 wt% Ni-catalyst. The reference uses olivine as a bed material which also has some catalytic effect. A large part of the tar formation is thus already reduced by the olivine. In this way, the 0 wt% Ni-catalyst does not represent a process free of the catalyst as the simulation does. Thus the tar formation is still expected to be greatly over-predicted. The relation between the catalyst solid weight fraction and the tar concentration is shown in Figure 4-20.

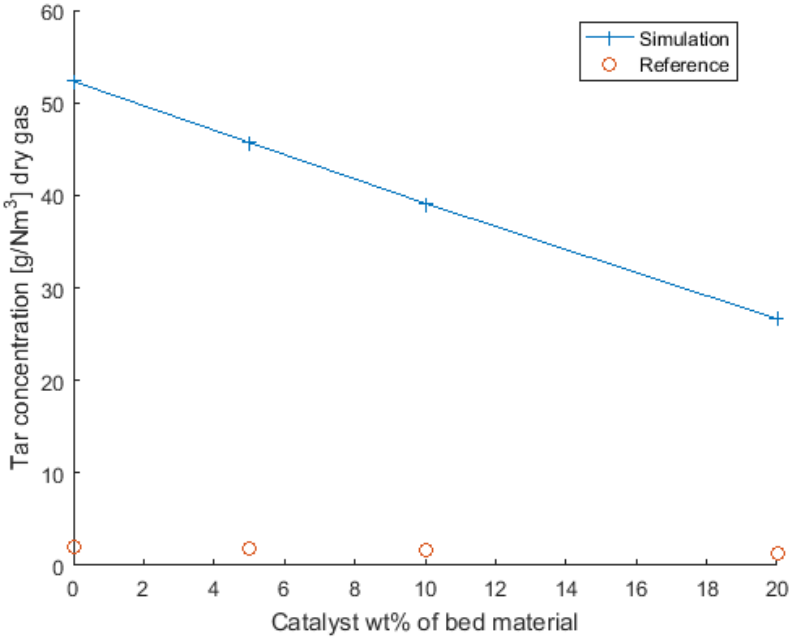

Figure 4-20: Tar concentration as a function of the Ni-catalyst fraction

For the simulation, the catalyst facilitates coking with a reaction rate based on the catalytic activities of a Ni-catalyst. The metallic area, for which coke can be formed, is multiplied by three because the sensitivity analysis in the next section showed little effect of the coke formation rate. The reaction rate is thus approximately three times as fast and may adsorb three times as much tar. Still, the tar formation is greatly overestimated. There is, however, a linear relation between the catalyst amount and the tar reduction for both the simulation and reference.

The catalyst is approximately 90% saturated for the calculations, which may explain the linear relation. In this case an additional catalyst will greatly increase coke formation, whereas for a low saturation an extra catalyst would add to an excess of catalyst that would almost have removed all tar.

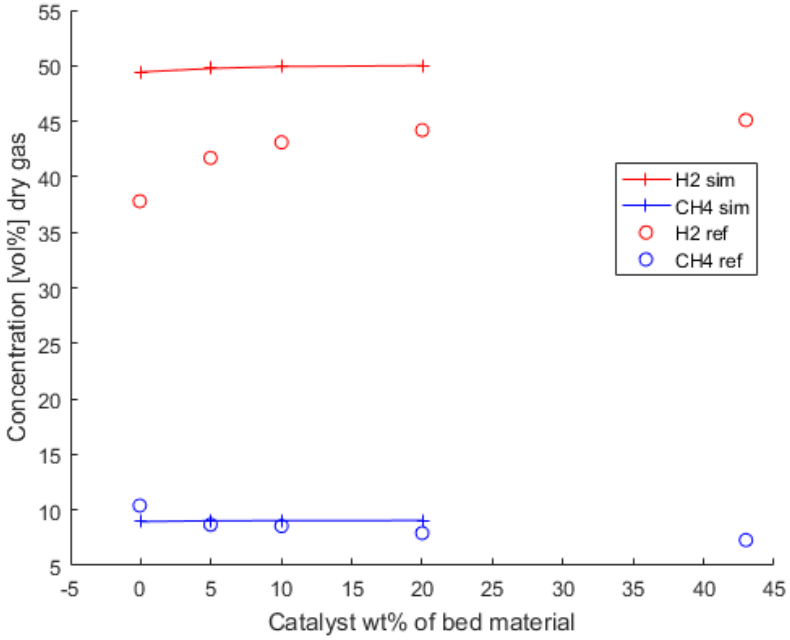

Figure 4-21: H_2 and CH4 outlet fraction as a function of the catalyst weight fraction.

In Figure 4-21 the simulation shows the correct trend for the formation of H_2 and CH_4 with the increase of bed material. Contrary to reference, the increase of H_2 fraction cannot be ascribed to increased gasification of tar component of catalysed steam reforming because this is not accounted for by catalytic contribution. For the simulation the increase in H_2 fraction must be related to the removal of carbon and oxygen as tar condensed on the catalyst. The hydrogen over-prediction is related to the water shift gas reaction.

Figure 4-22 shows the gas composition of the major gas components, CO, H_2, CO_2, and CH_4. This figure shows that the three components that have the greatest discrepancy are CO, CO_2 and H_2. CO is under-predicted, and H_2 and CO_2 are over-predicted. This indicates that the water gas shift reaction $CO + H_2O \leftrightarrows CO_2 + H_2$ is shifted more to the right than the reference which does not reach equilibrium. The bed and reactor height for the reference is not known as well as the minimum fluidisation velocity. The choice of these parameters influences the residence time and thus the time for reaching equilibrium.

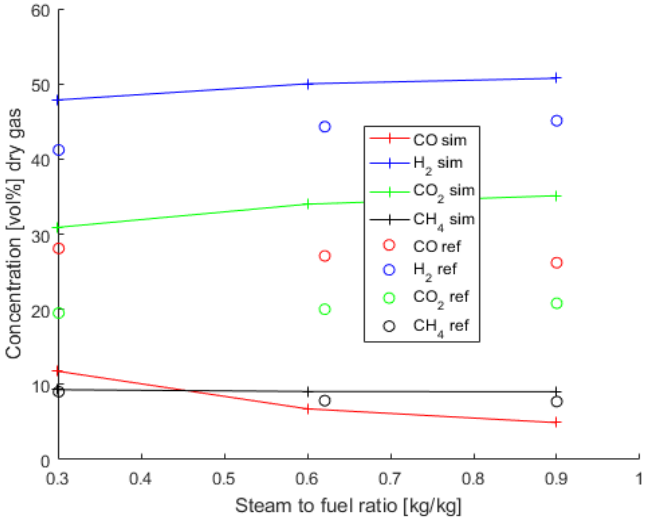

Figure 4-22: Major gas species volume fraction based on a dry gas. 20 wt% Ni-catalyst and 850C.

4.3.4 Sensitivity analysis

The reactor model is simplified to include some rather crude assumptions like isothermal and isobaric conditions. At the same time, some parameter values are rather uncertain because they are difficult to obtain or may change during operation. To understand the validity of some of the assumptions and the effect of some of the uncertainties, a sensitivity study is performed. This will show how changes in a parameter affect the output and which parameters have the largest influence within the value interval.

The parameter study includes a variation of some of the design parameters that are thought to have an influence on the output.

The uncertainty of the kinetics has been left out of the analysis. It is clear that to give a good quantitative prediction of the tar output some of the most important parameters are the kinetic rates. But to properly implement the uncertainty of the kinetic parameters, the covariance is needed to avoid over-predicting the effect of the parameters.

The model simplifications of isobaric and isothermal conditions are crude. Thus the effect of a potential temperature and pressure change is investigated to see if it exceeds the effect of the uncertainty of other parameters. If the pressure and temperature changes do not significantly change the output compared to that of the uncertainty of the other parameters, the simplification

of isobar and isothermal conditions may be assumed to have little or no consequence for the model accuracy.

The parameters that are tested are summarised in Table 4-7.

Table 4-7: Parameter uncertainty range for sensitivity analysis

Parameter number	Parameter	value
1	Coking rate on catalyst	$9.607 \cdot 10^{-4}$ m/s to $2.783 \cdot 10^{-2}$ m/s
2	Effective biomass particle radius	$0.1\ mm$ to $0.3\ mm$
3	The bubble diameter	$0.04m$ to $0.10m$
4	Metallic area	$0.38 \cdot 10^3$ to $0.42 \cdot 10^3\ \frac{m_{Ni}^2}{kg_{cat}}$
5	Minimum fluidisation velocity	0.04 to 0.1 m/s
6	Catalyst density	2128 to 2352 kg/m^3
7	Biomass density	475 to 525 kg/m^3
8	Char density	115 to 500 kg/m^3
9	Monolayer size of one mole of tar	5320 to 15961 m^2/mol
10	Reactor temperature	$875K$ to 1071K
11	Reactor pressure	$0.8 - 1.2\ bar$
12	Wake fraction	0.25 to 0.33
13	Void at minimum fluidisation	0.4 to 0.7
14	Diffusion coefficient	0 to $2.9 \cdot 10^{-4}$ m^2/s
15	Solid bulk density of catalyst	427.5 to 472.5 $\frac{kg}{m_{solid}^3}$

Coking rate is dependent on the catalyst, where the number of active sites for adsorption is assumed to be proportional to the adsorption rate. The minimum rate is estimated from a Ni catalyst based on the catalytic conversion as shown in Appendix I – Estimation of the catalytic coking rate

Bubble diameter may have a maximum size if the bed material particles are small; otherwise, it may be controlled by the introduction of baffles in the reactor.

Inlet velocity is partially controlled by the minimum fluidisation as it has to be above 6 times the minimum fluidisation to ensure reversal of the gas flow in the emulsion phase. It also has to be below the limit for the turbulent regime.

Minimum fluidisation is affected indirectly by the size and shape of the bed material. Depending on the bed material this may change because of attrition.

Reactor temperature and pressure may be varied within wanted limits. It is primarily reactor material that will set limits for what is physically possible.

The parameter in Table 4-7 is thought to influence the reactor model with regards to tar, char, and lignin and are analysed using a Morris screening to calculate an elementary effect. This will elucidate which parameters are of most importance for the resulting output. The calculation of elementary effect is shown in Appendix J – Calculation of elementary effect.

The mean elementary effect is used to rank the most important factors for the output parameter as shown in Table 4-8 for tar, lignin, and char. The higher the value, the more sensitive the output is to the uncertainty of the value.

Table 4-8: Absolute value of elementary effect for tar flow rate, lignin conversion and char conversion

Parameter	Elementary effect for tar in g/s	Parameter	Elementary effect for Lignin conversion	Parameter	Elementary effect for Char conversion
ϵ_{mf}	0.56	ϵ_{mf}	0.56	ϵ_{mf}	0.15
A_{mol}	0.36	u_{mf}	0.29	u_{mf}	0.09
u_{mf}	0.33	D_b	0.25	A_{mol}	0.08
D_b	0.25	T	0.15	D_b	0.07
T	0.17	P	0.01	T	0.05
$\rho_{bulk\ cat.}$	0.10	$\rho_{bulk\ cat.}$	0.001	$\rho_{bulk\ cat.}$	0.02
$A_{metallic}$	0.03	α	0.001	$A_{metallic}$	0.008
P	0.01	$\rho_{biomass}$	0.0003	ρ_{char}	0.008

ϵ_{mf} is the void at minimum fluidisation, A_{mol} is monolayer size of one mole of tar, u_{mf} is the minimum fluidisation, D_b is the bubble diameter, T is the temperature, $\rho_{bulk\ cat.}$ is the catalyst density, $A_{metallic}$ is the Metallic area, P is the pressure, α is the wake fraction, $\rho_{biomass}$ is the density of the biomass, ρ_{char} is the density of the char.

The Morris screening shows that the effect of the uncertainty of the temperature and pressure on the model tar output is less than that of several other parameters of the model. A more detailed model that may describe the temperature better may thus have only a minimal effect on the prediction of the tar formation.

It is noteworthy that the coking rate is not on the list even though its uncertainty spans with more than a factor 20. This is explained by the case that is being used. For this case, the catalyst is almost fully saturated and thus a change in coking rate will have only a negligible effect. For other situations with a higher catalytic amount or higher surface area, this factor may be more important for the result.

To determine whether a parameter is significant, Morris suggests plotting the mean of the elementary effect μ against the standard deviation σ with two lines equal to

$$\mu_i = \pm 2 \cdot \frac{\sigma_i}{\sqrt{r}}$$

where r is the number of samples for each elementary effect calculation.

This is shown for tar output, lignin conversion and char conversion in Figure 4-23, Figure 4-24, and Figure 4-25, respectively. The elementary effect plots only show the parameters that are larger than 3% of the most influential parameter. For tar output the bulk density of the catalyst is not significantly different from zero. The other parameters are, however, beyond the standard deviation.

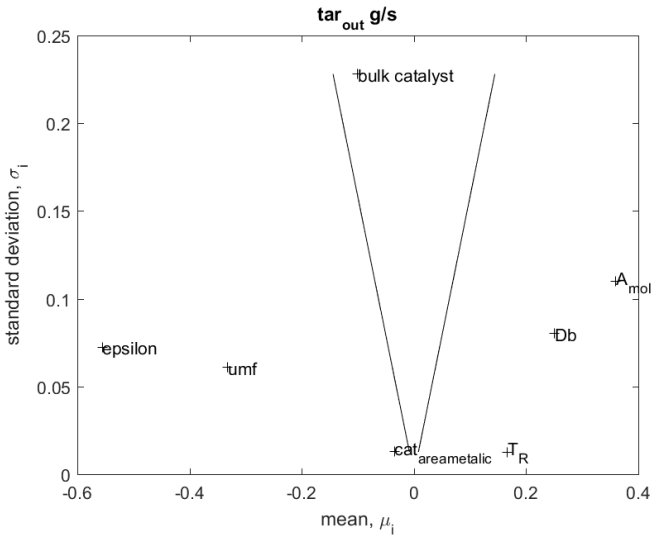

Figure 4-23: Elementary effect of parameters on the tar flow

From Figure 4-24 and Figure 4-25, it is seen that all the dominant parameters have a significant influence.

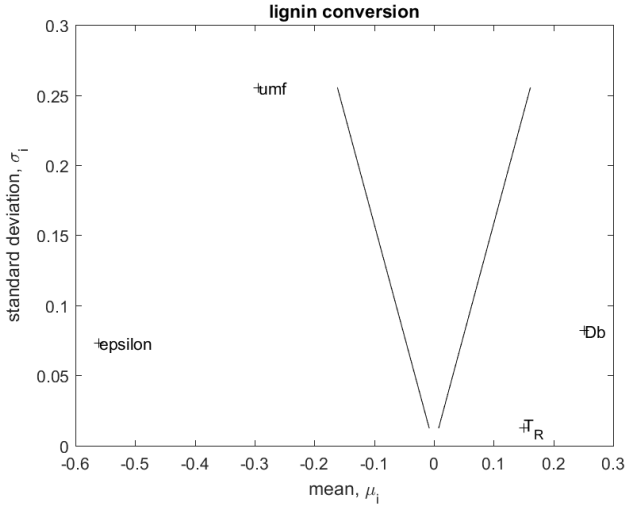

Figure 4-24: Elementary effect of parameters on the lignin conversion

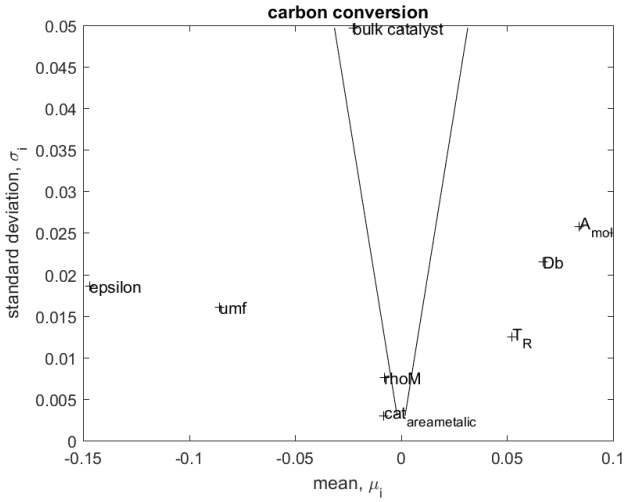

Figure 4-25: Elementary effect of parameters on the char conversion

4.3.5 Parameter study

The reactor model is designed to investigate the effect of different operating possibilities, but particularly the effect of the hydrodynamic effect in the fluidised bed. With the inclusion of a bubble phase and a counter-current emulsion phase, the system is able to see how bubble size, feed position, and recirculation of gas and solid will affect the system. Also, the system incorporates coking onto a catalyst that will also be investigated.

For an ordinary dual fluidised bed temperature, catalyst density and solid circulation rate are the easiest parameters to change, as these will not require any change to the equipment design.

The change of the coking rate is limited to that of the mass transfer and will require the development of a material able to form coke with a higher rate.

The dual fluidised bed design does not normally include gas circulation. The recirculation is here intended to investigate a possible design change of the system, where a fraction of the gas may be recirculated and exposed to the catalyst again.

The simulations are based on a base case, where only one parameter is changed. The base parameters are listed in Table 4-9 and consist of values for dual fluidised bed from the literature.

Table 4-9: Standard parameter used for parameter study

Parameter	Value
Density of pure catalyst	3250kg/m^3
Active site area of the catalytic material	1179 m^2_{Ni}/kg_{cat}
Area covered by one mole of tar	$1.0642 \cdot 10^4\ m^2/mol$
Reactor temperature	173.15K
Reactor pressure	1bar

Bubble diameter	20cm
Wake fraction of solid free bubble	0.33
Reactor diameter	0.304m
Solid volumetric circulation	$3.2 \cdot 10^{-5} m^3/s$
Void at minimum fluidisation	0.6
Solid weight distribution	30 % lignin, 35 % cellulose, and 35 % hemicellulose
Effective char particle size	3 mm
Density of residual char	$115 kg/m^3$
Density of biomass	$491.66 kg/m^3$
Biomass feed rate	$6.9 \cdot 10^{-3}\ kg/s$
Gas circulation fraction	0
Effective diffusion coefficient	$1.933 \cdot 10^{-4}$
Coking rate	$9.607 \cdot 10^{-4}$
Steam to biomass feed rate	0.6 kg/kg
Minimum fluidisation velocity	0.15m/s
Bed height	0.5m
Catalyst fraction of bed material	20%
Free board	1.66m
Feeding position	0.02m

4.3.5.1 Effect of solid recirculation

The solid circulation affects the biomass that is transported to the combustor for heat generation. This is intended to provide the energy for gasification of the remaining biomass in the gasifier. In practice, extra fuel is often added to the combustor to ensure the correct gasification temperature. This gives some room to control the solid circulation.

The solid circulation is simulated with a ±50% solid volume circulation of the base case. The change of the tar and gas composition with respect to the solid circulation is seen in Figure 4-26.

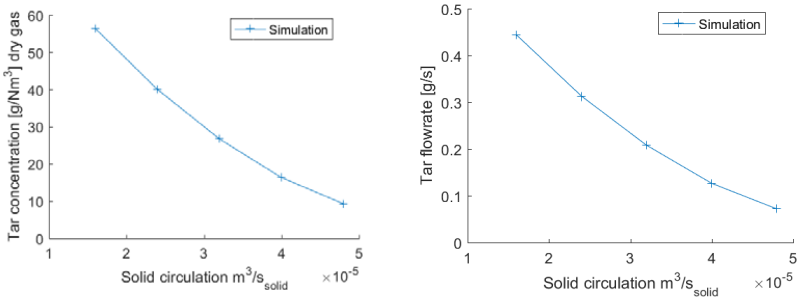

Figure 4-26: Effect of solid circulation on tar concentration and throughput

The increase in solid circulation significantly reduces the tar output. The increased solid circulation leads to a decrease in the lignin and carbon concentration in the bed and an increase

of fresh catalyst for coke formation. As a consequence of lower lignin concentration and increased catalyst for coke formation, the tar formation is diminished.

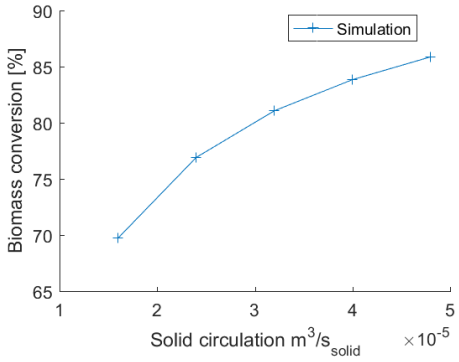

Figure 4-27: Effect of solid circulation on the biomass conversion by gasification

Because of the assumption of instant devolatilisation of cellulose and hemicellulose, the minimum biomass conversion by gasification is 70%. The increase of solid circulation to the combustor apparently produces an increase in biomass conversion, which cannot be explained at the moment.

4.3.5.2 Effect of coking rate

The effective coking rate is assumed to be a parameter that may be affected by the catalyst design as described in 4.3.1.3 Measures for improving the adsorption equilibrium. The coking rate is limited by the mass transfer from the solid-free bubble to the wake, which is estimated to be around 10 times that of the reaction rate of a Ni-catalyst. The lower limit is taken to be that of the reaction rate of a Ni-catalyst.

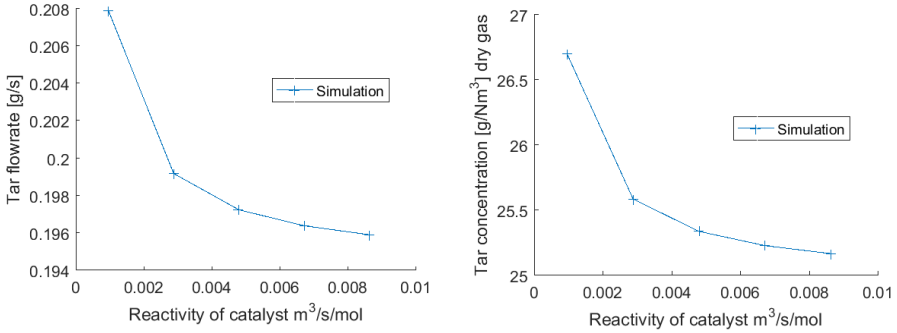

Figure 4-28: Effect of coking rate on tar concentration and throughput

Figure 4-28 shows a small decrease in the tar flow rate as the coking rate increases. This is attributed to an almost saturated catalyst and the coke formation rate is thus not effective. This was also seen for the sensitivity analysis.

4.3.5.3 *Effect of catalyst amount*

The fraction of the catalyst is often limited because catalyst may be expensive to produce and need regeneration relative quickly. The base case 20% of the bed material is regarded as a catalyst. For the parameter investigation, the parameter is ranged from 10% to 50% of the solid bed material. The catalyst amount is reported in $kg/m^3_{solid\ bed\ material}$.

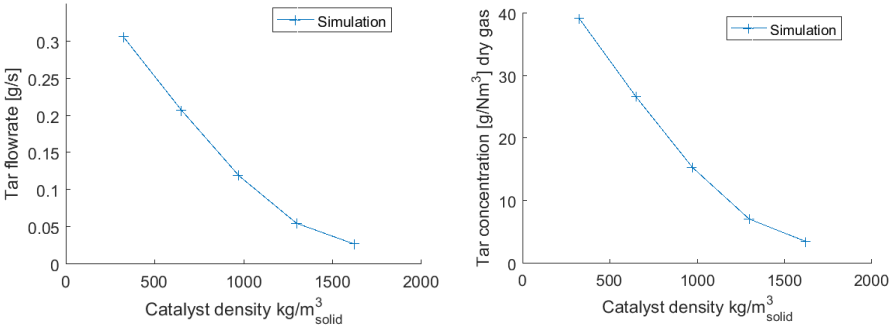

Figure 4-29: Effect of catalyst density on tar concentration and throughput

A linear relation with the increased bed material in the start indicates that the catalyst is saturated. The levelling at the higher concentration shows that the catalyst begins to be unsaturated at a high amount of catalyst. At this point, an increase in coke formation might be more beneficial. The gas concentration is not affected considerably by the presence of a coking catalyst.

4.3.5.4 *Effect of temperature*

The temperature is easy to chance but is limited by other problems that follow the increase of temperature. The variation in the temperature is varied between 90% and 115% of the base case to be within a reasonable temperature that would be expected in gasification in a fluidised bed.

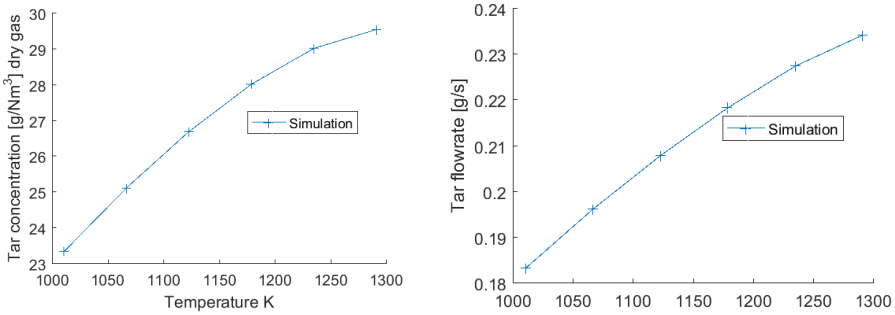

Figure 4-30: Effect of temperature on tar concentration and throughput

For simulation with 20% catalyst, the heating of the gas leads to an expansion of the gas and thus a higher gas flow rate and lower residence time. The increase in homogeneous tar conversion from the temperature increase is not of the same magnitude as the decrease of tar removal by coking. Thus, tar concentration increases with temperature for systems with the catalyst as shown in Figure 4-30. The effect of a temperature change is moderate within the possible operating condition in comparison with catalyst increase.

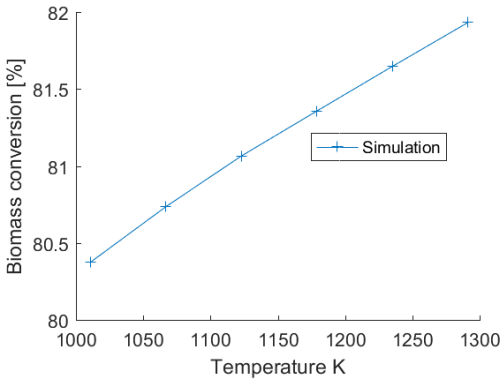

Figure 4-31: Effect of temperature on the biomass conversion

Figure 4-31 shows a slight increase in biomass conversion with temperature, which is expected from the increased gasification rate.

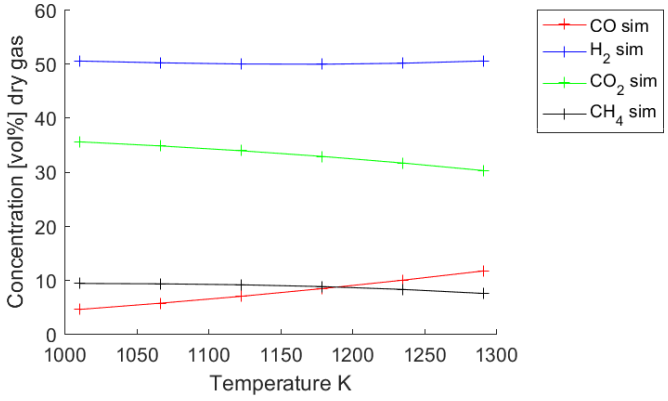

Figure 4-32: Effect of temperature on the gas composition

Figure 4-32 shows the change of gas composition as a consequence of the shift of equilibrium of the water gas shift reaction. The trend of the gas composition is similar to what is reported in the literature [2].

4.3.5.5 Effect of gas circulation

Gas circulation is investigated in a way different from the others as the steam to biomass condition is also reduced as the recirculation is increased. This is done to avoid a high increase in the gas flow through the fluidised bed.

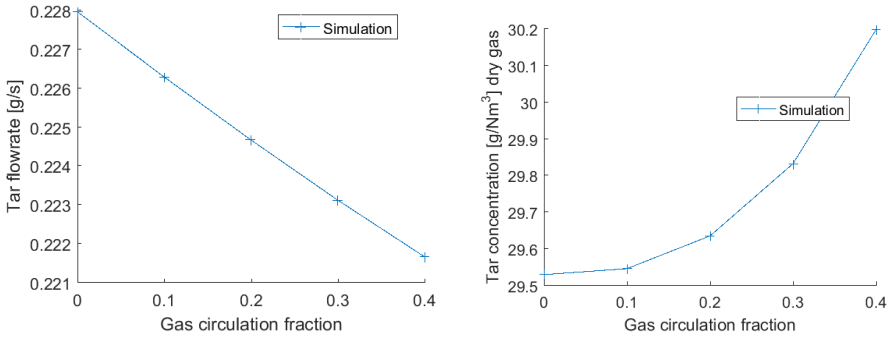

Figure 4-33: Effect of gas recirculation on tar concentration and throughput

The recycled tar-filed gas enters the bubbling bed at the bottom of the reactor along with the gas for gasification. This means that the recycled tar is introduced to the bubble gas phase. The effective contact time between catalyst and tar is thus increased. The effect of recirculation is low as shown in Figure 4-33. This is attributed to the low free catalyst available to convert the tar.

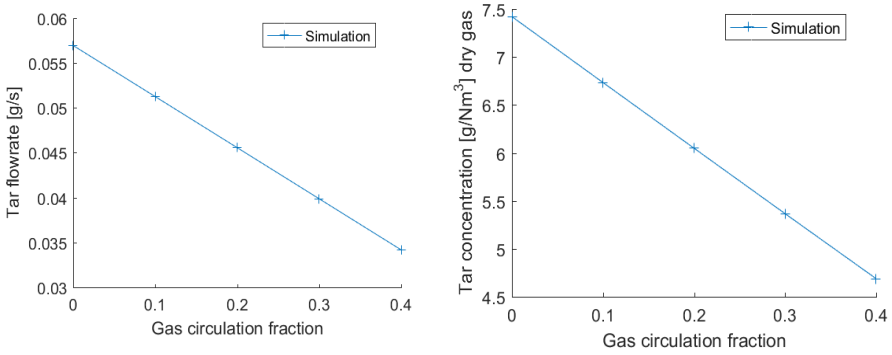

Figure 4-34: Effect of gas recirculation on tar concentration and throughput

Figure 4-34 shows a simulation with an excess catalyst for the coking of tar, which shows a clear linear relation with recirculation.

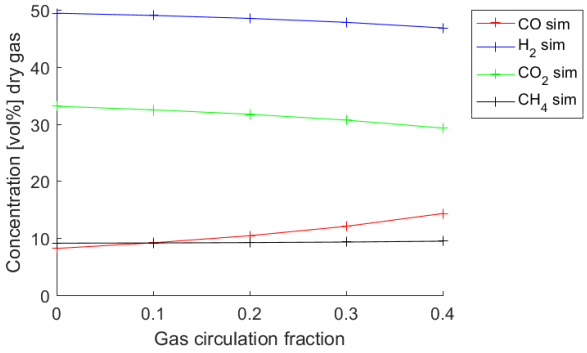

Figure 4-35: Effect of gas recirculation on tar concentration and throughput

The change of gas composition is due to the lower amount of water in the inlet stream as the steam-to-biomass ratio is lowered to take into account the recirculation of gas. This shifts the water gas reaction (R 2-9) towards water formation.

4.3.5.6 Effect of bubble size

The effective bubble size is a parameter change that may be affected by several factors, like the bed material particle size, installations of baffles, and the gasification velocity. The parameter is varied by ±50% of the base case.

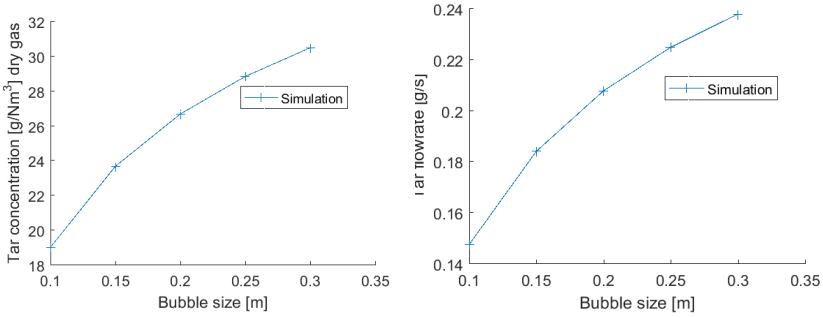

Figure 4-36: Effect of bubble size on the tar concentration and throughput

Figure 4-36 shows a reduction in tar as bubble diameter is decreased. The ratio between the tar-free bubble and the wake stays the same as the bubble size is decreased. Thus, the primary reason for tar reduction will be from the increased residence time by a slower rising bubble and increased surface area for mass transport to the emulsion.

4.3.5.7 Effect of feeding height

The feeding is a design parameter for the reactor. With the fluidised bed being 0.5m, the feeding position is varied almost over the entire bed height.

Figure 4-37 shows that tar formation is predicted to be increased as the feeding position is increased. This is expected as the biomass is closer to the outlet to the combustor if fed at the bottom of the gasifier.

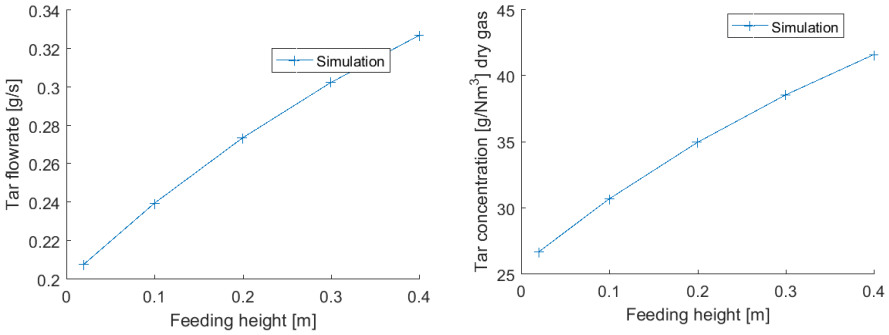

Figure 4-37: Effect of feeding position on the tar concentration and throughput

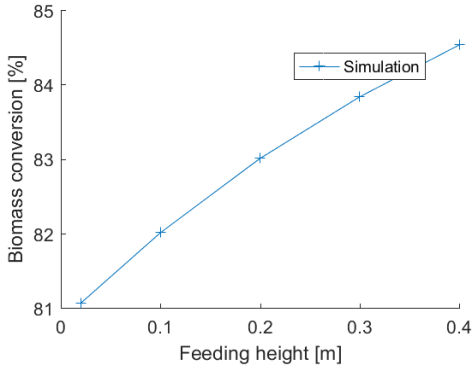

Figure 4-38: Effect of feeding position on the biomass conversion

Figure 4-38 shows an increase in biomass conversion with feeding position. This may be because of the increased residence time of biomass as it is fed to the reactor further from the out-take to the combustor.

5 RECOMMENDATIONS AND FUTURE FOCUS

Some recommendations can be made based on the modelling and the experiment. Extrapolation of model results should always be done with caution. The models used here are specific to the steam gasification environment and dual fluidised beds where reversal of the gas flow in the emulsion is occurring. The model result also largely depends on the kinetics of the lignin devolatilisation and the assumption of the biomass distribution. Thus, the recommendation will be limited in that they are based on the special cases shown in the thesis.

5.1 PRE-TORREFACTION CONCEPT

The torrefaction experiment revealed that a large part of the tar formed from the biomass is already released at low temperatures, around 200°C. However, the torrefaction in itself does not influence the yield of problematic tar from lignin during gasification. The composition of tar still remains phenolic derivatives which will be problematic.

Because a large part of the tar from lignin is released during the torrefaction, one way of achieving a reduction of the tar formation may be by discarding the gas formation from the torrefaction before gasification. However, this would come at the cost of a significant loss in fuel.

To utilise the early release of tar from biomass, it will have to be separated from the biomass and used as a fuel for the combustion, where tar is not a problem. In this way the energy from the torrefaction gas is still utilised. The low temperature needed for the release of tar means that low-temperature excess gas may be used for the torrefaction process to utilise the heating value of the biomass fully.

Separated tar released during torrefaction may also be condensed and used for the co-production of valuable chemical species. Light gas can then still be used sent for gasification or combustion.

5.2 VALIDATION OF THE ASSUMPTION IS NEEDED

The reactor model shows the promising possibilities of utilising catalyst to form coke as an alternative to removing tar from the gasifier. The model, however, still has assumptions that will have to be true for the method to work. The model assumes that it is possible to shift the adsorption isotherm to increase the reaction rate to form coke. Furthermore, the model assumes that catalyst is only deactivated by coke and that coke will be combusted completely in the time it resides in the combustor. It is crucial to validate the degree to which these assumptions are true before a finite recommendation of this process can be given.

5.3 RECIRCULATION IN COMBINATION WITH CATALYST

Recirculation has shown two different trends with regards to the conversion of naphthalene. Naphthalene is a very problematic tar and should be avoided. The gas phase model showed that recirculation increased the concentration of naphthalene contrary to the reactor model that showed a decrease of naphthalene when sufficient catalyst is available. This means that recirculation should only be used if the gasification is done together with a catalytic conversion. The thermal treatment is simply not sufficient to reform naphthalene, and thus naphthalene is accumulated by recirculation.

6 CONCLUSION

The thesis is focused on the tar formation from biomass gasification in dual fluidised beds. The problematic source for tar in gasification is originating from lignin. Lignin forms a primary tar of phenolic derivatives.

The primary reaction of tar formation has been investigated, showing that during gasification the primary tar is expected to undergo hydrogen abstraction and donation that leads to the formation of phenol. Phenol is, in turn, the leading precursor to the formation of naphthalene. Phenol degrades to cyclopentadienyl through unimolecular degradation and cyclopentadienyl is degraded to light gases and naphthalene. Because of the unimolecular degradation of phenol, the process is hard to manipulate.

The gas-phase model shows that degradation of cyclopentadienyl can be manipulated to a small degree to form methylcyclopentadiene and light gases in order to diminish the naphthalene. Introduction of CH_4 and H_2 into the feeding gas will reduce the naphthalene concentration.

The product gas from the gasification contains CH_4 and H_2 and thus recirculation of this was simulated. It showed that naphthalene formation greatly increased with recirculation of the product gas. Simulation, however, shows a reduction of naphthalene with an increase in pressure when exceeding pressures of 10 bars. As expected, the gas-phase model shows that temperature has a considerable effect on the tar formation when exceeding 1000°C.

Contrary to the gas-phase model, the fluidised bed model with a catalyst for coke formation shows a reduction of tar with recirculation when sufficient catalyst is available. Furthermore, it showed that, to maximise the tar conversion, the bubble size will have to keep the small, catalyst fraction high, and the feeding position should be at the bottom of the bed. For systems where tar removal is dominated by coking, a temperature increase may increase the tar throughput because of decreased residence time in the fluidised bed.

The reactor model uses an assumption of instant devolatilisation of hemicellulose and cellulose. This assumption may, however, not be that appropriate according to the particle model. The use of relatively large biomass particles of a couple of millimetres in fluidised beds will take several seconds to devolatilise, which would be sufficient for considerable movement in the fluidised bed. This means that the devolatilisation will take place over the entire reactor, and the steep concentration curve will not be observed.

Torrefaction experiments of lignin showed that torrefaction was, to some degree, able to shift the composition of the primary tar released from lignin. But as the phenolic group was not removed by torrefaction, it changes little for the tar evolution in the gasification. The experiment, however, also showed that a large part of the tar from pulp lignin is released at relatively low temperatures ($T<300°C$). This may be used to separate a large part of the tar before pyrolysis for either combustion in the combustor or co-production of Vanillin.

7 REFERENCES

[1] C. Di Blasi, "Combustion and gasification rates of lignocellulosic chars," *Prog. Energy Combust. Sci.*, vol. 35, no. 2, pp. 121–140, Apr. 2009.

[2] C. Higman and M. Van Der Burgt, *Gasification*. Gulf Professional Publishing, 2007.

[3] P. Basu, *Biomass Gasification, Pyrolysis, and Torrefaction*. Academic Press, 2013.

[4] M. Mayerhofer, P. Mitsakis, X. Meng, W. de Jong, H. Spliethoff, and M. Gaderer, "Influence of pressure, temperature and steam on tar and gas in allothermal fluidized bed gasification," *Fuel*, vol. 99, pp. 204–209, Sep. 2012.

[5] S. Valin, S. Ravel, J. Guillaudeau, and S. Thiery, "Comprehensive study of the influence of total pressure on products yields in fluidized bed gasification of wood sawdust," *Fuel Process. Technol.*, vol. 91, no. 10, pp. 1222–1228, Oct. 2010.

[6] S. Kern, C. Pfeifer, and H. Hofbauer, "Gasification of wood in a dual fluidized bed gasifier: Influence of fuel feeding on process performance," *Chem. Eng. Sci.*, vol. 90, pp. 284–298, Mar. 2013.

[7] P. Mitsakis, M. Mayerhofer, X. Meng, H. Spliethoff, and M. Gaderer, "Optical measurement of tars in a fluidized bed gasifier: influence of fuel type and gasification parameters on their formation," *Biomass Convers. Biorefinery*, vol. 3, no. 2, pp. 157–167, Feb. 2013.

[8] I. Olofsson, A. Nordin, and U. Söderlind, "Initial Review and Evaluation of Process Technologies and Systems Suitable for Cost-Efficient Medium-Scale Gasification for Biomass to Liquid Fuels," Umeå, 2005.

[9] W. H. Chen, H. C. Hsu, K. M. Lu, W. J. Lee, and T. C. Lin, "Thermal pretreatment of wood (Lauan) block by torrefaction and its influence on the properties of the biomass," *Energy*, vol. 36, no. 5, pp. 3012–3021, 2011.

[10] P. C. a Bergman, a R. Boersma, R. W. R. Zwart, and J. H. a Kiel, "Torrefaction for biomass co-firing in existing coal-fired power stations," *Energy Res. Cent. Netherlands ECN ECNC05013*, no. July, p. 71, 2005.

[11] J. Corella, J. M. Toledo, and G. Molina, "A Review on Dual Fluidized-Bed Biomass Gasifiers," *Ind. Eng. Chem. Res.*, vol. 46, pp. 6831–6839, 2007.

[12] C. Pfeifer, S. Koppatz, and H. Hofbauer, "Steam gasification of various feedstocks at a dual fluidised bed gasifier: Impacts of operation conditions and bed materials," *Biomass Convers. Biorefinery*, vol. 1, no. 1, pp. 39–53, Feb. 2011.

[13] V. Wilk, J. C. Schmid, and H. Hofbauer, "Influence of fuel feeding positions on gasification in dual fluidized bed gasifiers," *Biomass and Bioenergy*, vol. 54, pp. 46–58, Jul. 2013.

[14] D. Kunii and O. Levenspiel, *Fluidization engineering*, Second edi. Butterworth-Heinemann, 1991.

[15] F. A. Zenz and D. F. Othmer, *Fluidization and fluid-particle systems*. Reinhold Pubblishing Corporation, 1960.

[16] J. F. Davidson and D. Harrison, *fluidised particles*. Cambridge University Press, 1963.

[17] UNFCCC, “Biomass definition,” 2013. [Online]. Available: http://cdm.unfccc.int/EB/020/eb20repan08.pdf.

[18] S. D. Ekşioğlu, A. Acharya, L. E. Leightley, and S. Arora, “Analyzing the design and management of biomass-to-biorefinery supply chain,” *Comput. Ind. Eng.*, vol. 57, no. 4, pp. 1342–1352, 2009.

[19] A. A. Rentizelas, A. J. Tolis, and I. P. Tatsiopoulos, “Logistics issues of biomass: The storage problem and the multi-biomass supply chain,” *Renew. Sustain. Energy Rev.*, vol. 13, no. 4, pp. 887–894, 2009.

[20] P. McKendry, “Energy production from biomass (part 1): overview of biomass,” *Bioresour. Technol*, vol. 83, no. 1, pp. 37–46, 2002.

[21] B. R. Hames, “Biomass Compositional Analysis for Energy Applications,” *Methods Mol. Biol.*, vol. 581, pp. 145–167, 2009.

[22] E. Butler, G. Devlin, D. Meier, and K. McDonnell, “Characterisation of spruce, salix, miscanthus and wheat straw for pyrolysis applications.,” *Bioresour. Technol.*, vol. 131, pp. 202–9, Mar. 2013.

[23] D.-A. Z. Wever, H. J. Heeres, and A. a. Broekhuis, “Characterization of Physic nut (Jatropha curcas L.) shells,” *Biomass and Bioenergy*, vol. 37, pp. 177–187, Feb. 2012.

[24] A. L. Brown, B. R. Hames, J. W. Daily, and D. C. Dayton, “Chemical Analysis of Solids and Pyrolytic Vapors from Wildland Trees,” *ENERGY and FUELS*, vol. 17, no. 4, pp. 1022–1027, 2003.

[25] H. Mansilla, R. Garcia, J. Tapia, H. Durán, and S. Urzúa, “Chemical characterization of Chilean hardwoods,” *WOOD Sci. Technol.*, vol. 25, no. 2, pp. 145–149, 1991.

[26] G. Lövestam, E. Johansson, S. Johansson, and J. Pallon, “ELEMENTAL MICROPATTERNS IN TREE RINGS - A FEASIBILITY STUDY USING SCANNING PROTON MICROPROBE ANALYSIS,” *Ambio*, vol. 19, no. 2, pp. 87–93, 1990.

[27] E. Sjöström, *Wood chemistry Fundamentals and applications*. Academic press inc., 1993.

[28] M. Lewin and I. S. Goldstein, *Wood structure and composition*. Marcel dekker inc., 1991.

[29] T. Wüstenberg, “3 Cellulose,” in *Cellulose and Cellulose Derivatives in the Food Industry: Fundamentals and Applications*, 2015, pp. 91–142.

[30] T. Fisher, M. Hajaligol, B. Waymack, and D. Kellogg, “Pyrolysis behavior and kinetics of biomass derived materials,” *J. Anal. Appl. Pyrolysis*, vol. 62, no. 2, pp. 331–349, 2002.

[31] A. Ebringerova, Z. Hromadkova, and T. Heinze, “Hemicellulose,” *Adv. Polym. Sci.*, vol. 186, no. August, pp. 1–67, 2005.

[32] D. K. Shen, S. Gu, and A. V. Bridgwater, “Study on the pyrolytic behaviour of xylan-based hemicellulose using TG-FTIR and Py-GC-FTIR,” *J. Anal. Appl. Pyrolysis*, vol. 87, no. 2, pp. 199–206, 2010.

[33] H. Hatakeyama and T. Hatakeyama, “Lignin Structure , Properties , and Applications,” *Biopolym. Lignin, Proteins, Bioact. Nanocomposites*, vol. 232, no. 1, pp. 1–63, 2009.

[34] T. Faravelli, A. Frassoldati, G. Migliavacca, and E. Ranzi, “Detailed kinetic modeling of the

thermal degradation of lignins," *Biomass and Bioenergy*, vol. 34, no. 3, pp. 290–301, Mar. 2010.

[35] C. F. Palma, "Modelling of tar formation and evolution for biomass gasification: A review," *Appl. Energy*, vol. 111, pp. 129–141, Nov. 2013.

[36] M. Y. Balakshin, E. Augsten, and H. Capanema, Ewellyn Augsten Chang, "Recent Advances in the Isolation and Analysis of Lignins and Lignin – Carbohydrate Complexes," *Charact. Lignocellul. Mater.*, pp. 148–170, 2009.

[37] R. K. Sharma, J. B. Wooten, V. L. Baliga, X. Lin, W. Geoffrey Chan, and M. R. Hajaligol, "Characterization of chars from pyrolysis of lignin," *Fuel*, vol. 83, no. 11–12, pp. 1469–1482, Aug. 2004.

[38] R. J. Evans, T. A. Milne, and M. N. Soltys, "DIRECT MASS-SPECTROMETRIC STUDIES OF THE PYROLYSIS OF CARBONACEOUS FUELS," *J. Anal. Appl. Pyrolysis*, vol. 9, pp. 207–236, 1986.

[39] A. Pyrolysis, E. S. P. B. V, and F. Products, "studies on isolated lignins and lignins in woody materials by pyrolysis-gas chromatography-mass spectrometry and off-line pyrolysis-gas chromatography with flame inoization detection," *J. Anal. Appl. Pyrolysis*, vol. 11, pp. 403–416, 1987.

[40] M. P. Pandey and C. S. Kim, "Lignin Depolymerization and Conversion: A Review of Thermochemical Methods," *Chem. Eng. Technol.*, vol. 34, no. 1, pp. 29–41, Jan. 2011.

[41] R. J. Evans and T. A. Milne, "Molecular characterization of the pyrolysis of biomass. Fundamentals," *Energy & Fuels*, vol. 1, no. 2, pp. 123–137, 1987.

[42] S. Wang, B. Ru, H. Lin, W. Sun, and Z. Luo, "Pyrolysis behaviors of four lignin polymers isolated from the same pine wood," *Bioresour. Technol.*, vol. 182, pp. 120–127, 2015.

[43] M. Kleen and G. Gellerstedt, "Characterization by pyrolysis-gas of chemical and mechanical pulps chromatography / mass spectrometry," *J. Anal. Appl. Pyrolysis*, vol. 19, pp. 139–152, 1991.

[44] R. J. Evans, T. A. Milne, and M. N. Soltys, "DIRECT MASS-SPECTROMETRIC STUDIES OF THE PYROLYSIS OF CARBONACEOUS FUELS III PRIMARY PYROLYSIS OF LIGNIN," *J. Anal. Appl. Pyrolysis*, vol. 9, pp. 207–236, 1986.

[45] R. El Hage, N. Brosse, P. Sannigrahi, and A. Ragauskas, "Effects of process severity on the chemical structure of Miscanthus ethanol organosolv lignin," *Polym. Degrad. Stab.*, vol. 95, no. 6, pp. 997–1003, 2010.

[46] T. Hosoya, H. Kawamoto, and S. Saka, "Influence of inorganic matter on wood pyrolysis at gasification temperature," *J. Wood Sci.*, vol. 53, no. 4, pp. 351–357, Feb. 2007.

[47] K. Raveendran, A. Ganesh, and K. C. Khilart, "Influence of minaral matter on biomass pyrolysis characteistics," *Fuel*, vol. 74, no. 12, pp. 1812–1822, 1995.

[48] M. Nik-Azat, M. R. Hajaligol, M. Sohrabi, and B. Dabir, "Mineral matter effects in rapid pyrolysis of beech wood," *Fuel Process. Technol.*, pp. 7–17, 1997.

[49] W. F. DeGroot and F. Shafizadeh, "THE INFLUENCE OF EXCHANGEABLE CATIONS ON THE CARBONIZATION OF BIOMASS," *J. Anal. Appl. Pyrolysis*, pp. 217–232, 1984.

[50] R. Parthasarathi, R. a. Romero, A. Redondo, and S. Gnanakaran, “Theoretical Study of the Remarkably Diverse Linkages in Lignin,” *J. Phys. Chem. Lett.*, vol. 2, no. 20, pp. 2660–2666, Oct. 2011.

[51] S. Kim, S. C. Chmely, M. R. Nimlos, Y. J. Bomble, T. D. Foust, R. S. Paton, and G. T. Beckham, “Computational Study of Bond Dissociation Enthalpies for a Large Range of Native and Modified Lignins,” *J. Phys. Chem. Lett.*, vol. 2, no. 22, pp. 2846–2852, Nov. 2011.

[52] K. Raveendran, A. Ganesh, and K. C. Khilar, “Pyrolysis characteristics of biomass and biomass components,” *Fuel*, vol. 75, no. 8, pp. 987–998, 1996.

[53] J. Park, J. Meng, K. H. Lim, O. J. Rojas, and S. Park, “Transformation of lignocellulosic biomass during torrefaction,” *J. Anal. Appl. Pyrolysis*, vol. 100, pp. 199–206, Mar. 2013.

[54] S. Wang, G. Dai, B. Ru, Y. Zhao, X. Wang, J. Zhou, Z. Luo, and K. Cen, “Effects of torrefaction on hemicellulose structural characteristics and pyrolysis behaviors,” *Bioresour. Technol.*, vol. 218, pp. 1106–1114, 2016.

[55] D. K. Shen, S. Gu, K. H. Luo, S. R. Wang, and M. X. Fang, “The pyrolytic degradation of wood-derived lignin from pulping process.,” *Bioresour. Technol.*, vol. 101, no. 15, pp. 6136–46, Aug. 2010.

[56] H. Zhou, Y. Long, A. Meng, S. Chen, Q. Li, and Y. Zhang, “A novel method for kinetics analysis of pyrolysis of hemicellulose, cellulose, and lignin in TGA and macro-TGA,” *RSC Adv.*, vol. 5, pp. 26509–26516, 2015.

[57] H. Yang, R. Yan, H. Chen, D. H. Lee, and C. Zheng, “Characteristics of hemicellulose, cellulose and lignin pyrolysis,” *Fuel*, vol. 86, no. 12–13, pp. 1781–1788, Aug. 2007.

[58] I. Milosavljevic, V. Oja, and E. M. Suuberg, “Thermal Effects in Cellulose Pyrolysis: Relationship to Char Formation Processes,” *Ind. Eng. Chem. Res.*, vol. 35, no. 3, pp. 653–662, 1996.

[59] T. Hosoya, H. Kawamoto, and S. Saka, “Pyrolysis behaviors of wood and its constituent polymers at gasification temperature,” *J. Anal. Appl. Pyrolysis*, vol. 78, no. 2, pp. 328–336, 2007.

[60] K. Werner, L. Pommer, and M. Broström, “Thermal decomposition of hemicelluloses,” *J. Anal. Appl. Pyrolysis*, vol. 110, pp. 130–137, 2014.

[61] W. H. Chen and P. C. Kuo, “Torrefaction and co-torrefaction characterization of hemicellulose, cellulose and lignin as well as torrefaction of some basic constituents in biomass,” *Energy*, vol. 36, no. 2, pp. 803–811, 2011.

[62] N. Shimada, H. Kawamoto, and S. Saka, “Different action of alkali/alkaline earth metal chlorides on cellulose pyrolysis,” *J. Anal. Appl. Pyrolysis*, vol. 81, no. 1, pp. 80–87, Jan. 2008.

[63] Y. Sekiguchi, J. S. Frye, and F. Shafizadeh, “Structure and formation of cellulosic chars,” *J. Appl. Polym. Sci.*, vol. 28, no. 11, pp. 3513–3525, Nov. 1983.

[64] Y. Chen, H. Yang, Q. Yang, H. Hao, B. Zhu, and H. Chen, “Torrefaction of agriculture straws and its application on biomass pyrolysis poly-generation,” *Bioresour. Technol.*, vol. 156, pp. 70–77, 2014.

[65] S. Zhou, B. Pecha, M. van Kuppevelt, A. G. McDonald, and M. Garcia-Perez, “Slow and

fast pyrolysis of Douglas-fir lignin: Importance of liquid-intermediate formation on the distribution of products," *Biomass and Bioenergy*, vol. 66, pp. 398–409, 2014.

[66] E. Jakab, O. Faix, and F. Till, "Thermal decomposition of milled wood lignins studied by thermogravimetry/mass spectrometry," *J. Anal. Appl. Pyrolysis*, vol. 40, pp. 171–186, 1997.

[67] T. A. Milne, R. J. Evans, and N. Abatzoglou, "Biomass Gasifier ' Tars ': Their Nature, Formation, and Conversion," 1998.

[68] H. Spliethoff, *Power Generation from Solid Fuels*. .

[69] R. Coll, J. Salvadó, X. Farriol, and D. Montané, "Steam reforming model compounds of biomass gasification tars: Conversion at different operating conditions and tendency towards coke formation," *Fuel Process. Technol.*, vol. 74, no. 1, pp. 19–31, 2001.

[70] S. Anis and Z. a. A. Zainal, "Tar reduction in biomass producer gas via mechanical, catalytic and thermal methods: A review," *Renew. Sustain. Energy Rev.*, vol. 15, no. 5, pp. 2355–2377, Jun. 2011.

[71] ECN, "Tar compound names and structures," 2014. [Online]. Available: http://www.thersites.nl/structures.aspx.

[72] T. Hosoya, H. Kawamoto, and S. Saka, "Cellulose–hemicellulose and cellulose–lignin interactions in wood pyrolysis at gasification temperature," *J. Anal. Appl. Pyrolysis*, vol. 80, no. 1, pp. 118–125, Aug. 2007.

[73] T. Hosoya, H. Kawamoto, and S. Saka, "Pyrolysis gasification reactivities of primary tar and char fractions from cellulose and lignin as studied with a closed ampoule reactor," *J. Anal. Appl. Pyrolysis*, vol. 83, no. 1, pp. 71–77, Sep. 2008.

[74] H. Stiles and R. Kandiyoti, "Secondary reactions of flash pyrolysis tars measured in a fluidized bed pyrolysis reactor with some novel design features," *Fuel*, vol. 68, no. 3, pp. 275–282, 1989.

[75] S. Wu, H. Yang, J. Hu, D. Shen, H. Zhang, and R. Xiao, "Pyrolysis of furan and its derivatives at 1100°C: PAH products and DFT study," *J. Anal. Appl. Pyrolysis*, vol. 120, pp. 252–257, 2016.

[76] C. Amen-Chen, H. Pakdel, and C. Roy, "Production of monomeric phenols by thermochemical conversion of biomass: a review.," *Bioresour. Technol.*, vol. 79, no. 3, pp. 277–99, Sep. 2001.

[77] F. X. Collard and J. Blin, "A review on pyrolysis of biomass constituents: Mechanisms and composition of the products obtained from the conversion of cellulose, hemicelluloses and lignin," *Renewable and Sustainable Energy Reviews*, vol. 38. Elsevier, pp. 594–608, 2014.

[78] M. Adam, R. Ocone, J. Mohammad, F. Berruti, and C. Briens, "Kinetic Investigations of Kraft Lignin Pyrolysis," *Ind. Eng. Chem. Res.*, vol. 52, no. 26, pp. 8645–8654, Jul. 2013.

[79] C. Fushimi, K. Araki, Y. Yamaguchi, and A. Tsutsumi, "Effect of Heating Rate on Steam Gasification of Biomass. 2. Thermogravimetric-Mass Spectrometric (TG-MS) Analysis of Gas Evolution," *Ind. Eng. Chem. Res.*, vol. 42, no. 17, pp. 3929–3936, Aug. 2003.

[80] S. Zhou, S. Liaw, and M. Garcia-perez, "Py-GC/MS Studies to Evaluate the Effect of

Torrefaction Temperature on Pyrolysis Products of Douglas Fir and Hybrid Poplar Wood," *Am. Soc. Agric. Biol. Eng.*, vol. 57, no. 6, pp. 1751–1759, 2014.

[81] M. Nowakowska, O. Herbinet, A. Dufour, and P.-A. Glaude, "Detailed kinetic study of anisole pyrolysis and oxidation to understand tar formation during biomass combustion and gasification," *Combust. Flame*, vol. 161, no. 6, pp. 1474–1488, 2014.

[82] S. Chu, A. V. Subrahmanyam, and G. W. Huber, "The pyrolysis chemistry of a β-O-4 type oligomeric lignin model compound," *Green Chemistry*, vol. 15, no. 1. p. 125, 2012.

[83] W. Fiddler, W. E. Parker, a E. Wasserman, and R. C. Doerr, "Thermal decomposition of ferulic acid," *J. Agric. Food Chem.*, vol. 15, no. 5, pp. 757–761, 1967.

[84] P. Hemberger, G. da Silva, A. J. Trevitt, T. Gerber, and A. Bodi, "Are the three hydroxyphenyl radical isomers created equal? – The role of the phenoxy radical –," *Phys. Chem. Chem. Phys.*, vol. 17, no. 44, pp. 30076–30083, 2015.

[85] A. M. Scheer, C. Mukarakate, D. J. Robichaud, M. R. Nimlos, H.-H. Carstensen, and G. B. Ellison, "Unimolecular thermal decomposition of phenol and d5-phenol: direct observation of cyclopentadiene formation via cyclohexadienone.," *J. Chem. Phys.*, vol. 136, no. 4, p. 44309, 2012.

[86] D. J. Robichaud, A. M. Scheer, C. Mukarakate, T. K. Ormond, G. T. Buckingham, G. B. Ellison, and M. R. Nimlos, "Unimolecular thermal decomposition of dimethoxybenzenes.," *J. Chem. Phys.*, vol. 140, no. 23, p. 234302, 2014.

[87] S. Lomnicki, H. Truong, and B. Dellinger, "Mechanisms of product formation from the pyrolytic thermal degradation of catechol," *Chemosphere*, vol. 73, no. 4, pp. 629–633, 2008.

[88] T. K. Ormond, A. M. Scheer, M. R. Nimlos, D. J. Robichaud, T. P. Troy, M. Ahmed, J. W. Daily, T. L. Nguyen, J. F. Stanton, and G. B. Ellison, "Pyrolysis of Cyclopentadienone: Mechanistic Insights from a Direct Measurement of Product Branching Ratios," *J. Phys. Chem. A*, p. 150217151436007, 2015.

[89] C. Liu, Y. Zhang, and X. Huang, "Study of guaiacol pyrolysis mechanism based on density function theory," *Fuel Process. Technol.*, vol. 123, pp. 159–165, Jul. 2014.

[90] J. Huang, X. Li, D. Wu, H. Tong, and W. Li, "Theoretical studies on pyrolysis mechanism of guaiacol as lignin model compound," *J. Renew. Sustain. Energy*, vol. 5, no. 4, 2013.

[91] H.-M. Yang, S. Appari, S. Kudo, J. Hayashi, and K. Norinaga, "Detailed Chemical Kinetic Modeling of Vapor-Phase Reactions of Volatiles Derived from Fast Pyrolysis of Lignin," *Ind. Eng. Chem. Res.*, vol. 54, no. 27, pp. 6855–6864, 2015.

[92] W. He, Q. Liu, L. Shi, Z. Liu, D. Ci, C. Lievens, X. Guo, and M. Liu, "Understanding the stability of pyrolysis tars from biomass in a view point of free radicals.," *Bioresour. Technol.*, vol. 156, pp. 372–5, Mar. 2014.

[93] P. Morf, P. Hasler, and T. Nussbaumer, "Mechanisms and kinetics of homogeneous secondary reactions of tar from continuous pyrolysis of wood chips," *Fuel*, vol. 81, no. 7, pp. 843–853, May 2002.

[94] M. Pecullan, K. Brezinsky, and I. Glassman, "Pyrolysis and Oxidation of Anisole near 1000 K," *J. Phys. Chem. A*, vol. 101, no. 96, pp. 3305–3316, 1997.

[95] J. Emdee, K. Brezinsky, and I. Glassman, “A kinetic model for the oxidation of toluene near 1200 K,” *J. Phys. …*, vol. 96, no. 15, pp. 2151–2161, 1992.

[96] I. W. C. E. Arends, R. Louw, and P. Mulder, “Kinetic Study of the Thermolysis of Anisole in a Hydrogen Atmosphere,” *J. Phys. Chem.*, no. 5, pp. 7914–7925, 1993.

[97] K. Roy, C. Horn, P. Frank, V. G. Slutsky, and T. Just, “High-temperature investigations on the pyrolysis of cyclopentadiene,” *27th Int. Symp. Combust.*, vol. 1, pp. 329–336, 1998.

[98] X. Zhong and J. W. Bozzelli, “Thermochemical and kinetic analysis on the addition reactions of H, O, OH, and HO2 with 1,3 cyclopentadiene,” *Int. J. Chem. Kinet.*, vol. 29, pp. 893–913, 1997.

[99] J. Manion and R. Louw, “Rates, products, and mechanisms in the gas-phase hydrogenolysis of phenol between 922 and 1175 K,” *J. Phys. Chem.*, pp. 3563–3574, 1989.

[100] E. Ikeda, R. S. Tranter, J. H. Kiefer, R. D. Kern, H. J. Singh, and Q. Zhang, “The pyrolysis of methylcyclopentadiene: Isomerization and formation of aromatics,” *Proc. Combust. Inst.*, vol. 28, no. 2, pp. 1725–1732, 2000.

[101] G. B. Bacskay and J. C. Mackie, “The pyrolysis of cyclopentadiene: quantum chemical and kinetic modelling studies of the acetylene plus propyne/allene decomposition channels,” *Phys. Chem. Chem. Phys.*, vol. 3, no. 12, pp. 2467–2473, 2001.

[102] N. R. Hore and D. K. Russell, “The thermal decomposition of 5-membered rings: a laser pyrolysis study,” *New J. Chem.*, vol. 28, no. 5, pp. 606–613, 2004.

[103] R. G. Butler and I. Glassman, “Cyclopentadiene combustion in a plug flow reactor near 1150 K,” *Proc. Combust. Inst.*, vol. 32, no. 1, pp. 395–402, 2009.

[104] R. K. Robinson and R. P. Lindstedt, “On the chemical kinetics of cyclopentadiene oxidation,” *Combust. Flame*, vol. 158, no. 4, pp. 666–686, 2011.

[105] S. Thomas, E. B. Ledesma, and M. J. Wornat, “The effects of oxygen on the yields of the thermal decomposition products of catechol under pyrolysis and fuel-rich oxidation conditions,” *Fuel*, vol. 86, no. 16, pp. 2581–2595, 2007.

[106] C. F. Palma, “Model for Biomass Gasification Including Tar Formation and Evolution,” *Energy & Fuels*, vol. 27, pp. 2693–2702, Nov. 2013.

[107] O. Faix, E. Jakab, F. Till, and T. Székely, “Study on low mass thermal degradation products of milled wood lignins by thermogravimetry-mass-spectrometry,” *Wood Sci. Technol.*, vol. 22, pp. 323–334, 1988.

[108] R. K. Sharma and M. R. Hajaligol, “Effect of pyrolysis conditions on the formation of polycyclic aromatic hydrocarbons (PAHs) from polyphenolic compounds,” *J. Anal. Appl. Pyrolysis*, vol. 66, no. 1–2, pp. 123–144, Jan. 2003.

[109] A. Jess, “Mechanisms and kinetics of thermal reactions of aromatic hydrocarbons from pyrolysis of solid fuels,” *Fuel*, vol. 75, no. 12, pp. 1441–1448, 1996.

[110] Y. Z. He, W. G. Mallard, and W. Tsang, “Kinetics of Hydrogen and Hydroxyl Radical Attack on Phenol at Hight Temperatures,” *J. Phys. Chem.*, vol. 92, no. 8, pp. 2196–2201, 1988.

[111] P. A. Simell, J. O. Hepola, and A. O. I. Krause, “Effects of gasification gas components on tar and ammonia decomposition over hot gas cleanup catalyst,” *FUEL*, vol. 76, no. 12, pp.

1117–1127, 1997.

[112] X. Meng, W. de Jong, N. Fu, and A. H. M. Verkooijen, “Biomass gasification in a 100 kWth steam-oxygen blown circulating fluidized bed gasifier: Effects of operational conditions on product gas distribution and tar formation,” *Biomass and Bioenergy*, vol. 35, no. 7, pp. 2910–2924, Jul. 2011.

[113] Y.-H. Qin, J. Feng, and W.-Y. Li, “Formation of tar and its characterization during air–steam gasification of sawdust in a fluidized bed reactor,” *Fuel*, vol. 89, no. 7, pp. 1344–1347, Jul. 2010.

[114] C. M. Huelsman and P. E. Savage, “Intermediates and kinetics for phenol gasification in supercritical water,” *Phys. Chem. Chem. Phys.*, vol. 14, no. 8, p. 2900, 2012.

[115] C. M. Huelsman and P. E. Savage, “Reaction pathways and kinetic modeling for phenol gasification in supercritical water,” *J. Supercrit. Fluids*, vol. 81, pp. 200–209, 2013.

[116] S. Koppatz, C. Pfeifer, and H. Hofbauer, “Comparison of the performance behaviour of silica sand and olivine in a dual fluidised bed reactor system for steam gasification of biomass at pilot plant scale,” *Chem. Eng. J.*, vol. 175, pp. 468–483, Nov. 2011.

[117] L. Devi, K. J. Ptasinski, and F. J. J. G. Janssen, “A review of the primary measures for tar elimination in biomass gasification processes,” *Biomass and bioenergy*, vol. 24, pp. 125–140, 2003.

[118] C. Pfeifer, S. Koppatz, and H. Hofbauer, “Catalysts for dual fluidised bed biomass gasification—an experimental study at the pilot plant scale,” *Biomass Convers. Biorefinery*, vol. 1, no. 2, pp. 63–74, Feb. 2011.

[119] C. Pfeifer, R. Rauch, and H. Hofbauer, “In-Bed Catalytic Tar Reduction in a Dual Fluidized Bed Biomass Steam Gasifier,” *Ind. Eng. Chem. Res.*, vol. 43, no. 7, pp. 1634–1640, Mar. 2004.

[120] B. Dou, J. Gao, X. Sha, and S. W. Baek, “Catalytic cracking of tar component from high-temperature fuel gas,” *Appl. Therm. Eng.*, vol. 23, no. 17, pp. 2229–2239, Dec. 2003.

[121] A. Dassey, B. Mukherjee, R. Sheffield, and C. Theegala, “Catalytic cracking of tars from biomass gasification,” *Biomass Convers. Biorefinery*, vol. 3, no. 2, pp. 69–77, Nov. 2012.

[122] D. Sutton, B. Kelleher, and J. R. H. Ross, “Review of literature on catalysts for biomass gasification,” *Fuel Process. Technol.*, vol. 73, no. 3, pp. 155–173, 2001.

[123] M. Virginie, J. Adánez, C. Courson, L. F. de Diego, F. García-Labiano, D. Niznansky, A. Kiennemann, P. Gayán, and A. Abad, “Effect of Fe–olivine on the tar content during biomass gasification in a dual fluidized bed,” *Appl. Catal. B Environ.*, vol. 121–122, pp. 214–222, Jun. 2012.

[124] J. Corella, A. Orio, and J.-M. Toledo, “Biomass Gasification with Air in a Fluidized Bed : Exhaustive Tar Elimination with Commercial Steam Reforming Catalysts,” *Energy & Fuels*, vol. 37, no. 8, pp. 702–709, 1999.

[125] S. Rapagnà, N. Jand, A. Kiennemann, and P. U. Foscolo, “Steam-gasification of biomass in a fluidised-bed of olivine particles,” *Biomass and Bioenergy*, vol. 19, pp. 187–197, 2000.

[126] M. Guisnet and P. Magnoux, “Organic chemistry of coke formation,” *Appl. Catal. A Gen.*, vol. 212, no. 1–2, pp. 83–96, 2001.

[127] C. Wu and P. T. Williams, “Investigation of coke formation on Ni-Mg-Al catalyst for hydrogen production from the catalytic steam pyrolysis-gasification of polypropylene,” *Appl. Catal. B Environ.*, vol. 96, no. 1–2, pp. 198–207, 2010.

[128] P. Dejaifve, A. Auroux, P. C. Gravelle, J. C. V??drine, Z. Gabelica, and E. G. Derouane, “Methanol conversion on acidic ZSM-5, offretite, and mordenite zeolites: A comparative study of the formation and stability of coke deposits,” *J. Catal.*, vol. 70, no. 1, pp. 123–136, 1981.

[129] C. P. B. Quitete, R. C. P. Bittencourt, and M. M. V. M. Souza, “Coking resistance evaluation of tar removal catalysts,” *Catal. Commun.*, vol. 71, pp. 79–83, 2015.

[130] H. Egsgaard, J. Ahrenfeldt, P. Ambus, K. Schaumburg, and U. B. Henriksen, “Gas cleaning with hot char beds studied by stable isotopes,” *J. Anal. Appl. Pyrolysis*, vol. 107, pp. 174–182, 2014.

[131] P. Brandt, E. Larsen, and U. Henriksen, “High tar reduction in a two-stage gasifier,” *Energy and Fuels*, vol. 14, no. 4, pp. 816–819, 2000.

[132] R. J. Evans and T. A. Milne, “Chemistry of tar formation and maturation in the thermochemical conversion of biomass,” *Dev. Thermochem. BIOMASS Convers.*, vol. 2, pp. 803–816, 1996.

[133] M. Campoy, A. Gómez-Barea, D. Fuentes-Cano, and P. Ollero, “Tar Reduction by Primary Measures in an Autothermal Air-Blown Fluidized Bed Biomass Gasifier,” *Ind. Eng. Chem. Res.*, vol. 49, pp. 11294–11301, 2010.

[134] Q. Sun, S. Yu, F. Wang, and J. Wang, “Decomposition and gasification of pyrolysis volatiles from pine wood through a bed of hot char,” *Fuel*, vol. 90, no. 3, pp. 1041–1048, 2011.

[135] Y. Song, Y. Wang, X. Hu, S. Hu, J. Xiang, L. Zhang, S. Zhang, Z. Min, and C. Z. Li, “Effects of volatile-char interactions on in situ destruction of nascent tar during the pyrolysis and gasification of biomass. Part I. Roles of nascent char,” *Fuel*, vol. 122, pp. 60–66, 2014.

[136] Y. Song, Y. Wang, X. Hu, S. Hu, J. Xiang, L. Zhang, S. Zhang, Z. Min, and C. Z. Li, “Effects of volatile-char interactions on in situ destruction of nascent tar during the pyrolysis and gasification of biomass. Part II. Roles of steam,” *Fuel*, vol. 122, pp. 60–66, 2014.

[137] B. Bayarsaikhan, N. Sonoyama, S. Hosokai, T. Shimada, J. I. Hayashi, C. Z. Li, and T. Chiba, “Inhibition of steam gasification of char by volatiles in a fluidized bed under continuous feeding of a brown coal,” *Fuel*, vol. 85, no. 3, pp. 340–349, 2006.

[138] D. Park, D. Park, S. J. Day, S. J. Day, P. F. Nelson, and P. F. Nelson, “Nitrogen release during reaction of coal char with O 2 , CO 2 , and H 2 O,” *Proc. Combust. Inst.*, vol. 30, no. x, pp. 2169–2175, 2005.

[139] M. L. Boroson, J. B. Howard, J. P. Longwell, and W. a. Peters, “Heterogeneous cracking of wood pyrolysis tars over fresh wood char surfaces,” *Energy & Fuels*, vol. 3, no. 6, pp. 735–740, 1989.

[140] P. Wang, L. Jin, J. Liu, S. Zhu, and H. Hu, “Isotope analysis for understanding the tar formation in the integrated process of coal pyrolysis with CO2 reforming of methane,” *Energy & Fuels*, vol. 24, no. 8, pp. 4402–4407, 2010.

[141] C. Dong, L. Jin, Y. Li, Y. Zhou, L. Zou, and H. Hu, “Integrated Process of Coal Pyrolysis with

Steam Reforming of Methane for Improving the Tar Yield," 2014.

[142] L. Jin, X. Zhou, X. He, and H. Hu, "Integrated coal pyrolysis with methane aromatization over Mo/HZSM-5 for improving tar yield," *Fuel*, vol. 114, pp. 187–190, 2013.

[143] L. Wei, Y. S. Tan, Y. Z. Han, J. T. Zhao, J. Wu, and D. Zhang, "Hydrogen production by methane cracking over different coal chars," *Fuel*, vol. 90, no. 11, pp. 3473–3479, 2011.

[144] a. Dufour, a. Celzard, V. Fierro, E. Martin, F. Broust, and a. Zoulalian, "Catalytic decomposition of methane over a wood char concurrently activated by a pyrolysis gas," *Appl. Catal. A Gen.*, vol. 346, no. 1–2, pp. 164–173, 2008.

[145] M. Asadullah, S. Zhang, Z. Min, P. Yimsiri, and C. Z. Li, "Effects of biomass char structure on its gasification reactivity," *Bioresour. Technol.*, vol. 101, no. 20, pp. 7935–7943, 2010.

[146] A. Demirbas and G. Arin, "An Overview of Biomass Pyrolysis," *Energy Sources*, vol. 24, no. 5, pp. 471–482, May 2002.

[147] S. Xiu and A. Shahbazi, "Bio-oil production and upgrading research: A review," *Renew. Sustain. Energy Rev.*, vol. 16, no. 7, pp. 4406–4414, Sep. 2012.

[148] K. M. Bryden and M. J. Hagge, "Modeling the combined impact of moisture and char shrinkage on the pyrolysis of a biomass particle," *Fuel*, vol. 82, no. 13, pp. 1633–1644, Sep. 2003.

[149] C. M. van der Meijden, J. W. Könemann, W. Sierhuis, A. van der Drift, and G. Rietveld, "Wood to Bio-Methane demonstration project in the Netherlands," 2013.

[150] M. Kumar and R. C. Gupta, "Scanning electron microscopic study of acacia and eucalyptus wood chars," *J. Mater. Sci.*, vol. 30, no. 2, pp. 544–551, 1995.

[151] A. Gani and I. Naruse, "Effect of cellulose and lignin content on pyrolysis and combustion characteristics for several types of biomass," *Renew. Energy*, vol. 32, no. 4, pp. 649–661, Apr. 2007.

[152] M. B. Fernandes, J. O. Skjemstad, B. B. Johnson, J. D. Wells, and P. Brooks, "Characterization of carbonaceous combustion residues. I. Morphological, elemental and spectroscopic features.," *Chemosphere*, vol. 51, no. 8, pp. 785–95, Jun. 2003.

[153] M. Dall'Ora, P. A. Jensen, and A. D. Jensen, "Suspension Combustion of Wood: Influence of Pyrolysis Conditions on Char Yield, Morphology, and Reactivity," *Energy & Fuels*, vol. 22, no. 5, pp. 2955–2962, Sep. 2008.

[154] "NIOSH Pocket Guide to Chemical Hazards," *Center for Disease Control and Prevention*. [Online]. Available: http://www.cdc.gov/niosh/npg/npgd0110.html. [Accessed: 13-Apr-2015].

[155] M. R. Hajaligol, J. B. Howard, and W. A. Peters, "An experimental and modeling study of pressure effects on tar release by rapid pyrolysis of cellulose sheets in a screen heater," *Combust. Flame*, vol. 95, no. 1–2, pp. 47–60, Oct. 1993.

[156] U. Wolfesberger, I. Aigner, and H. Hofbauer, "Tar Content and Composition in Producer Gas of Fluidized Bed Gasification of Wood — Influence of Temperature and Pressure," *Environ. Prog. Sustain. Energy*, vol. 28, no. 3, 2009.

[157] A. Dufour, B. Ouartassi, R. Bounaceur, and A. Zoulalian, "Modelling intra-particle

phenomena of biomass pyrolysis," *Chem. Eng. Res. Des.*, vol. 89, no. 10, pp. 2136–2146, Oct. 2011.

[158] U. Wolfesberger-schwabl, I. Aigner, and H. Hofbauer, "Mechanism of Tar Generation during Fluidized Bed Gasification and Low Temperature Pyrolysis," *Ind. Eng. Chem. Res.*, vol. 51, pp. 13001–13007, 2012.

[159] C. Hanping, L. Bin, Y. Haiping, Y. Guolai, and Z. Shihong, "Experimental Investigation of Biomass Gasification in a Fluidized Bed Reactor," *Energy & Fuels*, vol. 22, no. 14, pp. 3493–3498, 2008.

[160] I. Narváez, A. Orio, M. P. Aznar, and J. Corella, "Biomass Gasification with Air in an Atmospheric Bubbling Fluidized Bed. Effect of Six Operational Variables on the Quality of the Produced Raw Gas," *Ind. Eng. Chem. Res.*, vol. 35, no. 7, pp. 2110–2120, 1996.

[161] Y. Chhiti, M. Peyrot, and S. Salvador, "Soot formation and oxidation during bio-oil gasification: experiments and modeling," *J. Energy Chem.*, vol. 22, no. 5, pp. 701–709, Sep. 2013.

[162] D. Kunii and O. Levenspiel, "Bubbling bed model," *I&EC Fundam.*, vol. 7, no. 3, pp. 446–452, 1968.

[163] K. Yoshida, D. Kunii, and O. Levenspiel, "Axial dispersion of gas in bubbling fluidized beds," *Ind. Eng. Chem. Fundam.*, vol. 8, no. 3, pp. 402–406, 1969.

[164] J. F. Davidson, R. Clift, and D. Harrison, *fluidization*, Second edi. Academic press inc., 1985.

[165] T. Chiba and H. Kobayashi, "Solids exchange between the bubble wake and the emulsion phase in a gas-fluidized bed," *J. Chem. Eng. japan*, vol. 10, no. 3, pp. 206–210, 1977.

[166] O. Kunii, D, Levenspiel, "Bubbling bed model for kinetic processes in fluidized beds," *I&EC Process Des. Dev.*, vol. 7, no. 4, pp. 481–492, 1968.

[167] C. Chavarie and J. R. Grace, "Performance Analysis of a Fluidized Bed Reactor. II. Observed reactor behavior compared with simple two-phase models," *Ind. Eng. Chem. Fundamen.*, vol. 14, no. 2, pp. 79–86, 1975.

[168] C. Chavarie and J. R. Grace, "Performance Analysis of a fluidized bed reactor. III. modification and extension of canventional two-phase models," *Ind. Eng. Chem. Fundam.*, vol. 14, no. 2, pp. 86–91, 1975.

[169] B. V. Babu and a. S. Chaurasia, "Heat transfer and kinetics in the pyrolysis of shrinking biomass particle," *Chem. Eng. Sci.*, vol. 59, no. 10, pp. 1999–2012, May 2004.

[170] B. . Babu and a. . Chaurasia, "Modeling for pyrolysis of solid particle: kinetics and heat transfer effects," *Energy Convers. Manag.*, vol. 44, no. 14, pp. 2251–2275, Aug. 2003.

[171] C. A. Koufopanos, N. Papayannakos, G. Maschio, and A. Lucchesi, "Modelling of the pyrolysis of biomass particles. Studies on Kinetics, Thermal and Heat Transfer Effects.," *Can. J. Chem. Eng.*, vol. 69, 1991.

[172] R. S. MILLER and J. BELLAN, "A Generalized Biomass Pyrolysis Model Based on Superimposed Cellulose, Hemicelluloseand Liqnin Kinetics," *Combust. Sci. Technol.*, vol. 126, no. 1–6, pp. 97–137, 1997.

[173] C. M. van der Meijden, H. J. Veringa, B. J. Vreugdenhil, and B. van der Drift, “Bioenergy II: Scale-Up of the Milena Biomass Gasification Process,” *Int. J. Chem. React. Eng.*, vol. 7, no. 1, 2009.

[174] H. Zheng and R. Vance Morey, “An unsteady-state two-phase kinetic model for corn stover fluidized bed steam gasification process,” *Fuel Process. Technol.*, vol. 124, pp. 11–20, Aug. 2014.

[175] J. Blondeau and H. Jeanmart, “Biomass pyrolysis at high temperatures: Prediction of gaseous species yields from an anisotropic particle,” *Biomass and Bioenergy*, vol. 41, pp. 107–121, Jun. 2012.

[176] C. Di Blasi, “Modeling chemical and physical processes of wood and biomass pyrolysis,” *Prog. Energy Combust. Sci.*, vol. 34, no. 1, pp. 47–90, Feb. 2008.

[177] Y. Haseli, J. a. van Oijen, and L. P. H. de Goey, “Modeling biomass particle pyrolysis with temperature-dependent heat of reactions,” *J. Anal. Appl. Pyrolysis*, vol. 90, no. 2, pp. 140–154, Mar. 2011.

[178] W.-C. R. Chan, M. Kelbon, and B. B. Krieger, “Modelling and experimental verification of physical and chemical processes during pyrolysis of a large biomass particle,” *Fuel*, vol. 64, no. 11, pp. 1505–1513, Nov. 1985.

[179] Y. Haseli, J. a van Oijen, and L. P. H. de Goey, “A detailed one-dimensional model of combustion of a woody biomass particle.,” *Bioresour. Technol.*, vol. 102, no. 20, pp. 9772–82, Oct. 2011.

[180] C. Di Blasi, “Physico-chemical processes occurring inside a degrading two-dimensional anisotropic porous medium,” *Int. J. Heat Mass Transf.*, vol. 41, no. 24, pp. 4139–4150, Oct. 1998.

[181] E. Ranzi, A. Cuoci, T. Faravelli, A. Frassoldati, G. Migliavacca, S. Pierucci, and S. Sommariva, “Chemical Kinetics of Biomass Pyrolysis,” *Energy & Fuels*, vol. 22, no. 6, pp. 4292–4300, Nov. 2008.

[182] E.-J. Shin, M. R. Nimlos, and R. J. Evans, “A study of the mechanisms of vanillin pyrolysis by mass spectrometry and multivariate analysis,” *Fuel*, vol. 80, no. 12, pp. 1689–1696, 2001.

[183] C. Gomez, E. Velo, F. Barontini, and V. Cozzani, “Influence of Secondary Reactions on the Heat of Pyrolysis of Biomass,” *Ind. Eng. Chem. Res.*, vol. 48, no. 23, pp. 10222–10233, Dec. 2009.

[184] D. L. Pyle and C. A. Zaror, “Heat transfer and kinetics in the low temperature pyrolysis of solids,” *Chem. Eng. Sci.*, vol. 39, no. 1, pp. 147–158, 1984.

[185] S. Oka, “Heat and Mass Transfer In Fluidized Beds,” vol. 20031425, pp. 147–210, Sep. 2003.

[186] “Primary Reference Fuels (PRF) + PAH + Real Fuels (Version 1412, December 2014),” *http://creckmodeling.chem.polimi.it*, 2017. [Online]. Available: http://creckmodeling.chem.polimi.it/menu-kinetics/menu-kinetics-detailed-mechanisms/menu-kinetics-prf-pah-real-fuels-mechanism.

[187] H. S. Fogler, *Elements of chemical reaction engineering*, Fourth edt. 2006.

[188] J. C. Slattery and R. B. Bird, “Calculation of the diffusion coefficient of dilute gases and of the self-diffusion coefficient of dense gases,” *AIChE J.*, vol. 4, no. 2, pp. 137–142, 1958.

[189] J. K. Morse, “The Structure and Dimensions of the Benzene Ring,” *Proc. Natl. Acad. Sci. U. S. A.*, vol. 13, no. 12, pp. 789–793, 1927.

[190] S. Gerber, F. Behrendt, and M. Oevermann, “An Eulerian modeling approach of wood gasification in a bubbling fluidized bed reactor using char as bed material,” *Fuel*, vol. 89, no. 10, pp. 2903–2917, 2010.

[191] M. Marquevich, X. Farriol, F. Medina, and D. Montane, “Hydrogen production by steam reforming of vegetable oils using nickel-based catalysts,” *Ind. Eng. Chem. Res.*, vol. 40, pp. 4757–4766, 2001.

[192] F. V. Tinaut, A. Melgar, J. F. Pérez, and A. Horrillo, “Effect of biomass particle size and air superficial velocity on the gasification process in a downdraft fixed bed gasifier. An experimental and modelling study,” *Fuel Process. Technol.*, vol. 89, no. 11, pp. 1076–1089, 2008.

[193] M. Mayerhofer, S. Fendt, H. Spliethoff, and M. Gaderer, “Fluidized bed gasification of biomass – In bed investigation of gas and tar formation,” *Fuel*, vol. 117, pp. 1248–1255, Jan. 2014.

[194] V. Wilk and H. Hofbauer, “Conversion of fuel nitrogen in a dual fluidized bed steam gasifier,” *Fuel*, vol. 106, pp. 793–801, 2013.

[195] J. C. Schmid, U. Wolfesberger, S. Koppatz, C. Pfeifer, and H. Hofbauer, “Variation of Feedstock in a Dual Fluidized Bed Steam Gasifier — Influence on Product Gas, Tar Content, and Composition,” *Environ. Prog. Sustain. Energy*, vol. 31, no. 2, pp. 205–215, 2012.

[196] M. K. Karmakar and A. B. Datta, “Hydrodynamics of a dual fluidized bed gasifier,” *Adv. Powder Technol.*, vol. 21, no. 5, pp. 521–528, Sep. 2010.

[197] F. Thurner and Mann, “Kinetic investigation of wood pyrolysis,” *Ind. Eng. Chem. Process Des. Dev.*, vol. 20, pp. 482–488, 1981.

[198] C. Hirsch, “Chapter 4 The Finite Difference Method for Structured Grids,” in *Numerical Computation of Internal and External Flows (Second Edition) The Fundamentals of Computational Fluid Dynamics*, .

[199] R. L. Steinberger and R. E. Treybal, “Mass transfer from a solid soluble sphere to a flowing liquid stream,” *AIChE J.*, vol. 6, no. 2, pp. 227–232, 1960.

[200] R. B. Bird, W. E. Stewart, and E. N. Lightfoot, *Transport Phenomena*, 2nd ed. John Wiley and Sons, 2007.

[201] M. D. Morris, “Factorial Sampling Plans for Preliminary Computational Experiments,” *Technometrics*, vol. 33, no. 2, pp. 161–174, 1991.

[202] a Saltelli, M. Ratto, T. Andres, F. Campolongo, J. Cariboni, D. Gatelli, M. Saisana, and S. Tarantola, *Chapter 1: Introduction to Sensitivity Analysis*. 2008.

[203] R. S. S. Miller and J. Bellan, “A Generalized Biomass Pyrolysis Model Based on Superimposed Cellulose, Hemicellulose and Liqnin Kinetics,” *Combust. Sci. Technol.*, vol. 126, no. 1–6, pp. 97–137, Jul. 1997.

[204] C. Di Blasi and C. Branca, “The Effects of Water Leaching on the Isothermal Degradation Kinetics of Straw,” *Ind. Eng. Chem. Res.*, vol. 39, pp. 2169–2174, 2000.

8 APPENDIX

8.1 APPENDIX A – PARTICLE MODEL

List of symbols

$C_p = heat\ capasity \left[\frac{kJ}{kg\ K}\right]$	$\rho = density \left[\frac{kg}{m^3}\right]$
$b = shape\ factor, 0 = slap, 1 = cylender, 2 = sphere[1]$	
$T = Temperatur\ [K]$	$t = time[min]$
$\lambda = thermal\ condutivity \left[\frac{kJ}{min\ m\ K}\right]$	$r = radial\ coordinate\ [m]$
$\Delta H = heat\ of\ reaction \left[\frac{kJ}{kg}\right]$	
$k = reaction\ coeffecient \left[\frac{1}{s}\right]$	$\mu = dynamic\ viscosity\ [Pa\ s]$
$P = pressure[Pa]$	$h_{conduct} = thermal\ heattransfer\ coeeficient \left[\frac{kJ}{min\ m^2\ K}\right]$
$\sigma = Stefan–Boltzmann\ constant \left[\frac{kJ}{min\ m^2 K^4}\right]$	$\epsilon = emissivity\ factor\ [1]$

The general model for heat transport is well known and easily solved, but when kinetics are included it becomes a combination of partial derivatives and ordinary differential equations.

The heat accumulation can be defined in the following manner [170], [171]:

$$\underbrace{\frac{\partial\left(T \cdot C_p(T) \cdot \rho_{total}\right)}{\partial t}}_{\substack{energy\ accumulated\ by\ heat \\ transport\ and\ generation}} = \underbrace{\lambda(T) \cdot \left(\frac{\partial^2 T}{\partial r^2} + \frac{b}{r}\frac{\partial T}{\partial r}\right)}_{\substack{conductive \\ energy\ transport}} + \underbrace{(-\Delta H) \cdot \left(-\frac{\partial \rho_{bio}}{\partial t}\right)}_{energy\ from\ reaction} + \underbrace{T\ C_p(T)\left(\frac{\partial \rho_{total}}{\partial t}\right)}_{energy\ by\ mass\ transport}$$

Both the temperature and the density is assumed to change with respect to time, while the heat capacity is a state equation dependent on temperature.

$$\underbrace{C_p(T) \cdot \rho_{total} \cdot \frac{\partial T}{\partial t} + C_p(T) \cdot T \cdot \frac{\partial \rho_{total}}{\partial t}}_{\substack{energy\ accumulated\ by\ heat \\ transport\ and\ generation}} = \underbrace{\lambda(T) \cdot \left(\frac{\partial^2 T}{\partial r^2} + \frac{b}{r}\frac{\partial T}{\partial r}\right)}_{\substack{conductive \\ energy\ transport}} + \underbrace{(-\Delta H) \cdot \left(-\frac{\partial \rho_{bio}}{\partial t}\right)}_{energy\ from\ reaction} + \underbrace{T\ C_p(T)\left(\frac{\partial \rho_{total}}{\partial t}\right)}_{energy\ by\ mass\ transport}$$

At the centre of the particle (r=0 i=0) a symmetry condition is assumed, for this the equation cannot be evaluated as there is divided with zero. Instead the following relation is used as done in [170]:

$$\lim_{r\to 0}\frac{1}{r}\frac{\partial T}{\partial r}=\frac{\partial^2 T}{\partial r^2}$$

For the edge of the particle (r=R) the heat is added by a conductive and radiation term and transported into the rest of the particle.

$$\lambda(T)\cdot\frac{\partial T}{\partial r}=h_{conduc}\left(T_f-T\right)+\sigma\cdot\epsilon\cdot\left(T_f^4-T^4\right)$$

As temperature is dependent, on both location and time, this system cannot be solved directly with the ode solver in matlab; neither can the PDE solver be use for solving the system because it will be a combination of PDE and ODEs. To solve the combination of equations the partial derivatives in the radial direction is discretised, to from a system of odes that may be solved by matlab's ODE solver.

The system is set up with N+1[7] number of points in the radius thus creating *N* number of spaces of the length *h* defined by $h=R/N$.

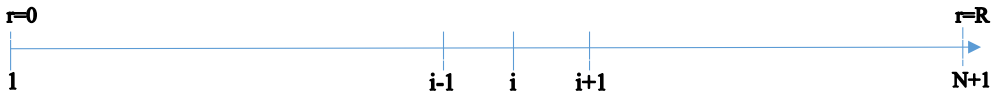

A central difference scheme is used, to discretise the differential system in the radial direction. Thus, we get for the differential equations:

$$\frac{\partial T}{\partial r}=\frac{T_{i+1}-T_{i-1}}{2h}$$

$$\frac{\partial^2 T}{\partial r^2}=\frac{T_{i+1}+T_{i-1}-2T_i}{h^2}$$

For the boundary condition at the surface the differential is defined by the boundary condition. A backwards scheme has been used for the second order derivative, giving:

$$\frac{\partial^2 T}{\partial r^2}=\frac{2}{3\cdot h}\frac{\partial T}{\partial r}-\frac{2}{3\cdot h^2}\left(T_{i-1}-T_{i-2}\right)$$

See Appendix B – Discretisation of particle model for further information.

It is now possible to set up a system of N+1 coupled differential equation describing the energy in the particle

The change in density of the biomass is calculated by the reaction rate of the biomass. At the centre of the particle (i=1), the temperature will be the same on both side because of the symmetry thus, $T_{i+1}=T_{i-1}$.

[7] For programming reasons the first point have index 1 and not 0

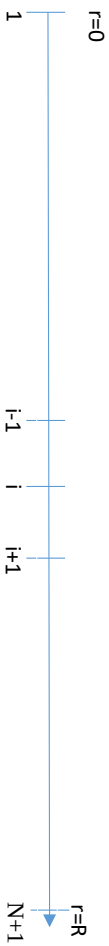

$$\underbrace{\frac{\partial\left(T_1 \cdot C_p(T) \cdot \rho_{total}\right)}{\partial t}}_{\substack{energy\ accumulated\ by\ heat \\ transport\ and\ generation}} = \underbrace{\lambda(T) \cdot \left(\frac{T_{1+1} + T_{1+1} - 2T_1}{h^2} + b\frac{T_{1+1} + T_{1+1} - 2T_1}{h^2}\right)}_{\substack{conductive \\ energy\ transport}} + \underbrace{(-\Delta H) \cdot \left(-\frac{\partial \rho_{bio}}{\partial t}\right)}_{energy\ from\ reaction}$$

For the middle part of the geometry the ordinary differential equation becomes

$$\underbrace{\frac{\partial\left(T_i \cdot C_p(T) \cdot \rho_{total}\right)}{\partial t}}_{\substack{energy\ accumulated\ by\ heat \\ transport\ and\ generation}} = \underbrace{\lambda(T) \cdot \left(\frac{T_{i+1} + T_{i-1} - 2T_i}{h^2} + \frac{b}{h\,(i-1)}\frac{T_{i+1} - T_{i-1}}{2h}\right)}_{\substack{conductive \\ energy\ transport}} + \underbrace{(-\Delta H) \cdot \left(-\frac{\partial \rho_{bio}}{\partial t}\right)}_{energy\ from\ reaction}$$

At the surface the differential for the boundary condition is substituted into the differential equation

$$\underbrace{\frac{\partial\left(T_{N+1} \cdot C_p(T) \cdot \rho_{total}\right)}{\partial t}}_{\substack{energy\ accumulated\ by\ heat \\ transport\ and\ generation}} = \frac{2}{3h}\left(\frac{h_{conduc}}{\lambda}\left(T_f - T\right) + \sigma \cdot \epsilon \cdot \frac{\left(T_f^4 - T^4\right)}{\lambda}\right) - \frac{2}{3\,h^2} \cdot \left(T_{i-1} - T_{i-2}\right) + \frac{2}{h \cdot (i-1)}\left(\frac{h_{conduc}}{\lambda}\left(T_f - T\right) + \sigma \cdot \epsilon \cdot \frac{\left(T_f^4 - T^4\right)}{\lambda}\right) + \underbrace{(-\Delta H) \cdot \left(-\frac{\partial \rho_{bio}}{\partial t}\right)}_{energy\ from\ reaction}$$

The heat capacity is calculated as an avenged fraction of biomass and char components

$$C_p(T) = \sum_{\substack{i=biomass \\ or\ char}} C_{p_i}(T) * x_i$$

where x_i is the weight fraction. The thermal conductivity λ is calculated in analog way.

Temperature is evaluated by the differential output for all radial positions

$$T_i = \frac{\left(T_i \cdot C_p(T) \cdot \rho_{total}\right)}{C_p(T) \cdot \rho_{total}}$$

8.1.1 Simple kinetic scheme

A simple kinetic scheme will be used for the particle model analysis.

Biomass -> tar, gas, and char

$$\frac{\partial \rho_{biomass}}{\partial t} = -k_t \, \rho_{biomass}$$

$$\frac{\partial \rho_{char}}{\partial t} = -k_C \, \rho_{biomass}$$

$$\frac{\partial \rho_{tar}}{\partial t} = -k_L \, \rho_{biomass}$$

$$\frac{\partial \rho_{gas}}{\partial t} = -k_G \, \rho_{biomass}$$

$$\frac{\partial \rho_{total}}{\partial t} = -\frac{\partial \rho_{biomass}}{\partial t} + \frac{\partial \rho_{char}}{\partial t}$$

$$k_t = k_C + k_L + k_G$$

$$k_C = 7.4 \cdot 10^5 \exp\left(\frac{-106.5}{RT}\right)$$

$$k_L = 4.12 \cdot 10^6 \exp\left(\frac{-112.7}{RT}\right)$$

$$k_G = 1.43 \cdot 10^4 \exp\left(\frac{-88.6}{RT}\right)$$

Kinetics are from [197]

8.2 APPENDIX B – DISCRETISATION OF PARTICLE MODEL

Section based on [198]

Discreet representation of the model equation have been used to solve the dependency with respect to position. Often the problems is not a boundary problem but an initial value problem. For the numerical solution of the initial value problems, a finite difference scheme is used. The central difference scheme comes from the Taylor series. The Taylor series is an approximation of a function $f(x)$ around the point a.

$$f(x) = f(a) + \frac{f'(a)}{1!}(x-a) + \frac{f''(a)}{2!}(x-a)^2 + \cdots$$

An approximation of the differential is found from the Taylor series in which the differential appear. The idea of the finite difference is using the definition of a differential

$$f'(x) = \frac{df(x)}{dx} = \lim_{\Delta x \to 0}\left(\frac{f(x+\Delta x) - f(x)}{\Delta x}\right)$$

and remove the limit to get a finite approximation

$$f'(x) \approx \left(\frac{f(x+\Delta x) - f(x)}{\Delta x}\right)$$

With the removal of the limit there is an error, the truncation error, in the result that is lowered as Δx goes towards 0. The Taylor series where x is replaced by $x + \Delta x$ and a is replaced by x, shows that this is indeed an approximation to the differential.

$$f(x+\Delta x) = f(x) + \frac{f'(x)}{1!}\Delta x + O(\Delta x)$$

$$\frac{f(x+\Delta x) - f(x)}{\Delta x} = f'(x) + O(\Delta x)$$

Where $O(\Delta x)$ indicate the order of the truncation error.

By considering grid of equally distributed points we set the value of our function at point i equal to x_i,

$$f(x_i) = f_i$$

Furthermore, we can set $x_i = i\Delta x$

We can now set up the difference schemes used for the modelling. Appling the above relations at point I we obtain the finite difference approximation for the first derivative.

$$\frac{df_i}{dx} = \frac{f_{i+1} - f_i}{\Delta x} + O(\Delta x)$$

This is a first order forward difference approximation. To use this it is required that the value of point i and $i + \Delta x$ is known. We can achieve a backwards difference scheme by using $-\Delta x$.

$$f(x-\Delta x) = f(x) - \frac{f'(x)}{1!}\Delta x + O(\Delta x)$$

$$\frac{df_i}{dx} = \frac{f_i - f_{i-1}}{\Delta x} + O(\Delta x)$$

Both, are called one-sided difference formulas.

The truncation error is of opposite signs. This can be used to give a second order truncation error if the two difference formulas is added together.

$$2\frac{df_i}{dx} = \frac{f_{i+1} - f_i}{\Delta x} + \frac{f_i - f_{i-1}}{\Delta x} + O(\Delta x^2) = \frac{f_{i+1} - f_{i-1}}{\Delta x} + O(\Delta x^2)$$

$$\frac{df_i}{dx} = \frac{f_{i+1} - f_{i-1}}{2\,\Delta x} + O(\Delta x^2)$$

This is known as the central difference formula.

Second order on-sided differences can be expressed in the form

$$\frac{df_i}{dx} = \frac{af_i + bf_{i-1} + cf_{i-2}}{\Delta x} + O(\Delta x^2)$$

The Taylor expression for f_{i-2} and f_{i-1} is set up

$$f_{i-2} = f_i - 2\Delta x\frac{df_i}{dx} + \frac{(2\Delta x)^2}{2}\frac{df_i}{dx} - \frac{(2\Delta x)^3}{6}\frac{df_i}{dx} + \cdots$$

$$f_{i-1} = f_i - \Delta x\frac{df_i}{dx} + \frac{(\Delta x)^2}{2}\frac{df_i}{dx} - \frac{(\Delta x)^3}{6}\frac{df_i}{dx} + \cdots$$

The first equation is multiplied c and the second by b. The equations are added to af_i which leads to

$$af_i + bf_{i-1} + cf_{i-2} = (a + b + c)f_i - \Delta x(b + 2c)\frac{df_i}{dx} + \frac{(\Delta x)^2}{2}(b + 4c)\frac{df_i}{dx} + O(\Delta x^3)$$

To get a comparable equation to what was suggested in the start of the section we need the following to be true

$$a + b + c = 0$$

$$(b + 2c) = -1$$

$$b + 4c = 0$$

From this we get the second order accurate on-sided formula

$$\frac{df_i}{dx} = \frac{3f_i - 4f_{i-1} + f_{i-2}}{2\Delta x} + O(\Delta x^2)$$

The same can be done for a positive development of Δx giving the forward second order on-sided formula

$$\frac{df_i}{dx} = \frac{-3f_i + 4f_{i-1} - f_{i-2}}{2\Delta x} + O(\Delta x^2)$$

8.3 APPENDIX C – MODIFIED BUBBLING BED MODEL

The derivation of the bubbling bed model with the inclusion of a solid out-take at the bottom of the gasifier is shown here.

8.3.1.1 Bubble velocity

A bubbling bed consist of particles that are fluidised by gas. When the bed is fluidised by a gas at a superficial velocity[8] u_0 that is above the minimum fluidisation velocity u_{mf}, gas voids, called bubbles, are seen to rise through the denser continuous phase called the emulsion[163]. The bubble rise velocity of a single bubble relative to the solid is derived by the Davidson model as [162][164]:

$$u_{br} = 0.711(g d_b)^{1/2} \qquad \text{(Eq 8-1)}$$

For small bubbles, the bubble rise velocity is lower than that of the gas percolating through the emulsion $u_{br} < u_f = \frac{u_{mf}}{\epsilon_{mf}}$. The gas in the emulsion will thus travel through the bubble. For larger bubbles $u_{br} > u_f$ a cloud of gas surrounds the bubble, which circulate into the bubble as shown

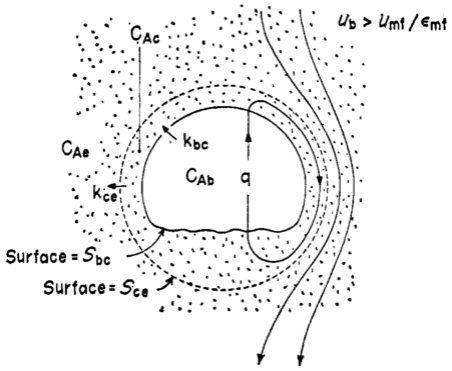

Figure 8-1: Individual contributions to flow of gas between bubble and emulsion [162]

in Figure 2-44.

The cloud is related to the bubble by the following relation [162]

$$\left(\frac{d_c}{d_b}\right)^3 = \frac{u_{br} + 2\,u_f}{u_{br} - u_f} \qquad \text{(Eq 8-2)}$$

For velocities, $\frac{u_{br}}{u_f} > 5$ the cloud size is 10% of that of the bubble. This will be considered a negligible cloud size.

The gas flow in the bubble is $3\,u_{mf}$ at the maximum cross section, and thus the upward volumetric flowrate in the bubble is [162]

[8] Velocity based on an empty reactor

$$q = \frac{3\pi}{4} u_{mf} d_b^2 \quad \text{(Eq 8-3)}$$

From [164] the bubble velocity from a crowd of bubbles can be related to the velocity of a single bubble by

$$u_b = u_{br} + u_0 - u_{mf} \quad \text{(Eq 8-4)}$$

For large bubbles where the bobble caries its own gas with it, the total flow through the two phases is related by[162]

$$u_0 = (1 - \delta)\, u_{mf} + \delta\, u_b \quad \text{(Eq 8-5)}$$

$$u_b = \frac{u_0 - (1 - \delta) u_{mf}}{\delta} \quad \text{(Eq 8-6)}$$

At high gas velocities, u_0 dominates and the bubble velocity may be described by[162]

$$u_b \cong \frac{u_0 - u_{mf}}{\delta} \quad \text{(Eq 8-7)}$$

For low velocities, the bubble fraction is low and thus the same expression will be effective.

Combining (Eq 8-4) and (Eq 8-6) gives an expression for the bubble fraction.

$$\delta = \frac{u_{mf} - u_0}{2 \cdot u_{mf} + \alpha u_{mf} - u_{br} - u_0} \quad \text{(Eq 8-8)}$$

8.3.1.2 Emulsion phase

For the emulsion phase, the upward flow of gas may not be the same as the flow for minimum fluidisation, because of drag from downward flowing particles from the solid circulation. [162]

$$u_e \neq u_f = \frac{u_{mf}}{\epsilon_{mf}} \quad \text{(Eq 8-9)}$$

The bubbles drag a wake of solid behind them, increasing circulation of solids with a downward movement of the solid in the emulsion phase to counter the solid movement. Furthermore, for a dual fluidised bed, circulation of solid out of the bottom of the reactor contribute to an increase downward flow in the emulsion.

The relative velocity between gas and solids remains at u_f. The upward velocity of gas flowing through the emulsion is then [163]

$$u_e = \frac{u_{mf}}{\epsilon_{mf}} - u_s \quad \text{(Eq 8-10)}$$

The solids traveling downwards in the emulsion occupies everything except for the bubble and the wake. The solid transport in the emulsion should be equal to the solid traveling upward in the

wake [162] and that which are being circulated to the combustor for any point under the place of re-entry of bed material from the combustor.

$$(1-\delta-\alpha\delta)u_s = \alpha\delta u_b + \frac{U_{cirk}}{(1-\epsilon_{mf})A} \quad \text{(Eq 8-11)}$$

The solid velocity downwards in the emulsion is thus

$$u_s = \frac{\alpha\delta u_b + \frac{U_{cirk}}{(1-\epsilon_{mf})A}}{1-\delta-\alpha\delta} \quad \text{(Eq 8-12)}$$

Where α is the wake size as a fraction of the bubble size.

$$\alpha = \frac{volume\ of\ wake\ following\ a\ rising\ bubble}{volume\ of\ a\ bubble}$$

It is assumed that gas do not travel with the particles to the combustor. For large fast bubbles with negligible clouds ($u_b > 5u_f$ or $u_0 > 2u_{mf}$) the relationship between total flow of gas and the flow in the emulsion phase and bubble phase is [162]

$$u_0 = (1-\delta-\alpha\delta)\epsilon_{mf}u_e + (\delta + \alpha\delta\epsilon_{mf})u_b \quad \text{(Eq 8-13)}$$

Combining the three previous (the unique equations) equations give the bubble velocity independent of the solid or emulsion velocity

$$u_b = \frac{u_0 + \frac{U_{cirk}}{A(1-\epsilon_{mf})}\epsilon_{mf} - (1-\delta-\alpha\delta)\,u_{mf}}{\delta} \quad \text{(Eq 8-14)}$$

For large gas velocities u_0 will dominate and for low gas velocities the bubble fraction will be low

$$u_b \cong \frac{u_0 - u_{mf}}{\delta} \quad \text{(Eq 8-15)}$$

This indicate that the bubble velocity will increase with an increase of outtake of particles in the bottom, which is counter intuitive. This should be as a consequence of the decreased velocity in the emulsion because of increased drag from the particles and a constant u_0. The circulation contribution is not expected to be high relative to u_0 at vigorous bubbling at which the u_b can be reduced to.

$$u_b \cong \frac{u_0 - u_{mf}}{\delta} \quad \text{(Eq 8-16)}$$

using the first u_b leads to an expression for the velocity in the emulsion phase [162]

$$u_e = \frac{u_{mf}}{\epsilon_{mf}} - \left(\frac{\alpha u_0 + \alpha\epsilon_{mf}\frac{U_{cirk}}{A} + \frac{U_{cirk}}{A}}{1-\delta-\alpha\delta} - \alpha u_{mf}\right) \quad \text{(Eq 8-17)}$$

The term $\alpha\epsilon_{mf}$ is expected to be much smaller than 1 because the size of the wake as a fraction of the bubble (α) is about 0.3 and void at minimum fluidisation (ϵ) is around 0.4. Thus $1 \gg \alpha\epsilon \sim 0.1$ and thus u_e reduces to

$$u_e = \frac{u_{mf}}{\epsilon_{mf}} - \left(\frac{\alpha u_0 + \frac{U_{cirk}}{A}}{1 - \delta - \alpha\delta} - \alpha u_{mf} \right) \quad \text{(Eq 8-18)}$$

For vigorously bubbling, the circulation of the solid may become so large that gas is flowing downwards in the emulsion phase. This flow reversal should occur, without circulation to combustor, when [163]

$$\frac{u_0}{u_{mf}} > 6 \sim 11 \quad \text{(Eq 8-19)}$$

8.4 APPENDIX D – ESTIMATION OF LIGNIN REACTION

The lignin reaction rate is based on devolatilisation rates of kraft lignin in a fluidised bed [78]. They set up a kinetic scheme where lignin forms char tar and gas indecently through competing reactions, and extent it with secondary cracking of tar. From the literature review it is clear that tar and char is form through two different reactions which both forms some gas. The kinetics are estimated from experiments performed in the temperature region 440-560C which is lower than normal gasification conditions. The data is thus extrapolated to a temperature of the reactor conditions of 600 to 850C.

The data is furthermore based on mass devolatilisation and does thus not predict the molar formation of different gases. At a gasification environment it is assumed that the prevailing gas species are CO, CO2, CH4, H2, H2O, and phenol. Measurements of my own lignin sample shows a composition as below

Basis	N %	C %	H %	S %	O % by difference
Mass fraction	0.000	49.622	4.441	16.046	29.891
Mole fraction	0.000	37.882	40.398	4.589	17.131
Coniferyl alcohol mole fraction	0.000	40	48	0	12

This is very close to that of coniferyl alcohol which is a monolignol. One mole of lignin is thus defined to have the formula $C_{37.9}H_{40.4}O_{17.1}$. The primary tar that leaves the lignin has aliphatic side chains that are removed fast in the secondary process at high temperatures. And thus it is assumed that the tar formation rate may show the rate of formation of phenol which is a rather stable tar at gasification conditions because of the isomers stabilising effects. The aliphatic removal will thus result in gas formation that is assumed to be of the prevailing gas species, resulting in the following reaction for the tar reaction.

$$C_{37.9}H_{40.4}O_{17.1} \rightarrow 3.79\ C_6H_5OH + 2.24\ CO_2 + 8.83\ H_2O$$

For the carbon formation it is assumed to follow a condensation reaction inside the particle and not all the aliphatic carbon will be released before it is considered. The carbon is assumed to be pure carbon where it most likely will contain some hydrogen and other inorganics in reality. The methoxy group on conifer alcohol is assumed to form methane as the prevailing gas while two of the carbon in the aliphatic carbon is assumed to form CO. The remaining oxygen and hydrogen will be balanced by water and free hydrogen. Thus the carbon formation is given the following reaction:

$$C_{37.9}H_{40.4}O_{17.1} \rightarrow 36.35\ C + 1.55\ CH_4 + 17.1\ H_2O$$

The molar mass of the lignin is thus 769,523g/mol

8.5 APPENDIX E – COMPOSITION OF INSTANT DEVOLATILISATION GAS FROM CELLULOSE AND HEMICELLULOSE

Cellulose and hemicellulose easily broken down to light gases because of the C-O bond in the cyclic structure of the cellulose and hemicellulose unit structure that are easily opened. The resulting aliphatic chain is easily thermally cracked to lighter product that are not considered tar in this regards. This will typically be C2 to C4 components which under high temperature and pyrolytic condition may add to the growth of aromatic components. The condition under gasification environment is however of a lower temperature and they are considered to easily be reformed to CO, CO2, CH4, H2O and H2. Thus these two pseudo components of biomass are assumed to form gas instantaneously to simplify the model.

Cellulose has the formula $(C_6H_{10}O_5)_n$ which give the following reaction:

$$C_6H_{10}O_5 \rightarrow 3CO + 1CO_2 + 2CH_4 + 1H_2$$

For the hemicellulose part we assume xylose $(C_5H_8O_5)_n$ to be the dominant form giving the following reaction:

$$C_5H_8O_5 \rightarrow 3CO + 1CO_2 + 4H_2$$

From the model input basis it is most convenient to give the gas flow rate together with a composition. The formed gas flow rate per kg of pseudo component are calculated for each part and the combined composition is then calculated.

As the gas is at high temperature and low pressure the ideal gas low is valid and the volume of gas per kg of cellulose is thus:

$$\ddot{V} = \frac{R\,T}{P}\frac{m_{ref}\,b}{M}$$

Where $\ddot{V}$ is the volume of gas per kg of pseudo biomass, R is the gas constant, T is the reactor temperature, P is the reactor pressure, m_{ref} is the reference mass of 1kg, M is the molar mass of cellulose, and b is the multiple of mole formed from the conversion of the pseudo biomass.

The concentration of component i is calculate from a combination of the volume and mol formed from the two pseudo biomasses.

$$c_i = \frac{m_1\frac{m_{ref}}{M_1}b_{i1} + m_2\frac{m_{ref}}{M_2}b_{i2}}{m_1\ddot{V}_1 + m_2\ddot{V}_2}$$

Where the subscript i indicate the i'th component and subscript 1 and 2 indicate cellulose and hemicellulose.

8.6 APPENDIX F – MASS TRANSFER COEFFICIENT CALCULATIONS

The mass transfer constant k_c can be determined from its relation to the Sherwood number:

$$Sh = \frac{k_c l_0}{\mathfrak{D}_{AB}}$$

The Sherwood number can be estimated from [199]

$$Sh = Sh_0 + 0.347\left(Re\, Sc^{\frac{1}{2}}\right)^{0.62}$$

$$Sh_0 = 2.0 + 0.569(Gr\, Sc)^{0.25} \text{ for } GrSc < 10^8$$

$$Sh_0 = 2.0 + 0.0254(Gr\, Sc)^{1/3} Sc^{0.244} \text{ for } GrSc > 10^8$$

$$Gr = \frac{g l_0^3 \beta_D \Delta X_A}{v^2}$$

$$Sc = \frac{v}{\mathfrak{D}_{AB}}$$

$$\beta_D = \left|\frac{1}{\rho}\left(\frac{d\rho}{dX_A}\right)\right|$$

$$Re = \frac{l_0 u_0 \rho}{\mu}$$

The concentration gradient of tar is assumed to be small because of the dilution with steam together with a low l_0 which means that the second term of Sh_0 becomes much smaller than 2. The Sherwood number then simplifies to:

$$Sh_0 = 2.0$$

8.7 APPENDIX G – DIFFUSION COEFFICIENT ESTIMATION

The diffusion coefficient is estimated based on the proposed expression for $\mathfrak{D}_{AB}$ at low pressures (<10atm) [188]

$$\mathfrak{D}_{AB} = a\left(\frac{T}{\sqrt{T_{AC}T_{CB}}}\right)^{b}(P_{CA}\,P_{CB})^{\frac{1}{3}}(T_{CA}T_{CB})^{5/12}\left(\frac{1}{M_A}+\frac{1}{M_B}\right)^{1/2}P$$

Where a and b is constants from experiments:

water with nonpolar gases: $a = 3.640 * 10^{-4}$ and $b = 2.334$

nonpolar gas pairs: $a = 2.745 * 10^{-4}$ and $b = 1.823$

T is the temperature in kelvin T_{AC} and T_{CB} is the critical temperature in K for the two components P_{CB} and P_{CA} is the critical pressure of the two components in atm, M is the molecular weight in g/mol and P is the total pressure in atm.

Diffusion coefficient is estimated based on water with nonpolar gases as water is used for steam reforming. And showed for some temperatures within the operation range of the dual fluidised bed

Table 8-1: Diffusivity of compounds in steam in cm^2/s

compound	773K	873K	973K	1073K	1173K
phenol	0,67466278	0,89619611	1,15433318	1,450425949	1,78573648
benzene	0,77235389	1,02596524	1,32148053	1,66044751	2,04431098
cyclopentadiene	NA	NA	NA	NA	NA
methyl phenol	0,59795402	0,79429914	1,02308618	1,285513374	1,58269929
methane	2,23606296	2,97030013	3,82585458	4,807207185	5,91854085
naphthalene	0,56346045	0,74847921	0,96406844	1,211357265	1,49139972
Carbon monoxide	2,35260078	3,12510449	4,02524823	5,057746395	6,2269999
water	1,46241861	1,94262069	2,50216609	3,143985366	3,8708142
carbon dioxide	1,50139427	1,99439446	2,56885259	3,227777325	3,97397724
hydrogen	11,8051665	15,6815296	20,1983804	25,3793754	31,2465979
air	2,39915985	3,18695177	4,10490977	5,157841564	6,35023514
nitrogen	2,42207976	3,2173977	4,14412524	5,207116006	6,41090088

NA= not available

8.8 APPENDIX H – VISCOSITY ESTIMATION

Viscosity is the resistance to flow and the constant for a gas or fluid that tells how forces are propagated perpendicular to a flow direct in the manner:

$$\tau_{yx} = -\mu \frac{dv_x}{dy}$$

Where τ_{yx} is the force per area transported in the y direction with a flow in the x direction, μ is the dynamic viscosity, $\frac{dv_x}{dy}$ is the change of velocity in the x direction with change in the y direction. This definition is an empirical correlation that fits well for molecules weights less than 5000g/mol and is used for Newtonian fluids. Polymeric liquids, suspensions, pastes, slurries, and other fluid are not applicable with this equation and are referred to as non-Newtonian fluids [200].

Kinematic viscosity is defined as the kinematic viscosity divided by the density

$$v = \frac{\mu}{\rho}$$

The dynamic viscosity has units of Pa s. for gases at low density the viscosity increases with temperature while for liquids it decreases. This section will only deal with viscosity for gases as no liquid is of interest in the dual fluidised bed.

The viscosity reaches a limit at low densities. For low density gases it is thus possible to calculate the viscosity. For this the critical viscosity is necessary which can be calculated by the following to equation if triticale values are available [200]:

$$\mu_c = 61.6\ (M\ T_c)^{\frac{1}{2}} (V_c)^{-\frac{2}{3}}$$

$$\mu_c = 7.7\ (M)^{\frac{1}{2}} P_c^{\frac{2}{3}} (T_c)^{-\frac{1}{6}}$$

Where μ_c will be in $\mu\ Pa\ s$, P_c is the critical pressure in atm, T_c is the critical temperature in K, V_c is the critical volume in cm^3/mol.

From the this information and the figure 1.3-1 in [200] the viscosity can be found. The calculation of a combination of gases can be done from an average of the critical values of the component if they are not too different. This is however not the case as we have water mixed with non-polar components.

The pressure for the gasification environment is much small than the critical pressure of any of the contributing components and thus we are at the low density limit. At this point the viscosity should follow a straight line in a double logarithmic plot.

From molecular theory the viscosity of gases at low density may be calculated from Lennard-Jones parameters as:

$$\mu = \frac{5}{16} \frac{\sqrt{\pi m \kappa T}}{\pi \sigma^2 \Omega_\mu} = 2.6693 \cdot 10^{-5} \frac{\sqrt{MT}}{\sigma^2 \Omega_\mu}$$

Where Ω_μ can be found from tables relating to the dimensionless temperature $\kappa T/\varepsilon$. $\kappa T/\varepsilon$ can be estimated from:

$$\frac{\varepsilon}{\kappa} = 0.77T_c$$

$$\sigma = 0.841V_c^{1/3} \text{ or } \sigma = 2.44\left(\frac{T_c}{P_c}\right)^{\frac{1}{3}}$$

Where σ is the characteristic diameter of the molecule in Å, ε is a characteristic energy, M is the molar mass, T is the temperature in K, Ω_μ is a slowly changing function of the dimensionless temperature $\kappa T/\varepsilon$ called the collision integral for viscosity. The viscosity will have the units Pa s.

For a calculation of a mixture of gases the following semi empirical equation can be used [200]:

$$\mu_{mix} = \sum_{\alpha=1}^{N} \frac{x_\alpha \mu_\alpha}{\sum_\beta x_\beta \Phi_{\alpha\beta}}$$

In which the dimensionless quantity $\Phi_{\alpha\beta}$ is defined as

$$\Phi_{\alpha\beta} = \frac{1}{\sqrt{8}}\left(1 + \frac{M_\alpha}{M_\beta}\right)^{-\frac{1}{2}}\left[1 + \left(\frac{\mu_\alpha}{\mu_\beta}\right)^{\frac{1}{2}}\left(\frac{M_\beta}{M_\alpha}\right)^{\frac{1}{4}}\right]^2$$

8.9 APPENDIX I – ESTIMATION OF THE CATALYTIC COKING RATE

The coking rate on the catalyst is assumed to be minimum that of the conversion rate of the catalyst which for a specific Ni catalyst is 1g of tar per gram of catalyst per min [69].

The catalyst conversion rate is assumed to be dependent on the concentration of tar, the number of active sites, and a specific catalytic rate.

For the literature for which the reaction rate has been taken the tar feeding rate is 0.68 g/min and the S/C ratio is 3.8 and thus the feeding rate of steam is 2.6g/min. there is 0.4 m^2 of metal per gram of catalyst.

The tar to steam feeding ratio is thus 0.05. The pressure is assumed to be constant and the temperature 800C. From this the total concentration and the tar concentration can be calculated, which give a tar concentration of 0.56mol/m^3. If under these conditions, there is a conversion rate of 1 g tar per g of catalyst per min this give a reaction rate constant of $9.6 \cdot 10^{-4}$ m/s. This would be an approximated minimum value for the coking rate.

The upper limit would be that of the transport limit. For a particle 0,3mm and an expected concentration for tar in the order of $0{,}08 \mathrm{mol/m^3}$. There is $2.48 \cdot 10^{-8}$ mol/s transferred to a single particle. This result in $0{,}89 \mathrm{\ mol/s/kg_{cat}}$ and a reaction rate constant of 0.028 m/s

8.10 Appendix J – Calculation of elementary effect

The reactor model is simplified to include some rather crude assumptions like isothermal and isobaric conditions. At the same time some parameter values are rather uncertain because they are difficult to obtain or may change during operation. To understand the validity of some of the assumption and the effect of some of the uncertainties, Morris screening is performed. This will which parameters have the largest influence within the value interval.

The parameter that is thought to influence the reactor model considerably with regards to tar, char, and lignin is analysed using a Morris screening to calculate an elementary effect. This will elucidate which parameters are of most importance for the resulting output. Decreased uncertainty of these parameters will increase the model accuracy the most.

The elementary effect is calculated by the following formulary [201]

$$d = \frac{Y(X_1, X_2, \dots, X_i + \Delta X, \dots, X_k) - Y(\boldsymbol{X})}{\Delta X}$$

This is a form of finite derivative expressing of the change in the out-put by a change in the input. In the Morris sampling this change is investigated at a number of different points within the space of the parameter uncertainty giving a more global understanding of the effect of the input parameter. This is thus a measure for the sensitivity that a parameter express.

In [202] they argue that a sensitivity measure as the derivative assumes that all parameters are equally important despite the standard deviation. They suggest to normalise the derivative by multiplying by $\frac{\sigma_{X_i}}{\sigma_Y}$. Which is the standard deviation of the parameter which is changed, divided by the standard deviation of the output. Giving an elementary effect as

$$\mu_i = \frac{Y(X_1, X_2, \dots, X_i + \Delta, \dots, X_k) - Y(\boldsymbol{X})}{\Delta} \frac{\sigma_{X_i}}{\sigma_Y}$$

The mean value may be used to rank the most important factors for the output parameter. The higher the value, the more sensitive the output is to that parameter.

8.11 Appendix K – Content of electronic appendix

Some of the appendixes are only available in electronic form and are listed here

- Torrefaction experiment data
- Detailed set of equations used for the reactor model
- Code for reactor model
- Code for particle model
- Code for gas phase model
- Element analysis
- Excel for catalyst calculation

Department of Chemical and Biochemical Engineering - CHEC
Technical University of Denmark
Søltofts Plads, Building 229
2800 Kgs. Lyngby
Denmark
Phone: +45 45 25 28 00
Web: www.kt.dtu.dk